Spring 5-1-2013

The Enrichment of Stable Cesium and Rubidium in Savannah River Site Soils

Laura K. Zaunbrecher
Georgia State University

Recommended Citation
Zaunbrecher, Laura K., "The Enrichment of Stable Cesium and Rubidium in Savannah River Site Soils." Dissertation, Georgia State University, 2013.
https://scholarworks.gsu.edu/geosciences_diss/4

THE ENRICHMENT OF STABLE CESIUM AND RUBIDIUM IN SAVANNAH RIVER SITE SOILS

by

LAURA K. ZAUNBRECHER

Under the Direction of W. Crawford Elliott

ABSTRACT

The following dissertation investigates the sequestration of Cs and Rb in the wedge zone regions of hydroxy-interlayered vermiculite (HIV), a clay mineral commonly found in the southeastern United States. Savannah River Site soils are studied from the highly contaminated Department of Energy Site. The soils are found to preferentially adsorb Cs and Rb (to a lesser extent) with respect to K and be highly enriched with respect to upper continental crust. Enrichment is found to be a function of weathering progression. Molecular modeling results support the hypothesis that Cs is the sterically favorable ion in the interlayer wedge zone of HIV.

INDEX WORDS: Cesium, Hydroxy-interlayered vermiculite, Clay mineralogy, Molecular modeling

THE ENRICHMENT OF STABLE CESIUM AND RUBIDUM IN SAVANNAH RIVER SITE SOILS

by

LAURA K. ZAUNBRECHER

A Dissertation Submitted in Partial Fulfillment of the Requirements for the Degree of

Doctor of Philosophy

in the College of Arts and Sciences

Georgia State University

2013

THE ENRICHMENT OF STABLE CESIUM AND RUBIDIUM IN SAVANNAH RIVER SITE SOILS

by

LAURA K. ZAUNBRECHER

Committee Chair: W. Crawford Elliott

Committee: Daniel M. Deocampo
Donald Hamelberg
Seth E. Rose

Electronic Version Approved:

Office of Graduate Studies
College of Arts and Sciences
Georgia State University
May 2013

ACKNOWLEDGEMENTS

I would like to acknowledge and extend my gratitude to the Department of Energy Subsurface Biogeochemical Research program for funding this research and Georgia State University and the people here who have made this dissertation possible. First, I wish to thank my mentor and advisor, Dr. W. Crawford Elliott, for giving me the opportunity to complete my PhD. "Dr. E" has helped make me the scientist I am today with unwavering support and guidance through sharing his wealth of knowledge of clay mineralogy and geochemistry. He provided the occasion to grow as a leader, presenter, and critical thinker and made the pursuit of my degree a fun and rewarding experience.

Thank you to all my committee members: Drs. Daniel Deocampo, Seth Rose, and Donald Hamelberg, for taking the time to read and improve this dissertation. I thank Dr. Eirik J. Krogstad for training in ICPMS, sample preparation training, lab techniques and skills, and data interpretation. The co-PI of this project, Dr. J. Marion Wampler, has also been a great mentor to me and dramatically improved the quality of this work. I look forward to continued collaboration work with all of you.

The dissertation could not have been completed without the help of the scientists at the Savannah River National Laboratory: Dr. Dan Kaplan, co- PI on this project, and Dr. Laura Bagwell, who helped with collection of soils and determining location of samples to fit parameters we needed.

I'm also grateful for the opportunity to work with the people in the SSRL lab at Stanford University, where I conducted the synchrotron diffraction work used in this study. I thank Drs. John Chorover and John Barger for the beam line time and training to use the software and equipment. Dr. Nicolas Perdrial of the University of Arizona was crucial to this work. He assisted in the

training and data collection at SSRL and completed the mineral quantifications that were so important to this work.

I thank also Drs. Randall Cygan and Stephanie Teich-McGoldrich of Sandia National Laboratories for taking the time to train me in molecular modeling and completing the molecular dynamics model runs in this work. Dr. Qian Zhao of Georgia Institute of Technology also helped with Materials studio, CLAYFF, and visualization of the molecular modeling data.

I must also acknowledge the people in my lab that made it such a wonderful working environment. Peter Farina, fellow graduate student and radiation safety specialist, and undergraduate Nick Eberts who helped with the ^{137}Cs size fraction experiment. Jack Reed, I loved always breaking the curve in our classes together, and all your help with computer issues through the years! Rebecca Pickering, lab mate and friend, always kind enough to lend an ear whether to discuss science or gossip, love you girl! Saee Razi, thank you for helping with the collection of samples and being a good friend who can always provide much needed laughs. Much thanks to undergraduates Amanda Lanning and Alexandra Simpson who both completed undergraduate theses projects that contributed to this work. I'm so proud of all the hard work you have done and am confident you will both contribute greatly the field of geology.

Outside of the university environment, I have had great support from my triathlon team, Endurance Concepts, and coach Dan Arnett. Thank you for keeping me active and focused on my athletic goals while pursuing my degree and helping my reach new levels of my athletic ability.

There are a certain professors that I would not be here without, John Meriwether, my undergraduate physics advisor, who introduced me to world of radioactive isotopes, and my masters adviser, Kim Cobb, for continued support in the sciences.

Most importantly, I need to thank my large family for their encouragement and support. In particular, my brothers: Nick, for the wisdom only an older brother can provide; Matt, for your competitive nature, which will always be a inspiration to me; Benjamin, for your ability to triumph when others doubt you, your strength and maturity beyond your years, and your God-given brilliance. Thank you all for the healthy dose rivalry and competition in 'Chaos Manor' but mostly the love and support for one another. Analise, my best friend, my twin sister, my other half. We did it. My parents played a crucial role in getting me to where I am today; their encouragement for my love of science and mathematics, and most of all, believing in me. Mom and Dad, thank you for my intellectually stimulating upbringing. Charles Garabedian**, y**ou have been here for me every hard step of the way to finally reaching this accomplishment. Without your faith and support I may not have made it through those all-nighters and painfully stressful deadlines. And of course my incredibly supportive friends: Patrick Reeves, Olivia Rado, Rachel White, Jeanne Menard Elfert, and Krissa Soisson Stiger.

Thank you.

Laura Zaunbrecher
Atlanta, Ga.
January 8, 2013.

TABLE OF CONTENTS

LIST OF TABLES

LIST OF FIGURES

1 INTRODUCTION

The Savannah River Site (SRS) in southwestern South Carolina was a nuclear weapons production site during the 1950's resulting in the generation of extensive quantities of radioactive waste (Figure 1-1). Much of this waste was stored in unlined seepage basins. Presently, radionuclides (e.g. Cs, U, Sr, I) are leaking from these unlined basins into the soils, ground, and surface waters within the SRS. Over 50% of the radioactivity is from ^{137}Cs (*Carlton et al.* 1996), which, as an alkali metal, is readily up taken through biological processes (*Cremers et al.* 1990). Cs is also a highly mobile and soluble ion in surface and ground waters. Thus, it is of great importance to study the sorption and mobility of Cs in soil minerals to understand the subsurface movement and fate of radiocesium at this and other contamination sites.

.

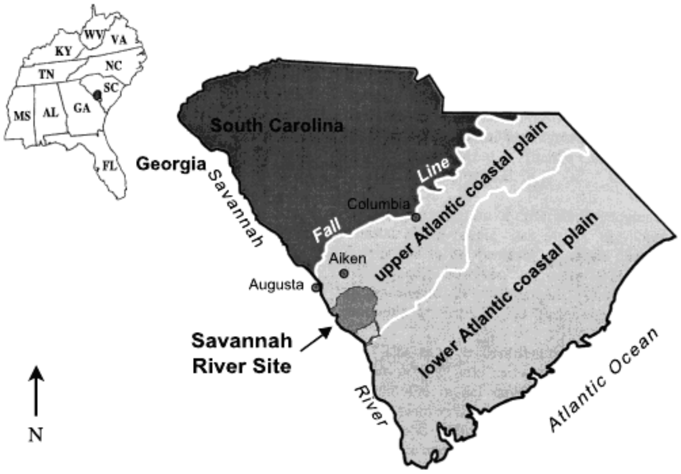

Figure 1-1: Map of the location of the Savannah River Site, in the Southeastern Atlantic Coastal Plain, SC, from *Wyatt and Harris*, (2004).

1.1 Geological Setting of the Savannah River Site

The subsurface lithology at SRS consists of Eocene to Miocene age sedimentary formations of unconsolidated quartz sands, calcareous sediments, and conglomerates, interbedded with thin layers of clay (*Wyatt and Harris*, 2004). Subsurface sediments were deposited in fluvial to marine shelf environments (*Harris et al.* 1997) resulting in the alternating aquifer-confining unit stratigraphy. These formations are generally increasing in thickness from the northwest to the southeast. The basement rock is up to 120-200 meters deep in the study area for this project (*Aadaland*, 1995). Figure 1-2 is a cross section of the lithology and deposition environments at the SRS from Wyatt and Harris, (2004).

The shallow Piedmont aquifer is present with a water table ranging from 0 to 150 feet and is recharged by the Savannah River, surface streams, and precipitation (*Clarke and West*, 1997). This aquifer flows into the deeper underlying South Eastern Coastal Plain aquifer. Several nuclear reactors are located in the recharge zones with subsurface flow amounting to several hundred feet per year in a southwesterly direction (*Anonymous*, 2009).

Soils at the SRS site and in southeastern United States in general are comprised mostly of the clay minerals kaolinite, gibbsite, and Al-hydroxy interlayered vermiculite (HIV) and some carbonates (*Dennehy et al.* 1989; *Fallaw and Price*, 1995; *Karathanasis*, et al. 1983). These soils have been extensively characterized by multiple researchers (*Barnhisel*, 1978; *Rich*, 1968; *Weed and Nelson*, 1962; *Fiskell and Perkins,* 1970; *Bryant and Dixon*, 1963; *Harris et al*, 1992). This study focuses on the Fuquay soil series relative to its ability to sorb Cs and other alkali and alkaline earth metals.

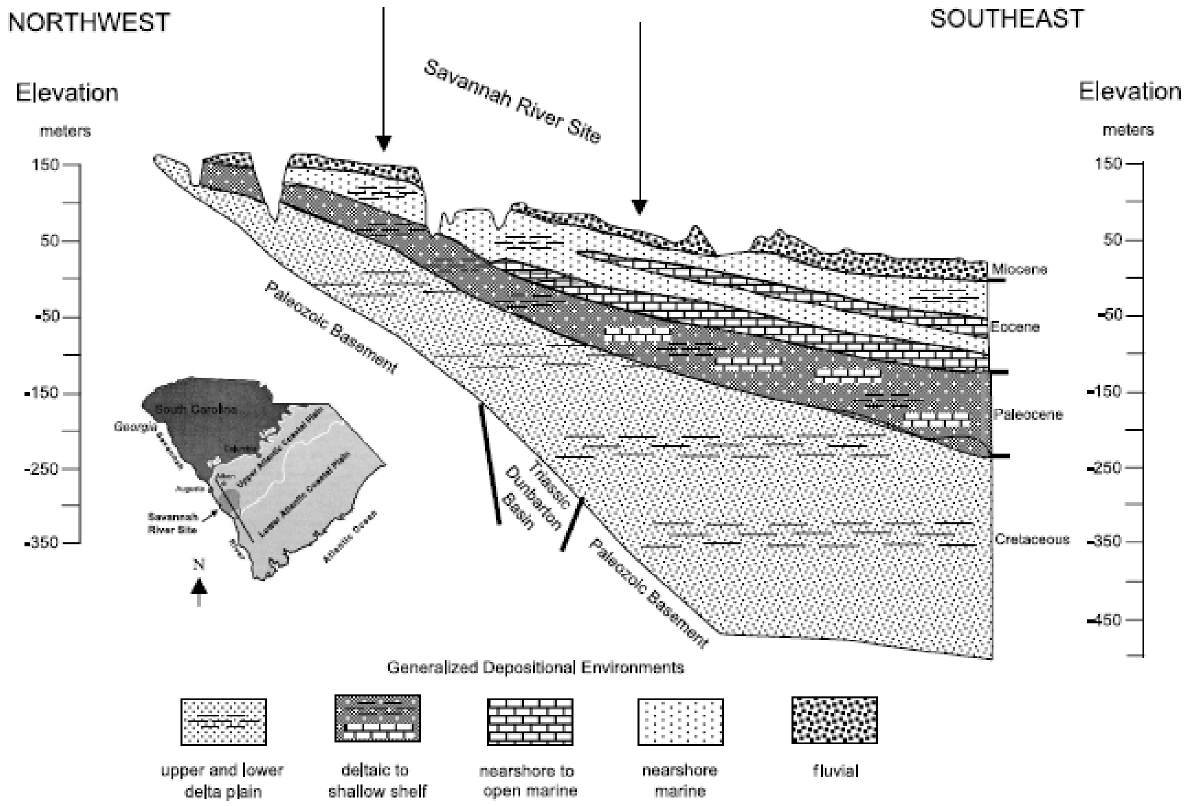

Figure 1-2: Cross section of lithology near the SRS.
The black line on the small South Carolina map represents the cross section location. (From *Wyatt and Harris,* 2004.)

1.2 Cs adsorption and clays

Historically, many researchers have studied the chemical mechanisms of Cs sorption on soils (*Tamura and Jacobs*, 1960; *Schulz et al.* 1960; *Coleman et al.* 1963). Micaceous particles in soils and sediments were found to be highly effective in the sorption and retention of radiocesium (e.g.; *Lomenick and Tamura*, 1965; *Cremers et al.* 1988, *Francis and Brinkley*, 1976; *Maes et al.* 1999; *Zachara,* 2002; *Hinton et al.* 2002). The micaceous mineral illite was found to have a particular affinity for radiocesium (*Tamura and Jacobs*, 1960).

Illite in the Consauga shale near the Oak Ridge National Labratory (ORNL) in Tennessee exhibited a special affinity for Cs and adsorbed higher levels of Cs than other common 2:1 clay minerals (*Tamura and Jacobs*, 1960). They found that ion exchange and surface area together do not explain the sorption of Cs on illite in the shale alone, and that the c-axis spacing of 10 Å may be responsible for the unusually high affinity for Cs with respect to the cation exchange capacity (CEC) of illite.

It was Jacobs and Tamura (1961) that first considered that some of the exchange sites on illite were highly selective towards Cs. A single equilibrium coefficient was sufficient for modeling adsoption on samples of kaolinite and smectite, but could not accurately model the adsorption of Cs by illite. Their observations led them to propose three types of Cs-sorption on 2:1 clay minerals: (1) easily exchangeable Cs (on basal surfaces that is easily removed by leaching cations); (2) "fixed" Cs at lattice edge sites (removable by another sterically favorable cation); and (3) "fixed" Cs in the interlayer region that has been trapped by collapse of the lattice about the cation. They suggested it is the edge sites of illite, though few in number, are sterically favoring Cs and resulting in the multiple equilibrium coefficients needed to model Cs sorption on illite. Sterically favorable refers to the energetically optimal interaction between ions based on size and position relative to surrounding ions.

Schulz et al. (1960) tested the exchange of radiocesium on common clay minerals and found that vermiculite strongly retained Cs in a nonexchangeable form. Various electrolyte solutions were tested to remove Cs from vermiculite without success and the Cs remained fixed. However, Cs adsorbed onto montmorillonite and kaolinite was released back into solution when exposed to other electrolytes.

Similarly, Coleman et al. (1963) studied the ion-exchange of Cs by K and Ca on vermiculite, montmorillonite, and five soil samples. Their results found a high affinity for Cs with respect to K and even more so than Ca on the minerals and soils. Soils containing the dioctahedral vermiculite-chlorite intergrade (now called hydroxy-Al interlayered vermiculite (HIV)) had the greatest affinity for Cs.

Jackson (1963) studied the weathering sequence of mica to illite to vermiculite. When larger hydrated cations replaced ions in the interlayer of mica it created a "frayed edge" where the edge of the mica particle at 10 Å was splayed to expanded layers of 14 Å, the spacing of vermiculite. Jackson (1963) found that weathering products of mica give soils a strong preference for K over Ca. He proposed it was the wedge-zone between the mica core and the frayed edge site (FES) (unweathered to weathered) that allowed for K atoms to reoccupy cavities in the siloxane surfaces which held K in the original mica structure. This results in the rebuilding of the mica lattice. He hypothesized that as weathering progresses, the splaying of the edge of micaceous particles, could be responsible for high selectivity of K ions.

Building on the ideas of Jackson (1963), Rich and Black (1964) stated that K ions are concentrated in weathering mica particles at frayed edge sites or in wedge-shaped zones that can occur deep within the clay particle. The K ions are selected preferentially in these narrowing zones with respect to ions that are strongly hydrated, in this case Ca. Rich (1964) examined acidic soils formed from the weathering of muscovite rich rocks and with a concentration of dioctahedral vermiculite clay. He found that in aqueous solutions with low K concentration (~0.1 meq/L), the K was selected preferentially to larger hydrated cations like Ca^{+2} and Mg^{+2}. Jackson (1963), Rich and Black (1964) and Rich (1964) all attributed a higher affinity for K over Ca to a wedge shaped zone in the interlayer of 2:1 layer phyllosilicates.

Micas, vermiculite, and illite consistently uptake large amounts of Cs in aqueous solutions when saturated with divalent cations such as Ca^{+2}, Sr^{+2}, and Ba^{+2}, but when the saturating ion is monovalent (K^+ or NH_4^+) the uptake is much less (*Sawhney*, 1964). However, the opposite is to be true for kaolinites and montmorillonite. The Cs remained fixed in the illites, vermiculites, and micas after desorption experiments with the divalent cations leading *Sawhney*, (1964) to conclude that Cs sorption is not a typical ion-exchange process and that Cs may become fixed in a nonexchangeable form in mica crystals.

Sawhney (1965) and Sawhney (1966) reported on exchange selectivity of Cs with respect to ions in solution and a large range of concentrations. In 1965, he found that selectivity of Cs-Ca versus Cs-K on illite over the range of 10^{-5} to 10^{-1} meq decreased by a factor of a million and a factor of eight respectively as the concentration of Cs increased. In 1966, he investigated the Cs sorption of Ca- and K-saturated montmorillonite, illite, and vermiculite. He found that illite quickly reached equilibrium with solution as only planar and edge sites are available for exchange. Montmorillonite also reaches equilibrium as its expansibility allows for exchange on all the available sites. Vermiculite, however, varied depending on the saturating cation. In the case of Ca-saturated vermiculite, it continued to sorb Cs beyond 500 hours of study at a slower and slower rate. This is attributed to varying sorption rates of the exchangeable sites. First the planar and edge sites were saturated followed by a slow diffusion of Cs into the interlayers. In the case of K, the sorption decreased with time which is likely attributable to the collapse of the interlayer space around the K ions. Cs as a larger ion can no longer fit in the sites. Sawhney concluded as a result of these studies, that a portion of Cs is fixed in the interlayer and replaces K in illite; that Cs sorption in the 2:1 clay minerals illite and vermiculite do not follow the same exchange relationships derived for dilute aqueous solutions.

Another study conducted at ORNL compared the desorption of radiocesium from sediments at the bottom of a radioactively contaminated creek bed versus lab mineral standards (*Lomenick and Tamura*, 1965). Radioactively contaminated water was drained to this creek for a period of up to 12 years. Desorption of ^{137}Cs from the creek samples was essentially ineffective after 24 hours, with less than 1% of adsorbed ^{137}Cs being removed by different acids and bases. Comparatively, the lab mineral standards that had been spiked with ^{137}Cs for 24 hours released large quantities of the contaminants into the desorbing alkali solutions. This high degree of fixation by the creek bed sediment is due to diffusion of ^{137}Cs into the illite lattice over the course of a decade (*Lomenick and Tamura*, 1965). It illustrated the strong adsorption capacity between ^{137}Cs and soil particles and the limited mobility of ^{137}Cs by chemical processes.

Cation exchange selectivity (CES) of K versus divalent cations on mica, vermiculite, and montmorillonite increased in clays that were K-saturated and dried to induce collapse of expanded interlayer regions to form interlayer wedges (*Dolcater et al.* 1968). The presence of interlayer wedges decreased the CEC of the minerals but increased the CES for K supporting the concept that strongly hydrated cations are sterically hindered at wedge sites.

Comparing the CES of K and Cs on Ca-saturated smectite, Sawhney (1970) found that Cs CES is 10 times higher than K regardless of initial saturating ion concentrations. This selectivity is attributed to the low hydration energy of Cs. He found that "illite and micas had larger selectivity than vermiculite at low concentrations of K^+ and Cs^+ ions, presumably due to larger selectivity of frayed-edge sites in illite and mica than interlayer sites in vermiculite" (*Sawhney,* 1970; *Sawhney*, 1972). Because of the greater layer density charge in vermiculite, layer collapse is more likely in vermiculite than the other minerals, reducing the sites available for exchange and thus the CES (*Sawhney*, 1972).

Bradbury and Baeyens (2000) designed an adsorption model for concentration dependent ^{137}Cs uptake on clay rich rocks with three sites of differing sorption capacities, similar to Brouwer et al (1983). They suggested (1) frayed edge site (FES), (2) type II, and (3) planar sites, were where the uptake of Cs occurs. By studying sorption competition by other ions (K^+, Na^+, NH_4^+, and Ca^{2+}) for the same sites, they adjusted previously constructed models for Cs. The selectivity coefficients in their model are from previous literature and but the model differed from Brouwer et al, (1983) by attributing 20% of the sorption to “site II” whereas the same site in the Brouwer model only accounted for 3% of the CEC on illite. The high affinity sites (FES) only accounted for 0.25% of the CEC and the rest was attributed to the planar edges.

Illite’s molecular structure allows for the selective exchange of Cs and other cations from FES into the mineral’s interlayer (*Sawhney*, 1972; *Francis and Brinkely*, 1976; *Evans et al.* 1983; *Cremers et al.* 1988, *Comans and Hockley*, 1992). This particular molecular environment is especially favorable for the sorption of low hydration energy monovalent cations (*Zachara*, 2002). The low hydration energy of Cs makes it more selective than other monovalent cations in these FES’s (Brouwer *et al.* 1983; Zachara *et al.* 2002). Similarly to illite, the interlayer cations of vermiculite can easily be replaced by cesium or other hydrated cations as weathering progresses (*Sawhney*, 1972).

Soils containing the mineral hydroxy-interlayered vermiculite (HIV) also have a strong affinity for Cs sorption (*Coleman et al.* 1963; *Maes et al.* 1999). Here, the 2:1 layers of the clay minerals splay from the 10 Å mica phase to a 14 Å hydroxy-interlayered phase as a result of weathering. This site acts like the FES's of illite in terms of its preference for large, weakly-hydrated, monovalent cations (*Rich and Black*, 1964; *Rich*, 1964).

Soils at the SRS are weathered to form micaceous minerals such as hydroxy-interlayered vermiculite (HIV) and illite from mica precursors (*Harris et al.* 1992). The HIV and weathered micaceous minerals are believed to sorb significant amounts of Cs at the SRS and elsewhere (*Rich and Black*, 1964; *Elprince et al.* 1977; *Barnhisel and Bertsch*, 1989). The conceptual model of Cs sorption in HIV was developed by Wampler et al. (2012) and is shown in Figure 1-3.

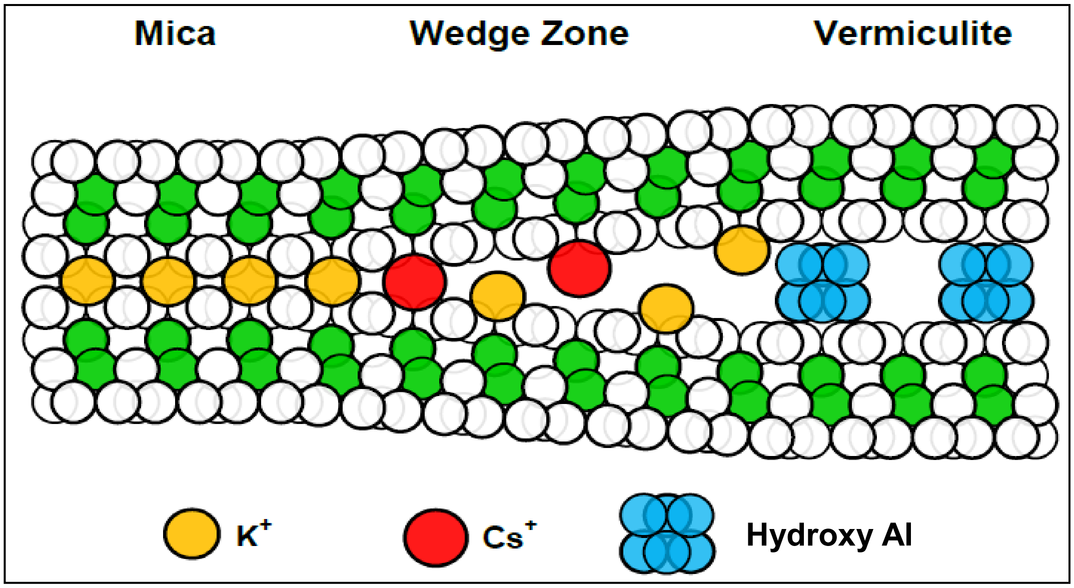

Figure 1-3: Schematic of HIV model
Modified from Wampler et al. (2012), a Schematic cross-section of an interlayer wedge zone in HIV-mica intergrade. This shows the easily accessible sites for Cs sorption and exchange as well as sites near the apices where Cs exchange is sterically hindered and thereby slow (i.e. the difficult to exchange site).

Cesium is sorbed onto illite or onto the HIV-mica intergrade mineral surfaces through ion exchange at three sites: (1) edges sites other than the interlayer, (2) the siloxane surface in the interlayer (regular exchange sites,(RES)), and (3) hard-to-exchange sites in interlayer wedge sites (*Wampler et al.* 2012) (Figure 1-3).

SRS soils provide a good field area to study the sorption of Cs. The SRS soils are well leached, highly weathered, acidic soils, low in concentrations of alkali metals like K. The Cs/K ratio of leachates from this study are interpreted to show that SRS soils have sorbed and retained Cs in exchange sites in clay minerals during pedogenesis. Wampler et al. (2012) showed the Cs/K leachate ratios of SRS soils are well above the average compared to upper continental crust (UCC), and these leachate ratios show that Cs has been retained throughout extensive weathering of these soils while K was removed from exchangeable sites. Thus, the study of how naturally occurring Cs and Rb is retained in soils permit predictions of the sorption of anthropogenic ^{137}Cs released from nuclear facilities. The study of stable Cs is a useful proxy to understand further the sorption of radiocesium by these soils.

Previous work has studied SRS soils from a single depth horizon (*Goto et al.* 2008, *Wampler et al.* 2012), where this dissertation allows the examination of variations in soil properties with depth. These data help us to characterize the evolution of the chemical species in the soils through pedogenesis on a time scale that cannot be investigated in the laboratory. The behavior of natural Cs is important for understanding the long-term implications to radiocesium contaminated environments and the long-term stewardship of radiological disposal facilities.

Kaolinite and HIV are the predominant clay minerals in the near-surface soils of the Savannah River Site (SRS) in South Carolina (*Kaplan et al.* 1997; *Goto et al.* 2008a; *Goto et al.* 2008b). The interlayer wedge zone, where vermiculite grades into mica, is uptaking of radiocesium (*Goto et al.* 2008a; *Goto et al.* 2008b) and shown in Figure 1-3. The exchange site in the interlayer wedges are thought to be highly selective for Cs because of their similarity to the well-known and highly Cs-selective FES's of illite (*e.g. Maes et al.* 1999). The soil mineralogy provides insight to soil properties such as cation exchange capacities, soil pH, and soil order. Specific minerals can have profound effects of soil chemistry and cation exchange capacity. For instance, K is more easily released in trioctahedral minerals versus dioctahedral minerals (*Thiry, et al.* 2005) due to both the orientation of the OH group in the octahedral layer (*Bassett,* 1960; *Sawhney and Voigt,* 1969; *Schroeder,* 1974) and the K-O bond length (*Leonard and Weed*, 1970; *Sawhney*, 1972). Being able to predict the rate of movement of cesium (stable or radiocesium) in soil and ground water and how tightly it is bound to particles preventing its dispersion is beneficial for designing environmental remediation actions to control radionuclide contamination at the SRS.

1.3 HIV and Muscovite Precursor

HIV is a form of vermiculite with hydrous aluminum polymers in the interlayer and a product of the weathering from mica in southeastern US soil (*Harris et al.* 1992). It is often considered an intergrade material between the minerals vermiculite and chlorite. HIV however, lacks the fully developed octahedral sheet in the interlayer like chlorite and instead has islands of hydrated aluminum in the interlayer region. The Al pillars serve to prevent the collapse of interlayer space around other interlayer cations, and reduce the CEC that is normally associated with vermiculite (*Barnhisel and Bertsch*, 1989). The rate of diffusion of ions into interlayer regions of HIV is greatly reduced as a result of "tortuous pathways" created in the interlayer but the hydrous Al pockets (*Harris et al.* 1992). HIV contains wedge zones deep within the interlayer that are associated with remnant mica cores as shown in the conceptual model above (*Wampler et al.* 2012). These mica cores are known to exist as a result of K measurements and the presence of radiogenic Ar that has remained in the mica cores for around 300 million years

(*Naumman*, 2011, *Naumann et al.* 2012). The finding of Appalachian mica-like K-Ar age values for the soil clay fractions is strong support for the presence of remnant muscovite in HIV particles, which supports the inference that the HIV in U.S. southern coastal plain soils is weathered (transformed) from a mica parent mineral (*Harris et al.* 1992; *Naumann et al.* 2012).

1.4 Purpose of the Study

This research tests the hypotheses that: (1) Cs has been favorably enriched with respect to K in the soils at the SRS as a result of long-term weathering processes; (2) that this Cs will negatively affect the ability of soils at the SRS to adsorb ^{137}Cs by occupying the limited and highly selective exchange sites; and that (3) HIV is the major contributing mineral to the concentrating of alkali metals in the SRS soils at a unique wedge structure provides the appropriate environment for selective sorption of Cs.

2 MINERALOGY

2.1 Introduction

This project employs well developed methods for the collection of soils, separation of size fractions, identification of minerals in silt and clay fractions, and measurement of the mass fractions of alkali and alkaline earth metals (described in a separate chapter) (*Pauling*, 1930; *Jackson*, 1969; *Moore and Reynolds*, 1997). The techniques used in this study are described in the following sections.

2.2 Methodology

2.2.1 Field collection and sample splitting

Three soil cores were collected using hand augers from areas of the Savannah River Site (SRS) that do not contain radioactive metals from nuclear reactors or leach ponds at the SRS (Figure 2-1, D. Kaplan personal communication). The auger samples comprise 8 cm to 20 cm core segments. Each sample was collected and emptied into durable plastic bags and labeled.

Core 1, “Fuquay upland-unit soil” (Fuquay), is collected from the Fuquay soil series (loamy, siliceous, thermic Plinthic Paleudults, *Looney et al.* 1990). The Fuquay soil series covers approximately 11.3% of the area at the SRS and was selected for the high clay content in this type of soil (*Looney et al.* 1990, *Wampler et al.* 2012). Core 1 is a thick, zonal soil that is well developed on the upland soil region of the SRS site. It was collected in Spring 2009 by Drs. Daniel Kaplan, W. Crawford Elliott, and J. Marion Wampler (Figures 2-1 and 2-2). The lithofacies of the upland unit are characterized by a highly variable, high-energy, fluvial depositional environment and is either Oligocene or Miocene (*Prowell*, 1996).

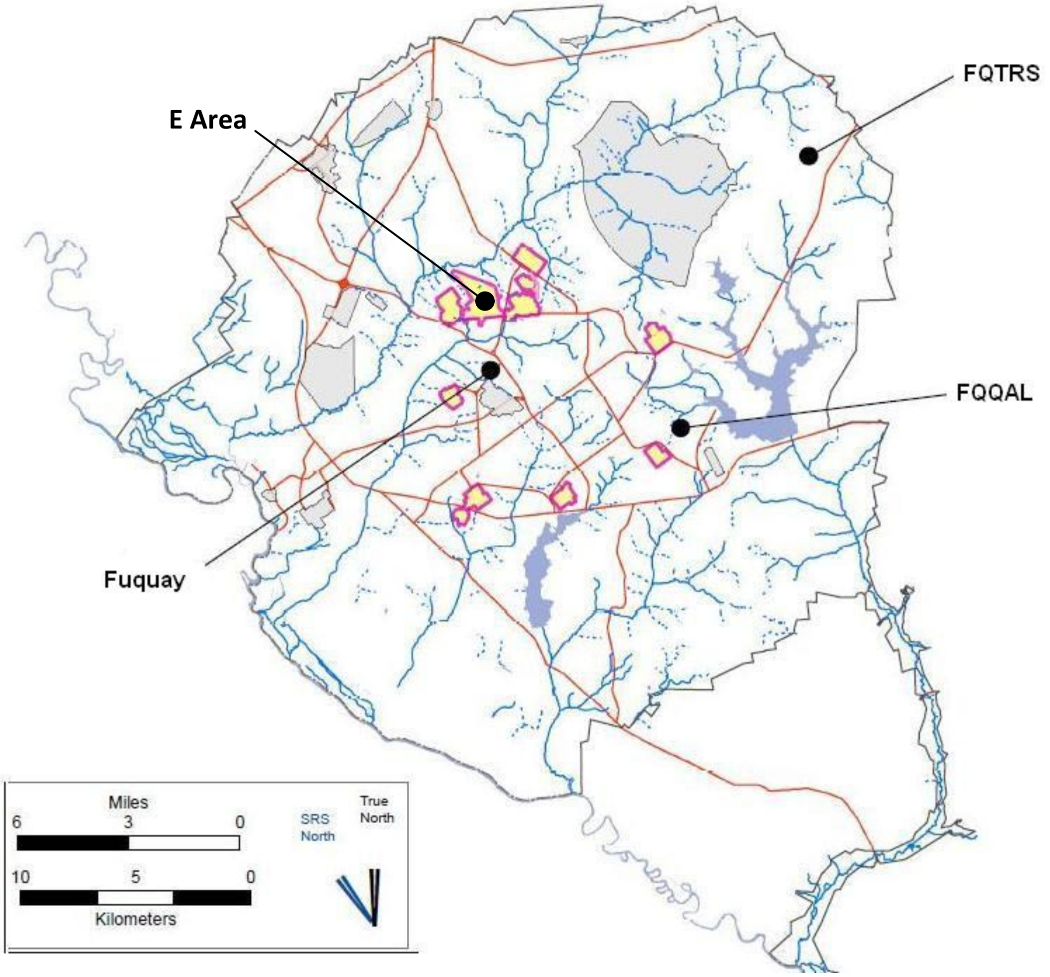

Figure 2-1: Map of the Savannah River Site showing the locations of the three soil cores and E-area is where drill core SRS BGO 3A was taken. Areas of yellow with pink outline are operation/waste-production areas, other non-nuclear areas are in gray, major roads in are in red, and streams are in blue. Map altered from original by Laura Bagwell of Savannah River National Lab.

Cores 2 and 3 were also collected from the Fuquay soil series. Core 2 was collected from the Fuquay series formed on the Tobacco Road Sand (FQTRS). This soil is azonal and immature. The coarse-grained beds and ovoid shaped gravel suggest a shallow marine depositional environment of either Oligocene or Eocene (*Fallaw and Price*, 1995; *Prowell*, 1996). Core 3 was collected from the Fuquay series formed on Quaternary Alluvium (FQQAL). As is the material in Core 2, the soil in Core 3 is azonal. The alluvium is from the modern flood plain and is likely Holocene (*Prowell*, 1996). Cores 2 and 3 were collected in Summer 2010 by Saee Razi of Georgia State University, Drs. Dan Kaplan and Laura Bagwell of the Savannah River National Laboratory, and myself (Figures 2-1 and 2-2).

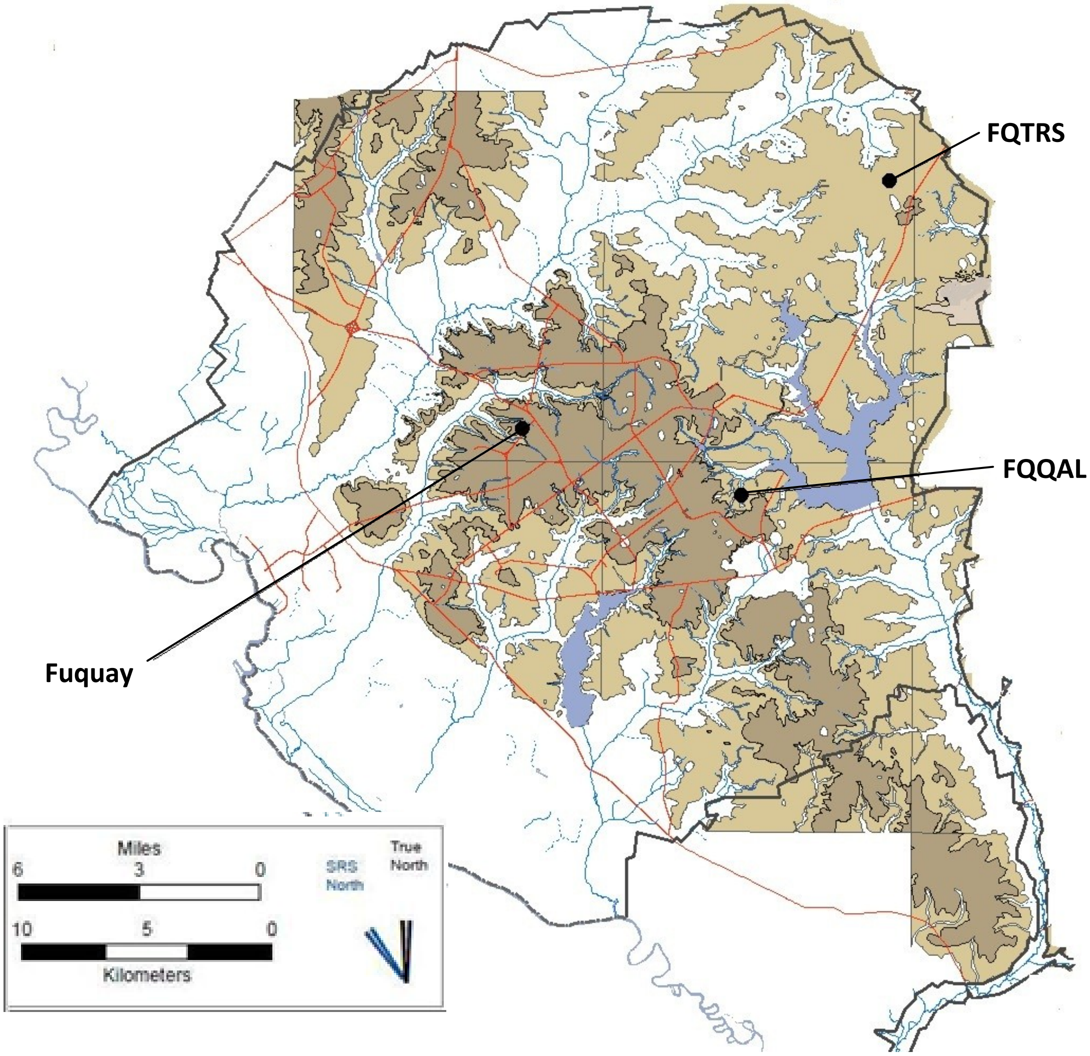

Figure 2-2: Map of Savannah River Soil units
Tobacco Road Sand in tan, upland unit in dark brown, blue is rivers and lakes, and red is the major roads, from V. Rogers soil survey maps. E-Area where drill core taken not shown.

The three soils collected span a range of soil weathering stages found at the SRS. Soils were augered to a depth where further core collection was limited by the length of the auger itself (Fuquay Upland soil, 203 cm deep) or by clay so compacted at depth that further sampling was impracticable (FQQAL and FQTRS, 104 cm and 89 cm respectively).

To determine the mineralogy at depth in the SRS, seven additional samples were obtained from the deep drill core SRS BGO-3A, from an uncontaminated portion of the E-Area (*Grogan et al.* 2008). These samples ranged in depth from 8 meters to 31 meters. This core extends below the water table.

Samples were scanned with a Geiger counter on return to GSU and were not radioactive (<0.1 mR/hr). The soils were passed through a 2 mm screen that was cleaned between samples. The < 2 mm fraction was riffled in a large Humboldt sample splitter, model H-3963 (spacing size, 1 cm), to produce four < 2 mm splits for each soil sample. One sample split was used for mineralogic analysis. Two other splits were used for chemical studies. One of the splits is unused at this time. The use of a sample splitter ensured the production of four representative splits of a single field sample.

2.2.2 Chemical Pretreatments and size separations

Prior to size separation into sand, silt, and clay fractions for mineralogic determination, the bulk samples were treated chemically to remove carbonate cements, organic matter, and ferric oxides following the procedures of Jackson (1969). Forty grams of soil were dispersed in 200 mL of 1 M sodium acetate-acetic acid buffer solution (NaOAc buffer, pH = 5) to begin the Jackson treatments (*Jackson*, 1969). Buffer solution was at a pH of 5 to ensure that the phyllosilicate minerals did not dissolve. Each dispersed soil was heated overnight in an oven at 50°C to dissolve carbonate cements. After completing this treatment, the sediment was transferred to centrifuge tubes and spun at 1100 rpm (285 rcf) for 7-8 minutes. Supernatant solution was discarded and an additional ~50 mL of sodium acetate buffer added to begin rinsing of the remaining solids by repeated addition of buffer solution and centrifugation. After one hour, if no further reaction was observed, the samples were centrifuged again and the supernatant solution was discarded, leaving the soil material saturated in Na and wetted by the buffer solution.

Organic matter was removed by addition of 10 mL of 30% hydrogen peroxide at room temperature. After one hour, an additional 10 mL was added and allowed to react overnight in an oven at 50°C. Once the natant was clear, the solids were spun down in the centrifuge and rinsed twice with NaOAc, then rinsed once with methanol.

Ferric oxides were removed by the citrate-bicarbonate-dithionite (CBD) method (*Jackson*, 1969). This method uses Na-dithionate to reduce ferric iron cements, Na-bicarbonate as a buffer of the pH to keep the solution near neutral, and Na-citrate as the chelating agent for the reduced iron. Forty mL of 0.3 M Na-citrate and 5 mL of 1 M Na-bicarbonate ($NaHCO_3$) were added to and thoroughly mixed with each sample. The mixtures were allowed to react for one hour in a water bath at 50°C. Sodium hyposulfite (sodium dithionate) ($Na_2O_4S_2$) (1 g) was stirred into the sediments three times at intervals of 5 minutes. Lastly, 15 mL of methanol was added to encourage flocculation. The samples were then centrifuged at 1100 rpm (285 rcf) for 8 minutes and the supernatant discarded. The samples were then rinsed with NaOAc buffer solution twice and once with methanol to be ready for size separations.

The solids remaining after pre-treatments were separated into sand, silt, and clay size fractions by standard timed settling techniques *Jackson* (1969). Particles were suspended in deionized water and allowed to settle for 20 seconds per 5 cm of fluid for the sand fraction (50 µm – 2 mm), ~150 seconds per 5 cm of fluid for the course silt fraction (50 µm - 20 µm), and ~8 hours per 5 cm for the fine-silt fraction (20 µm – 2 µm). The remaining fluid held the clay fraction (<2 µm). Each sand and silt fraction was dried and weighed, and the percentages of sand, coarse silt, and fine silt were calculated from the mass values. The percentage of clay was calculated by difference.

One untreated sample split from each core was sieved on a 62 µm screen to produce a <62 µm size fraction for chemical analyses as described later in Section 3.2.1.

2.2.3 X-ray Diffractometry

X-ray diffraction (XRD) methods have been used to identify the minerals in soil and sediment clay fractions since the 1930s (*Pauling*, 1930). These minerals typically cannot be identified by conventional petrographic techniques because of their small size. XRD was employed to identify the minerals present in the separated clay and fine silt fractions. A Phillips Norelco X-ray Diffractometer, Model 12045 at GSU was used in this study. Clay suspensions were dropped on to glass petrographic slides (23 mm×46 mm) and dried in air, producing air-dried, oriented mounts (*Moore and Reynolds*, 1997). The air-dried mounts were scanned under standard CuKα radiation (produced at 35 kV and 15 mA) in steps of 0.02° 2Θ through an angle range of 2-32° 2Θ for a counting time of 1 or 2 seconds per step. The MDI program 'Talk' controlled the scanning and acquisition of diffraction data. The MDI program Jade was used to determine *d* values of diffraction peaks.

Minerals were identified from the *d* values of the peaks observed in these diffraction scans (*Moore and Reynolds*, 1997) (Table 2-1). Initial identifications of phyllosilicate minerals were based on the 00*l* reflections from the air-dried mounts. Some minerals share the same *d* values and to differentiate between, for example, vermiculite, Al-hydroxy-interlayered vermiculite (HIV), smectite, and chlorite, which all have a ~14.4 Å *d* value, additional treatments were employed to look for expansion or contraction of layers that are characteristic of each mineral. Treatments included: 1) overnight saturation in glycol vapors; (2) K-saturation; (3-5) K-saturation and heated to (3) 110°C, (4) 330°C, and (5) 550°C.

Table 2-1: Common phyllosilicate mineral *d* values with treatments (Å)*

Mineral	**Air-dried (Å)**	**Glycol Saturated**	**K saturated**	**Heated to 550°C**
Kaolinite	7.2	7.2	7.2	-
Illite	10.0	10.0	10.0	10.0
Gibbsite	4.8	4.8	4.8	-
Quartz	4.25, 3.33	4.25, 3.33	4.25. 3.33	4.25, 3.33
HIV	14.4	14.4	14.4	~12.5-10.0
Smectite	14.4	17.0	~11.5	~9.5
Chlorite	14.4	14.4	14.4	14.4
Vermiculite	14.4	14.4	10.5	~10

*From Moore and Reynolds (1997)

The mineral HIV is identified by the lack of expansion with glycol vapors and by the partial collapse of the interlayers of K-saturated samples (the 00*1* peak shifts toward 10Å) upon sequential heating to 110°C, 330°C, and 550°C. The greater the degree of hydroxy-interlayer filling, the greater the temperature required for the collapse to occur, and the smaller the degree of collapse of the interlayer, the smaller the shift of the 00*1* peak (*Barnhisel and Bertsch*, 1989).

Some clays curled on the slides regardless of the pretreatments applied. This curling prevents the use of conventional XRD of an oriented mount. Possible causes of these ‘peelers’ are: (1) high concentrations of quartz or other angular crystals or grains that distort the orientation of the clay platelets, (2) clay minerals that remain partially flocculated during sample preparation and destroy orientation, (3) a large range in the size of the particles on the slide, causing ultra-fine particles to remain on top while larger particles sink to the bottom of the slurry on the slide, leading to ‘differential shrinkage’ while drying, or (4) the presence of “gelatinous, hydrated colloidal material” including iron hydroxides and organic material (*Moore and*

Reynolds, 1997). The last of these possible causes is not likely in the case of clays that have undergone Jackson's treatments to remove any organics, iron oxides, and amorphous materials.

For clay samples that curled during traditional air-drying techniques to make slides, the Millipore® Filter Transfer Method was used. Samples FQ138-157, FQ158-178, and FQ179-203 (FQ is from the Fuquay core and numbers indicate range in sample depths in cm) peeled after multiple rinses and could not be scanned as oriented clay mounts. The Millipore Filter Transfer Method uses a vacuum filter apparatus designed by the Millipore Corporation. It includes a side-necked vacuum flask with a funnel shaped glass filter overlain by a reservoir, all clamped together. Filter paper that retains the desired size fraction is placed over the filter piece and the sample is poured into the reservoir in suspension. Applying a vacuum pulls the water through the filter leaving a thin layer of clay on the filter paper. After unclamping the apparatus and removing the filter paper, it is inverted onto a glass slide and placed into an oven at 50°C. After 3-6 minutes, a noticeable change of the paper resulting in the appearance of streaks indicates that the clay sample is at the correct moisture for the paper to be removed from the slide, leaving the sample behind.

Another possible cause of clay curling is the presences of halloysite, which curls upon drying. Testing for halloysite was done by spraying air-dried clay on slides with formamide. Formamide treatment expands halloysite after an hour of saturation, causing an easily identifiable peak at 10 Å, formed at the expense of the original kaolinite/halloysite 7.2Å 00*1* peak (*Churchman et al.* 1984).

The mineralogy of the 2-20 µm size fractions was determined using XRD through the same set of angles and conditions. The mineralogy of the fine silt was determined because of preliminary findings (Sections 2.2.4, and 2.3.4) that suggested there are minerals capable of sorbing cations in this size fraction.

2.2.4 ^{137}Cesium Size Fraction Experiment

Two bulk soil samples (20 g)from the Fuquay Core (Core 1) were spiked with 1 microcurie of ^{137}Cs at the beginning of the Jackson treatments to remove carbonate cements, organic matter and iron (III) oxides. Aliquots of supernatant solution were taken at each step of the Jackson treatments and measured for ^{137}Cs activity with a Packard LA1600 liquid scintillation counter. This experiment was performed to see if Cs, as represented by ^{137}Cs, was bound tightly during the procedure to ensure that the treatments were not removing any Cs prior to measurement of stable Cs with ICP-MS (Section 3.2.1). After size separations, each of the four size fractions (sand, coarse silt, fine silt, and clay) was measured for ^{137}Cs activity using the same scintillation detector to determine how the ^{137}Cs was distributed between the solid and the supernatant. Standard error is estimated at 3-5% (P. Farina, personal communication, 2012).

2.2.5 Synchrotron Radiation Diffractometry

High intensity synchrotron radiation enables the detection and quantification of small amounts of illite or mica in clays not detected with traditional XRD. The presence of small amounts of mica in Fuquay clay fractions has been inferred from the Paleozoic K-Ar ages (250-350 Ma) of leached (10% nitric acid leaches) and unleached soils (*Naumann*, 2010; *Naumann et al*, 2012) but was not detected by traditional XRD (*Goto*, 2001; this study). More generally, this methodology permits the acquisition of diffraction data useful for semi-quantitative determinations of minerals present in the clay fractions of the SRS soils.

Synchrotron X-ray diffraction scans were performed at the Stanford Synchrotron Radiation Lightsource (SSRL). Powdered and air-dried clays were mounted between two layers of Scotch Magic Tape® to obtain a homogeneous thin layer sample which could be mounted in a vertical sample holder. Analysis was conducted on Beam Line 11-3 using Se Kα radiation from 2-60° 2Θ (http://www-ssrl.slac.stanford.edu/beamlines/bl11-3/). The beam was calibrated using a laboratory standard of finely ground LaB_6 crystals. Data were reduced using the Advanced Diffraction Machine (ADM) software (*Lande et al.* 2007). A pattern was taken of just the tape to provide a background subtraction pattern. The Debye ring patterns acquired by synchrotron analysis were converted to Cu Kα radiation wavelengths and plotted in terms of intensity versus 2Θ by Dr. Nico Perdrial of the University of Arizona using the ADM software.

2.2.6 Rietveld modeling for quantitative analysis

Quantitative phase analysis was performed using the Rietveld module included in the X'Pert HighScore Plus software. The procedure for analysis was adapted from the procedure described by *Perdrial et al*. (2011). The modeling is done by using known reference XRD patterns from the American Mineralogical Crystal Structure Database (AMCSD) database (*Downs and Hall-Wallace*, 2003) and overlapping the synchrotron pattern with known patterns at varying percent contribution to the total pattern. The contribution from each known pattern is adjusted until a satisfactory goodness of fit is achieved, determined by a chi-squared value. A goodness of fit chi-squared value of <20 indicate a reasonable confidence level. Adaptations pertained to the number of phases used to fit the spectrum. To account for heterogeneities in the preferential orientation of clays, two different references for both the 7 Å and 14 Å clays were used for analysis.

2.3 Results

2.3.1 Soil Characteristics

2.3.1.1 Size Fractions

The percentages of sand, silt, and clay are tallied in Table 2-2. The soil samples from the three cores collected in this study range in texture from sand to clay (Figure 2-3). The Fuquay samples contain high sand contents ranging from 42% to 91% sand (by mass) at varying depths down core (Table 2-2, Figure 2-3). FQTRS samples contain by far the most sand (74–92%). The samples from the FQQAL core are the most variable in sand concentration (19–85%). .

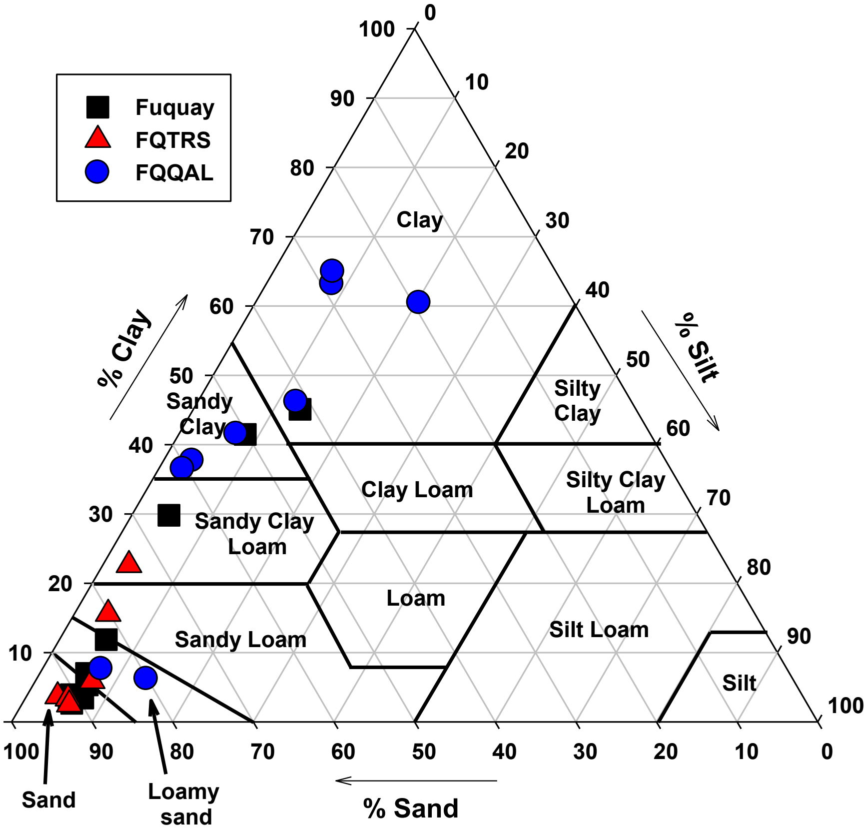

Figure 2-3: Ternary diagram of the textures of samples of the three soil cores in this study. Percentages are by mass.

Table 2-2: Savannah River Site soil particle size distribution in percent

Sample Name	Sand (mass %)	Silt (mass %)	Clay (mass %)	Texture
FQ[a] 0-20	87.2	5.8	7.0	Sand, loamy sand
FQ 21-36	91.3	5.6	3.2	Sand
FQ 37-56	91.2	6.1	2.7	Sand
FQ 57-76	88.0	6.8	5.3	Sand, loamy sand
FQ 77-96	90.6	5.5	3.9	Sand
FQ 97-117	89.5	7.1	3.4	Sand
FQ 118-137	82.3	5.8	11.9	Loamy sand
FQ 138-157	65.6	4.6	29.8	Sandy clay loam
FQ 158-178	50.3	8.3	41.5	Sandy Clay
FQ 179-203	41.7	13.3	45.1	Clay loam
TRS[b] 0-15	92.4	3.9	3.7	Sand
TRS 16-31	91.3	5.3	3.4	Sand
TRS 32-46	91.6	5.9	2.5	Sand
TRS 47-61	87.1	7.1	5.9	Sand
TRS 62-76	80.2	4.2	15.6	Sandy loam
TRS 77-89	74.1	3.3	22.6	Sandy clay loam
QAL[c] 0-15	85.1	7.3	7.6	Loamy sand
QAL 16-28	80.2	13.6	6.2	Loamy sand
QAL 29-38	58.8	3.6	37.6	Sandy clay
QAL 39-46	41.6	12.2	46.2	Clay
QAL 47-61	28.7	8.2	63.2	Clay
QAL 62-76	19.2	20.3	60.4	Clay
QAL 77-84	27.7	7.4	65.0	Clay
QAL 85-91	51.4	7.1	41.6	Sandy Clay
QAL 92-104	60.5	3.0	36.5	Sandy Clay loam

[a] FQ is the original Fuquay core, [b] TRS is Fuquay soil formed on the parent material, Tobacco Road Sand, [c] QAL is Fuquay soil formed on Quaternary Alluvium. The numbers represent the depths of the samples in cm.

All three cores have low concentrations of silt and are dominated by the sand and clay. Silt content ranges from 4.6% to 13% of the Fuquay samples, from 3.3% to 7.1% of the FQTRS samples, and from 3.0% to 20% of the FQQAL samples.

The fraction of clay in the Fuquay samples is low, as low as 2.6%, in the upper part of the core and high, as high as 45.1%, in the deeper part of the core (Figures 2-3 and 2-4). FQTRS samples contain the lowest clay contents (2.5 - 22.6%). Lastly, the FQQAL samples contain the greatest range in the percentages of clay (6.2 - 65.0%) (Figure 2-4).

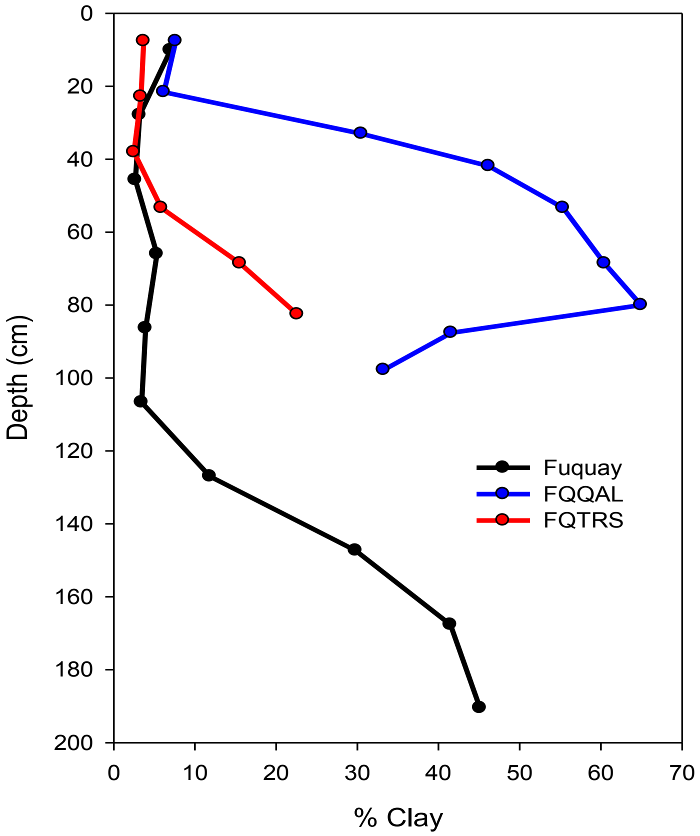

Figure 2-4: Clay percentage as a function of depth within the three soil cores. Fuquay, Fuquay on Tobacco Road Sand (FQTRS), and Fuquay on Quaternary alluvium (FQQAL).

Clay masses were determined by difference from the starting mass of the bulk soil, removing the dry mass of the sand and silt fractions. For some samples, the dry mass of the clay fraction was measured after the Jackson treatments were completed (*Simpson*, 2012). For these samples, the mass decrease could be quantified and attributed to the removal of iron oxides, carbonate cements, and organic matter and to loss of particles during the procedure. This allowed for a more accurate determination of the clay mass fraction in these samples, and in some cases there was a large difference between the clay mass determined by difference and that measured directly. Table 2-3 tabulates the percentage of solid mass lost during the Jackson treatments and the percent difference from the original reported values in Table 2-2.

Table 2-3: Comparison of mass fractions of clay in soil samples determined by direct measurement of clay mass compared to those calculated by difference

	—Clay mass fraction—		
Sample	determined directly (%)	determined by difference (%)	Difference (%)[a]
FQ 0-20	1.6	7.0	124
FQ 21-36	0.6	3.2	137
FQ 37-57	2.6	2.7	2
FQ 58-76	3.4	5.3	44
FQ 77-97	1.8	3.9	75
FQ 98-117	3.5	3.4	3
TRS 0-15	0.2	3.7	176
TRS 16-31	2.6	3.4	26
TRS 32-46	2.4	2.5	3
TRS 47-61	4.0	5.9	39
QAL 0-15	4.3	7.6	57
QAL 16-28	2.6	6.2	81
QAL 46-61	49.4	46.2	7
QAL 76-84	56.3	60.4	7

[a] Relative to the average of the two values.

In the most extreme case (TRS0-15), the difference between the two values for mass fraction of clay is 176% of the average of the two values. The results indicate that substantial amounts of some soil samples were destroyed by the Jackson treatments, so it better to tabulate the directly measured mass of the clay when possible for calculations involving the mass of clay. In cases where the mass of clay was not measured directly, the error in clay content may be relatively very large.

Additional information about soil colors of cores FQTRS and FQQAL are presented in Appendix A for dry soil material.

2.3.2 X-ray Diffractometry

2.3.2.1 Fuquay Upland Soil

The Fuquay upland soil core extended to a depth of 203 cm and was divided into ten ~20 cm sections, each bagged as a separate sample of the soil. The positions of the X-ray diffraction peaks are the same for the Na-saturated air-dried clay from all ten segments of the Fuquay core, but the relative intensities of the peaks vary with depth (Figure 2-5). The first peak, at the lowest 2Θ (6.2°), has a low intensity at each depth. This peak corresponds to a *d* value of 14.4 Å, which was interpreted as the basal 00*1* spacing of vermiculite, HIV, or chlorite. The *d* value is understood as *d/n* where *n* =1 from Braggs Law ($n\lambda = 2d\sin\Theta$). The next peak corresponds to a *d* value of 7.2 Å, typical of the kaolinite basal 001 spacing, but the 002 reflection from 14.4 Å phyllosilicates also contributes to this peak. This 7.2 Å diffraction peak was much more intense than the 14.4 Å peak for every sample except the three from 21 cm depth to 76 cm (Figure 2.5). At those depths, the intensity of the two peaks is comparable. The *d* value for the third peak observed was 4.8 Å. This peak was interpreted as the combination of a reflection from gibbsite and the (003) reflection from 14.4 Å clay(s). The secondary gibbsite peak at 2Θ = 20.45° is not observed and may have too low of an intensity to be detected among the other minerals here. A peak at 3.57 Å is present in the pattern for each depth and is the most prominent peak for clays from deeper than 117 cm. This peak is the (002) kaolinite peak or 4th order reflection of 14.4 Å clay.

In addition to phyllosilicate minerals, quartz was identified in the clay fractions based on the presence of two diffraction peaks at 3.33 Å and at 4.25 Å. For clays at depths less than 117 cm, other than from the uppermost sample (FQ 0-20), the quartz 3.33 Å peak has the greatest intensity of all the peaks. For clays deeper than 117 cm, the 3.33 Å quartz peak was of low intensity and the peak at 4.25Å was weak or absent (Figure 2-5).

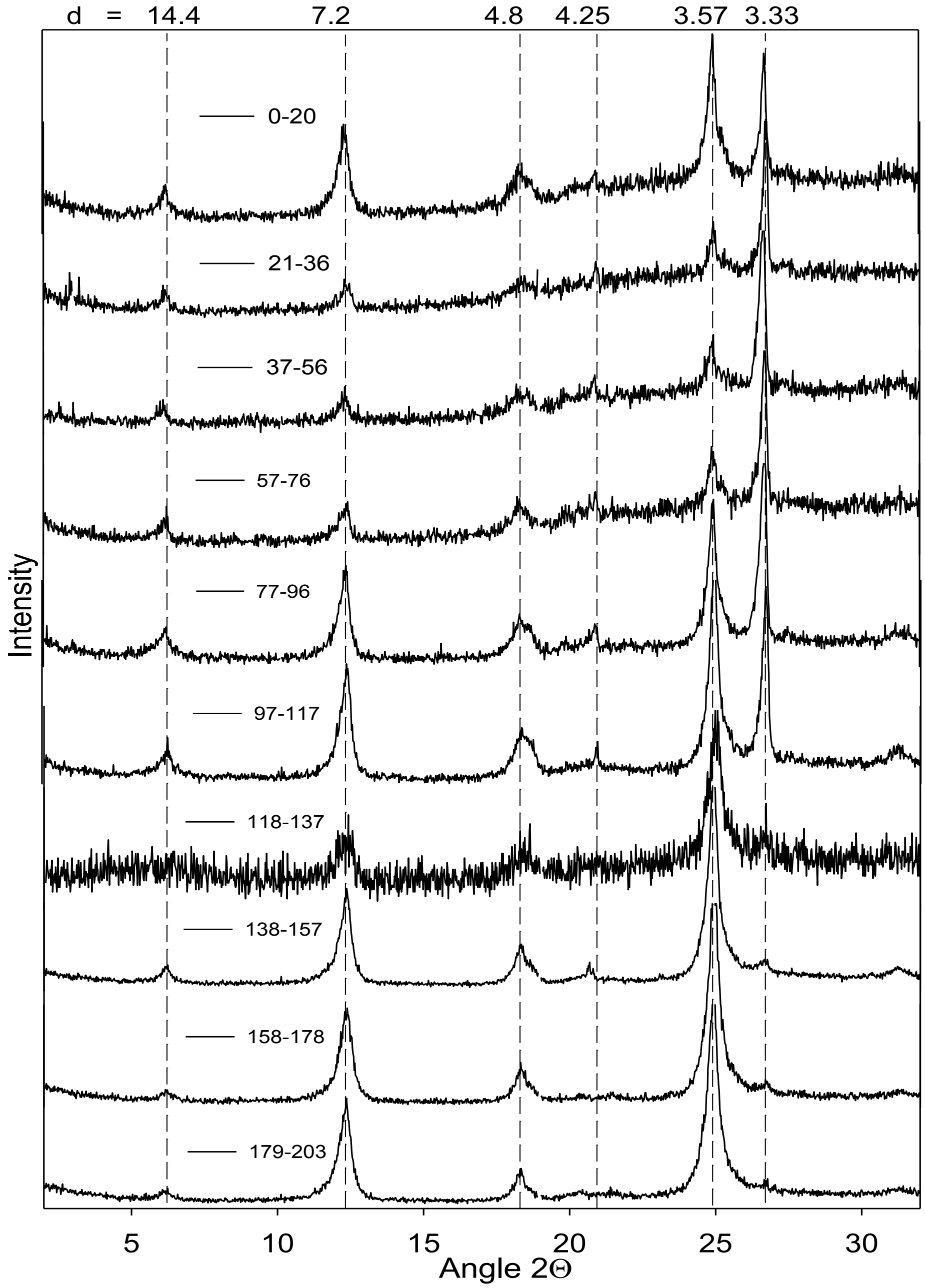

Figure 2-5: XRD patterns of oriented, air-dried clay from the Fuquay core samples. Labels represent the depth of the soil core segment in centimeters. d is the *d* value of the peak (Table 2-1), number range indicates the depth of the sample in cm.

Additional treatments were required to identify the 14.4 Å clay(s) and to distinguish between the 7.2 Å second-order reflection of the 14 Å clay(s) and the 001 of kaolinite. Figure 2-6 shows the XRD patterns for surface sample FQ0-20 after the glycol, and multiple K and heat treatments. Patterns of the treatments down core are presented in Appendix B. None of the clays displayed any response to saturation with glycol (Figures 2-6 and B1-B9). Thus smectite is ruled out as a possible mineral in these clays at all depths of the Fuquay core. Distinguishing between secondary 002 HIV/vermiculite/chlorite peaks and kaolinite 001 is aided by the heating of potassium saturated samples to 550°C, which causes kaolinite to become amorphous and eliminates its peaks entirely (*Moore and Reynolds*, 1997). Potassium saturation (without heating) of the clay samples showed no shift of the 14.4 Å peak, whereas if vermiculite where present and saturated with K, its *d* value would reduce to around 10 Å. Heating of the K-saturated clay samples sequentially from 110°C, to 330°C, to 550°C showed no effect on the patterns until 550°C where the 7.2 Å and 3.57 Å peaks collapsed and the 14.4 Å peak shifted to smaller *d* value around 12.5 Å (Figures 2-6 and B1-B9). The collapse of the 7.2 Å and 3.57 Å peaks affirms these are from kaolinite. Chlorite would remain at 14.4 Å *d* value despite the heating to 550°C. Thus, the combined evidence of lack of glycol expansion, lack of K-saturation collapse, and the 14.4Å peak only collapsing after being heated to 550°C identifies the 14.4 Å clay as the chlorite-vermiculite intergrade, hydroxy-interlayered vermiculite (HIV) (*Mosser-Ruck et al.* 2005). Thus, the minerals present in this core as identified by XRD are kaolinite, quartz, gibbsite, and HIV.

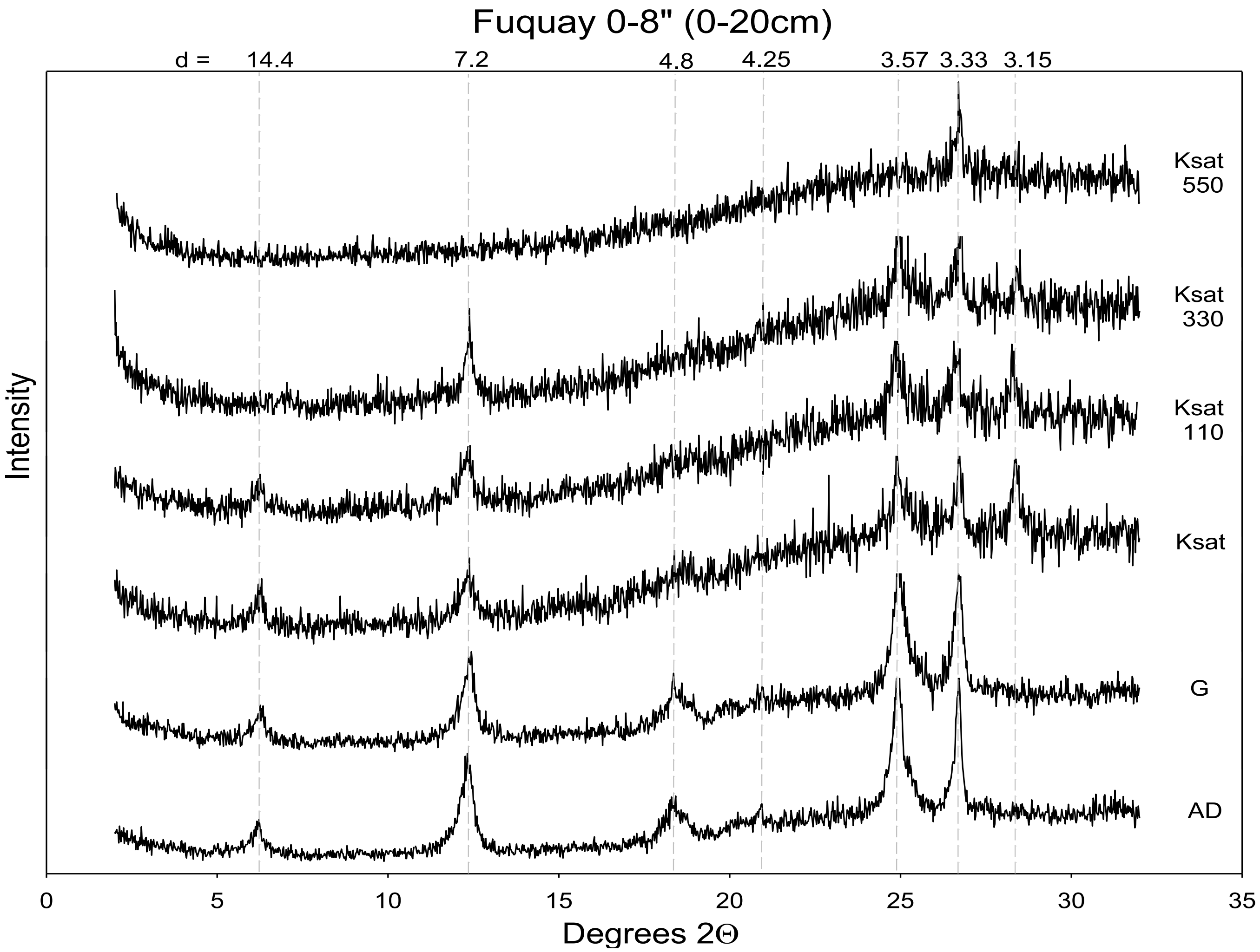

Figure 2-6: XRD of Fuquay soil sample depths 0-20 cm

AD = Air dried, G = Glycol, Ksat = K-saturation, Ksat110 = K-saturation and heated to 110°C, Ksat330 = K-saturation at 330°C, and Ksat550 = K-saturation at 550°C. Note the emergence of a KCl peak (3.15Å) after addition of KCl, and the disappearance of the kaolinite peak with heating (7.2Å and 3.57Å). HIV peak (14.4Å) slowly dissipates with heating and a slight collapse to smaller *d* value.

Several other minor peaks are present in only a few of the sample depth horizons. A small but discernible peak at 4.46 Å is present in samples FQ37-56, FQ57-76, and FQ 77-97 (Figures B2-B4 in Appendix B). This *d* value is associated with the disordered kaolinite 020 peak and suggests that disordered or multiple phases of kaolinite are present in these clays, and may be present at other depths as well, but the intensity is too small to be detected by XRD. After K-saturation, FQ0-20, FQ21-36, and FQ37-56 show the KCl peak at 3.15Å (Figures 2-6, B1, B2). Lastly, two samples at intermediate depths, FQ98-117 and FQ77-97, have small broad peaks at 2.98 Å (Figures B4 and B5). This is the 005 for phyllosilicates and only shows up prominently at these depths.

2.3.2.2 FQTRS Core

Core Fuquay on Tobacco Road Sand (FQTRS) extends to a depth of 89 cm, the shallowest core in this study. It was divided into 6 sections ~15 cm each. Air-dried slides of the Na-saturated clay from each depth show 5 common diffraction peaks at all 6 depths. There is the 14.4 Å HIV/vermiculite/chlorite peak, 7.2 Å kaolinite 001, second-order HIV/vermiculite/chlorite peak, 4.8 Å gibbsite peak or third order HIV/vermiculite/chlorite peak, 3.57 Å kaolinite 002 peak, and quartz at 3.33 Å (Figure 2-7). Identical to the Fuquay Core, each sample was saturated with glycol vapor as well as K and heated sequentially to 110°C, 330°C, and 550°C to determine if the 14.4 Å peak is vermiculite, chlorite, or HIV (Figures B10-B15). There was no observed expansion as a result of glycol, eliminating smectite as a possible mineral. For each sample depth, the result of K-saturation and heating is the same, a collapse of the 14.4 Å peak to smaller *d* value after 550°C indicating, that just like the Fuquay core, the 14.4 Å phase mineral is HIV. We also note the collapse of the 7.2 Å and 3.57 Å peaks, indicating that these peaks are kaolinite that has become amorphous at 550°C.

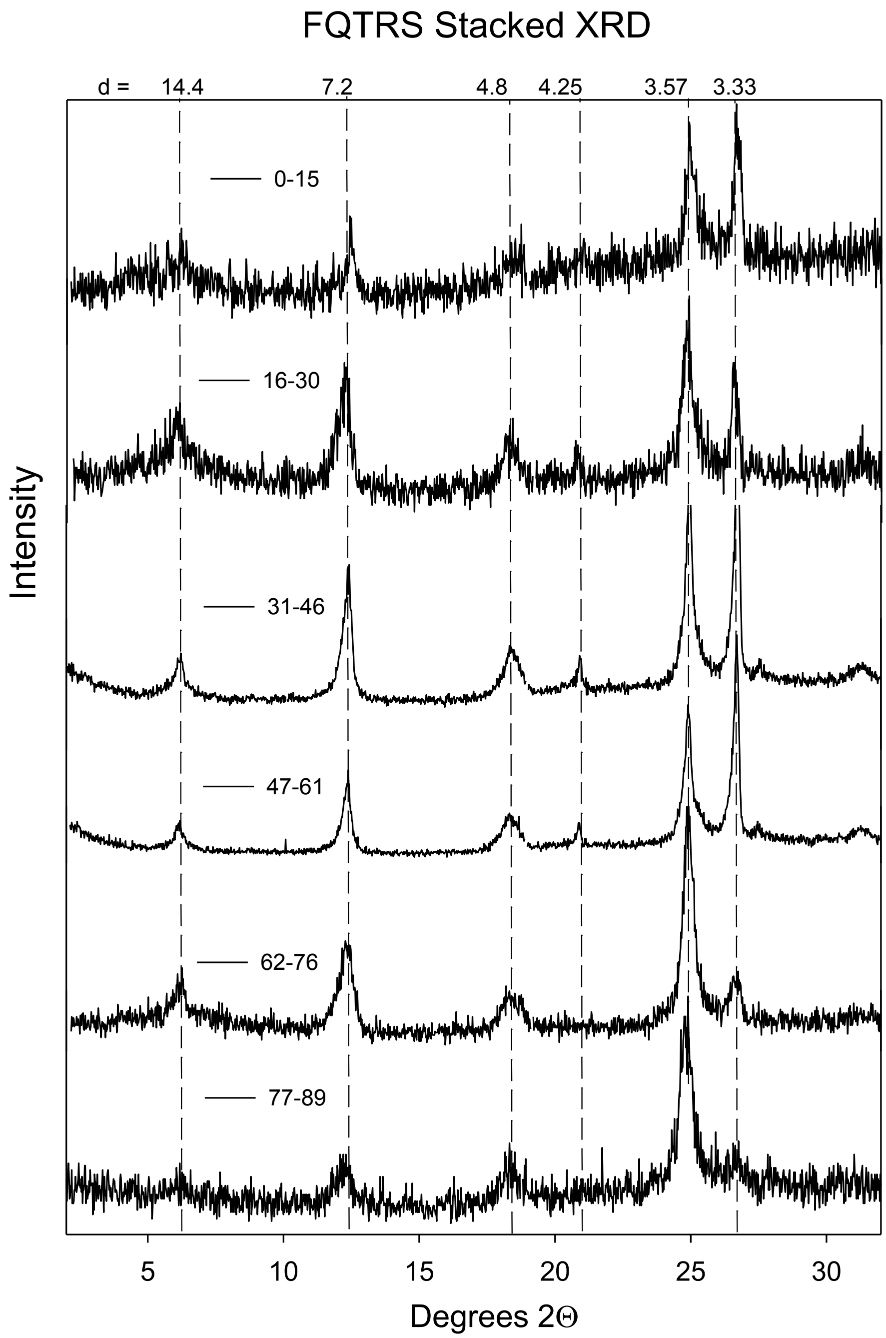

Figure 2-7: Stacked XRD AD patterns from FQTRS
Number range indicates depth of the sample in cm.
The amount of quartz (d = 3.33Å) is decreasing with depth.

A quartz peak at 4.25 Å is visible in samples TRS0-15, TRS16-31, TRS32-46, and TRS47-61. As depth increases, the intensity of the quartz peak (3.33 Å) is a greatly reduced and barely visible at the depths for samples TRS61-76 and TRS77-89 (Figure 2-7), indicating a reduction in the quantity of this mineral in the clay size fraction in the deepest two samples of this core.

2.3.2.3 FQQAL Core

The depth went to 104 cm before the clay was too compact to auger further. This core was sectioned into 9 sections ranging from 10-15 cm of depth, with care taken to separate horizons (Table A1). This core was very clay rich resulting from alluvial deposits. The clays from the three shallowest samples, QAL0-15, QAL16-28, and QAL29-38, display peaks at 7.2 Å and 3.57 Å for kaolinite, and a similarly intense 3.33Å peak for quartz (Figure 2-8). All the other depths also show peaks for kaolinite but have little to no quartz peak, indicating a decrease in the quantity of clay-sized quartz with depth (Figure 2-8). There is a small broad hump around 14.4Å but no definitive HIV peak in this core, with the exception of maybe sample QAL29-38 (Figure 2-8). The glycol, K, and heating treatments were not completed on this core as there was no clear indication of the 14.4 Å peak.

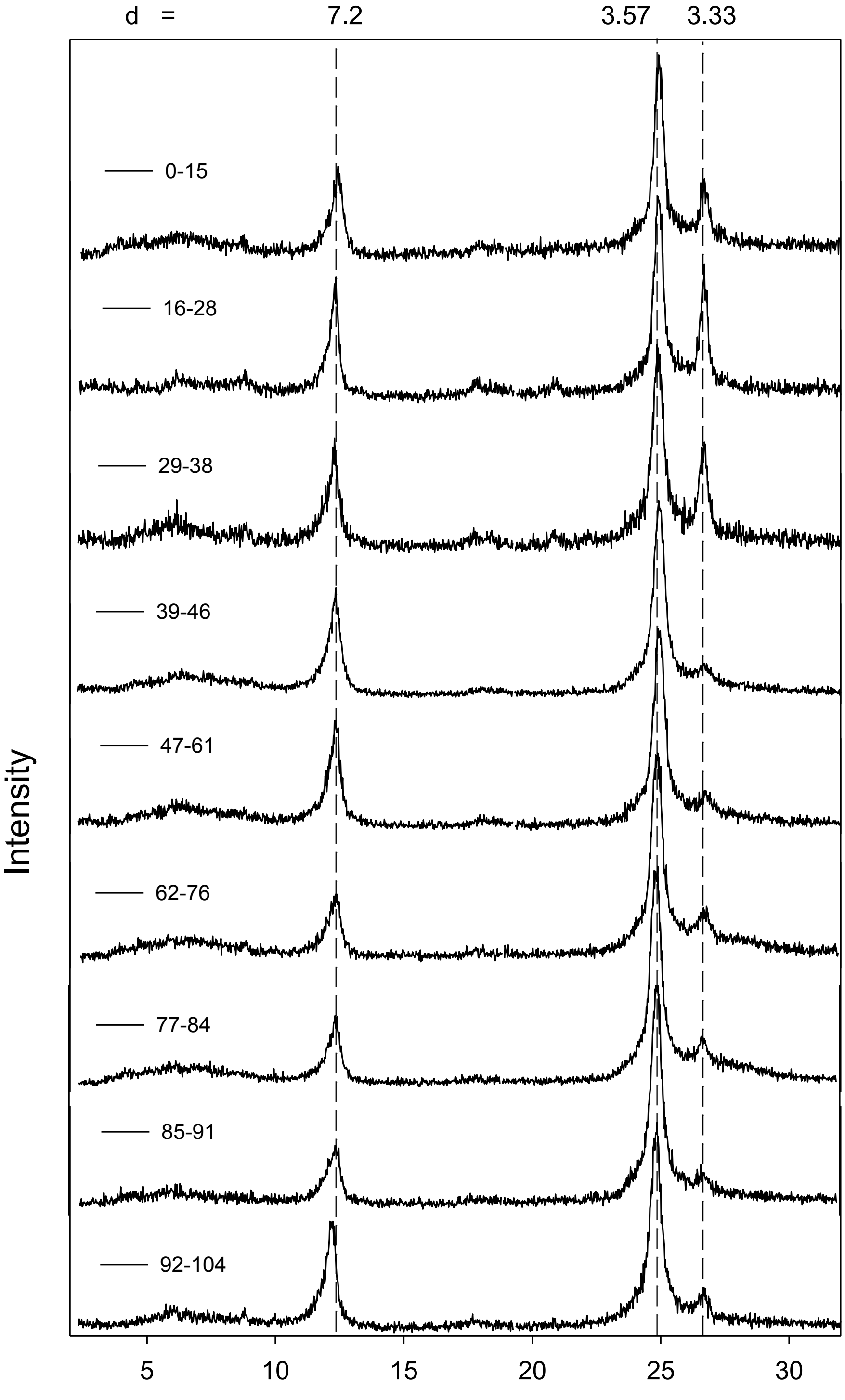

Figure 2-8: Stacked XRD AD patterns from FQQAL.
Additional treatments where not done here as there was little to no indication of a 14.4Å peak.

2.3.2.4 SRS BGO 3A Drill Core

Samples from drill core SRS BGO 3A are representative of a wide range of depths ranging from the shallowest at 8 meters, to near and into the water table at SRS at 31meters. XRD patterns for SRS28 and SRS46 both have peaks at 7.2Å and 3.57Å identifying the major mineral at theses depths as kaolinite (Figures 2-9 and 2-10). (The sample names represent the depth of the sample in feet and are retained for simplicity rather than altering the sample names to reflect SI units. Thus sample SRS28, is the sample at depth 28 feet, or 8.5 meters). There is also a very minor and hardly distinguishable peak at 3.33Å corresponding to minor contribution by quartz. The next sample from 23 meters (76 feet), SRS76 has a more variable mineralogy. Low-intensity peaks at 10.0Å and 5.0Å are indicative of mica and/or illite's first and second-order reflections (Figure 2-11). Additionally, the 7.2Å and 3.57Å kaolinite peaks and 3.33Å quartz peak are present with high intensity, indicating these minerals make up the majority of the clay fraction. Lastly, the kaolinite *hkl* 3.0Å is present but with very low intensity. There was no change to pattern after saturating the clay with K, except the emergence of the 3.15 Å KCl peak.

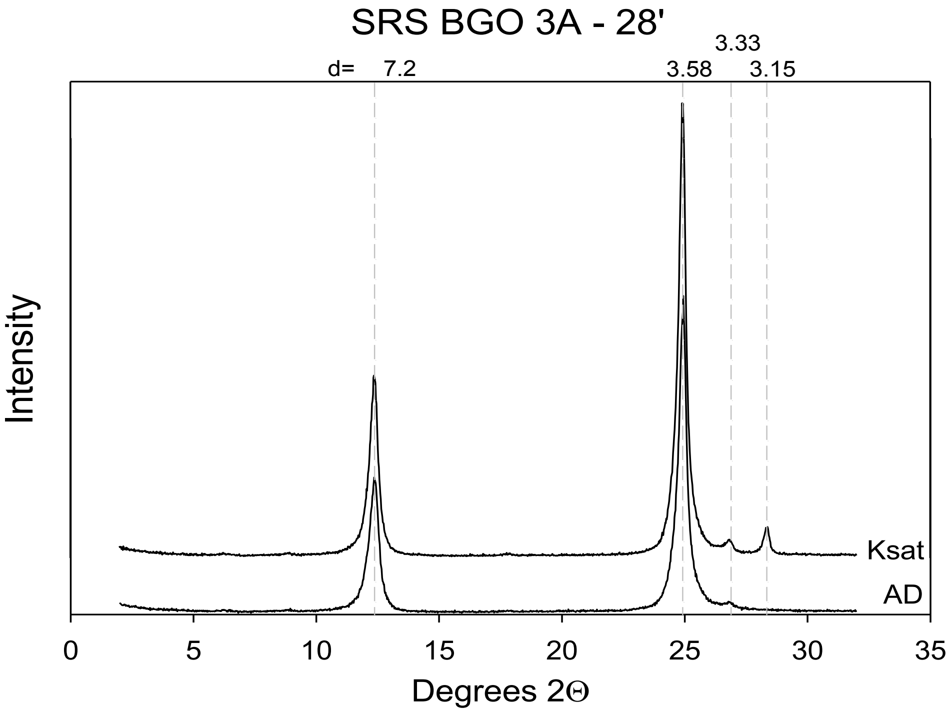

Figure 2-9: XRD patterns of clay from drill core SRS BGO 3A at 8 meters (28 feet) indicates only kaolinite and a very minor quartz peak.

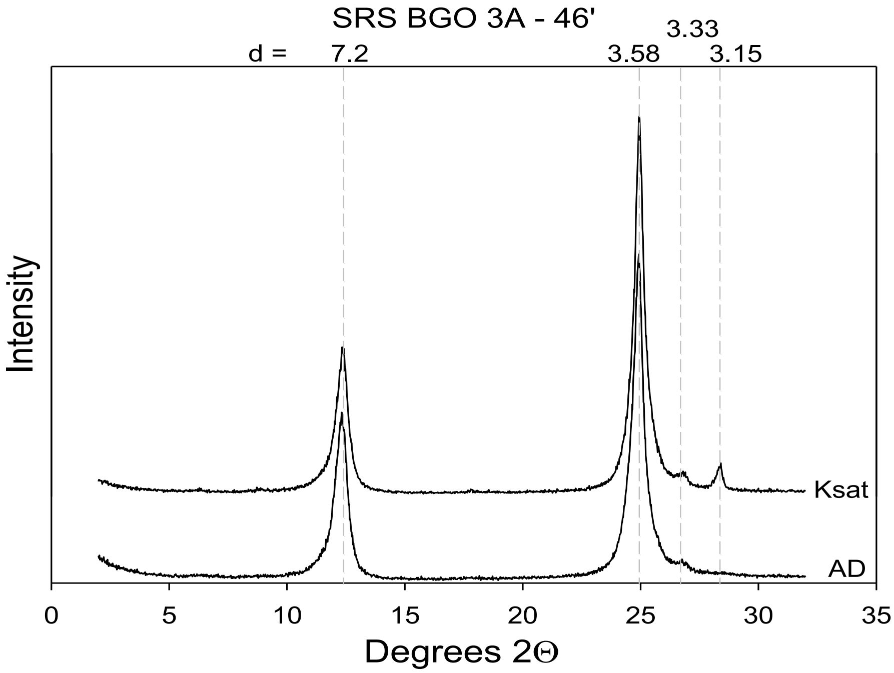

Figure 2-10: XRD patterns of clay from drill core SRS BGO 3A at 46 feet indicates only kaolinite and a very minor quartz peak.

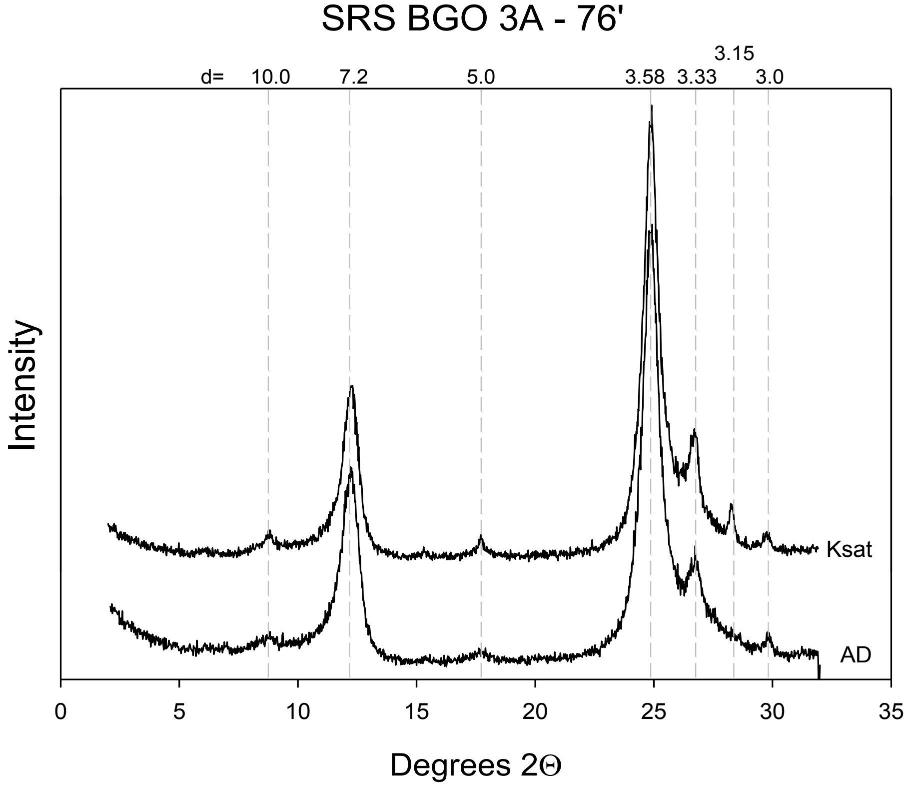

Figure 2-11: XRD patterns of SRS BGO 3A 76 feet identifies peaks for illite/mica, kaolinite, and quartz

Sample SRS94 has a very low intensity broad peak around 14.4 Å (Figure 2-12). After glycol saturation, a peak at 17 Å suggests expansion as a smectitic clay would. Also, with K-saturation, the peak would collapse to ~11.5 Å. In this case, the small peak around 11.5 Å in the K-sat curve is likely overlapping with a 10 Å mica/illite peak, producing a broad peak around in the K-sat pattern. Other peaks include the 7.2 Å and 3.57 Å kaolinite primary and secondary peaks, as well as 3.33 Å quartz, and the 10 Å and 5 Å mica/illite peaks.

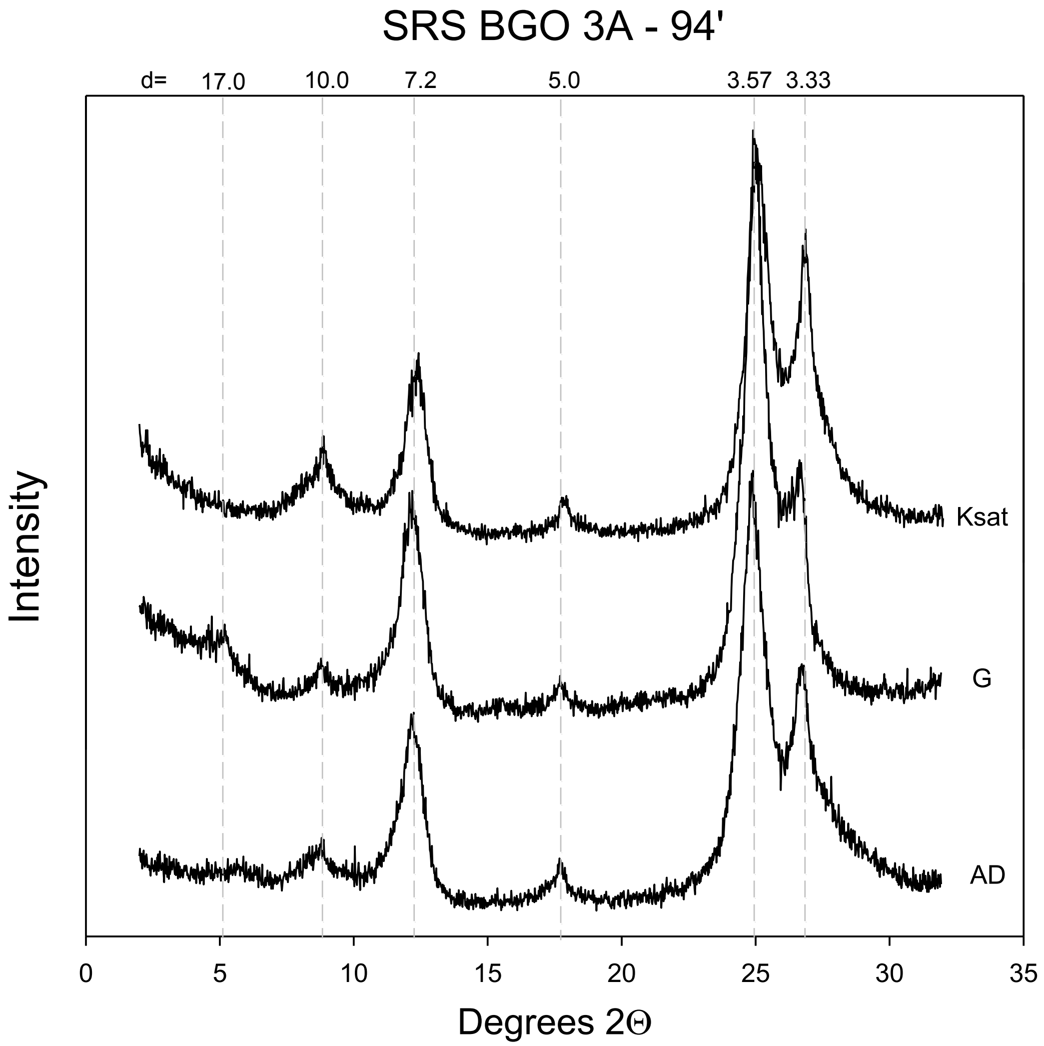

Figure 2-12: XRD patterns of SRS BGO 3A at 94 feet identifies peaks for smectite, illite/mica, kaolinite, and quartz.

The three deepest samples, SRS97-98, SRS98-99, and SRS101-102, all share the same diffraction pattern characteristics. The air-dried patterns have a broad peak around ~14.4Å, and more narrow peaks at 10.0Å, 7.2Å, 5.0Å, 3.57Å and 3.33Å. The 7.2Å and 3.57Å and the 10Å and 5Å are the first and second-order peaks of kaolinite and mica/illite respectively (Figures 2-13, 2-14, and 2-15). The 3.33Å is the easily identifiable quartz peak. To determine the 14.4Å mineral, glycol and K-saturation methods were used. The mineral expanded to ~17Å with glycol saturation, and collapsed to ~11.5Å when saturated with K, indicative of the mineral smectite at these depths. The glycol pattern also has small peaks at 8.5Å and 5.7Å which are the second and third order peaks of the 17Å expanded phase of the mineral smectite.

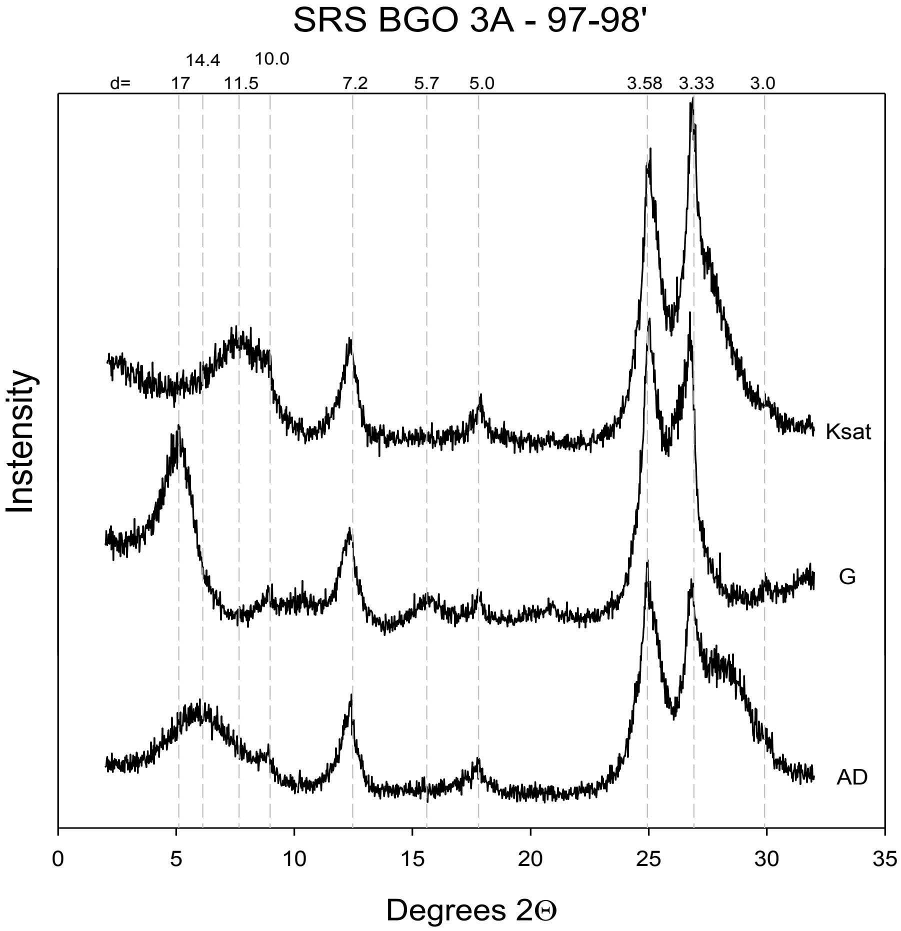

Figure 2-13: XRD patterns of drill core SRS BGO 3A 97-98 feet identifies peaks for the minerals smectite, kaolinite, and quartz.

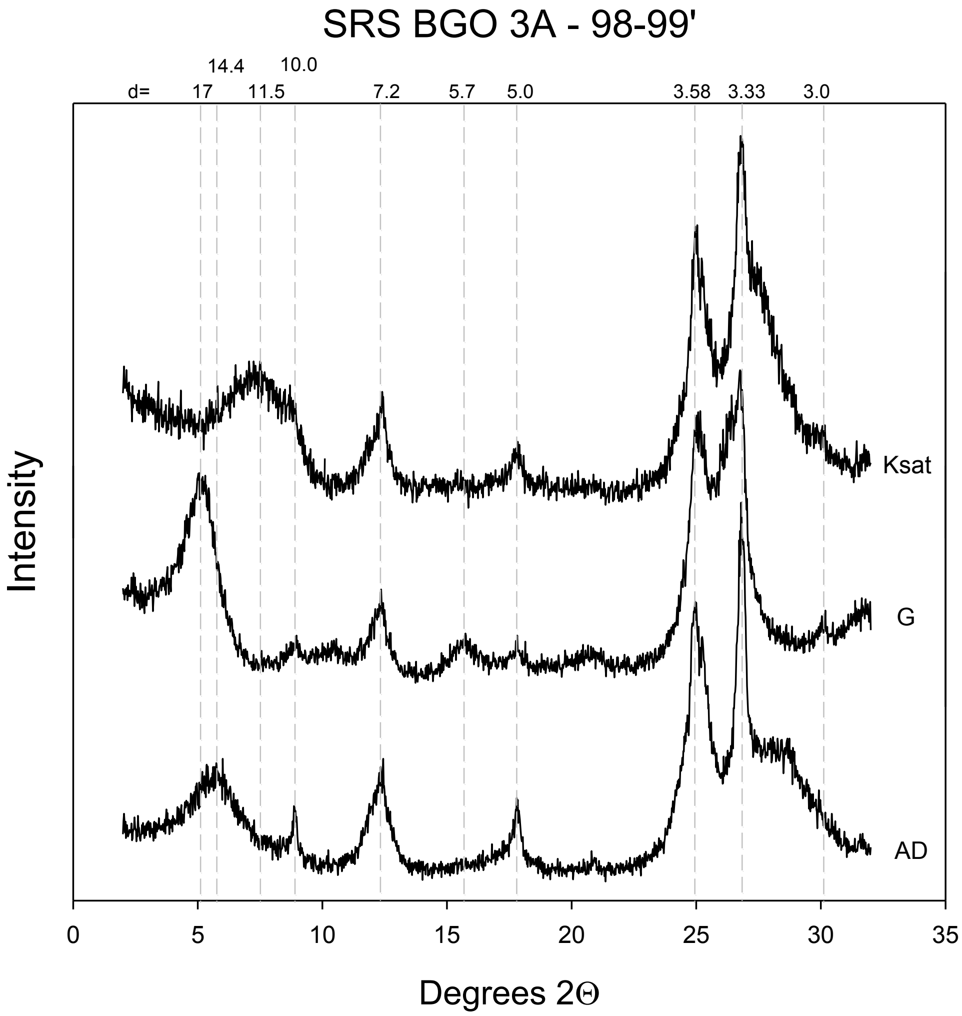

Figure 2-14: XRD patterns of drill core SRS BGO 3A at a depth of 98-99 feet indicates the minerals present are smectite, illite/mica, kaolinite, and quartz

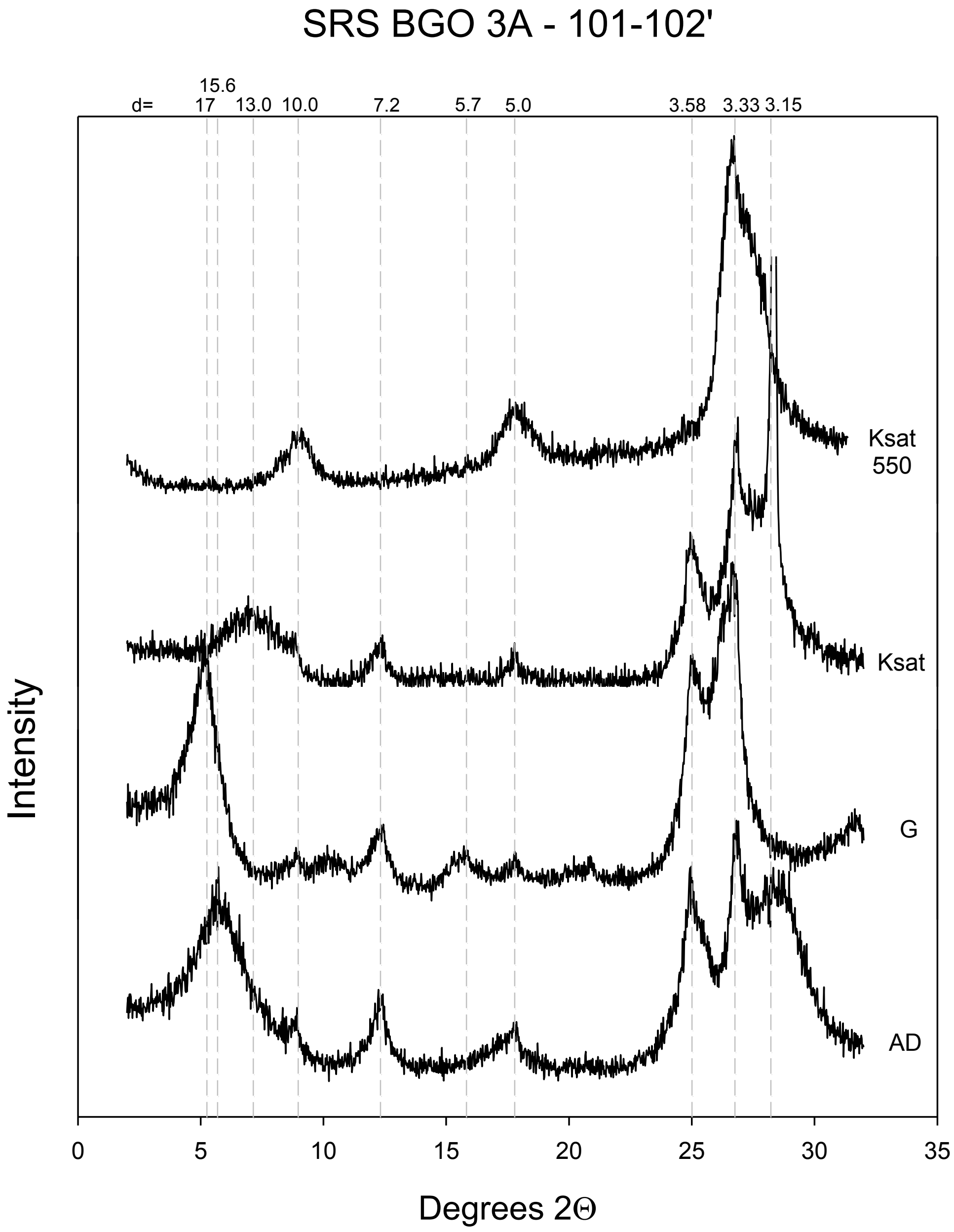

Figure 2-15: XRD patterns of SRS BGO 3A 101-102 feet identifies the minerals present as smectite, kaolinite, and quartz, with a minor illite/mica peak in the AD pattern.

2.3.3 Synchrotron Diffraction Patterns

A consequence of converting from SeKα to CuKα wavelength was a loss in the resolution from having an intensity reading every 0.02° 2Θ as with conventional XRD to having an intensity reading only every 0.1° 2Θ. Nonetheless, the greater intensity of the beam allows for identification of *hkl* reflections and minerals that are in low quantities and not distinguished beyond background intensity in conventional XRD. Diffraction patterns for clay from each soil core were taken as both oriented mounts (dried in an oven at 50°C) and random powder mounts. The random mounts proved to be much more useful and provided the data that are presented here.

Figures 2-16, 2-17, and 2-18 show the stacked patterns (ordered by depth) of synchrotron diffraction for random mounts of clay from Fuquay (FQ), FQTRS, and FQQAL, respectively. The minerals identified at the SSRL are HIV, kaolinite, and quartz, in all three cores, with small amounts of illite found in FQTRS and FQQAL and gibbsite found in FQ and FQTRS. These diffraction patterns are consistent with conventional XRD patterns described in previous sections. However, illite was observed in some of these clays but was not found with conventional XRD. It was identified primarily at all depths in the FQQAL and FQTRS cores through its hkl peaks as the 10 Å peak is not evident to the eye. The two deepest samples of FQ and FQQAL have a small shoulder peak at a *d* value of 4.1Å. This corresponds to either a kaolinite *hkl* or 2m illite peak. In the FQ core, there are no other illite peaks so it is likely from kaolinite. In FQQAL, it could be a combination of both illite and kaolinite as indicated by other minerals identified. These random mounted patterns that include *hkl* peaks allow for the modeling and quantification of the minerals in a more precise manner than with conventional XRD patterns.

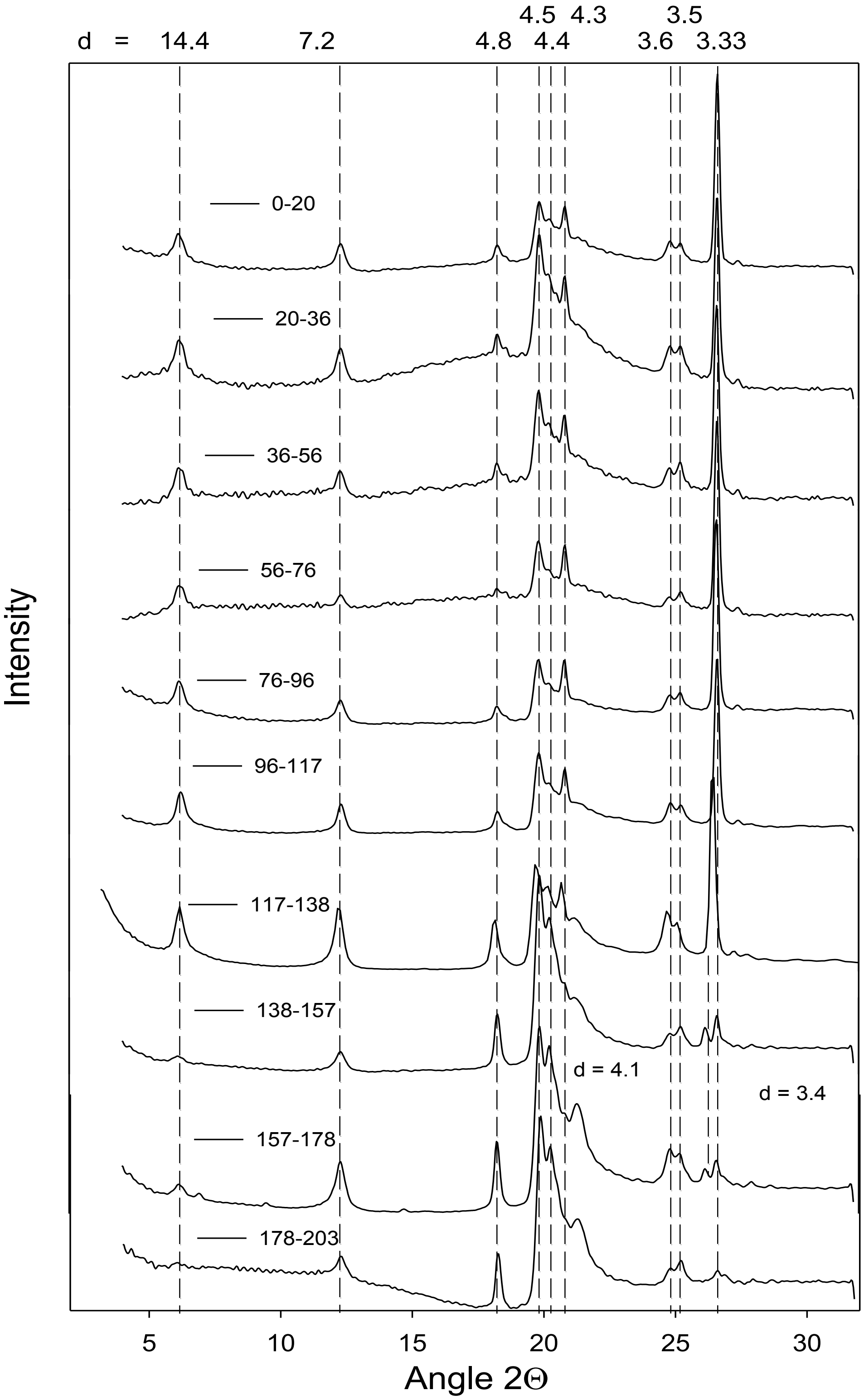

Figure 2-16: Synchrotron diffraction data for clay from Fuquay core samples identified by depth in centimeters, presented as intensity versus 2θ for CuKα radiation. Identifiable minerals are HIV, kaolinite, some gibbsite, and quartz.

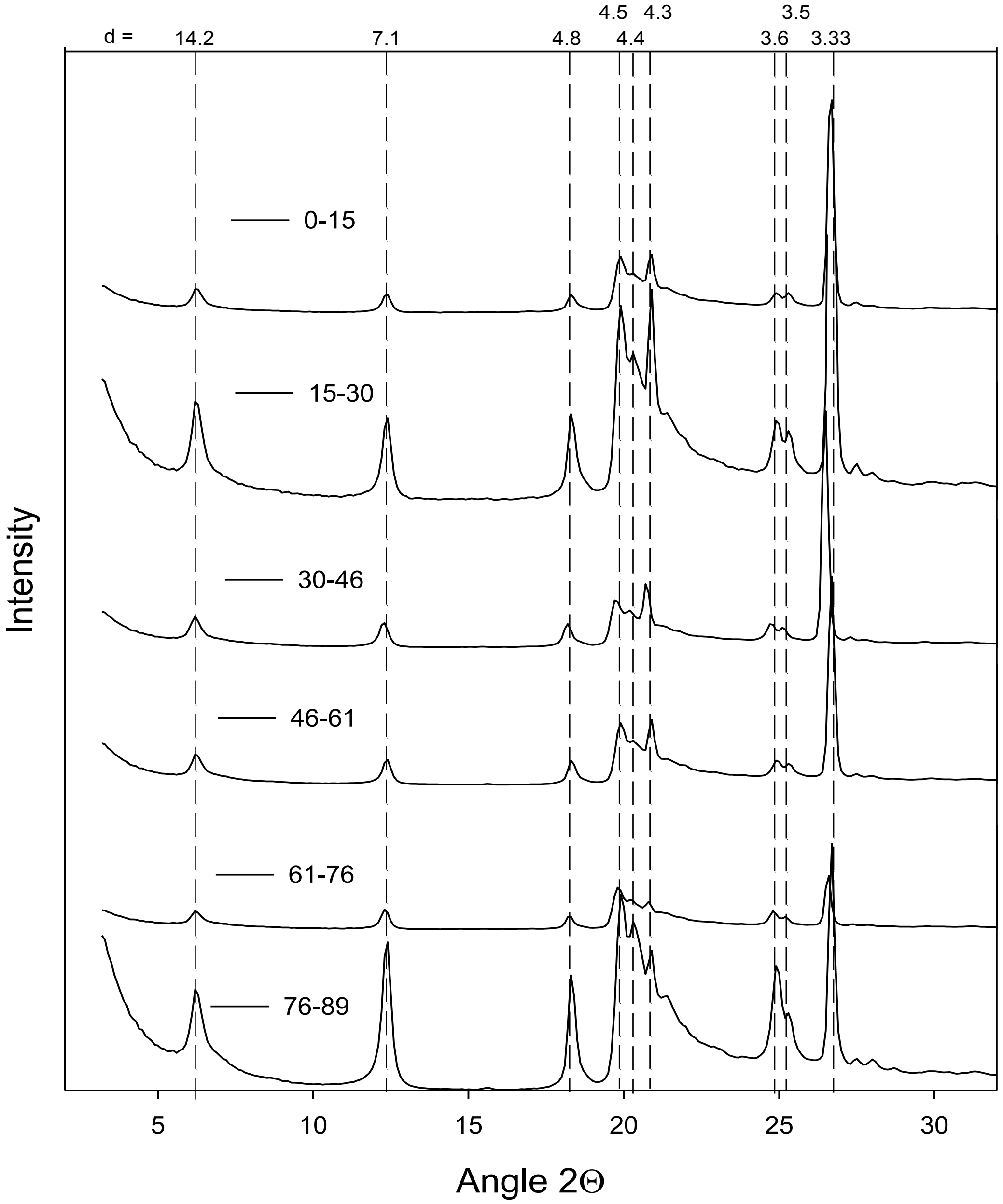

Figure 2-17: Synchrotron diffraction data for clay from FQTRS core samples identified by depth in centimeters, presented as intensity versus 2θ for CuKα radiation. Minerals identified are HIV, kaolinite, gibbsite, illite, and quartz.

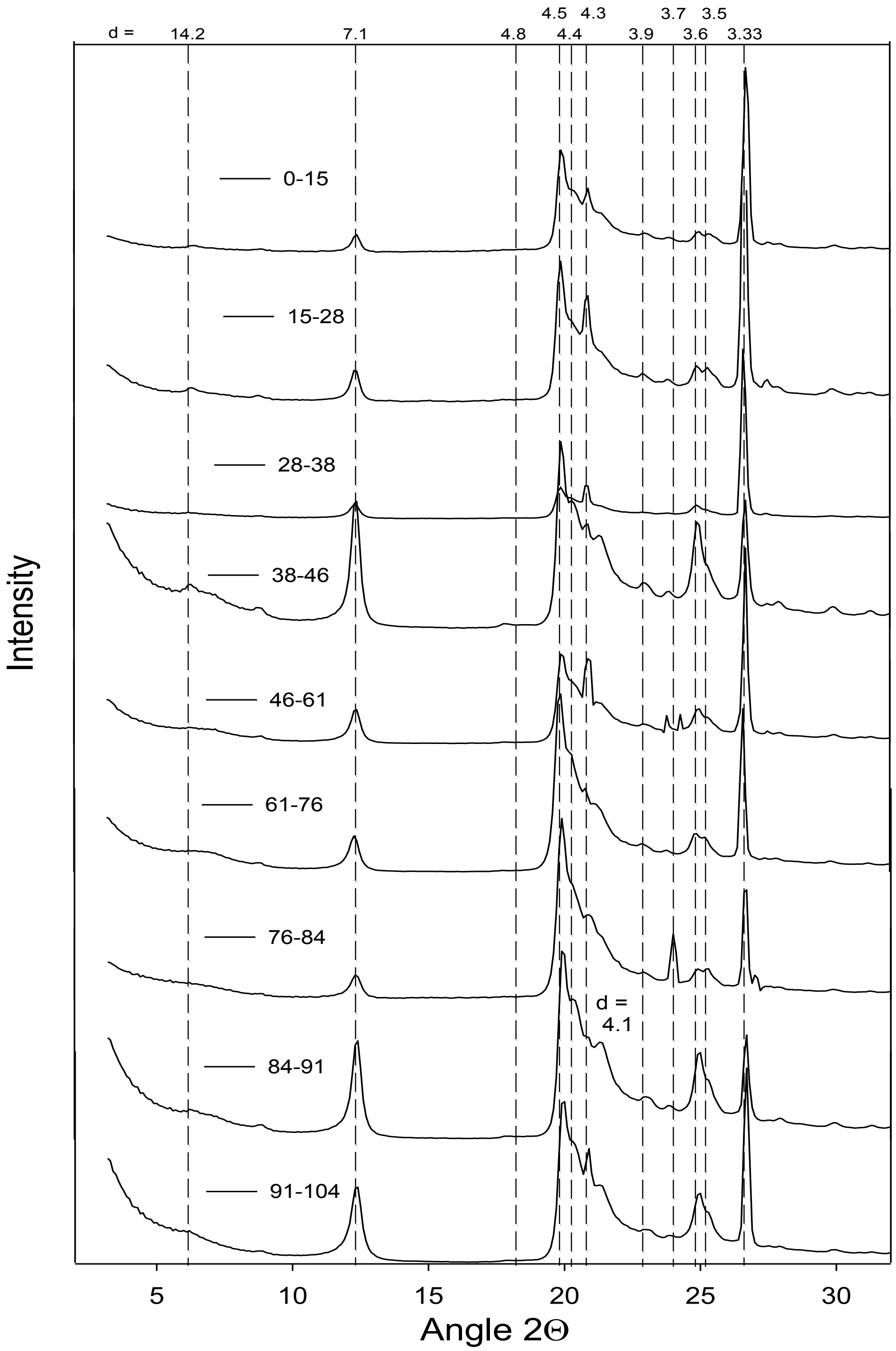

Figure 2-18: Synchrotron diffraction data for clay from FQQAL core samples identified by depth in centimeters, presented as intensity versus 2θ for CuKα radiation. The 14.4 Å peak is not very distinct, but HIV, kaolinite, illite, and quartz are all present.

2.3.3.1 Mineral Quantification - Rietveld Modeling

Modeling of the quantity of each mineral present was based on known patterns of minerals and determining how contributions of the various minerals present could be combined to best match the pattern generated by the synchrotron diffraction (*Downs and Hall-Wallace,* 2003; *Perdrial et al.* 2011) . Figure 2-19 is a representative figure of the Rietveld model fit to the diffraction data, showing the contributions by each mineral to the overall modeled pattern, and the goodness of fit to the actual pattern. The quantitative data are listed for all three cores in Table 2-3.

In the Fuquay core, minerals contributing to the patterns at all the depths include HIV, kaolinite, gibbsite, and quartz. The quantity of HIV was found to range from as low as 1.3% in clay from the deepest sample (FQ179-203) to 26.0% at the surface. Kaolinite, which is present in several forms, makes up anywhere from 28.6% of the clay in sample FQ57-76 to a maximum value of 84.8% in the deepest segment of the core. Gibbsite is a minor component of the clay at all the depths, with a maximum value of 12.8% in the deepest sample and a minimum value of 3.6% in FQ57-76. Where gibbsite and kaolinite are lowest, quartz attains its highest value of 48.9% in FQ57-76, and the minimum value of 1.3% is for FQ179-203 where the clay is almost completely dominated by kaolinite (Table 2-3).

Minerals identified in core FQTRS are HIV, kaolinite, gibbsite, quartz, and illite, which is not identifiable in the FQ core. HIV in this core ranges from 7.7% in TRS16-31 to 20.2% in the deepest sample, TRS77-89 (Table 2-3). Kaolinite is fairly consistent with depth in this core ranging from 35.8% to 42.6%. Gibbsite at the surface is only 4.7% of the clay, but it increases with depth to 18.3% in the deepest sample. Quartz is also fairly consistent with depth in the core with a range of 23.0% to 33.9% in the top five segments but the deepest sample is an exception with only 7.8% modeled quartz contribution. Illite is present in the core ranging from 7.3% to 13.2%. In general, the minerals in this core are fairly consistent with depth.

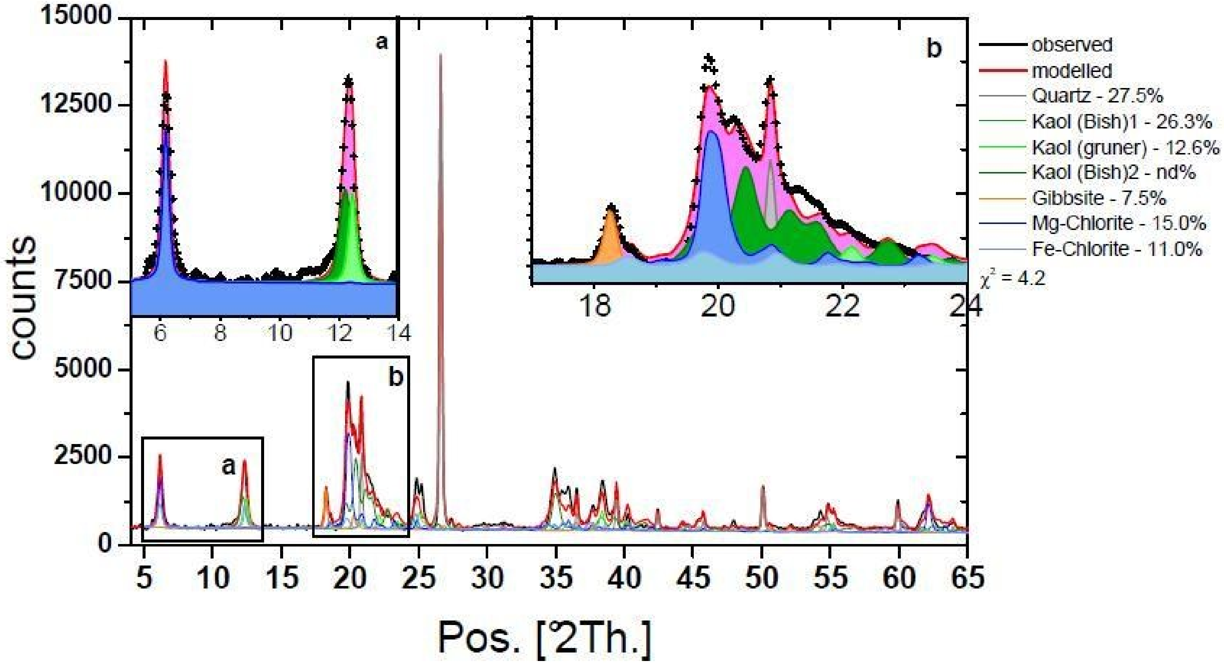

Figure 2-19: Example of the quantitative fitting from Rietveld modeling. Sample shown is from FQ0-20, surface of FQ Core. Black dots are from the diffraction pattern from synchrotron radiation, the different minerals contributing to each peak are represented by different colors. The red line is the model diffraction pattern based on the contributions by each mineral indicated in the top right corner. Three kaolinites are in green to capture the disorder, Mg-Chlorite and Fe-Chlorite are the model character for HIV.(a) and (b) are zoomed in sections around the *d* values for HIV which has a high quantity (26%) in this sample.

Table 2-4: Rietveld phase quantification of minerals (in %) in the three SRS soil cores

Sample Name	**HIV** $(Fe,Mg,Al)_6(Si,Al)_4O_{10}(OH)_8$	**Illite** $K(Al,Mg,Fe)_2(Si,Al)_4O_{10}[(OH)_2\cdot(H_2O)]$	**Kaolinite** $Al_2Si_2O_5\ (OH)_4$	**Gibbsite** $Al(OH)_3$	**Quartz** SiO_2	$\chi^{2\,a}$
FQ 0-20	26.0	0.0	38.9	7.5	27.5	4.2
FQ 21-36	16.4	0.0	53.0	9.9	20.8	17.0
FQ 37-56	24.7	0.0	32.6	9.7	33.0	7.2
FQ 57-76	19.0	0.0	28.6	3.6	48.9	6.9
FQ 77-96	16.2	0.0	35.5	6.9	41.4	8.6
FQ 97-117	19.1	0.0	40.4	7.0	33.5	9.0
FQ 118-122	12.7	0.0	39.4	10.4	37.5	12.3
FQ 123-157	2.1	0.0	84.7	10.4	2.8	9.1
FQ 158-178	2.3	0.0	84.5	11.1	2.1	24.2
FQ 179-203	1.3	0.0	84.8	12.8	1.0	19.8
TRS 0-15	19.1	7.3	37.3	4.7	31.6	2.4
TRS 16-31	7.7	6.7	42.6	11.5	31.5	3.2
TRS 32-46	12.6	8.7	41.1	9.5	28.1	4.4
TRS 47-61	8.5	9.2	35.8	12.6	33.9	4.2
TRS 62-76	14.7	13.2	38.6	10.5	23.0	1.3
TRS 77-89	20.2	11.5	42.2	18.3	7.8	6.4
QAL 0-15	6.1	22.1	47.2	0.0	24.5	5.2
QAL 16-28	5.3	27.3	34.8	0.0	32.6	4.2
QAL 29-38	9.2	13.4	39.2	0.0	38.2	1.9
QAL 39-46	12.0	17.1	69.1	0.0	1.8	2.3
QAL 47-61	12.7	16.1	50.6	0.0	20.6	7.8
QAL 62-76	12.9	12.7	52.4	0.0	21.9	7.0
QAL 77-84	6.7	18.5	68.9	0.0	5.9	2.2
QAL 85-91	14.0	13.6	64.9	0.0	7.6	3.4
QAL 92-104	1.9	13.2	72.7	0.0	12.0	4.0

[a] χ^2 represent the goodness of fit on 3-point smoothed patterns and corresponds to $\chi^2 = [\Sigma_i (I_{obs} - I_{calc})_i^2 / \sigma^2(I_{obs})_i] / (n - p)$; with I the intensity, $\sigma(I_{obs})$ the estimated error of the measure (fixed to 10% of the counts), n the number of points used for simulation and p the number of parameters estimated. Quantification method developed from *Perdrial et al*. (2011).

Core FQQAL is characterized by the minerals HIV, illite, kaolinite, and quartz, (Table 2-3). No gibbsite peaks were observed or modeled in this core. In the other soil cores the HIV content of clay is 20% or more, but the maximum value in FQQAL is 14%. HIV is at a minimum, 1.9%, in the deepest sample. Illite is much more abundant in this core than the others with percentages ranging from 12.7% to 27.3%. Kaolinite is the predominant clay mineral with a range from 34.8% near the top to 72.7% in the deepest sample. Quartz varies with the changing horizons in the core and is most abundant near the surface where it is from 24% to 38% in the top three segments. It decreases drastically with a change in horizon to only 1.8% in QAL39-46 where there is a corresponding large increase in the amount of kaolinite. In QAL47-61 and QAL62-76 quartz concentration increases back to around 20% and then it decreases again to ~7% for QAL77-84 and QAL85-91. The deepest sample has 12% quartz in the clay.

Though synchrotron patterns were taken for clay from drill core SRS BGO-3A, a decision was made that mineral quantification for the deep drill core samples was not necessary for this current project, that mineral identification was sufficient data for this core.

2.3.3.2 Mineral Quantification - Formamide treatment

Additional quantification work was conducted to determine if any of the kaolinite in the cores was actually halloysite. This was prompted by the observation that many of the clay samples curled when air-dried onto slides for XRD analysis. When dehydrated halloysite is saturated with formamide it re-expands from 7.2Å to 10Å. However, after multiple treatments with formamide, no evidence of halloysite was found in any of the samples from all three soil cores.

2.3.4 ^{137}Cs Size Fraction Experiment

Figure 2-20 shows the count rate for disintegrations per minute per gram of sample for the sand, coarse silt, fine silt, and clay size fractions of FQ samples FQ158-178 and FQ21-36 after the Jackson treatments of Cs-137 spiked soils. High activity was observed for both the fine silt and clay sized fractions. The >20-50 µm sample FQ158-178 was spilled in the oven and lost. The high cesium content in the fine silt fraction was unexpected as clay minerals are the primary sorbents of cations such as cesium (*Francis and Brinkley, 1976*). This finding prompted the investigation into the mineralogical identification of the fine silt size fraction of the SRS soils.

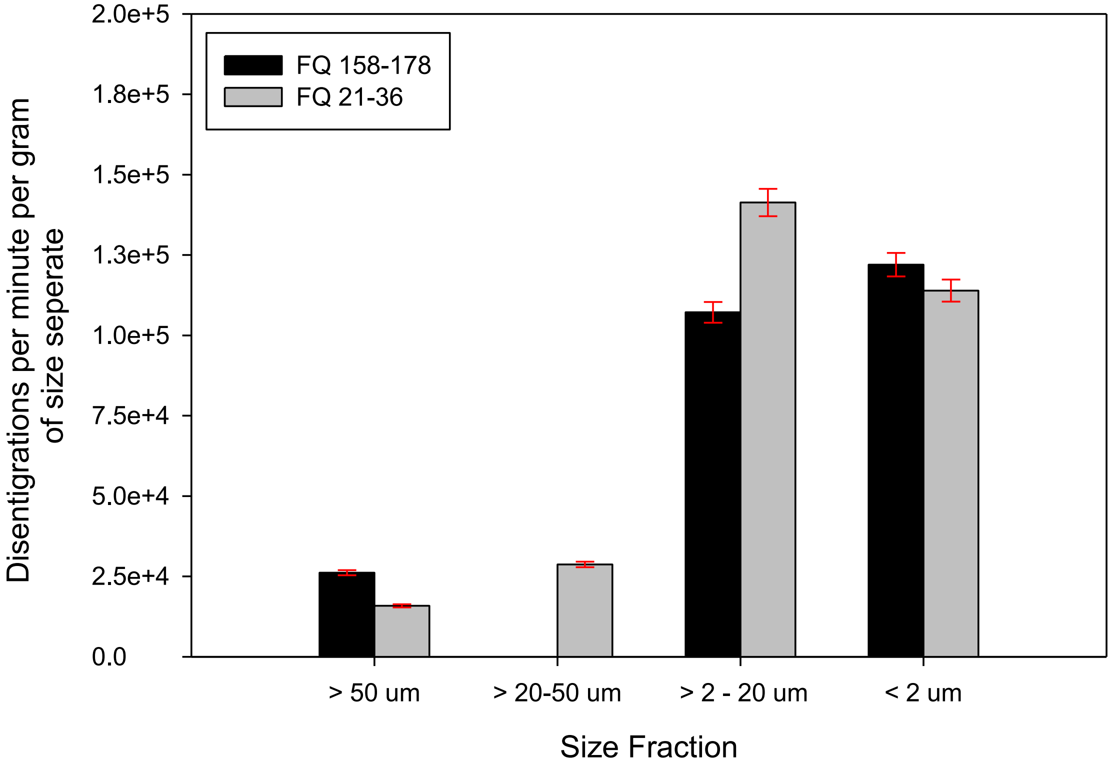

Figure 2-20: ^{137}Cs in the size fractions of two FQ samples. Standard error is estimated at 3-5%, 5% shown. Sample FQ 158-178 (>20-50µm) was lost.

2.3.5 Mineralogy of Clay versus Fine Silt

The chemical work in this study was performed on the <62 μm size fraction of the soils. Preliminary data from a ^{137}Cs sorption experiment (see Section 2.3.4) suggested there may be minerals present in the 2-20 μm fraction (fine silt) contributing to the sorption of alkali metals. This was additional inspiration to the primary project objectives to investigate the mineralogy of the fine silt size range. Most of the following data were obtained under my supervision as research for the undergraduate Honor's thesis by Amanda Lanning (*Lanning*, 2012).

Figure 2-21 shows the XRD patterns of air-dried clay from the Fuquay soil core samples overlain by the patterns from the fine silt (2-20 μm) size fractions. Each depth has very low intensity for the quartz peak and have been scaled to amplify its presence (Figure 2-21). There is a small ratio of signal to noise from the fine silt for the two deepest samples (FQ158-178 and FQ179-293), so for these two samples the pattern has been smoothed by a 5-point running mean to better show the peaks. Quartz is present in the fine silt at all depths, as indicated by the 3.33Å peak and the less intense 4.25Å 101 peak. In agreement with results of the ^{137}Cs sorption study, a small but discernible 14.4 Å peak is evident for fine silt from samples FQ21-36, FQ36-56, FQ57-76, and FQ137-157. There may also be 14.4 Å peaks for the two deepest samples, but the signal to noise ratio was too high to determine the significance of those peaks. Based on the extensive mineralogical study conducted on the clay size fraction, this 14.4Å peak is likely due to silt sized HIV as in the clay size fraction. Samples FQ158-178 and FQ179-293 also have small kaolinite and gibbsite peaks at 3.57Å and 4.85Å.

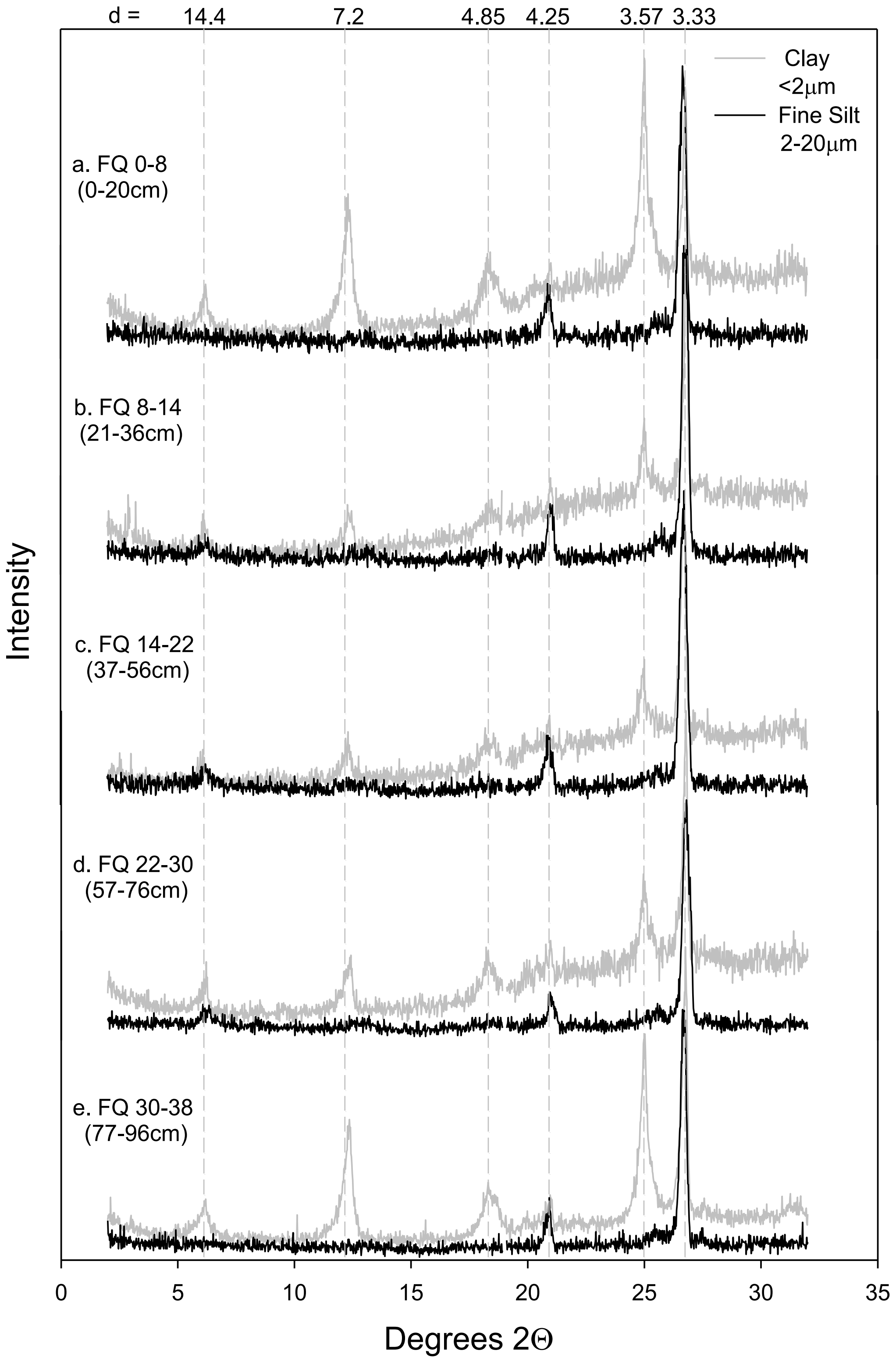

Figure 2-21: Fuquay clay (gray) and fine silt (black) XRD patterns. The intensities are scaled so the quartz peaks are equal graphically as a visualization tool but may not be of the same magnitude.

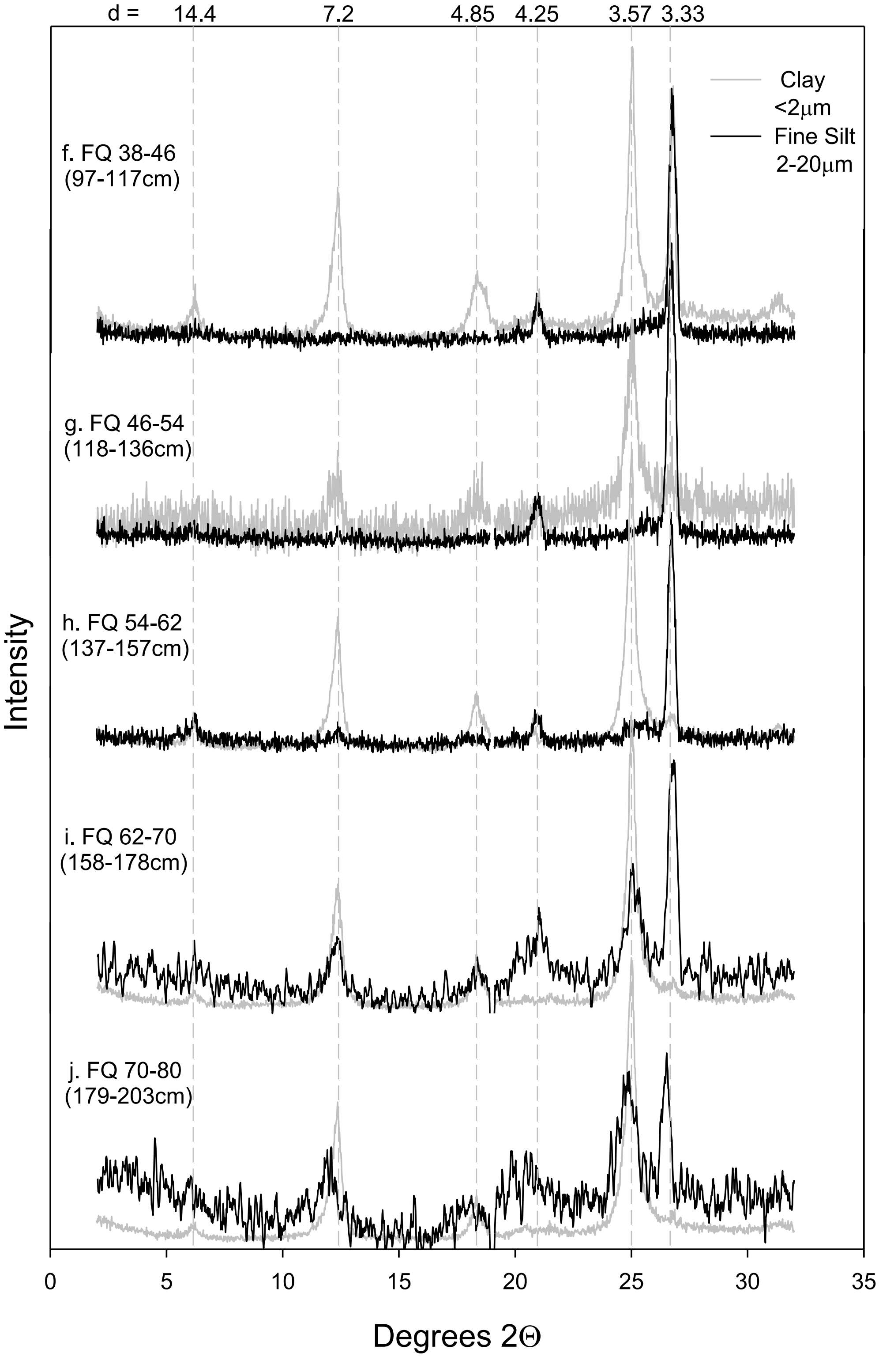

Figure 2-21(cont.): Fuquay clay (gray) and fine silt (black) XRD patterns.

Figure 2-22 shows the XRD pattern of air-dried clay from each FQTRS soil core segment overlain by the corresponding pattern for fine silt. As in the Fuquay core, diffraction from quartz in fine silt from each depth in the FQTRS core caused peaks at 3.33 Å and 4.25 Å. There are also small but discernible peaks at 14.4Å and 7.2 Å in TRS47-61 and TRS62-76. The peaks at d = 7.2 Å are second order reflections from the 14.4 Å mineral but may include some contribution from kaolinite (Figure 2-22). The 14.4 Å mineral at these two depths is interpreted to be HIV, in accordance with the clay mineralogy of the same samples.

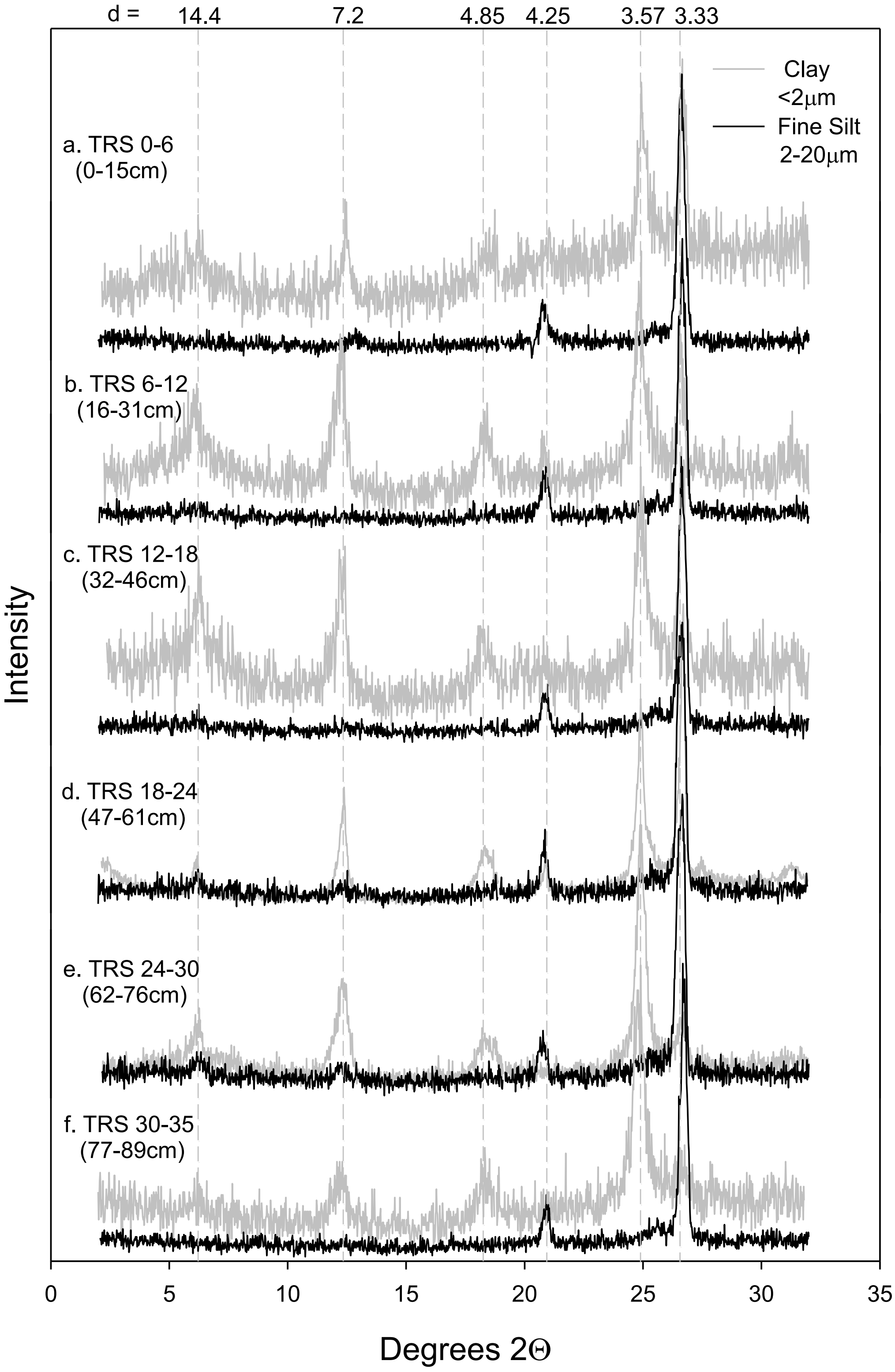

Figure 2-22: FQTRS clay (gray) and fine silt (black) XRD patterns.

The fine silt fraction of the FQQAL core has much greater variability in mineral content. Figure 2-23 shows the XRD pattern of air-dried clay from each segment of the FQQAL soil core overlain by the corresponding fine silt (2-20 µm) size fraction XRD pattern. As for the other two cores, every sample has peaks at 3.33 Å and 4.25 Å corresponding to quartz. However, in contradiction to the other cores, patterns for all depths below 29 cm have a sharp peak at 10.0 Å, corresponding to mica. This peak is either very small or is not visible in the diffraction patterns of the clay size fraction for this core. There is silt-sized kaolinite in all FQQAL samples except the upper two and FQQAL62-76, as shown by peaks in the XRD patterns at 7.2 Å and 3.57 Å. Silt sized gibbsite is identified by a peak at 4.85Å for depths between 47 and 84 cm.

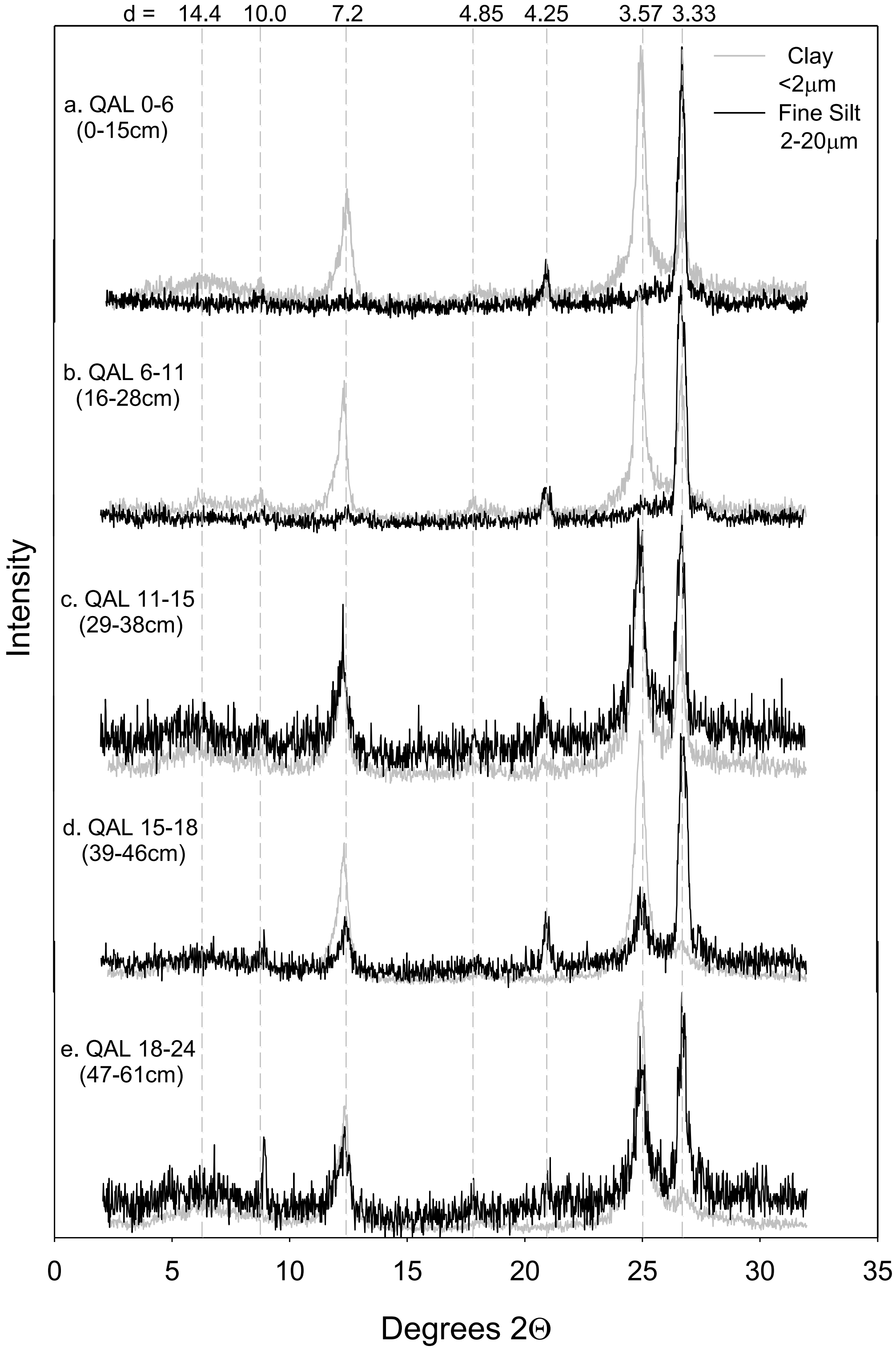

Figure 2-23: FQQAL clay (gray) and fine silt (black) XRD patterns.

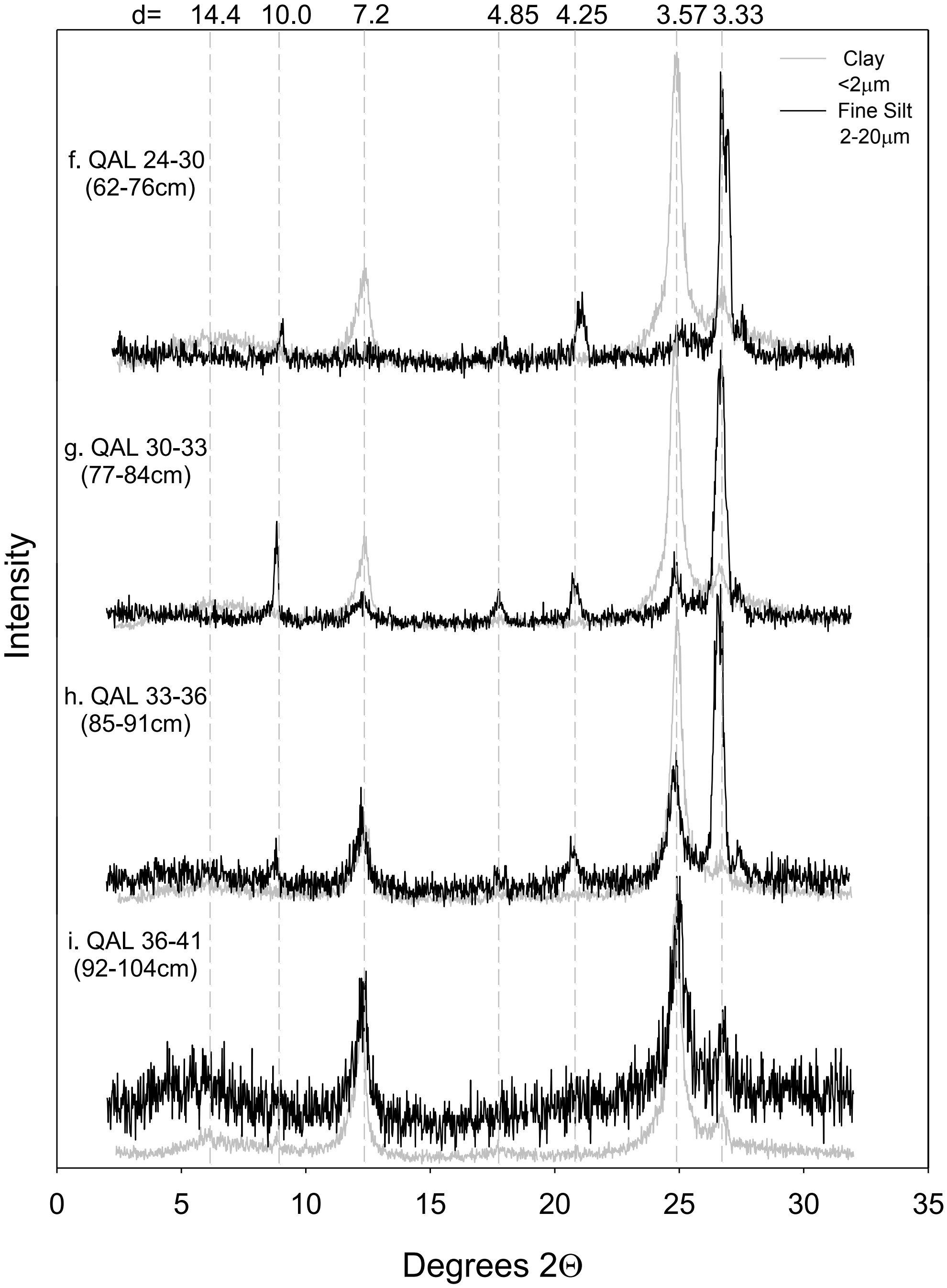

Figure 2-23(cont.): FQQAL clay (gray) and fine silt (black) XRD patterns.

2.3.6 Mineralogy of Sand Size Fraction

Sand (50 µm – 2 mm) in the Fuquay and FQTRS cores upon visual inspection is made up entirely of quartz. However, the deepest samples of core FQQAL have visible shiny mica flakes among quartz grains. Investigation of the grains in immersion oil under a microscope showed only quartz as the significant mineral. Sample SRS28 from the drill core SRS BGO-3A has many flakes of mica clearly visible to the naked eye. Mica was, however, not detected in the clay size fraction at this sample depth by XRD.

2.4 Interpretation

HIV and kaolinite are the predominant minerals found the SRS soils in this study. Illite, gibbsite, and quartz are found in lesser abundances in the clay fractions of the SRS soils. Quartz and occasionally HIV are found in the silt fractions of these soils. The clay and silt fractions of these SRS soils are extensively characterized with the combination of XRD and synchrotron diffraction patterns. The sand fraction contained quartz and thus the sand fraction was not studied in later chemical analyses. The large surface area and low charge of quartz will provide inconsequential contribution to ion sorption (*Findley*, 1998).

While traditional XRD methods permitted conventional identification of these minerals, the use of synchrotron patterns was needed to quantify the minerals present in the clay fractions via Rietveld methods (*Perdrial et al. 2011*) and to identify illite present in two of these soils (FQQAL, and FQTRS). The *hkl* peaks were crucial to identifying illite in these clay fractions samples that was not identified with traditional XRD. The 10Å peak is not evident in the diffraction patterns of cores FQTRS or FQQAL (Figures 2-17 and 2-18) and it *hkl* peaks that made the identification of the illite phase.

Mineral phase quantification based on diffraction data is a useful tool, as it provides reproducible and representative results. Many clay mineralogy studies are now incorporating Rietveld modeling, with applications such as studying changes in mineral assemblages when storing wastes and increasing pCO_2 to the dissolution of primary and clay minerals near contamination sites (*Perdrial et al.* 2011). By processing the XRD pattern through the Rietveld method (*Rietveld,* 1969), quantifications are more reliable than from peak height estimations of quantities because important drawbacks such as peak overlap and preferred orientation from powder XRD quantification can be overcome. The application of Rietveld analysis to quantification of clay minerals was limited due to the difficulty in describing refineable structures for disordered phyllosilicates (*Bish and Post*, 1993). Variability in mineral composition, mineral phases close to the detection limit, and the presence of poorly crystallized material, can cause some deviations in modeling. In this study, to capture the kaolinite properly, three slightly varying patterns of kaolinite were used as in studies to account for the disorder (*Perdrial et al.* 2011).

A caveat to this method is that we have chi squared values to represent a goodness-of-fit of the model pattern to the diffraction pattern, but a chi-squared value that is good for the pattern as a whole, may not capture individual minerals well. Neither XRD nor synchrotron identified mica in the samples, but K-Ar data suggests that mica cores are present (*Naumann et al.* 2012). It is likely that the mica cores are too small to be detected and that the intensity of diffraction peaks from other minerals are great enough to obscure any small reflection from the mica that is occurring beyond detection by both methods.

The amount of weathering of the soils can be approximated by the mineralogy present in the clay fractions. At first approximation, the presence of kaolinite and gibbsite show a mature and zonal soil that is well leached while the presence of smectite, illite show a less mature soil (*McBride*, 1994). In these soils, muscovite parent material has long weathered away leaving only mica (purported) cores and secondary phyllosilicate minerals behind as weathering products (HIV, kaolinite, gibbsite) and residual quartz. Illite can be either detrital or a result of chemical weathering of muscovite mica. As K is removed, the mica transforms to illite. Further weathering both removes more K from the interlayer and transforms the mica layer to vermiculite (or high charge smectite) or HIV. Further weathering of vermiculite removes silica sheets in greater proportion to Al-dioctahedral sheets leaving gibbsite as the final weathering product (*McBride*, 1994). The transformation of muscovite to vermiculite or a high charged smectite has been shown present in Piedmont soils (*Harris et al* 1992 and *Elliott et al.* 1997) and elsewhere (*Maes et al.* 1999). The Fuquay soil series is located in and ideal environment for the development of deep and mature soil profiles. The slope of the ground is only 0-10° allowing for percolation of water into the soils that are well drained and slowly permeable, allowing for leaching of ions from upper horizons and development of many soil horizons with time (Looney, Rogers).

Given the foregoing, the stage of weathering of the three SRS soils in order of decreasing extent is FQ, FQTRS and FQQAL. FQ has no illite present but does have gibbsite. The formation of gibbsite requires time for the weathering sequence to occur and remove K and Si from the minerals to form this end member oxide. FQTRS clays contain both illite and gibbsite, so it is an intermediate maturity soil. It has not had enough time for all the illite to weather by transformation completely into other pedogenic minerals, but has developed some gibbsite in the clay size fraction. FQQAL has no gibbsite present. This is a very immature soil that is alluvial in nature and may have detrital illite or weathered mica. Illite is typically found in younger soils.

The lack of gibbsite in the core suggests the soil is very young, so the duration of weathering is low.

In addition to the mineralogical identification, some clear correlations to the clay content of the sample and the minerals present were seen in this study. In Fuquay (FQ), the clay content is much greater in the three deepest samples. This is consistent with weathering moving smaller particles deeper into the soil as water percolates the water column. These three deepest samples are high in kaolinite concentration by over 80% whereas in the surface samples kaolinite ranges from 30-50% of the mineral makeup. The correlation of kaolinite with clay content is r = 0.92 in this core. HIV and quartz decreased with increased clay content in the FQ core. The correlation of these minerals and clay percentage are r = -0.90 and r = -0.86 respectively, where r is the correlation coefficient. Gibbsite is positively correlated with clay content and depth with r = 0.69. Additionally, these correlations are calculated based on clay percentages calculated by difference versus weight (Section 2.3.1 and Tables 2-1 and 2-2). Thus, there may be large errors in the percent clay calculated in this way which might change the correlation value. However, in all cases, the mass of clay by difference was always greater than the mass of clay measured, so the general trend for the clay content with depth is unlikely to change dramatically, even if the overall value of clay percentage changes.

Correlation with clay percentage to minerals is also high in the FQTRS core. The greatest correlations are the inverse correlation of clay content with quartz (r = -0.9) and a positive correlation of r=0.82 with illite. Gibbsite and HIV are both positively correlated with the clay content to a lesser extent with values of r = 0.7 and r = 0.57 respectively. The correlation coefficient of kaolinite and clay content is 0.22 in this core. The amount of clay sized quartz is lower at depths because the clay minerals are in greater quantities here as a result of illuviation down the water column during weathering.

None of the correlations are as strong in the FQQAL core as it is a young, immature soil with horizons still developing. Illite has the strongest negative correlation with $r = -0.66$. The correlation coefficients of clay content with kaolinite and HIV are $r = 0.50$ and $r = 0.51$ respectively. The correlation of clay and quartz is $r= - 0.47$. This core may have large errors in the clay percentage reported in Table 2-1 calculated by mass difference. This was a very iron rich sample as apparent by its dark red/orange color. The mass of iron removed from the clay by Jackson treatments is not accounted for in the size fraction percentage's reported in Table 2-1, as evident by the high percent differences in the two surface samples in Table 2-2 (57% and 81% difference).

Lastly, the ^{137}Cs size separation experiment found that the fine silt size fraction was adsorbing nearly as much ^{137}Cs as the clay size fraction (though in most samples, the fine silt is a smaller contributor to the sample by mass. The mineralogy of the fine silt is predominately quartz. Several samples in core FQQAL and FQ contain silt sized HIV, kaolinite, and gibbsite. FQQAL also has mica peaks in the deeper section of the core that are not in the clay size fraction. Of the minerals identified, gibbsite is not likely to sorb any ^{137}Cs. Silt sized HIV and mica are the likely to sorb ^{137}Cs. Sorption on the planar surfaces of the fine silt sized kaolinite can also sorb ^{137}Cs.

Another explanation for the high Cs in the fine silt size range could be the presence of clay particles coating fine silt and silt grains. Had clay particles still coated the silt size fraction, the contribution to the sorption may have been overestimated. These samples were all normalized by the weight of the sample, and so clay particles mixed with the silt would add little mass, but a large amount of surface area to the sample for sorption to have occurred. These samples have been treated with Jackson's methods so organic matter in the silt is not a possibility. As with the clay samples, mica peaks may be so small that they are obscured by the intensity of other mineral peaks.

3 CHEMICAL ANALYSIS

3.1 Introduction

One of the objectives of this project was to determine the degree to which stable Cs has been enriched by natural weathering processes in the SRS soils relative to other alkali metals. Rb was measured because it shares the tendency of Cs to become enriched relative to K in certain cation exchange sites on micaceous minerals, although to a smaller degree (*Brouwer et al.* 1983). Comparing Cs/K ratios to Rb/K ratios in soils and in acid extracts of the soils increases our understanding of the enrichment processes evident in these soils. Sr and Ba were also measured because they also form large cations, which compete with Cs and Rb ions for exchange sites on the mineral surfaces. Sr is of particular interest because ^{90}Sr is a fission product that was produced in large quantity at the SRS and is closely similar to ^{137}Cs in fission yield and half-life (*Anonymous*, 2009). Strong (50% HNO_3) and moderate (10% HNO_3) acid extractions were used to extract both exchangeable and fixed cations but should have had little effect on the original structural cations of micas. Simple ion exchange using concentrated ammonium acetate (NH_4OAc) solution tells of the concentrations of easily exchangeable and unbound Cs and K in the soils.

The untreated fine fractions of soils (<62µm, see Section 2.2.2) were analyzed for the mass fractions of certain alkali and alkaline earth metals. This fine fraction was selected for analysis as minerals in the clay and silt are the ones that will contribute to the adsorption of cations in the soils. The sand is almost entirely quartz and is not considered to play a role in the adsorption of metals.

3.2 Methodology

3.2.1 Strong acid extraction

Portions of the untreated fine fractions were treated with a strong acid in a manner similar to EPA method 3050B (*EPA*, 1996), which is intended to remove all exchangeable cations from the surface of particles, but also may dissolve some primary minerals (e.g. *Wampler et al*, 2012). One hundred milligrams of sample were weighed and transferred to 22 mL Savillex® vials cleaned in an acid bath of HNO_3 at ~80°C. Ten milliliters of 50% Optima® HNO_3 was added to the vials, which were then shaken vigorously. For the Fuquay soil cores, the acid extraction was done in a water bath at ~100°C, manually shaken every 5 minutes for the first half hour, and then every 15 minutes for the next 2.5 hours. The water bath method proved to be very cumbersome as the water evaporated at a rate that required additional water to be added frequently to keep the reacting mixture submerged and at the proper temperature. Acid extraction of the rest of the samples was done in an oven at 100°C, and the mixtures were shaken manually with the same frequency as listed above. After 3 hours of extraction, vials were centrifuged at 2000 rpm for 10 minutes. The supernatant liquid was poured into acid cleaned Savillex vials and 4 mL of high purity deionized water was added to the remaining sediment. The mixture was shaken and centrifuged for an additional 10 minutes at 2000 rpm, and the supernatant liquid was added to the original supernatant liquid.

Extractant solutions were spiked with two drops of Rb-Sr spike with highly enriched ^{85}Rb, amounting to ~60 μg ^{85}Rb per sample. Approximately 4 mL of spiked leach solution was transferred to a new Savillex vial, with care taken at each step to weigh the fluid for each sample. The remaining 10 mL of solution was set aside for K determinations described in Section 3.2.4. Vials were placed on a hot plate under clean air flowing into a hood to evaporate the solution for trace element determinations by inductively-coupled plasma mass spectrometry (ICP-MS) using a Thermo Scientific Element 2 high resolution, sector magnetic field ICP-MS at Georgia State University. The residue in the vials after evaporation was taken up in 2% Optima HNO_3 and isotopically analyzed for species at m/z = 85, 87, 88, 133, and 137. The symbols m and z stand for ionic mass and charge, respectively, in atomic units.

3.2.2 Mass calculations from intensity measurements

Mass fractions of Cs, Rb, Sr, and Ba were calculated from the measured ICP-MS beam intensities by reference to beam intensity values obtained from a tuning solution with known mass fractions of each of these elements. The calculations may be described as a series of steps.

First, the beam intensity due to ^{87}Rb was calculated by subtracting the contribution of ^{87}Sr to the signal at m/z = 87 by assuming equal instrument sensitivity for the different Sr isotopes and normal terrestrial isotopic composition of the Sr (Equation 3.1):

$$I(^{87}Rb) = I(m/z = 87) - I(m/z = 88) \times \frac{n(^{87}Sr_{terrestrial})}{n(^{88}Sr_{terrestrial})} \tag{3.1}$$

where I stands for beam intensity and n stands for amount of substance. (Thus $n(^{87}\mathrm{Sr}_{\mathrm{terrestrial}})/\ n(^{88}\mathrm{Sr}_{\mathrm{terrestrial}})$ is the molar ratio of ^{87}Sr to ^{88}Sr in normal terrestrial Sr.) This correction is relatively small, ~10% or less.

Next, the mass of ^{85}Rb that was added in the spike solution is calculated and reported in micrograms (Equation 3.2).

$$m(^{85}\mathrm{Rb}_{\mathrm{spike}}) = m(\text{spike solution}) \times w(^{85}\mathrm{Rb}_{\mathrm{spike}}), \tag{3.2}$$

where m stands for mass and $w(^{85}\mathrm{Rb}_{\mathrm{spike}})$ is the mass fraction of ^{85}Rb in the spike solution, 5.86×10^{-5}.

Next, the mass of ^{85}Rb in the spike is converted to amount of substance, *n*, by dividing by the molar mass (*M*) of ^{85}Rb, 84.91179 g mol^{-1}(Equation 3.3).

$$n\ (^{85}\mathrm{Rb}_{spike}) = \frac{m(^{85}\mathrm{Rb}_{\mathrm{spike}})}{M(^{85}Rb_{spike})} \tag{3.3}$$

From this information the amount of natural ^{87}Rb in the sample solution, $n(^{87}\mathrm{Rb}_{\mathrm{sample}})$, can be calculated from the intensities (Equation 3.4).

$$n\ (^{87}\mathrm{Rb}_{\mathrm{sample}}) = n(^{85}\mathrm{Rb}_{\mathrm{spike}}) \times \frac{\left(\frac{I(^{87}\mathrm{Rb})}{I(^{85}\mathrm{Rb})}\right) - \left(\frac{n(^{87}\mathrm{Rb}_{\mathrm{spike}})}{n(^{85}\mathrm{Rb}_{\mathrm{spike}})}\right)}{1 - \frac{\left(\frac{I(^{87}\mathrm{Rb})}{I(^{85}\mathrm{Rb})}\right)}{\left(\frac{n(^{87}\mathrm{Rb}_{\mathrm{terrestrial}})}{n(^{85}\mathrm{Rb}_{\mathrm{terrestrial}})}\right)}} \tag{3.4}$$

where $I(^{85}\mathrm{Rb})$ is the measured beam intensity at $m/z = 85$ and $I(^{87}\mathrm{Rb})$ was defined above. The molar ratio of ^{87}Rb to ^{85}Rb in the spike is a known value of 0.0015023, and the molar ratio of terrestrial ^{87}Rb to ^{85}Rb is 0.3856173. Dividing this amount of ^{87}Rb by the isotopic abundance of ^{87}Rb in terrestrial Rb (0.2783) gives the total amount of Rb (^{87}Rb and ^{85}Rb) in the original test solution (the one to which the spike was added).

Based on the known concentration of Rb we can calculate the rest of the element concentrations based on ratios with respect to the known value. The sensitivity of the Element ICP-MS can change from day to day, so for each sample run, the sensitivity of the machine for each isotopic species sensitivity, s_i, relative to the sensitivity for ^{85}Rb, is calculated from tuning solution data (Equation 3.5).

$$s_i = \left(\frac{I_i}{I(^{85}Rb)}\right) / \left(\frac{c(^{85}Rb)}{c_i}\right) \tag{3.5}$$

where I_i is the beam intensity for species i in the test solution, $I(^{85}\mathrm{Rb})$ is as defined above, and $c(^{85}\mathrm{Rb})/c_i$ is the ratio of concentrations of ^{85}Rb and species i in the tuning solution.

Next the amount, *n*, of each element (Cs, Sr, or Ba) in the test solution is calculated in Equation 3.6,

$$n = s_i \times I_i \times \frac{[n(^{85}Rb_{spike}) + n(Rb_{sample}) \times x(^{85}Rb)]}{[I(^{85}Rb) \times x_i]} \tag{3.6}$$

where the subscript *i* denotes the relevant isotopic species for each element and *x* stands for the mole fraction (isotopic abundance) an isotopic species in the element.

The amount of each element can be converted to mass by multiplying by the molar mass, and, finally, the mass fraction is calculated by dividing the mass of the element by the mass of the test portion.

3.2.3 Moderate acid extraction

Acid extraction of additional portions of the untreated soil fine fractions was done as described above for the strong acid extraction except that 10% Optima HNO_3 was used and the temperature was 80°C. All of these experiments were completed in the oven rather than a water bath. Species in solution were determined by ICP-MS.

3.2.4 Flame atomic absorption spectrophotometry

Ten milliliters of the ^{85}Rb-spiked acid extract solution in a Savillex vial was placed onto a hotplate in a fume hood and evaporated to dryness. The residue was taken up in a 0.01 mol/L

CsCl, 0.1 mol/L HNO_3 solution for K determination. This solution was poured into a blue capped polystyrene 50 mL centrifuge tube. The Savillex vials were rinsed several times with the CsCl/HNO_3 solution to ensure all salts were removed and added to the 50 mL tube to a total of 30-40 mL. The solutions were carefully weighed with a Denver Instrument balance, model M-310.

Potassium measurements were by flame atomic absorption spectrophotometry (FAAS) using a Perkin Elmer model 3110 atomic absorption spectrophotometer at Georgia State University. Absorbance values for standard solutions of KCl ranging in mass fraction K from 0.25 mg/kg to 2.5 mg/kg (in steps of 0.25 mg/kg) bracketed sample absorbance values, and a linear interpolation was applied to absorbance values for sample solutions. Dilutions were made to this range when necessary. Absorbance for each sample solution was measured 10 times over 1 s intervals and the average intensity value accepted when the relative standard deviation was less than 2% (*Wampler et al.* 2012). All of the sample solutions were measured twice with this method, and the average of the two averages of 10 measurements was taken.

3.2.5 Simple ion exchange

One gram portions were taken of all the bulk soil (<2 mm) samples from the three soils cores. These portions were loaded into 50 mL centrifuge tubes and ~33 mL of 1.0 N NH_4OAc was added. The mixtures were shaken for 5 min and then centrifuged, and the supernatant fluid was saved. This process was repeated in triplicate. The combined supernatant fluids from the three cation exchange steps was diluted to a total volume of 100 mL and measured for Cs concentration by ICP-MS at the Savannah River National Laboratory. K measurements of the solutions were made by FAAS at Georgia State University. The regression coefficients, r, were calculated using Excel formulae. Regression coefficients were calculated for simple ion exchange on bulk soil, acid extractions on fine fractions (-62 mm) and total ion concentrations on the -62 mm fractions.

3.3 Results of Chemical Analyses

The results of three experiments are presented here; (1) simple exchange with concentrated NH_4OAc, (2) a 10% HNO_3 acid extraction at 80°C, and (3) a 50% HNO_3 acid extraction at 100°C. Results are presented for each segment of each core.

3.3.1 Simple ion exchange with NH_4OAc

In the simple ion exchange experiment, ammonium ions were used to displace exchangeable cations (including Cs and K) on the regular exchange sites (RES) of the bulk soils (< 2 mm) of the SRS samples and examined by depth down the three soils cores. NH_4^+ was used because it is the ion that is most favorable on these sites and the method has been developed by the EPA to most effectively investigate these exchange sites in acidic soils (*EPA*, 1986). The Cs and K displaced from the soils were measured.

In the Fuquay core, the exchangeable Cs concentrations increased with increasing depth from 0.225 μg/kg to 1.33 μg/kg (Table 3-1). The exchangeable K concentrations also increased with depth from 5.57 mg/kg at the surface to 13.2 mg/kg at the deepest depth (Table 3-1) with the exception of FQ21-36 having a value of 11.41 mg/kg. Cs and K are weakly correlated with a correlation coefficient, r, of 0.63. However, when the outlier of high K for sample FQ21-36 is removed, this correlation improves to r = 0.81.

The exchangeable Cs concentrations measured on core FQTRS show a similar trend of increasing Cs values with depth but the data show a smaller overall variation in the concentration. In particular, the two deepest samples released 2-3 times more Cs than the shallowest three (0.5-0.6 μg/kg vs. 0.1-0.2 μg/kg) soils. The mid-depth sample TRS47-61 has an intermediate value of 0.412 µg/kg (Table 3-1). The exchangeable K concentrations in FQTRS show the same trend with the deepest two samples exchanging up to 3 times more K than the shallowest samples (6-7 mg/kg vs. 2-3 mg/kg).

Table 3-1: Cs and K removed from bulk soil by simple ion exchange

Sample	Cs (µg/kg)*	K (mg/kg)	Cs/K
FQ 0-20	0.225	5.57	4.04×10^{-5}
FQ 21-36	0.265	11.41	2.32×10^{-5}
FQ 37-56	0.238	5.97	3.99×10^{-5}
FQ 58-76	0.322	4.95	6.50×10^{-5}
FQ 77-96	0.282	8.43	3.34×10^{-5}
FQ 97-117	0.375	8.51	4.41×10^{-5}
FQ 118-137	0.661	5.51	1.20×10^{-4}
FQ 138-157	1.088	9.49	1.15×10^{-4}
FQ 158-178	1.36	10.73	1.27×10^{-4}
FQ 179-204	1.332	13.23	1.01×10^{-4}
TRS 0-15	0.215	3.49	6.16×10^{-5}
TRS 16-31	0.191	2.24	8.54×10^{-5}
TRS 32-46	0.217	2.48	8.75×10^{-5}
TRS 47-61	0.412	2.76	1.49×10^{-4}
TRS 62-76	0.538	7.42	7.25×10^{-5}
TRS 77-89	0.612	6.48	9.45×10^{-5}
QAL 0-15	0.429	8.47	5.07×10^{-5}
QAL 16-28	0.148	4.93	3.00×10^{-5}
QAL 29-38	1.192	13.73	8.68×10^{-5}
QAL 39-46	1.946	23.13	8.41×10^{-5}
QAL 47-61	1.478	20.99	7.04×10^{-5}
QAL 62-76	1.585	18.90	8.38×10^{-5}
QAL 77-84	2.543	16.70	1.52×10^{-4}
QAL 85-91	1.822	8.51	2.14×10^{-4}
QAL 92-104	1.356	6.99	1.94×10^{-4}

*Error on SRS ICP-MS is ±5% (Dan Kaplan, personal communication)

Of all the cores, the Fuquay soil on the Quaternary Alluvium (QAL) has the greatest amount of exchangeable Cs in the simple exchange experiment. QAL Cs values are lowest at the surface with QAL0-15 and QAL16-28 having only 0.429 µg/kg and 0.148 µg/kg respectively (Table 3-1). From 4 to 10 times as much Cs was exchanged from deeper soil samples, with a peak in the deeper mid-depths at QAL77-84 of 2.5 µg/kg and a small drop-off at the deepest sample back to 1.36 µg/kg. Overall the amount of exchangeable K is also greatest for this core. It follows a trend somewhat like the Cs pattern; the smallest concentrations are near the surface and near the bottom, and the highest value of 23.1 mg/kg is in the middle of the core at QAL39-46. Ion exchange with NH_4OAc did not release significant amounts of Cs into the solutions based on low Cs/K ratios Table 3-1.

3.3.2 Moderate (10%, 80°C) acid extraction

The moderate acid extraction was intended to remove all the alkali metals not bound within the silicate structures of the minerals including those released from bulk soil portions by simple exchange with NH_4OAc. The amounts of Cs, Rb, K, Sr, and Ba, extracted from the <62 µm fraction into the acid solution are listed in Table 3-2. The amounts of these metals in the residues after extractions are given in Appendix B.

Table 3-2: Cs, Rb, K, Sr, and Ba in moderate acid extracts

	Amount extracted in 10% leach				
Sample	**Cs[*]**	**Rb[*]**	**K[§]**	**Sr**	**Ba**
	mg/kg	**mg/kg**	**g/kg**	**mg/kg**	**mg/kg**
FQ 0-20 (0-8)	1.9	6.2	0.13	6.69	45.1
FQ 21-36 (8-14)	4.4	13.5	0.13	2.29	44.4
FQ 37-56 (14-22)	3.6	14.8	0.15	2.08	41.7
FQ 57-76 (22-30)	3.5	14.2	0.13	1.81	34.0
FQ 77-96 (30-38)	4.4	19.1	0.19	2.23	35.9
FQ 97-117 (38-46)	4.6	19.3	0.20	3.23	41.6
FQ 118-137 (46-54)	6.7	29.7	0.31	3.50	71.4
FQ 138-157 (54-62)	5.4	22.4	0.33	3.50	65.3
FQ 158-178 (62-70)	6.0	12.9	0.24	2.78	32.0
FQ 179-203 (70-80)	2.6	8.6	0.18	2.65	19.5
TRS 0-15 (0-6)	3.6	16.8	0.17	2.05	42.9
TRS 16-31 (6-12)	3.0	15.0	0.16	1.52	38.6
TRS 32-46 (12-18)	2.5	13.5	0.16	1.30	28.9
TRS 47-61 (18-24)	3.2	17.6	0.21	1.41	35.3
TRS 62-76 (24-30)	5.4	29.5	0.38	4.01	96.0
TRS 77-89 (30-35)	5.2	25.5	0.45	4.44	92.9
QAL 0-15 (0-6)	0.9	8.1	0.2	2.2	42.6
QAL 16-28 (6-11)	1.2	20.2	0.3	2.9	65.6
QAL 29-38 (11-15)	2.6	21.6	0.4	7.9	114.8
QAL 39-46 (15-18)	3.4	28.4	0.6	14.6	147.1
QAL 47-61 (18-24)	2.9	23.4	0.5	13.2	106.9
QAL 62-76 (24-30)	2.4	19.2	0.5	9.9	71.5
QAL 77-84 (30-33)	2.7	19.6	0.5	10.2	71.4
QAL 85-91 (33-36)	2.9	19.0	0.4	6.5	57.4
QAL 92-104 (36-41)	2.7	18.1	0.4	5.3	51.1

[*] The extracted amount of each element is expressed as a mass fraction relative to the mass of the <62 µm test portion. The ICP-MS errors for Cs and Rb based on duplicate runs of standard test solution are 10% and 6% respectively (Wampler et al. 2012, SI).

[§] K error from the AAS ranges from 1-2% (Wampler et al. 2012, SI)

Error for Sr and Ba is estimated at 10%.

3.3.3 Strong (50%, 100°C) acid extraction

The strong extraction removes all exchangeable cations and also breaks down part of the silicate structure, releasing some of the structural cations of mica (K) into solution (*Naumann*, 2011). The amount of each ion extracted by the 50% leach is listed in Table 3-3.

Table 3-3: Cs, Rb, K, Sr, and Ba in strong acid extracts

	Amount extracted in 50% leach				
Sample	**Cs mg/kg**	**Rb mg/kg**	**K g/kg**	**Sr mg/kg**	**Ba mg/kg**
FQ 0-20 (0-8)	2.2	8.7	0.18	6.1	39.5
FQ 21-36 (8-14)	4.6	19.1	0.19	3.9	54.4
FQ 37-56 (14-22)	4.2	19.0	0.28	4.2	28.7
FQ 57-76 (22-30)	4.4	20.2	0.30	4.5	50.3
FQ 77-96 (30-38)	4.8	24.1	0.24	3.3	45.1
FQ 97-117 (38-46)	5.4	26.4	0.34	4.6	52.7
FQ 118-137 (46-54)	8.2	40.5	0.59	6.3	95.3
FQ 138-157 (54-62)	8.8	36.7	0.83	10.2	107.2
FQ 158-178 (62-70)	3.5	14.2	0.33	4.1	38.0
FQ 179-203 (70-80)	3.0	11.3	0.32	4.2	27.5
TRS 0-15 (0-6)	4.0	22.3	0.33	3.2	45.4
TRS 16-31 (6-12)	3.1	18.7	0.26	3.1	47.6
TRS 32-46 (12-18)	2.6	16.2	0.25	2.8	36.2
TRS 47-61 (18-24)	3.4	21.7	0.35	3.2	48.6
TRS 62-76 (24-30)	7.4	46.6	0.98	8.3	145.8
TRS 77-89 (30-35)	7.1	41.3	1.04	8.7	133.8
QAL 0-15 (0-6)	0.9	8.6	0.19	2.4	40.2
QAL 16-28 (6-11)	1.3	13.6	0.26	2.9	68.9
QAL 29-38 (11-15)	2.7	26.3	0.57	10.0	138.3
QAL 39-46 (15-18)	4.0	38.0	0.97	18.8	183.9
QAL 47-61 (18-24)	3.3	31.3	0.90	16.7	134.4
QAL 62-76 (24-30)	2.6	24.9	0.81	12.8	88.4
QAL 77-84 (30-33)	3.0	25.4	0.81	13.3	87.7
QAL 85-91 (33-36)	3.3	26.3	0.68	9.1	71.7
QAL 92-104 (36-41)	3.2	24.5	0.69	7.8	66.9

* The extracted amount of each element is expressed as a mass fraction relative to the mass of the <62 μm test portion. The ICP-MS errors for Cs and Rb based on duplicate runs of standard test solution are 5% and 3% respectively (Wampler et al. 2012, SI).
Error for Sr and Ba is estimated at 10%.
[§]K error from the AAS ranges from 1-2% (Wampler et al. 2012, SI)

3.3.4 Total elemental concentration in SRS soils

Table 3.4 lists the total amounts of Cs, Rb, K, Sr, and Ba in the fine fractions of the samples from the three soil cores. For each sample, the total amount of each element is the sum of the amount extracted into the acid solution from a test portion of the soil fine fraction (<62 μm) and the amount of that element remaining in the residual solid material after the acid extraction. That total amount is expressed in Table 3-4 as a mass fraction relative to the mass of the test portion. The mass fractions of Cs the soil fine fractions are of the same order as the average value of Cs in rock of the upper continental crust (UCC) on earth (~4.9 mg/kg, *Rudnick and Gao*, 2004). Three middle samples in the Fuquay Core (FQ 97-117, FQ 118-137, and FQ 138-157) have values nearly twice that of the UCC average (Table 3.4). The two deepest samples of Fuquay on Tobacco Road Sand (TRS 62-76 and TRS 77-89) also are enriched to approximately twice (10.0 and 9.7 mg/kg, respectively) the value of average UCC. For Fuquay on Quaternary Alluvium, the five deepest samples have closely consistent values within 10% of the average UCC concentration. However the two surface samples (QAL 0-15 and QAL 16-28) are depleted in Cs by more than 50% with values of only 1.5 and 2.3 mg/kg respectively (Table 3-4).

Rb concentrations follow the same trend as Cs in FQ and TRS.

K values in the fine fractions of the core samples are drastically depleted with respect to the UCC average, 23.2 g/kg. Values are seemingly following the weathering progression of the soils with Fuquay have values ranging from 1.55 g/kg at the surface to a max of 3.13 g/kg at the 118-137 cm depth range, TRS ranges from 3.26 g/kg at the surface to 4.9 g/kg at the 62-76 cm depth range, and QAL with a reverse profile for K, has a minimum value of 4.27 g/kg at 77-84 cm range and maximum near the surface of 10.16 g/kg.

Ba in the fine fractions is somewhat depleted with respect to the UCC average, and most Sr values are less than 1/10th the UCC average.

Table 3-4: Total amounts of the alkali metals in the SRS soil cores based on 50% leach and residue

Sample	Total Cs mg/kg	Total Rb mg/kg	Total K g/kg	Total Sr mg/kg	Total Ba mg/kg
FQ 0-20 (0-8)	3.5	23.9	1.55	23.6	142.8
FQ 21-36 (8-14)	5.9	40.0	2.32	25.9	199.3
FQ 37-56 (14-22)	5.2	33.1	1.85	27.8	190.6
FQ 57-76 (22-30)	5.3	41.6	2.8	27.1	204.1
FQ 77-96 (30-38)	6.6	52.0	2.61	27.6	212.6
FQ 97-117 (38-46)	8.1	55.3	2.51	29.0	207.6
FQ 118-137 (46-54)	11.5	76.3	3.13	33.7	240.6
FQ 138-157 (54-62)	10.8	60.8	2.07	30.7	188.8
FQ 158-178 (62-70)	6.1	37.2	1.45	22.9	101.1
FQ 179-203 (70-80)	5.3	34.9	1.43	23.2	90.7
TRS 0-15 (0-6)	5.3	40.2	3.26	21.4	145.1
TRS 16-31 (6-12)	4.0	36.6	4.08	22.2	157.6
TRS 32-46 (12-18)	3.5	34.5	4.83	23.5	163.0
TRS 47-61 (18-24)	5.2	38.6	4.39	19.4	181.8
TRS 62-76 (24-30)	10.0	78.2	4.90	32.3	249.9
TRS 77-89 (30-35)	9.7	70.5	4.62	33.6	225.4
QAL 0-15 (0-6)	1.5	56.0	7.82	42.0	474.5
QAL 16-28 (6-11)	2.3	75.4	10.16	52.0	599.4
QAL 29-38 (11-15)	4.4	87.9	8.46	46.4	553.9
QAL 39-46 (15-18)	6.1	92.6	5.96	39.5	419.9
QAL 47-61 (18-24)	4.9	63.9	4.42	24.8	305.7
QAL 62-76 (24-30)	4.8	55.2	6.49	20.4	333.6
QAL 77-84 (30-33)	4.5	61.0	4.27	24.2	297.8
QAL 85-91 (33-36)	5.2	69.5	4.51	25.6	241.8
QAL 92-104 (36-41)	4.9	67.2	4.75	26.0	247.4
UCC*	4.9	84	23.2	320	624

*Values from Rudnick and Gao, 2004.
ICP-MS error for Cs and Rb based on duplicate runs of standard test solution are 5% and 3% respectively (Wampler et al. 2012, SI).
§K error from the AAS ranges from 1-2% (Wampler et al. 2012, SI)

3.3.5 Relative amounts extracted

Consistently among all three cores, the relative amount of Cs extracted from the soil fine fractions by acid was greater than for the other elements (Tables 3-5 and 3-6). The percentage of element extracted by 10% HNO_3 at 80°C decreased in the order Cs, Rb, Ba, Sr, K (Table 3-5) (Figures 3-1 – 3-3). Greater than 50% of the total Cs was removed on average from all three cores. About 30-40% of the Rb was removed on average from the fine fraction. Ba was the next greatest with about 20-30 percent of the total removed by leaching, followed by Sr ranging from around 10-20%. Only about 5% of the K was removed from the samples of each core.

Table 3-5: Fraction of alkali and alkaline earth metals extracted by moderate acid

Sample	Cs %	Rb %	K %	Sr %	Ba %
FQ 0-20 (0-8)	52	28	4	29	29
FQ 21-36 (8-14)	67	38	3	8	20
FQ 37-56 (14-22)	67	38	3	8	21
FQ 57-76 (22-30)	66	39	3	7	18
FQ 77-96 (30-38)	66	39	3	8	17
FQ 97-117 (38-46)	57	37	3	11	20
FQ 118-137 (46-54)	55	39	6	10	29
FQ 138-157 (54-62)	41	38	8	8	25
FQ 158-178 (62-70)	53	31	8	8	20
FQ 179-203 (70-80)	37	25	7	10	18
Average	56	35	5	11	22
TRS 0-15 (0-6)	67	63	5	10	20
TRS 16-31 (6-12)	68	41	4	7	23
TRS 32-46 (12-18)	68	38	3	5	16
TRS 47-61 (18-24)	66	42	4	5	19
TRS 62-76 (24-30)	49	39	8	11	35
TRS 77-89 (30-35)	50	36	10	13	41
Average	61	43	6	9	26
QAL 0-15 (0-6)	53	15	3	5	8
QAL 16-28 (6-11)	54	31	1	7	13
QAL 29-38 (11-15)	56	25	2	17	19
QAL 39-46 (15-18)	49	32	5	35	32
QAL 47-61 (18-24)	59	43	5	55	35
QAL 62-76 (24-30)	51	30	4	26	17
QAL 77-84 (30-33)	52	27	4	30	20
QAL 85-91 (33-36)	46	29	5	20	19
QAL 92-104 (36-41)	50	29	5	20	20
Average	52	29	4	24	20

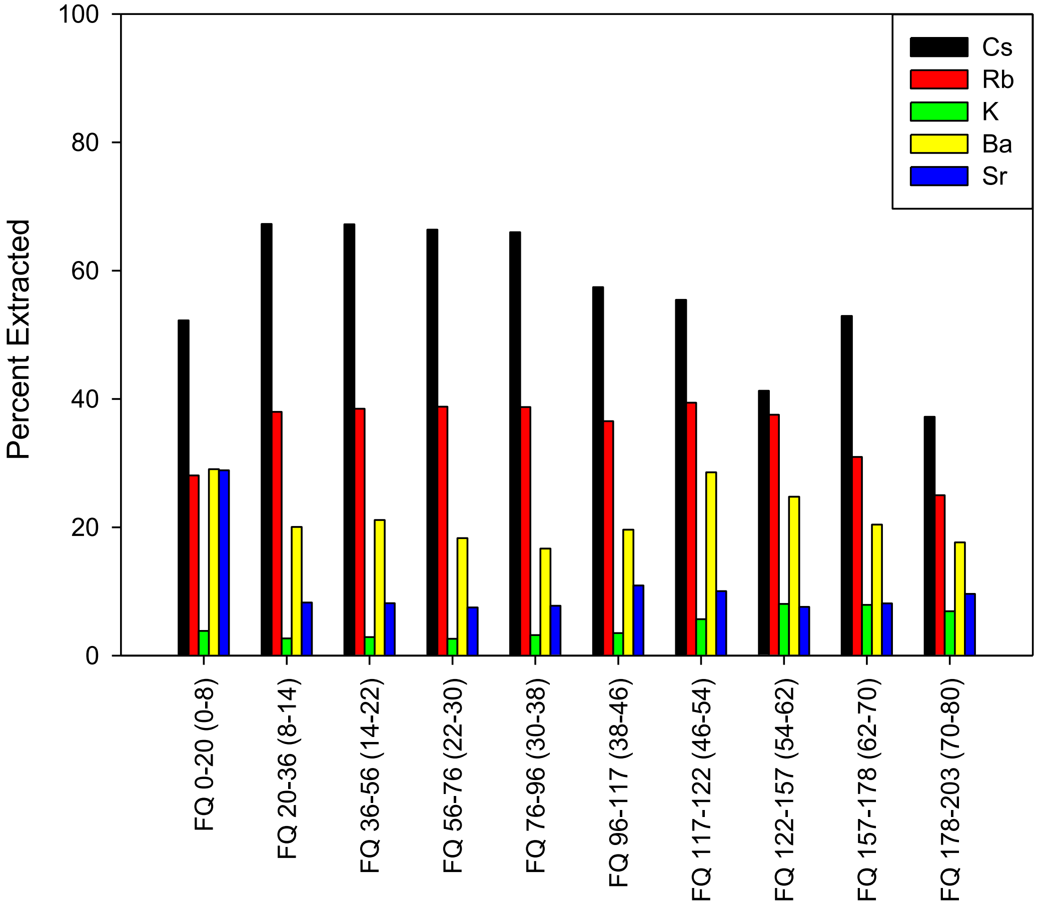

Figure 3-1: Percentages of Cs, Rb, K, Ba, and Sr extracted from the Fuquay core during the moderate acid extraction

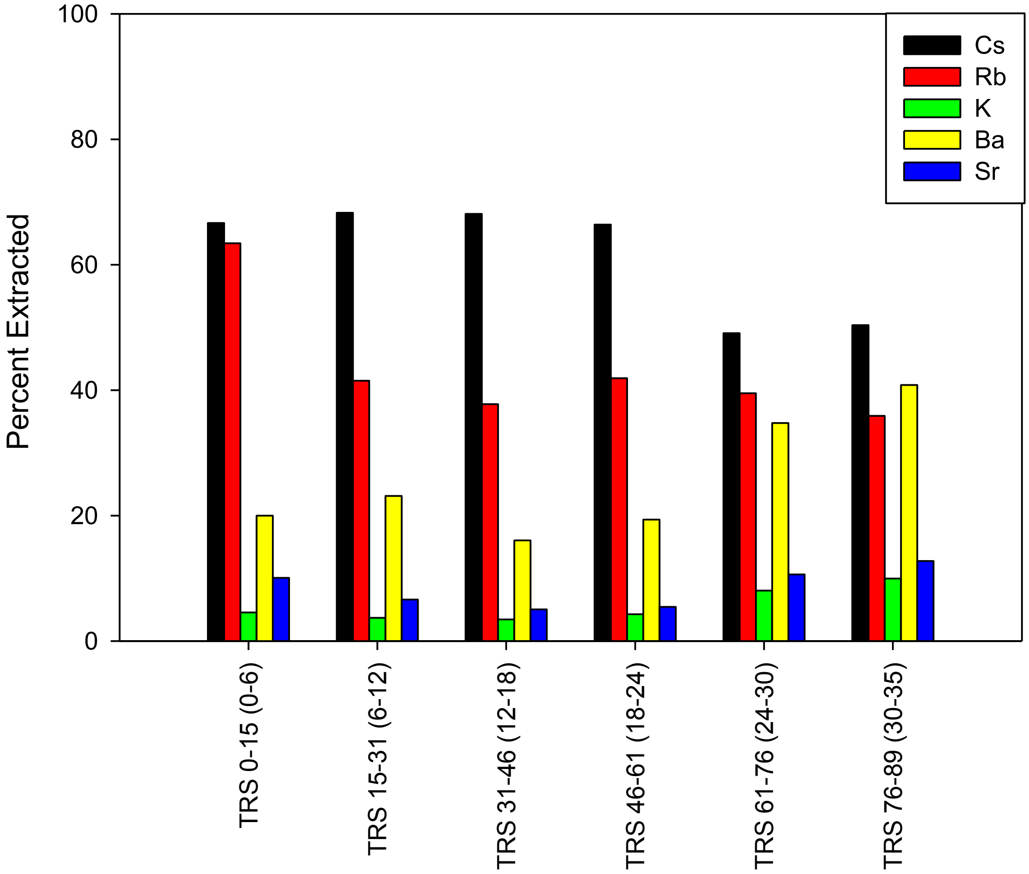

Figure 3-2: Percentages of Cs, Rb, K, Ba, and Sr extracted from the FQTRS core during the moderate acid extraction

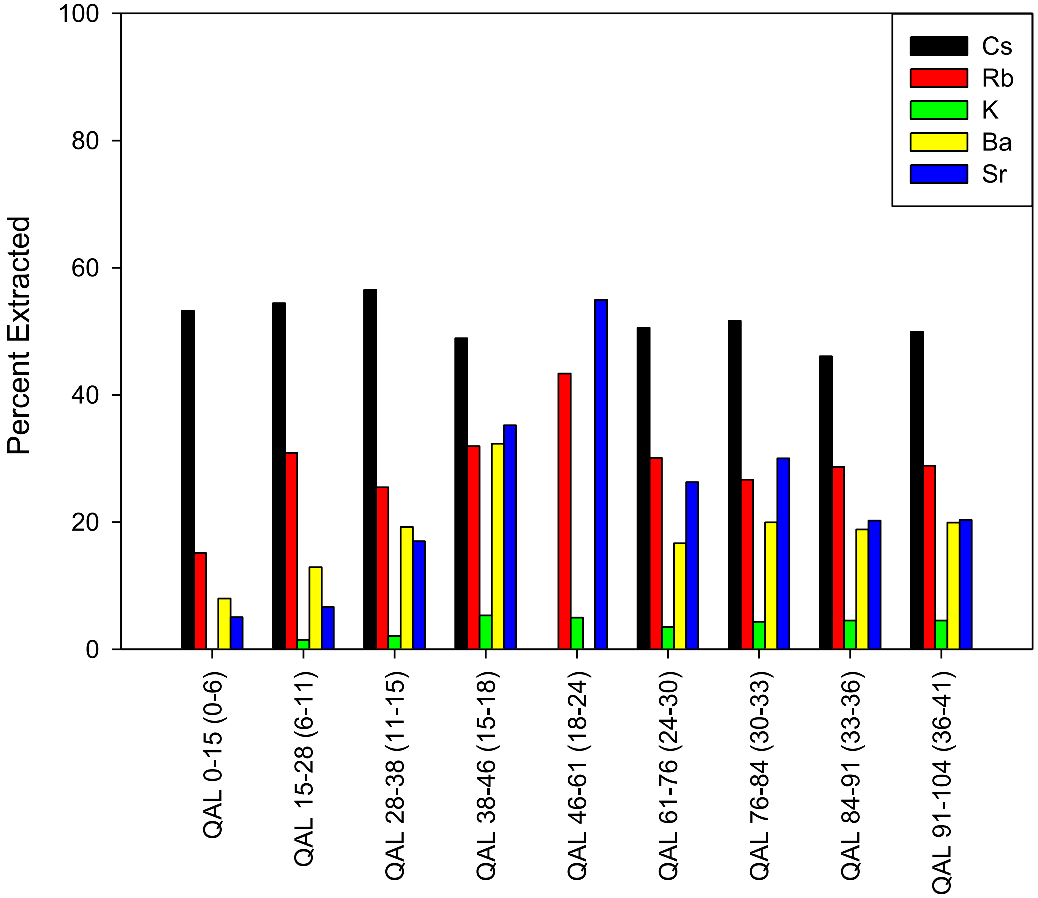

Figure 3-3: Percentages of Cs, Rb, K, Ba, and Sr extracted from the FQQAL core during the moderate acid extraction

The strong acid extraction removed ~60-75%, on average, of the Cs in each core (Table 3-6). The amount of Rb extracted from the fine fractions varied, on average, between 35% and 55%. From ~30% to ~40% of the Ba was extracted, and 18% to 37% of the Sr was removed from the samples. The K was the least affected by the extraction, which removed on average only 6-10% of the K that was originally in the samples. Figures 3-4 – 3-6 show the percentage of each element extracted from the fine fraction of each soil sample during the stronger acid extraction.

Table 3-6: Fraction of alkali and alkaline earth metals extracted by strong acid

Sample	Cs %	Rb %	K %	Sr %	Ba %
FQ 0-20 (0-8)	62	36	6	26	28
FQ 21-36 (8-14)	79	48	4	15	27
FQ 37-56 (14-22)	81	33	8	15	15
FQ 57-76 (22-30)	83	49	5	17	25
FQ 77-96 (30-38)	73	46	5	12	21
FQ 97-117 (38-46)	67	48	7	16	25
FQ 118-137 (46-54)	72	53	10	19	40
FQ 138-157 (54-62)	82	60	25	33	57
FQ 158-178 (62-70)	57	38	13	18	38
FQ 179-203 (70-80)	55	32	12	18	30
Average	71	44	9.5	19	31
TRS 0-15 (0-6)	75	55	6	15	31
TRS 16-31 (6-12)	79	51	8	14	30
TRS 32-46 (12-18)	76	47	9	12	22
TRS 47-61 (18-24)	66	56	8	16	27
TRS 62-76 (24-30)	75	60	9	26	58
TRS 77-89 (30-35)	74	59	8	26	59
Average	74	55	8.0	18	38
QAL 0-15 (0-6)	60	15	1	6	8
QAL 16-28 (6-11)	59	18	1	6	11
QAL 29-38 (11-15)	62	30	3	22	25
QAL 39-46 (15-18)	65	41	9	48	44
QAL 47-61 (18-24)	67	49	11	67	44
QAL 62-76 (24-30)	55	45	7	63	26
QAL 77-84 (30-33)	65	42	10	55	29
QAL 85-91 (33-36)	63	38	8	35	30
QAL 92-104 (36-41)	64	37	8	30	27
Average	62	35	6.4	37	27

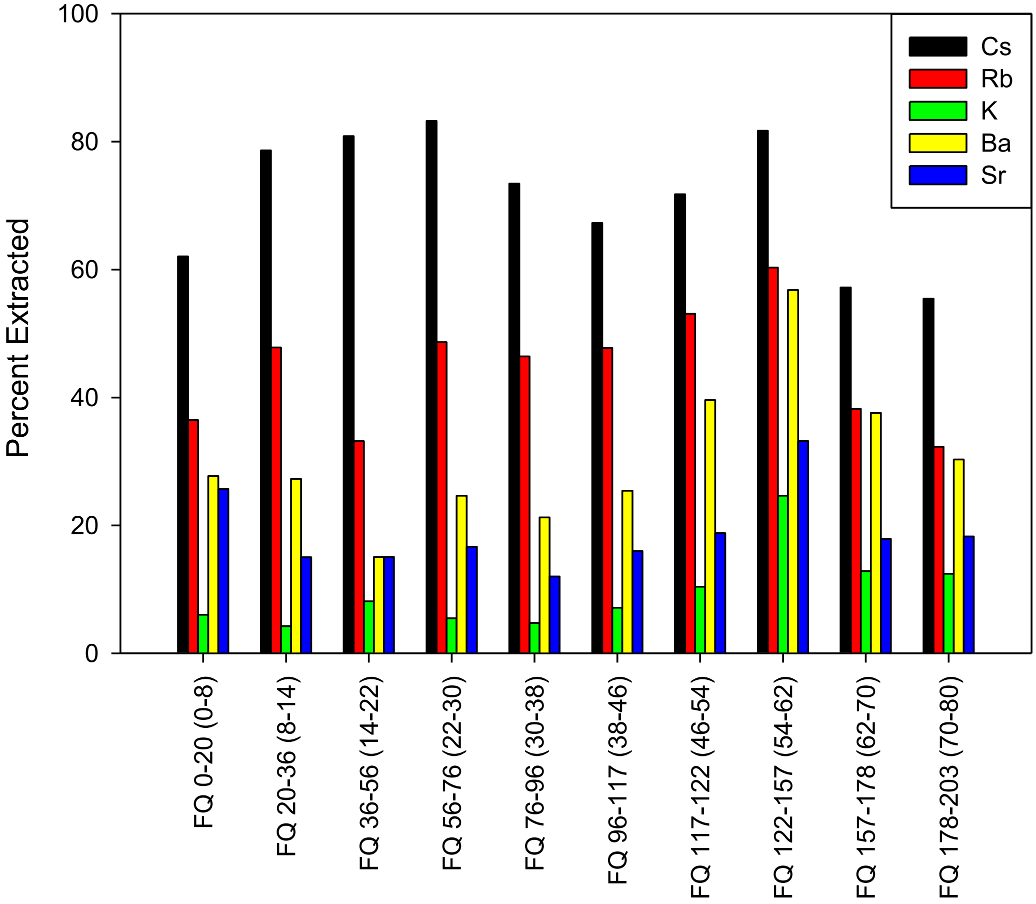

Figure 3-4: Percentages of Cs, Rb, K, Ba, and Sr extracted from the Fuquay core during the strong acid extraction

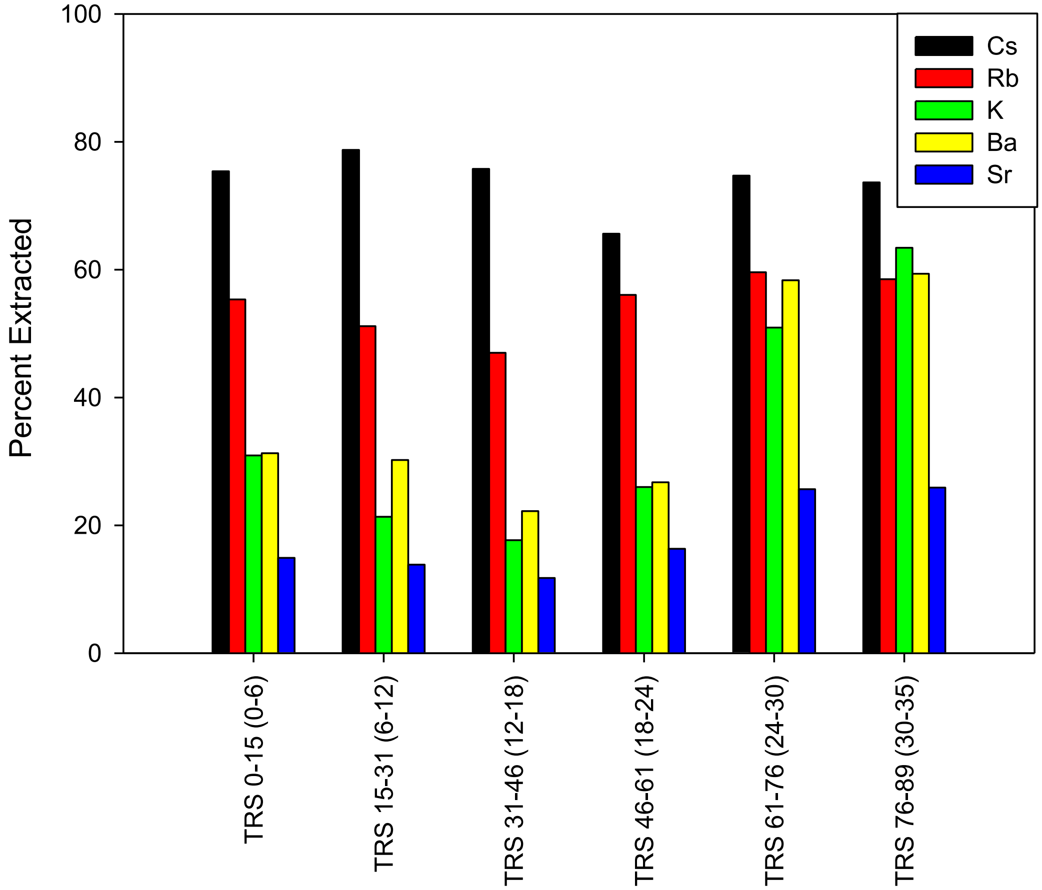

Figure 3-5: Percentages of Cs, Rb, K, Ba, and Sr extracted from the FQTRS core during the strong acid extraction.

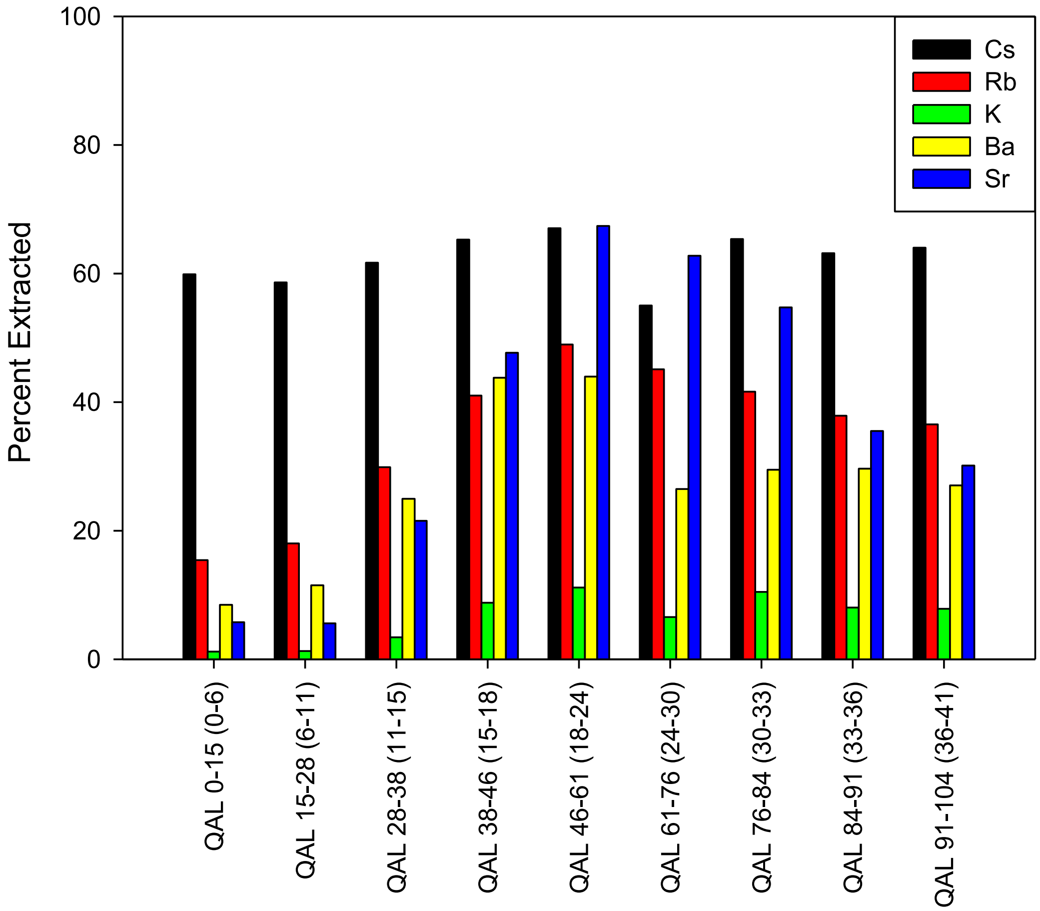

Figure 3-6: Percentages of Cs, Rb, K, Ba, and Sr extracted from the FQQAL core during the strong acid extraction

3.3.6 X-ray Diffraction of Leachate Residues

XRD data of the residue revealed only quartz peaks after extraction with 10% HNO_3 and 50% HNO_3.

3.3.7 Elemental Ratios

Elemental ratios are presented as the amount of each alkali or alkaline-earth minor or trace element relative to the amount of K. First considered are ratios of the total amounts of Cs, Rb, Sr, and Ba to the total amount of K in the fine fractions. Average values of these elemental ratios for the samples of each soil core are presented in Table 3-7. The enrichment factor for each trace element in each core was calculated by dividing the average ratio by the corresponding ratio of average abundances in rock of the UCC. Cs, Rb, and Ba are all enriched in the SRS soils with respect to the UCC, and the enrichment decreases as the maturity of the soil decreases.

Table 3-7: Comparison of alkali metals in SRS soil fine fractions to the UCC in respect to abundance ratios of other alkali and alkaline-earth elements to K

Core Name	Cs/K	Factor	Rb/K	Factor	Sr/K	Factor	Ba/K	Factor
UCC	0.0002		0.0036		0.014		0.027	
Fuquay	0.0031	16	0.021	6	0.013	1	0.082	3
FQ TRS	0.0014	7	0.011	3	0.006	0.4	0.043	2
FQ QAL	0.0007	3	0.011	3	0.005	0.4	0.061	2

Amounts of Cs, Rb, Ba, and Sr in each acid extract of each sample were normalized to the amount of K in the extract. In the solutions from the strong extractions, the ratios of Cs/K, Rb/K, Sr/K, and Ba/K are much greater than those of the UCC (Table 3-8). Cs and Rb are the most enriched and the enrichment decreases with the amount of weathering the soil has undergone. Ba is also substantially enriched relative to K, to about the same degree, 5-7 times, in the three cores. Sr is not enriched relative to K.

Table 3-8: Elemental Ratios and enrichment factors of strong leach.

Core Name	Cs/K	Factor	Rb/K	Factor	Sr/K	Factor	Ba/K	Factor
UCC	0.0002		0.0036		0.014		0.027	
Fuquay	0.015	75	0.069	19	0.016	1	0.18	7
FQ TRS	0.010	49	0.059	16	0.010	1	0.15	5
FQ QAL	0.004	21	0.039	11	0.015	1	0.16	6

Averages, across the samples of each soil core, of elemental amount ratios for solutions from the strong acid extraction and enrichment factors of minor and trace elements in solutions from the strong acid extraction.

The ratios and enrichment factors for the solutions from extraction with 10% HNO_3 at 80°C are presented in Table 3-9. The minor and trace elements were even more strongly enriched relative to K in these solutions than in the solutions from the strong extractions, because smaller relative amounts of K were removed with this treatment than with the strong extraction.

Table 3-9: Elemental Ratios and enrichment factors of moderate leach.

Core Name	Cs/K	Factor	Rb/K	Factor	Sr/K	Factor	Ba/K	Factor
UCC	0.0002		0.0036		0.014		0.027	
Fuquay	0.023	115	0.086	24	0.013	1	0.22	8
FQ TRS	0.016	80	0.083	23	0.009	1	0.22	8
FQ QAL	0.006	23	0.047	13	0.018	1	0.20	7

Averages, across the samples of each soil core, of elemental amount ratios for solutions from the moderate acid extraction and enrichment factors of minor and trace elements in solutions from the moderate acid extraction

The Cs/K ratio in each acid extract of the fine fraction of each individual sample is plotted versus the corresponding Rb/K ratio in Figure 3-7, with ratios from strong acid extractions of BGO 3A core samples and the UCC averages for comparison.

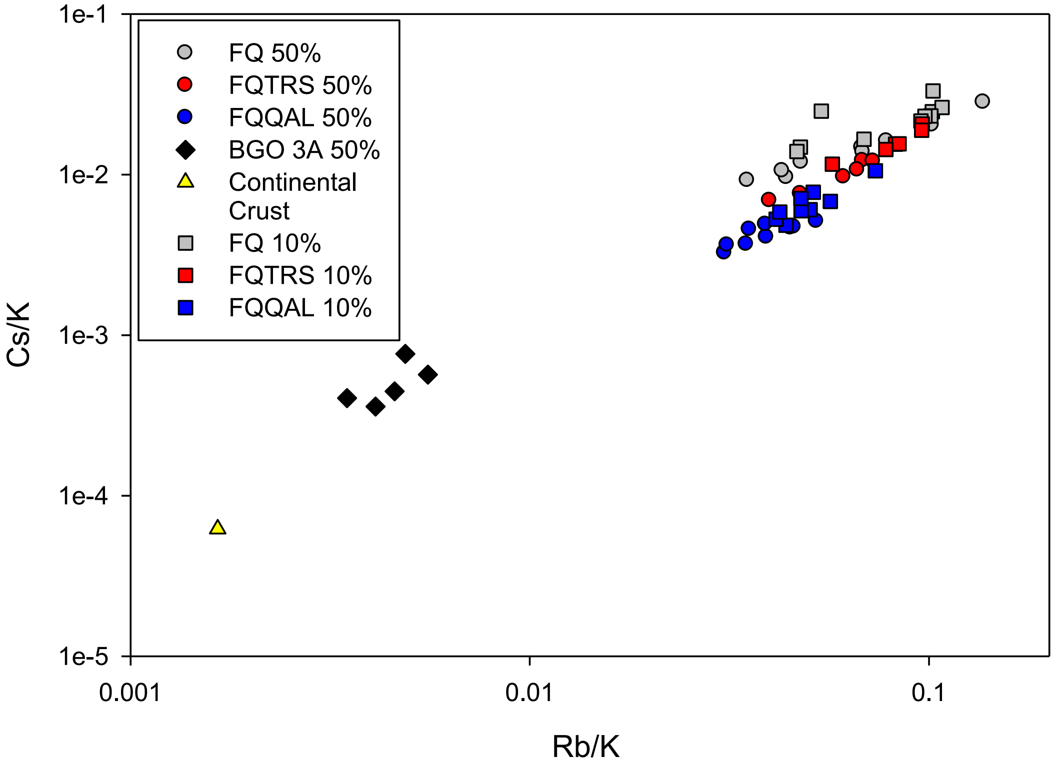

Figure 3-7: Comparison of Cs/K versus Rb/K for acid extracts of SRS soil fine fractions to ratios from acid extracts of SRS BGO 3A samples (black diamonds) and to corresponding average values for the upper continental crust (yellow triangle) from *Rudnick and Gao*, (2004).

3.4 Interpretation of Chemical Analysis

3.4.1 Simple ion exchange

In the simple ion exchange experiment (similar to EPA Method 9081 using NH_4Ac), exchangeable cation (Cs and K) concentrations increase with depth in cores FQ and FQTRS. The depth profiles of these cations are consistent with weathering of cations from the surface, leaching ions to deeper levels in the soils (Table 3-1). The correlation coefficients between Cs and K in FQ and FQTRS cores are 0.63 and 0.86 respectively. These positive correlation coefficients show that the relative proportions of K and Cs are exchangeable in these cores.

FQQAL has increasing concentrations of exchangeable Cs and K with depth up to a peak at 77 cm then decreases again. The correlation between Cs and K is 0.62. This data is also consistent with a weathering front moving down a soil core. FQQAL also has the greatest concentration of exchangeable ions in the three cores. It is an immature soil and this soil is not well leached. Thus, it has more ions available for exchange. Ion concentrations for the simple ion exchange experiment for both Cs and K are much smaller than in the acid extraction experiments (by factors of 10^{-4} and 10^{-2} respectively). This smaller ion concentration is likely because these ions are being held tightly in interlayer sites of phyllosilicate minerals that require a more rigorous extraction than simple ion exchange. The exchange time allowed in this experiment also was only ~15 minutes of immersion in the NH_4OAc whereas ions in the extraction experiments were exposed to HNO_3 acid for 3 hours. If we assume that all of these exchangeable ions are in the fine fraction of the soil, then the amounts of Cs and K removed from the samples are less than 1% of the total Cs and K in the soils.

3.4.2 Acid extractions

The depth profiles of the ions (Cs, Rb, K, Ba, and Sr) released during acid extraction in the three soil cores demonstrates similar variations in concentration with depth. The depth profile for the strong extraction on the Fuquay core is shown in Figure 3.8. The scale has been set to account for the maximum concentration variability for each ion. In Figure 3.8, the highest concentrations of exchangeable ions are released at around 120-140 cm, and then decrease sharply in the deeper samples. At this depth in the FQ core is where the soil clay content begins to rise (Figure 2-4). An increase in the clay content of the samples results in an increase in the amounts of ions sorbed and later released by acid extraction. Inflection points in these data seem to coincide with the large change in the percentage of clay in the soil. It is likely that the increase in clay sized particles and thus increase in exchange sites available is responsible for this chemical profile in the FQ core. Figures 3-8 and 3-9 show the ion concentrations with depth for the FQ core in the strong and moderate extraction with the gray highlighted area emphasizing the high clay content depth regions of the core as quantified in Section 2.2.1 in Table 2-2 and Figure 2-4. It is clear from Figures 3-8 and 3-9 that the profile of elements removed by either the strong or moderate extractions are very similar and that the highest ion concentrations are within the regions of high clay content.

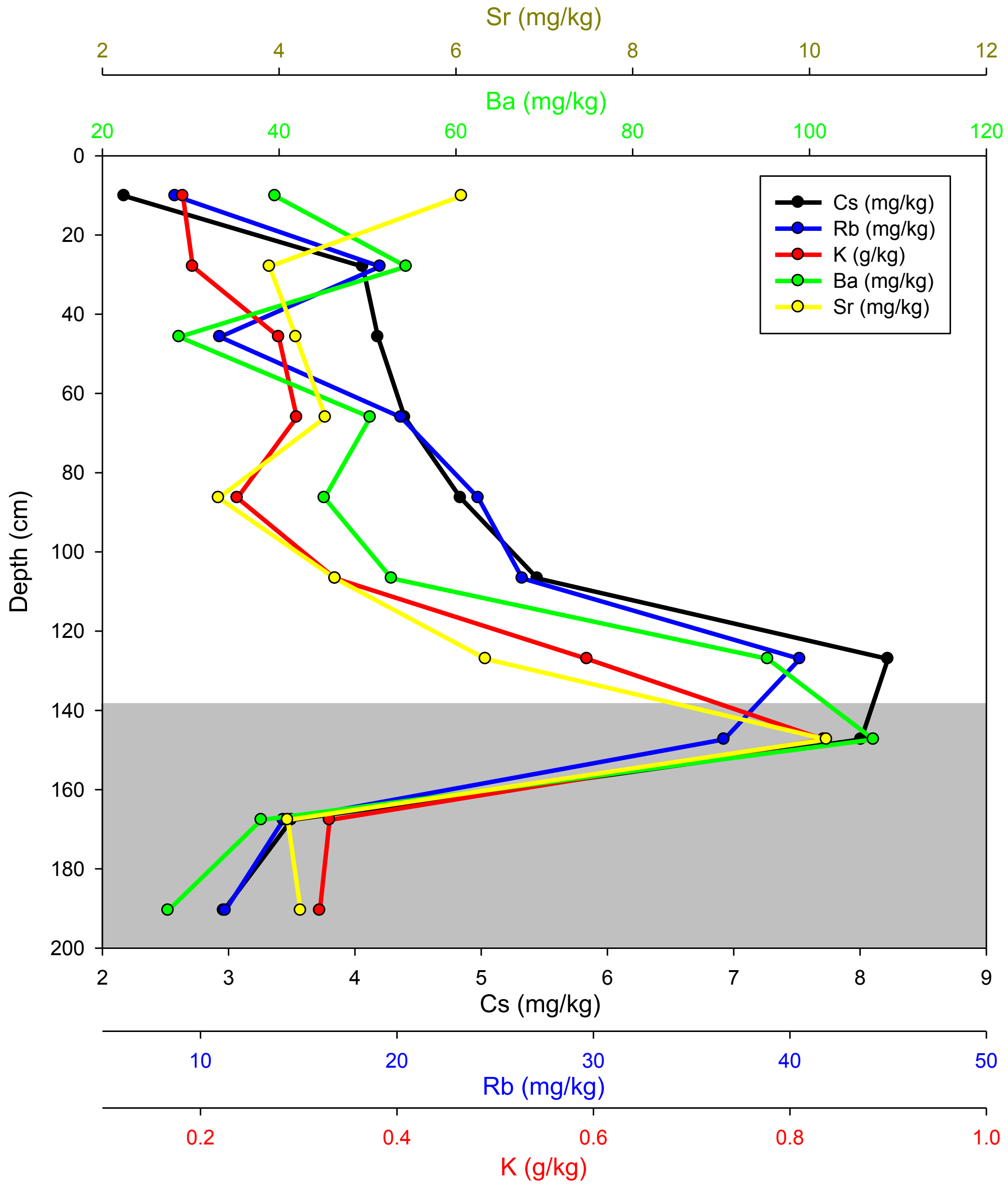

Figure 3-8: Metal concentrations from the <62µm size fraction of the Fuquay Core with depths for Cs, Rb, K, Ba, and Sr after strong extraction.

The axes on this graph are designed to maximize the variability of each element for comparison. Gray shaded region corresponds to high clay depth region in the core.

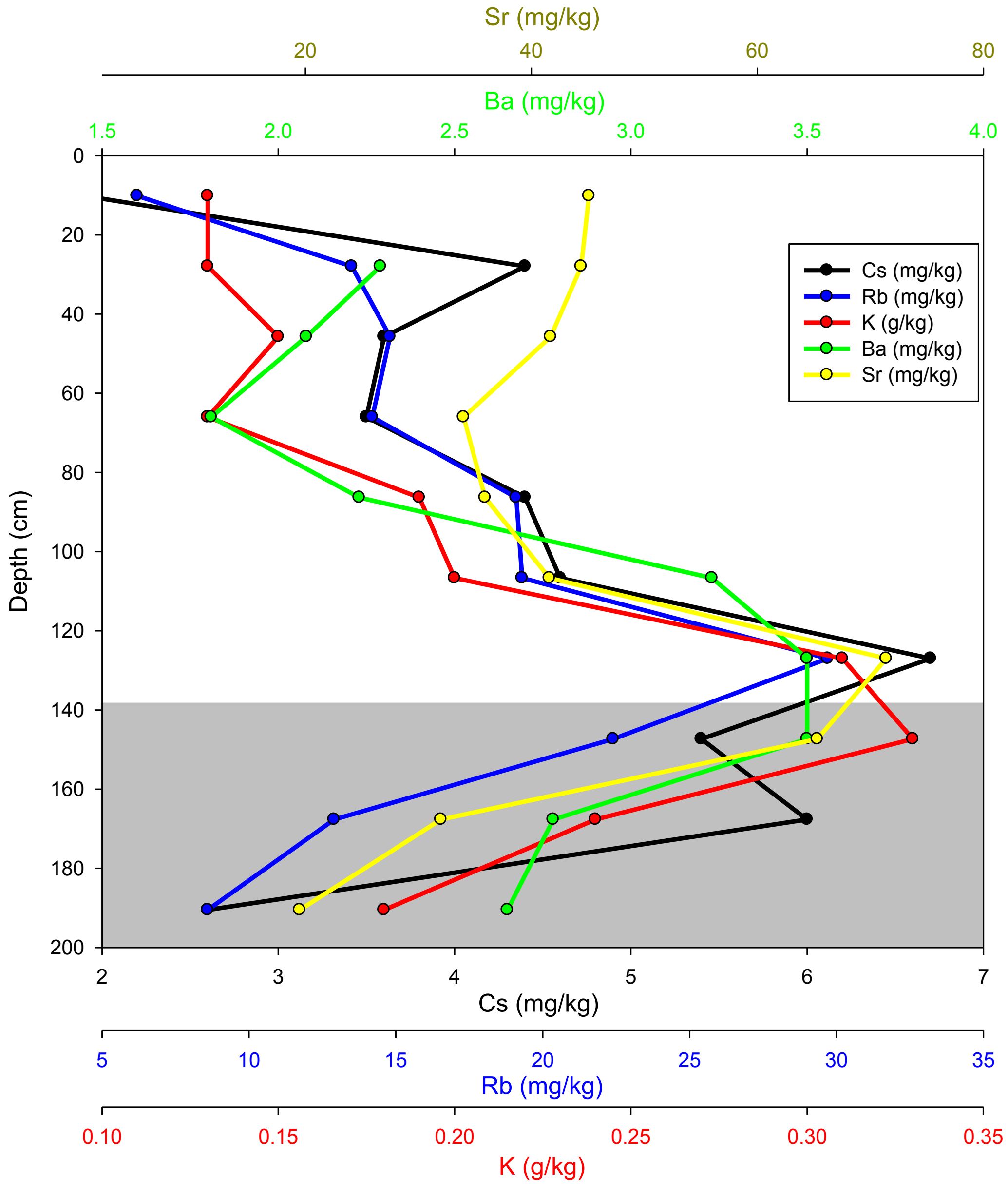

Figure 3-9: The alkali metal concentrations from the <62µm size fraction of the Fuquay Core with depths for Cs, Rb, K, Ba, and Sr after moderate extraction. The axes on this graph are designed to maximize the variability of each element for comparison. Gray shaded region corresponds to high clay depth region in the core.

Core FQTRS has a trend in ion concentrations which are relatively constant in the first 60 cm. These ion concentrations increase from 60 cm to the bottom of the core (Figure 3-10 (strong extraction) and Figure 3-11 (moderate extraction)). As with the FQ core, the clay content of the core increases at these depths (Figure 2-4).

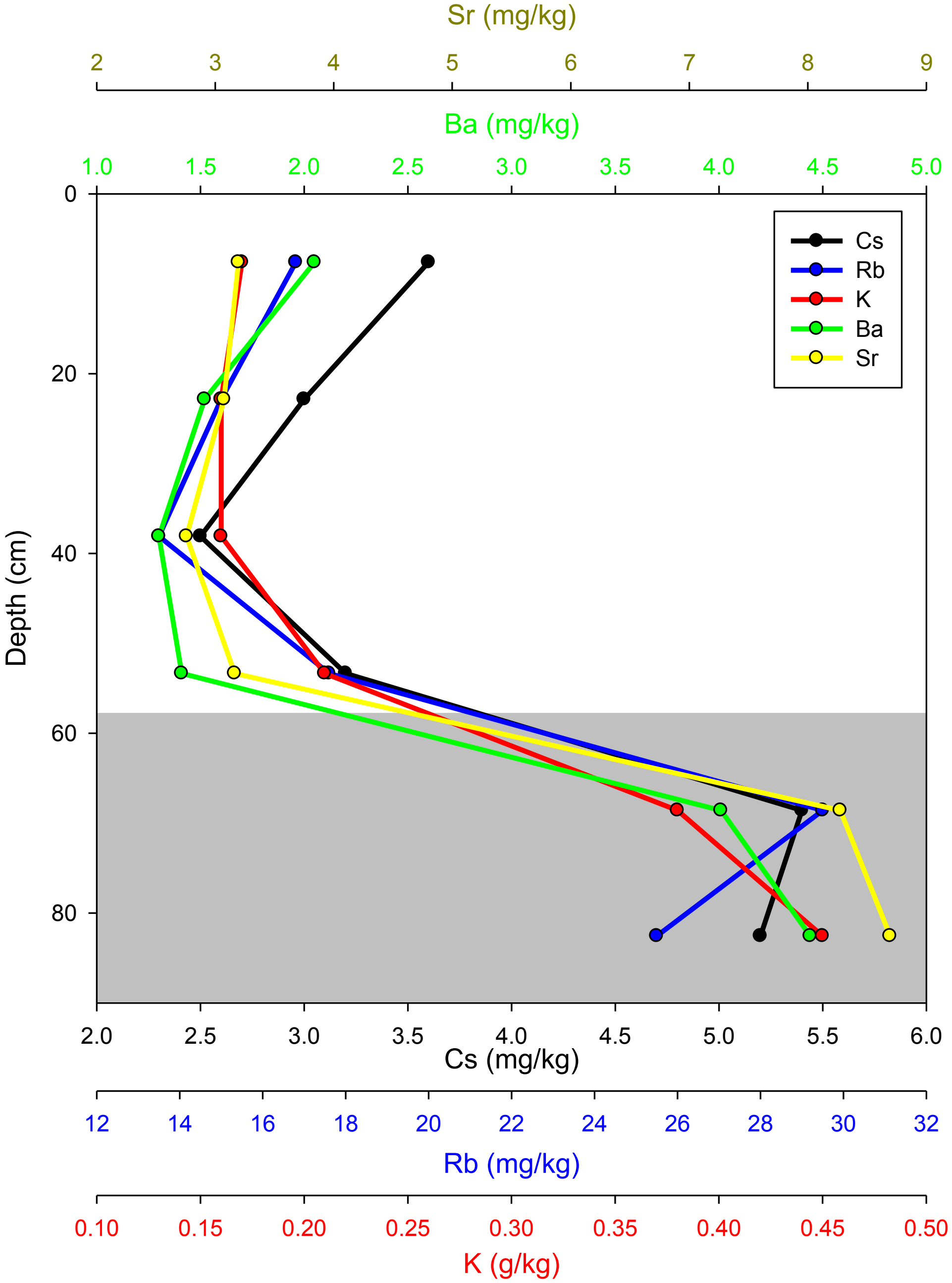

Figure 3-10: Concentrations of ions (Cs, Rb, K, Ba, and Sr) released from strong acid extraction of the <62µm size fraction of the FQTRS Core with depths. The axes on this graph are designed to maximize the variability of each element for comparison. Gray shaded region corresponds to high clay depth region in the core.

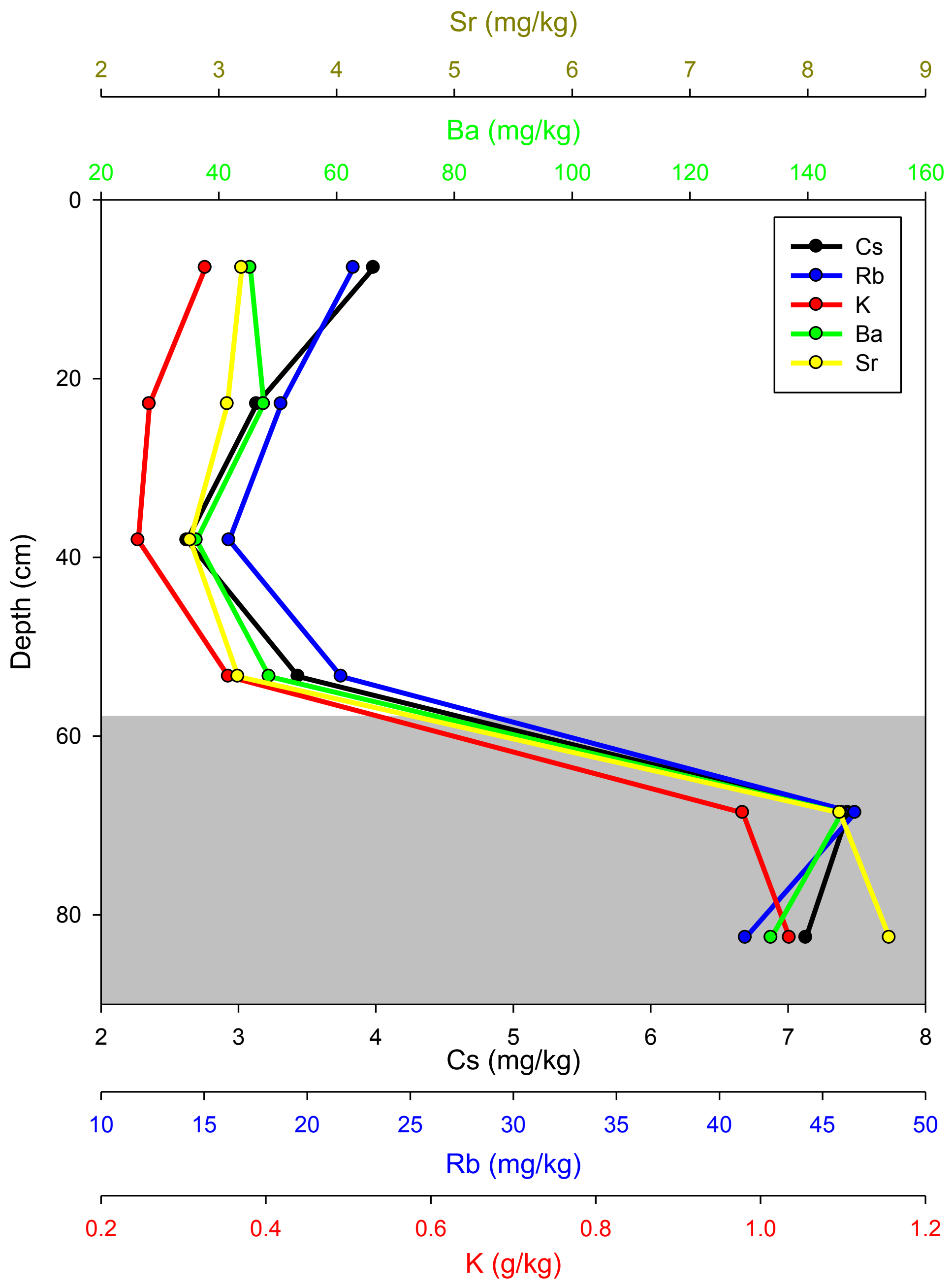

Figure 3-11: This figure shows the concentrations of ions (Cs, Rb, K, Ba, and Sr) released from moderate acid extraction of the <62µm size fraction of the FQTRS Core with depths. The axes on this graph are designed to maximize the variability of each element for comparison. Gray shaded region corresponds to high clay depth region in the core.

The FQQAL core has a sharp peak in ion concentrations around 45 cm and then falling concentrations of the ions with depth (Figure 3-12 and 3-13). The peak in ion concentration of this core (~45 cm) is shallower than the peak in clay content (~80 cm) (Figure 2-4). A possible explanation for this is that because this core was developed on alluvium deposits, its clay profile is representative of the deposition of the clays. As weathering progresses, clay particles and metals will be illuviated down the soil profile, resulting in the metal/clay correlation seen with the other cores above. In a young soil, ions are still near the surface of the core. Clay at depth may be from deposited clays and not from illuvation. Another possibility is that this sudden uptick in clay content is forming a low permeability or impermeable barrier and water is only slowly moving into the deeper horizons. Thus the ions are concentrated at this layer.

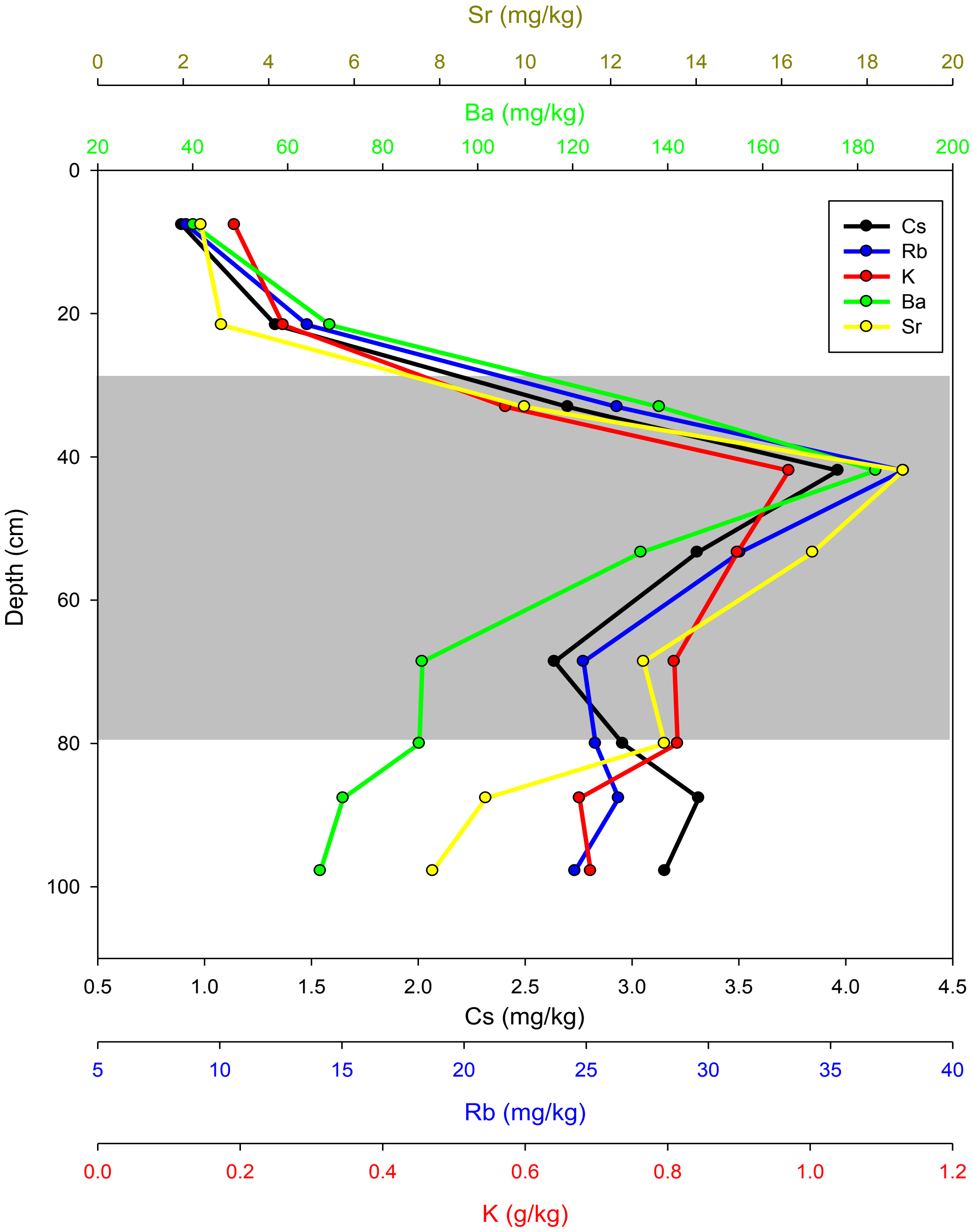

Figure 3-12: This figure shows the concentrations of ions (Cs, Rb, K, Ba, and Sr) released from strong acid extraction of the <62µm size fraction of the FQQAL Core with depths. The axes on this graph are designed to maximize the variability of each element for comparison. Gray shaded region corresponds to high clay depth region in the core.

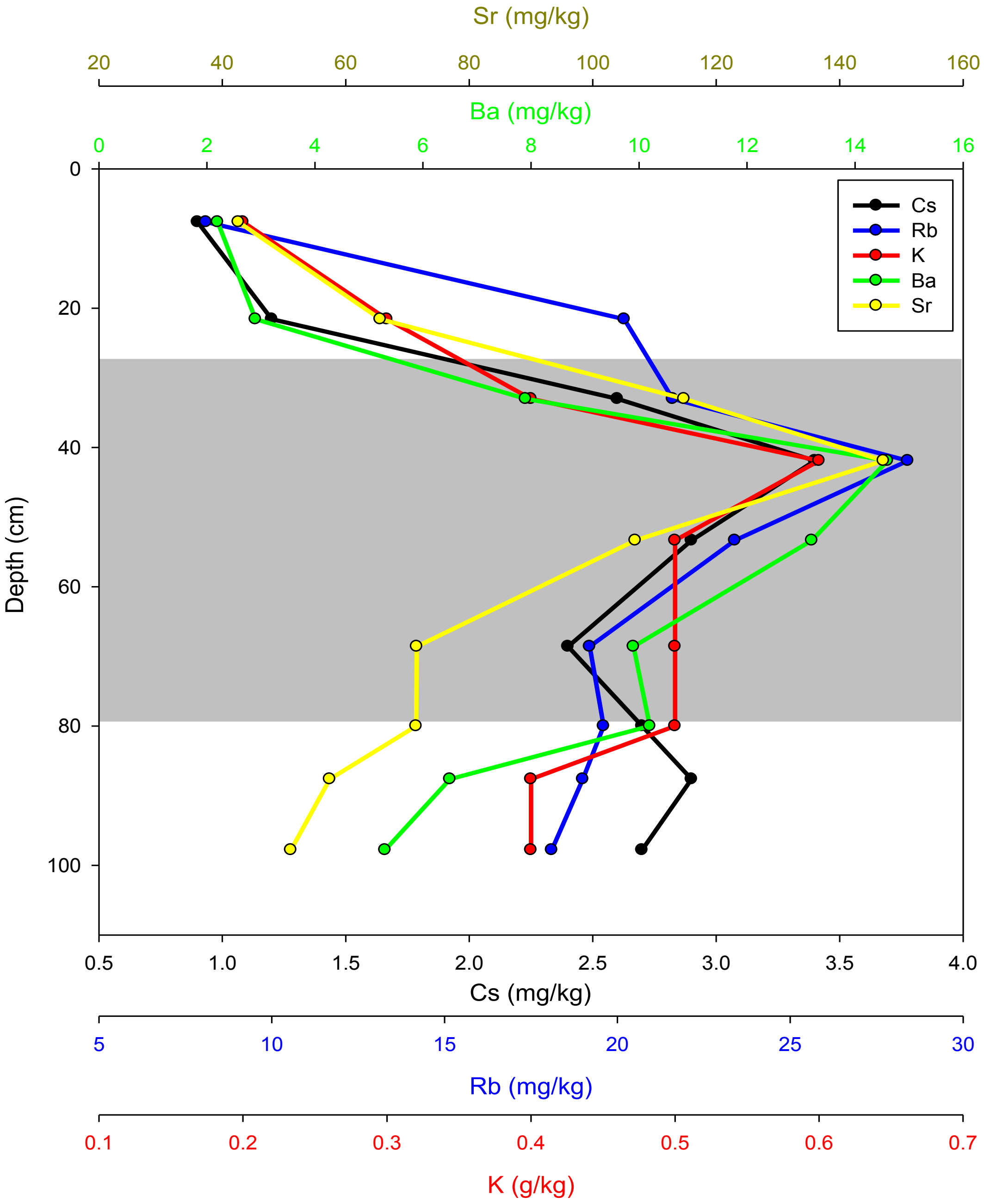

Figure 3-13: Concentrations of ions (Cs, Rb, K, Ba, and Sr) released from moderate extraction of the <62µm size fraction of the FQQAL Core with depths. The axes on this graph are designed to maximize the variability of each element for comparison. Gray shaded region corresponds to high clay depth region in the core.

3.4.3 Relative amount extracted

The moderate extraction of ions is designed to remove ions that are easily exchangeable and not bound to the silicate structure. The strong extraction is expected to remove all the exchangeable ions and even partially dissolve the crystal lattice to release both tightly held ions in interlayer zones and to release metals from within the layers themselves (Si, Al, Fe, Mg). Tables 3-6 and 3-7 summarize the percent of the total concentration in each soil core that was removed by each of the leaching methods. Noting the removal of ions with these different techniques provides insight to locations where the ions are in clay materials.

In all three cores, K is resistant to extraction. With the exception of the three deepest samples of the FQ core (where clay content is very high), no more than 10% of the total K is removed from the fine fraction of soils in either the strong or moderate leach. From this we can infer that very little of the K in the soils is exchangeable and K is bound within the primary silicate structures (e.g. K in mica interlayer).

In all cores, a higher percentage of Cs is removed from these soils due to the acid extractions. More than 50% of Cs is removed by the moderate acid leach and > 60% of Cs is removed by the strong leach with some values exceeding 70%. Unlike K that predominantly is in fixed silicate primary structures, a greater fraction of Cs is in exchangeable and difficult to exchange sites in all three cores. This Cs is accumulated during pedogensis. For Rb, the behavior is similar to Cs.

3.4.4 Composition of the leach residue

The assumption was made that the difference between the 50% and 10% acid leach experiments is that the 50% leach is partially breaking down the structural lattice of the minerals in the fine fraction and the 10% (moderate) leach is not dissolving primary minerals. To check this idea, the residues were analyzed using XRD before and after extraction under both acid extraction conditions. The residues of the 10% and 50% acid extractions were composed only of quartz. This data shows the 10% extraction may be dissolving the mineral structures (kaolinite, HIV) more than expected. If HIV and kaolinite were present, then they would be present in small amounts that could not be detected by XRD.

The percent difference between the two extraction scenarios should represent how much of the ion is coming out of the primary structure in the strong leach, versus exchangeable sites in the weaker leach. Table 3-10 shows the difference in the average percent extracted from the strong and moderate leaches. On average, K has the smallest difference in the amount removed through the extractions (2-4.5%). This is because K is in the primary structure of the minerals and the other ions are in exchangeable sites and show greater differences between strong and moderate extractions.

Table 3-10: Percent difference between average strong and moderate extraction.

Core	Cs	Rb	K	Sr	Ba
Fuquay	15	9	4.5	8	9
FQTRS	13	12	2	9	12
FQQAL	10	6	2.4	13	7

3.4.5 Elemental ratios

Lastly, the Cs/K versus Rb/K of leaches from acid extraction were compared to recent analyses from the SRS (*Wampler et al.* 2012) and to continental crust. These data compare well to the data from Wampler et al. and these data show the enrichment of Cs and Rb relative to K in these SRS soils (Figure 3-8). As shown in Table 3-7 through 3-9, the enrichment factors increase from total ion concentrations to strong acid extractions to moderate extractions for Cs and Rb in each core. Whereas, Sr is removed with the relative amounts as K for all three cores. Ba is slightly enriched relative to K for all cores. K and Sr have similar geochemical behaviors in these soils.

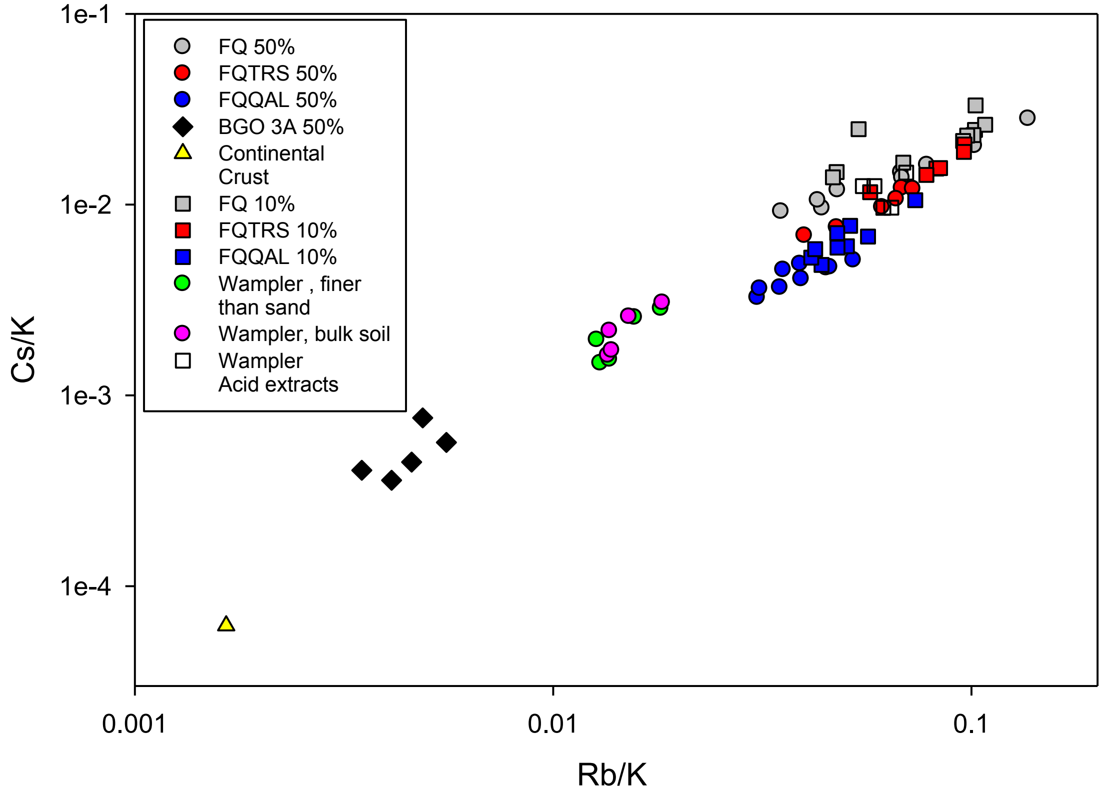

Figure 3-14: Comparison of strong and moderate acid leach ratios of Cs/K and Rb/K to the drill core, continental crust and recent data from *Wampler et al.* 2012. Drill core SRS BGO 3A (black diamonds) and continental crust (yellow triangle) from *Rudnick and Gao*, 2004. Here FQ is the Fuquay Core, FQTRS is Fuquay on Tobacco Road Sand, FQQAL is Fuquay on Quaternary Alluvium, and 50% is the 50% HNO_3 leach, 10% is the 10% HNO_3 acid leach solution. (Residue values are not shown on this plot-but summarized in bar graphs above).

4 MOLECULAR MODELING

4.1 Introduction

To understand complex processes in nature such as the weathering rates of silicate minerals or the transport of radioactive contamination in subsurface environments requires an understanding of the fundamental atomic-level processes and mechanisms that control the thermodynamics and kinetics of earth materials. Molecular modeling can assist in the interpretation of experimental data and help in the determination of the proper explanation of macroscopic observations. This can also help scientists predict future behavior of geochemical systems (*Cygan*, 2001).

For periodic systems such as clays, molecular modeling can be used to determine the lowest energy configuration of a given atomic structure. The configuration with the lowest free energy is also the most stable configuration. Molecular modeling is typically on the scale of Angstroms (10^{-10} m), the separation distances of atoms, and femtoseconds (10^{-15} s), which is appropriate for the time scale of molecular vibrations. Generally, a model is used to calculate the total energy of a periodic or molecular cluster system, and determine how the energy of the system changes when atoms are displaced, or changed, and the determination of the most stable configuration. Molecular modeling includes the testing of theoretical concepts by determining the lowest energy configurations of complex systems.

This chapter investigates what is the most favorable ion in the interlayer of model structures of mica, pyrophyllite, vermiculite, and the frayed edge site in a modeled mica/vermiculite intergrade structure (our HIV model). The ions included are Na^+, K^+, Rb^+, Cs^+, Sr^{2+}, and Ba^{2+}. The model calculates the energies of inner- and outer-sphere coordination of the ions within the interlayer of the minerals based on a geometry optimization. The lower the energies, the more favorable that ion is to the position it is placed in the clay mineral interlayer. Of particular interest in this project is which ion is the most energetically favorable in the interlayer wedge zone of HIV (modeled here for various layer charge distributions) and does it conform to the experimental data collected in this project?

Additionally, a molecular dynamics simulation is used to investigate Cs in the interlayer wedge zone of the composite clay model. This will be the first model to investigate a wedge site and the energetics of Cs in this location. It should help foster a greater understanding of the sequestration of Cs in clay minerals at the Savannah River Site in South Carolina and of how to cleanup radioactively contaminated Superfund sites like it.

4.2 Recent Studies using Molecular Modeling of Clays

Sandia National Laboratories (SNL) in Albuquerque, NM is one of the leading research facilities for molecular modeling work studying clay minerals and the applications of modeling clays. Recently, Teich-McGoldrich et al. (2012) from SNL used molecular modeling to investigate how the structure of muscovite behaves under different pressure and temperature scenarios that are simulating how these clays react and change with depth in the earth's surface. Examples of other studies include those on modeling the intercalation of organic molecules in smectite interlayers (*Zhao and Burns*, 2012) and the mechanisms of adsorption of numerous metals (Cs^+, Na^+, Cd^{+2}, and Pb^{+2}) on kaolinite surfaces (*Vasconcelos et al*. 2007).

Vasconcelos et al. (2007) simulated the adsorption of cation and anions on the surfaces of kaolinite, as this 1:1 layer clay gave the opportunity to test the sorption onto both the siloxane and gibbsite surfaces of kaolinite simultaneously. Aqueous chloride solutions of Na, Cs, Cd, and Pb were added to the interlayer space at various ionic strengths and allowed to interact with the surfaces. The ditrigonal cavities of the siloxane surface, had strong inner-sphere sorption of the monovalent cations, with Cs (and Na to a much lesser extent) losing their hydration shells to closely approach the clay surface. Similarly, Cl ions formed strong inner-sphere coordination with the ditrigonal spaces on the gibbsite surfaces. Divalent cations formed strong outer-sphere complexes to the ditrigonal cavities of the siloxane surface.

Molecular modeling has been applied to study sorption of the aqueous phases of radionuclides onto soil minerals (*Greathouse and Cygan*, 2005; *Greathouse and Cygan*, 2006). The dominant uranium species found in contamination sites is the uranyl cation (UO_2^{2+}). These simulation studies found that in the presence of carbonates, common in natural water systems, UO_2^{2+} forms complexes and is less likely to sorb to montmorillonite and other clay minerals surfaces.

The continuing rise in carbon dioxide concentrations in earth's atmosphere is a growing concern for the future of global climate change. Recent experimental work has shown that swelling clays such as smectite varieties are capable of the intercalation of CO_2 along with water in the interlayer region (*Romanov et al.* 2009). This observation led Cygan et al. (2012) to investigate the interlayer environment of Na-montmorillonite and the possible mechanisms for carbon sequestration potential. Molecular dynamics simulations of the intercalation of CO_2 and water in the interlayer were compared to experimental data to aid in the design of an effective model for the mechanism and diffusion of CO_2 into the water in interlayer regions.

4.3 CLAYFF

To design an effective molecular simulation requires an accurate force field for the potential energy. The force field describes the potential energy of interaction between atoms and molecules based on a set of analytical expressions as a function of configuration. Cygan (2004) has designed a useful force field for clays called CLAYFF developed at the Sandia National Laboratories (*Cygan et al.* 2004) and which is used in this molecular modeling project.

The force field treats metal-oxygen interactions as ionic (called non-bonded, also non-covalent bonds in CLAYFF). The atoms are treated as point charges and allowed translational movement freedom. A simple Lennard-Jones relationship for metal-oxygen interactions is combined with an electrostatic contribution to describe the forces and energy between the atoms. The atoms have been assigned partial charges in this force field based on periodic density functional theory (DFT) quantum calculations of well-defined structures of oxides, hydroxides, and other well know structures (*Cygan et al.* 2004). The partial charges are assigned to each atom (for example, oxygens in oxide and hydroxide) have different partial charges based on the environment they are in (Table 4-1, *Cygan et al.* 2004). The flexible single point charge (SPC) water model is used, and water molecules and hydroxyls are the only chemical species that are treated as bonded (covalent) entities in the force field. These covalent components use harmonic terms in the force field to describe the bond stretch and bend dynamics. This force field uses the below described equations and partial charges on atoms in a periodic system to calculate their interaction.

Table 4-1: CLAYFF Parameters[a]

Species	Symbol	Partial Charge
Water Hydrogen	h*	0.4100
Water Oxygen	o*	-0.8200
Bridging Oxygen	ob	-1.0500
Bridging Oxygen with Tetrahedral substitution	obts	-1.1688
Cesium	Cs	1.0
Potassium	K	1.0

[a] From *Cygan et al.* 2004, ob is an O in the hexagonal ring that is bonded to two Si atoms, whereas obst is an O in the Al-O-Si configuration in the ring, bonded to an Al atom that has been isomorphically substituted into tetrahedral layer.

The model will follow the classical mechanics potential energy function V(r) where we account for both bonding (water molecules and hydroxyl only) and nonbonding potentials, Equation (4.1).

$$V(r) = \sum_i V(r)_{bond\ stretch} + \sum_i V(\theta)_{angle} + \sum_i V(r)_{VDW} + \sum_i V(r)_{electrostatic} \tag{4.1}$$

Each of the terms is responsible for evaluating different contributions of the energy potential. Both the bond stretch and angle bend are modeled using a simple harmonic (Equations 4.2 and 4.3), with constants, $k_{\text{bond stretch}}$, a parameter capturing the stiffness or distortion capability of the bond, and $k_{\text{angle bend}}$, a parameter for the variation of the bond angle from the ideal angle position, or how far the angle is "bent." These are included in the water molecules in the model.

$$V(r)_{bond\ stretch} = \sum_i k_{bond\ stretch}(r_i - r_0)^2 \tag{4.2}$$

$$V(\theta)_{angle} = \sum_i k_{angle\ bend}(\theta_i - \theta_0)^2 \tag{4.3}$$

The values r_0 and θ_0 are the equilibrium positions for the molecules.

Finally, non-bonded potentials include the dispersive-repulsive force of van der Waals (VDW) interactions (Equation 4.4) and long-range electrostatics interactions (Equation 4.5), where A and B in Equation (4.4) are determined empirically based on observed structural data, and *r* is the distance between atoms.

$$V(r)_{VDW} = \sum_{ij} \frac{A_{ij}}{r_{ij}^{12}} - \frac{B_{ij}}{r_{ij}^{6}} \tag{4.4}$$

$$V(r)_{electrostatic} = \sum_{ij} k \frac{q_i q_j}{r} \tag{4.5}$$

In Equation (4.5), *k* is the Coulomb constant, and *q*s are the charges on the atoms. The parameters for these analytical expressions are based on experimental observations or quantum calculations of the system being modeled (*Cygan*, 2001).

In this project, our model is designed first to investigate the total potential energy of mica, pyrophyllite, vermiculite, and HIV lattice structures and compare this to the change in potential energy resulting from sorption of Cs, Rb, K, Na, Sr, and Ba onto the interlayer region of those minerals. It should be noted that the energies calculated here are differences from an equilibrium initial configuration and do not account for entropy and because these are preliminary modeled values, no error analysis is derived at this time.

4.4 Methodology

4.4.1 Energy Minimization

Energy minimization is a mathematical procedure where the configuration of atoms in a molecular model is altered until a minimum energy is reached. Energy minimization is also called geometry optimization and is based on a molecular mechanics approach. Molecular mechanics uses the above analytical expressions of the different energy components in a molecular system including van der Waals, bond stretching, angle bending, and electrostatics interaction.

A force field describing the interactions between ions in a chemical system is designed to evaluate the potential energy of the configurations of, in this case, a periodic clay system. The energy minimization technique, begins with a starting configuration of the clay, and gradually adjusts it until the net force on the atoms is minimized and the lowest potential energy value is achieved. The number of adjustments to the initial configuration may be just a few or can be thousands depending upon how far the initial configuration is from the minimized configuration, how many atoms and bonds are included in the system, and how effective the algorithm is at adjusting the energy (*Cygan*, 2001). Geometry optimization is performed at 0K so that kinetic energy and thermal vibrations of atoms are not taken into consideration as part of the energy of the system. These effects are accounted for by the parameterization of the force field. Force fields are parameterized by experimental data often at room temperature, under standard or applied pressures, and thus these components are accounted for in the force field itself (*Cygan*, 2001).

4.4.2 Building the models

Models were designed and visualized with Materials Studio® Software.

Three basic clay model structures were designed and tested under different cation and hydration scenarios to determine the most energetically favorable geometry and ion in the interlayer space of the minerals investigated. These models were designed as pyrophyllite and mica being the two end member cases and vermiculite as an intermediate species. A fourth more complex model of HIV was designed to simulate the wedge zone and is also intermediate to mica and pyrophyllite in terms of charge. Building the model starts with a unit cell and uses the symmetry of the cell to generate the other units. The units are expanded and disorder is added to the system to be more representative of a realistic clay system. The model uses a technique called "Al avoidance" that will not allow for the formation of any Al-O-Al sites to exist when adding disorder into the hexagonal ring. This is not likely to occur in nature and causes large instabilities in the modeled system (*Tossell*, 1993). Each model was optimized for the best geometric configuration with the ions Na^+, K^+, Rb^+, Cs^+, Sr^{+2}, and Ba^{+2} in the interlayer space under differing situations described below.

4.4.2.1 Pyrophyllite

The first model is Pyrophyllite, $Al_2Si_4O_{10}(OH)_2$, with a layer charge of zero, two model cases were run for each of the six ions listed above. Initial configuration energy is determined after applying the geometry optimization to the pyrophyllite structure with no ions in the interlayer, and thus a neutral charge. This energy is compared to the energy of the pyrophyllite with interlayer cations to determine which ion was most preferably held in the interlayer zone.

Case 1: A single ion is placed in the interlayer region. The first model simulates bonding as an inner sphere complex on the siloxane surfaces of the interlayer. Figure 4-1 shows the side and top view of the pyrophyllite model with a Cs ion in the interlayer and Figure 4-2 shows the model with Ba in the interlayer. These are examples of what the monovalent and divalent cation configurations look like, though there are slight variations with each ion. The energy of the optimized configuration is then calculated with the Forcite module of Materials Studio software package. A background charge screening is applied by Forcite to maintain a neutral simulation cell while having a cation in the interlayer or a charged clay without interlayer cations.

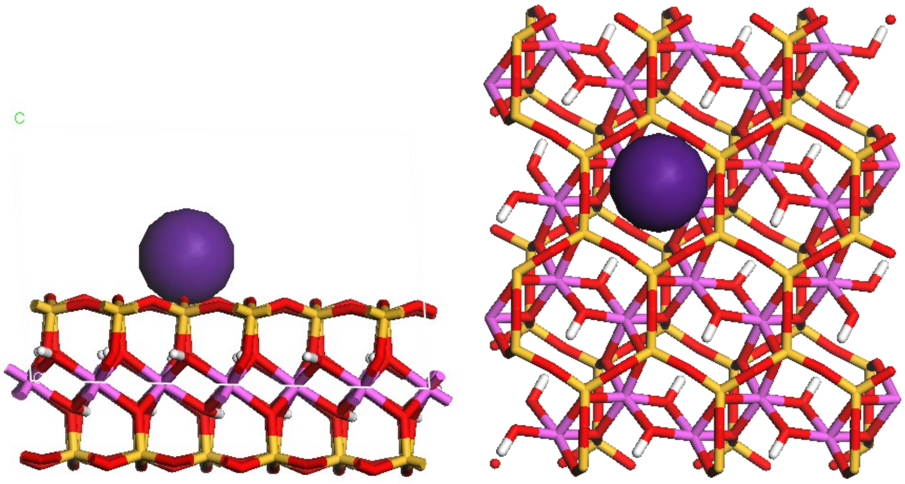

Figure 4-1: Cesium in the interlayer of model pyrophyllite (top layer not shown on the left). Note the position is within the hole in the hexagonal ring.

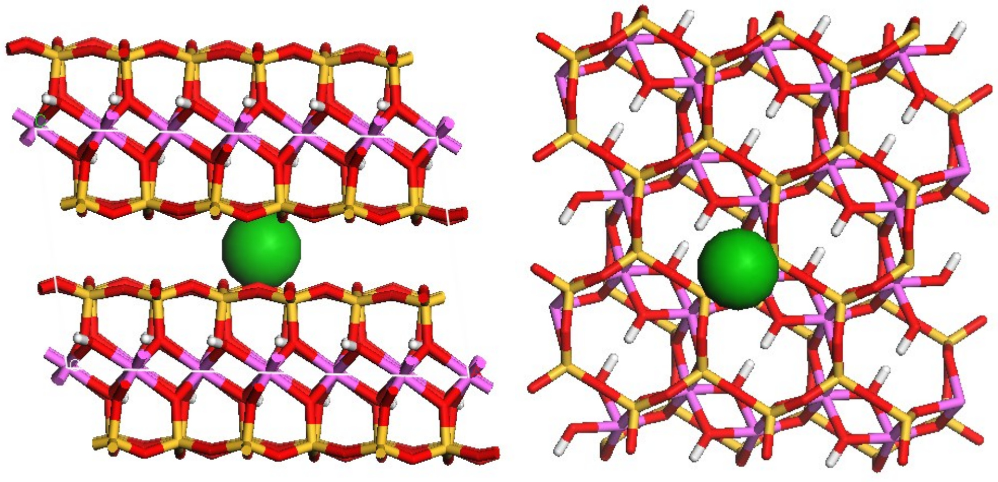

Figure 4-2: Barium in the interlayer of the pyrophyllite model

Case 2: A hydrated ion is placed into the interlayer region with the number of waters molecules appropriate to its coordination with water. For the ions studied here, Na required 6 water molecules, Ba required 10, and all the others (K, Rb, Cs, Sr) required 8 waters for the appropriate coordination with water (*Ohtaki and Radnai*, 1993). This case simulates the ion bonding as an outer sphere complex. Figures 4-3 and 4-4 demonstrate the model configurations for the cases of hydrated Cs and Ba in the interlayer space of pyrophyllite. In both cases, because the pyrophyllite structure is neutrally charged, the structure with the ion in place is a charged system of either +1 or +2 overall charge depending on the valence of the cation.

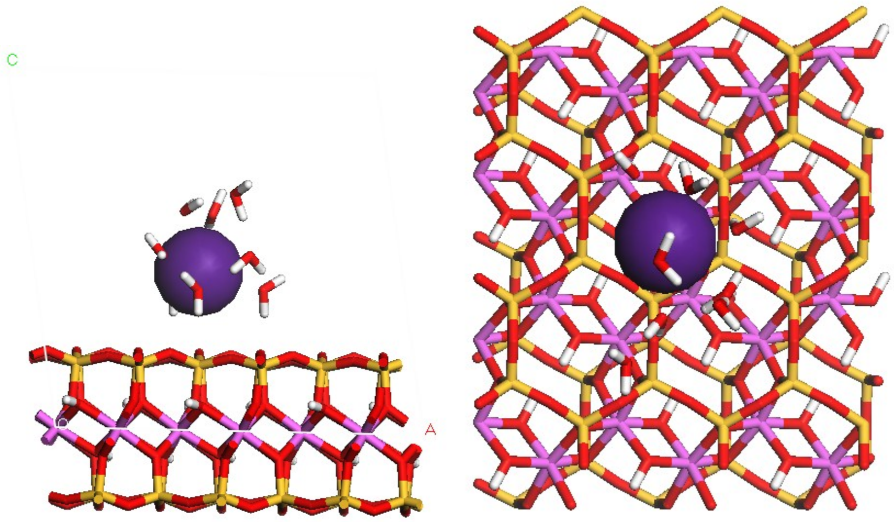

Figure 4-3: Geometry optimized hydrated Cs in the interlayer of the pyrophyllite model viewing first down the a-axis, then the c-axis. Top layer is not shown and an artifact of the visualization software.

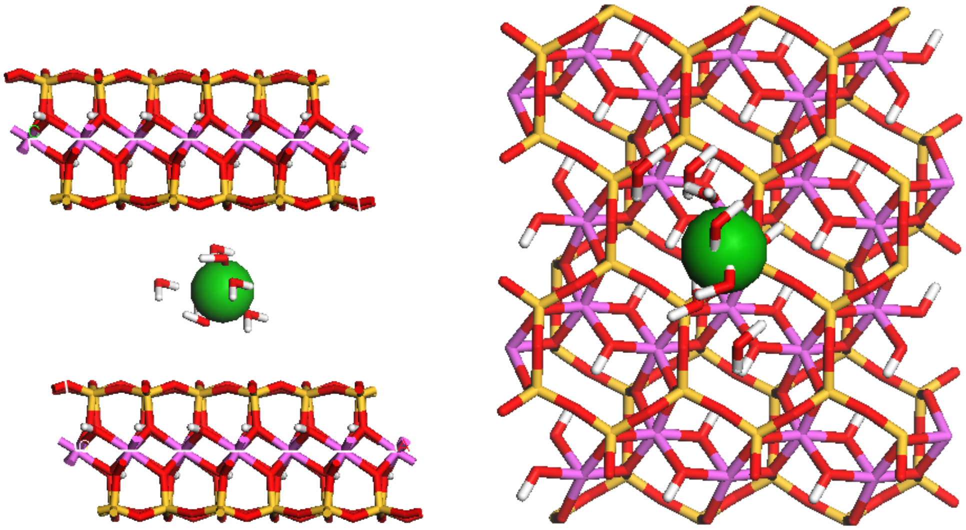

Figure 4-4: Hydrated Ba in the interlayer of pyrophyllite, top and side view

4.4.2.2 Mica

The structural model of mica was designed with unit cell, $X_1 \cdot Al_2Si_3AlO_{10}(OH)_2$, with a layer charge of -1 developed in the tetrahedral sheet. The experiment was repeated for mica for two cases with slight variation from the pyrophyllite cases. Case 1: the number of cations was added to appropriately balance the charge in the structure. Based on the size of the simulation cell of the mica model, to account for sufficient random distribution of charge over the periodic structure, there was a net charge of +16 (unit cell structure is expanded 16 times in three dimensions . To balance this charge, 16 monovalent cations (Figure 4-5) were added to the interlayer space of the unit cell, or 8 divalent cations (Figure 4-6). Thus, in this case the charges are balanced. These energy values are compared to the energy of the mica model with no ions in the interlayer.

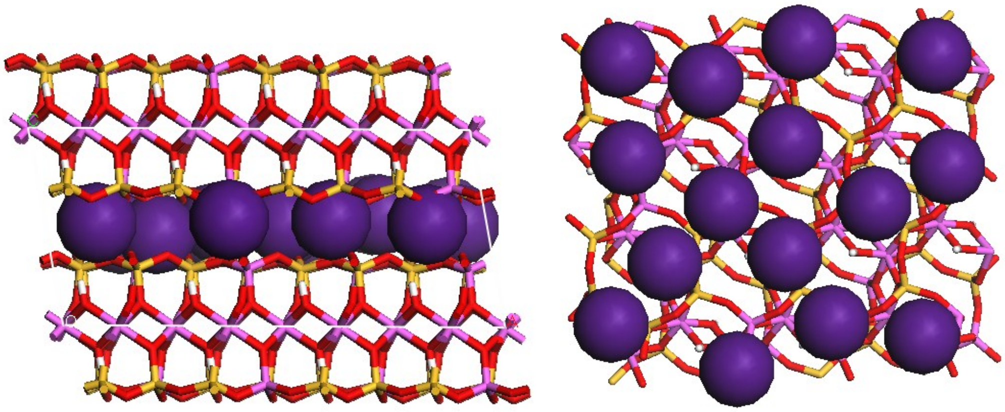

Figure 4-5: Cs in the interlayer of the mica model, side view, top view

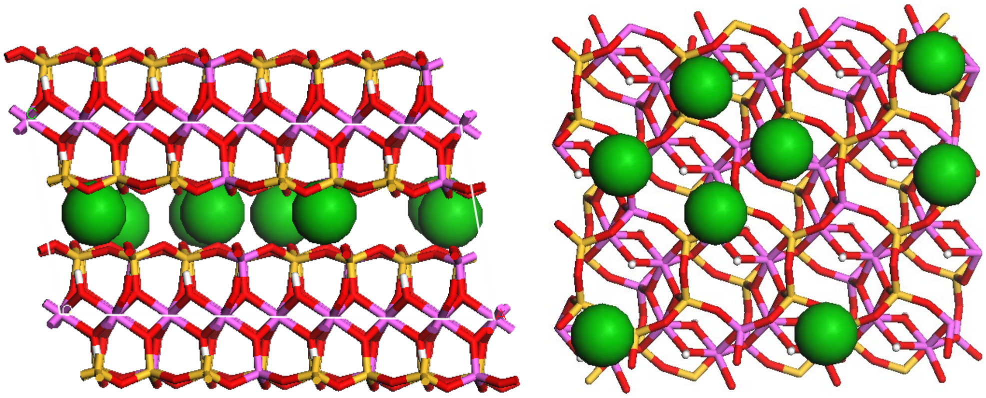

Figure 4-6: Ba in the interlayer of the mica model, side and top view

Case 2: A single hydrated cation was added to the interlayer of mica with the appropriate number of water molecules for the cations coordination with water (Figures 4-7 and 4-8). These are the same number of water molecules listed in the pyrophyllite case above. Here, the geometry optimization energy is compared to a mica model with only water in the interlayer, without the cation.

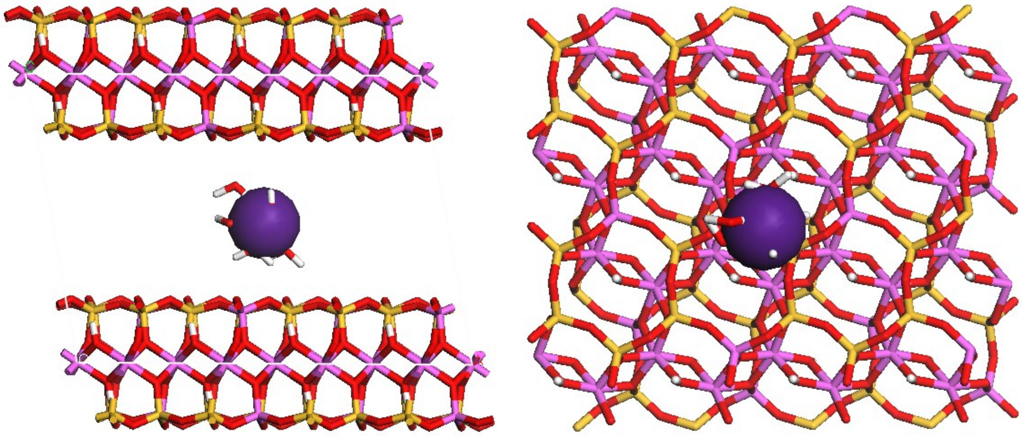

Figure 4-7: Hydrated Cs in the interlayer of mica, viewing from the a-axis, and looking down the c axis.

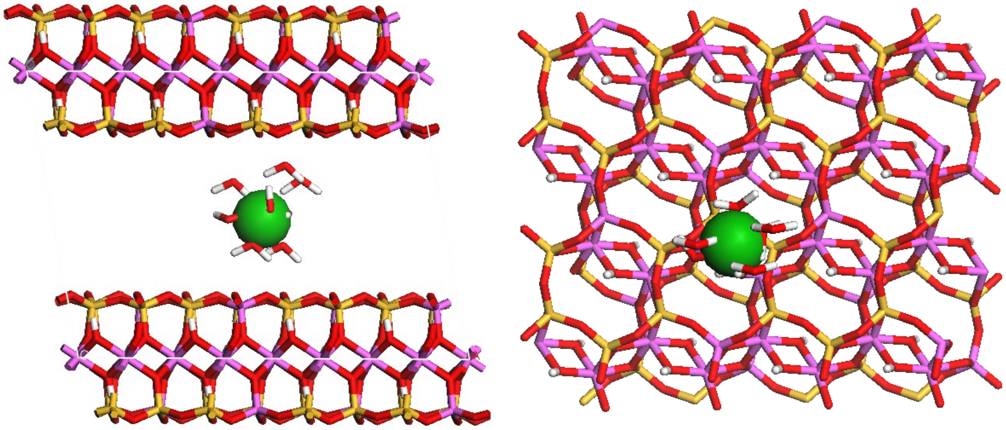

Figure 4-8: Hydrated Ba in the interlayer of mica, side and top view

4.4.2.3 Vermiculite

The vermiculite model, $X_{.75}Al_2Si_{3.25}Al_{0.75}O_{10}(OH)_2$, was designed as an intermediate between the pyrophyllite and mica models and has a layer charge of -0.75 situated in the tetrahedral sheet. Case 1: as with the mica, enough cations were added to the interlayer to balance the charge of the structure. In this case, that required 12 monovalent cations (Figure 4-9) and 6 divalent cations (Figure 4-10) per unit cell.

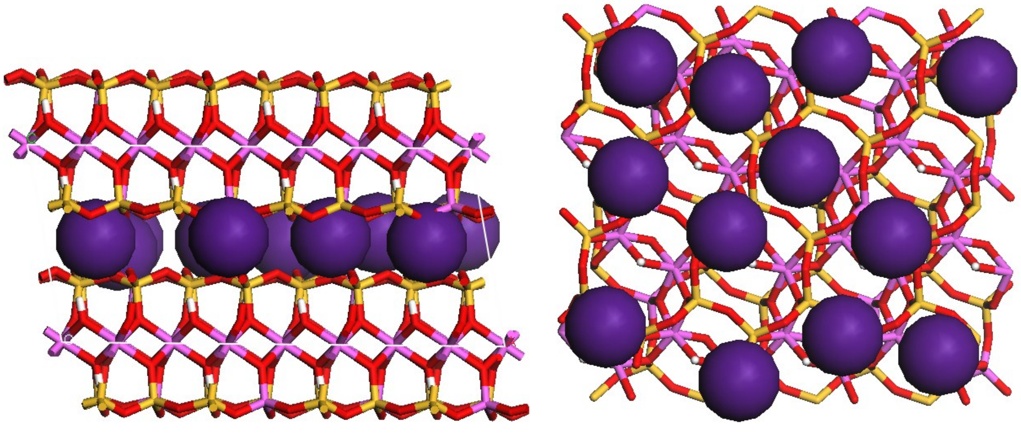

Figure 4-9: Cs in the interlayer of the vermiculite model, side and top view

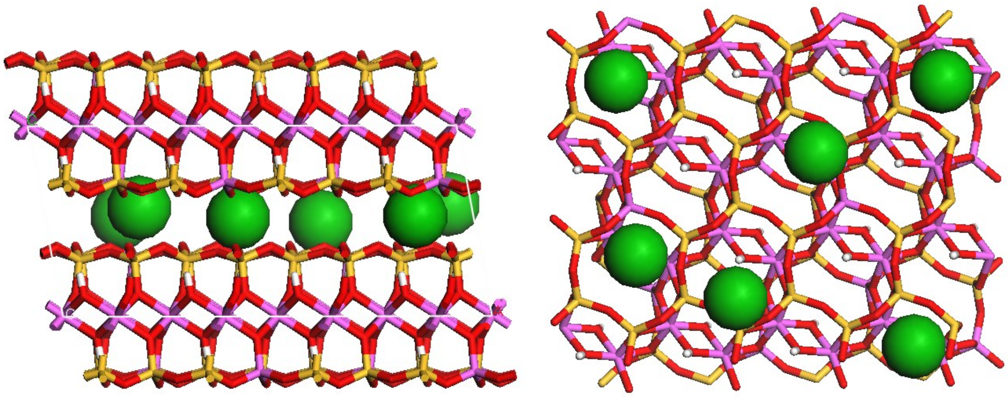

Figure 4-10: Ba in the interlayer of the vermiculite model, side and top view

Case 2: a single cation and the appropriate amount of water molecules for the coordination of a hydrated cation were added to the interlayer (Figures 4-11 and 4-12).

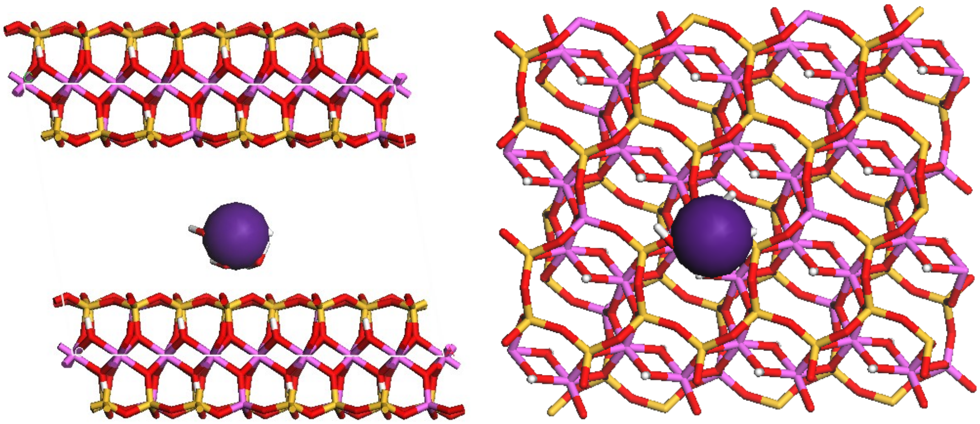

Figure 4-11: Hydrated Cs in the interlayer of vermiculite model.

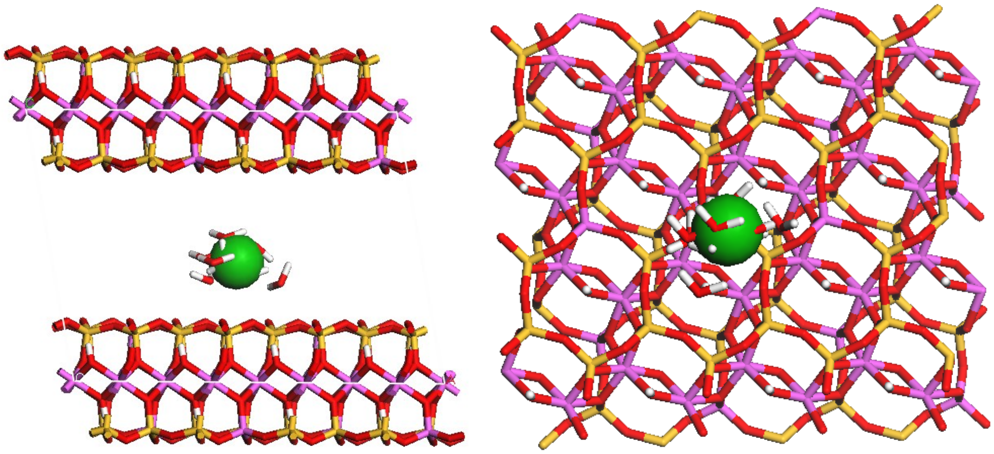

Figure 4-12: Hydrated Ba in the interlayer of vermiculite
Side and top view

4.4.2.4 HIV

The simulation approach was different for the HIV model as it is a much more complex model involving multiple charge domains and will be used for the molecule dynamics simulations of this system. However some preliminary model runs were done to inspect the ions in the interlayer wedge site of the mica grading to HIV (refer to the conceptual model Figure 1-3) in the following way. The model was designed to incorporate the interlayer wedge zone and was constructed using Na ions and water filling the interlayer wedge. The stoichiometry of the original model is $Na_{52}Al_{128}(Si_{2}0_{4}Al_{52})O_{640}(OH)_{128}\cdot 220H_2O$. Na ions were then replaced with alternating sets of K and Cs. K ions were directly linked to the siloxane surfaces of the 2:1 interlayers as in the same design as mica. Cs ions were then added along with water molecules into the modeled interlayer. The placement of the ions in the interlayer formed wedges as shown in Figure 4-13. The stoichiometry of the primary HIV simulation cell is $K_{28}Cs_{24}Al_{128}(Si_{204}Al_{52})O_{640}(OH)_{128}\cdot 220H_2O$, which incorporates variability in the placement of Al ions in the tetrahedral sheet. The Cs/K ratios in this model are not representative of the natural distribution of Cs and K in the soils as the model is unable to model pedogenic uptake of Cs into the wedge zone, and is merely a representation of Cs in the interlayer region.

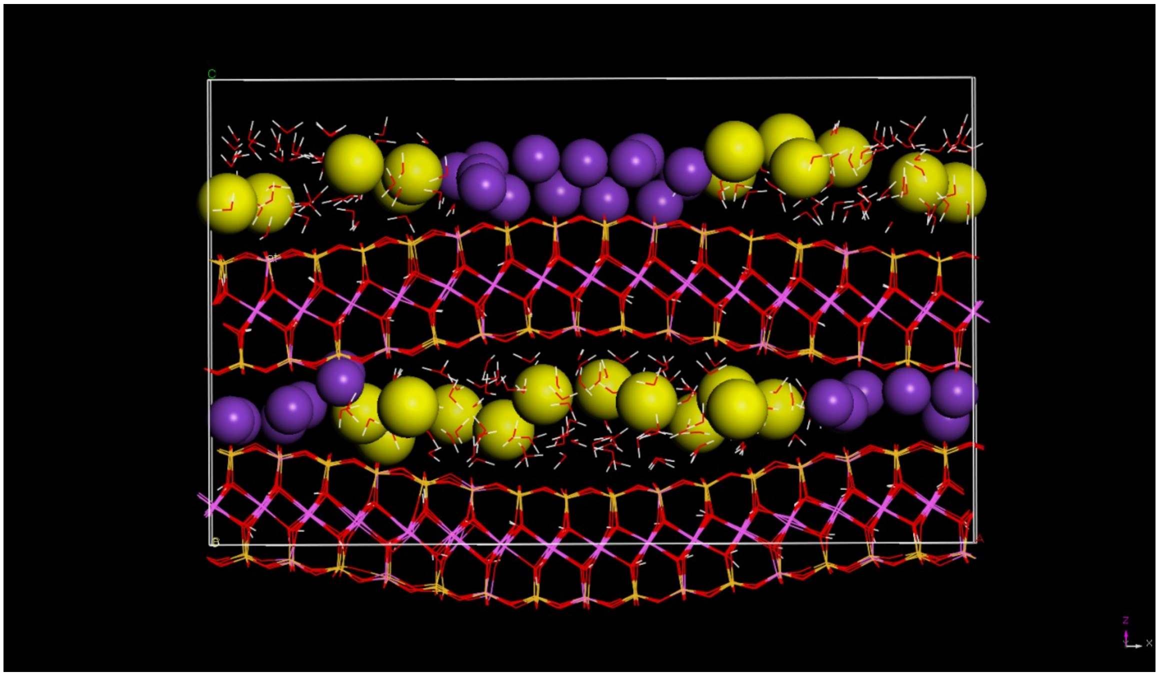

Figure 4-13: K and Cs HIV (frayed edge) model.
K atoms are shown in purple. Cs atoms are shown in yellow.

Energy calculations on this system were performed in a different manner than the previous models. Here, to model the location of Cs (and other ions) in the wedge zone, first, all waters were removed from the interior of the interlayer in the model. Then, interior Cs was removed leaving only ions near the wedge zone, assigning an initial configuration of the ions to the model system. The 2:1 structure was then constrained allowing only ions in the interlayer region to move, as a large imbalance of charge would arise and deformation of the structure if a geometry optimization of this configuration attempted. First energy was calculated with the Forcite module in Material Studio for the system with a completely empty interlayer region, then with 12 Cs (Rb, K, and Na) ions in the interlayer, and 6 Ba and Sr ions in the interlayer region.

These energies were compared to one another to determine the most favorable ion in the interlayer. Figures 4-14 and 4-15 show the configuration of Cs and Ba in the interlayer of the HIV model which is designed without the typical Al-hydroxy cation pillars in the interlayer.

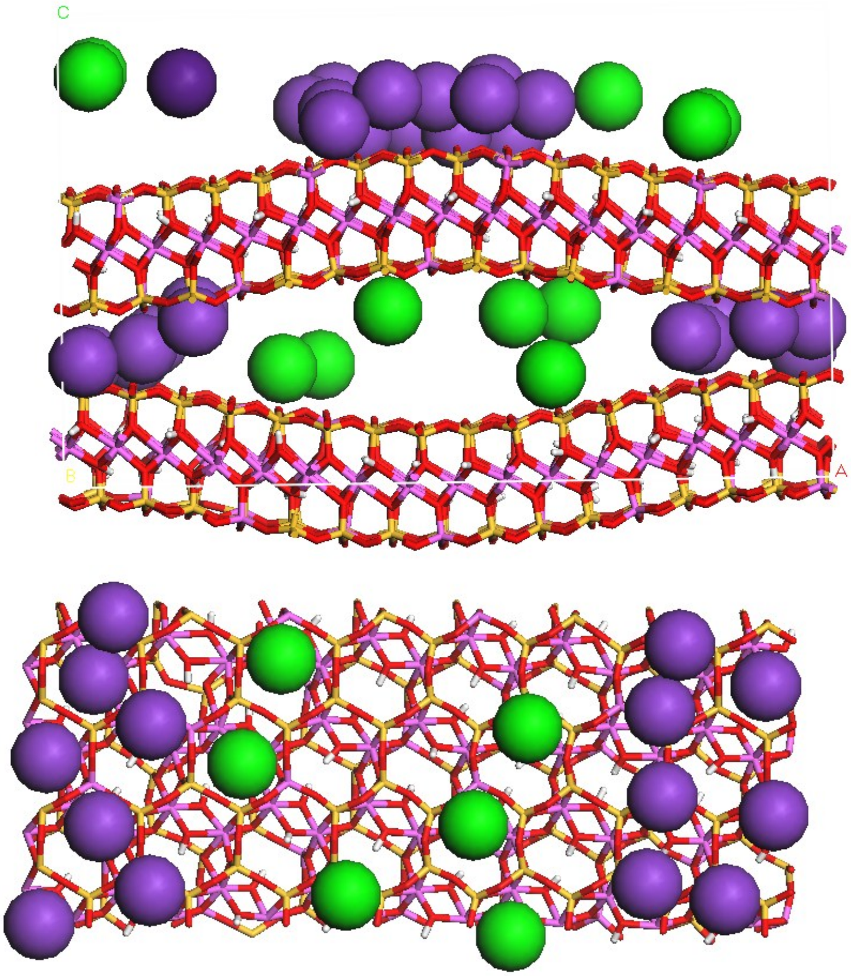

Figure 4-14: Cs in the interlayer of the model HIV view down a-axis (top) and c-axis (bottom), Cs ions are green, K ions are purple.

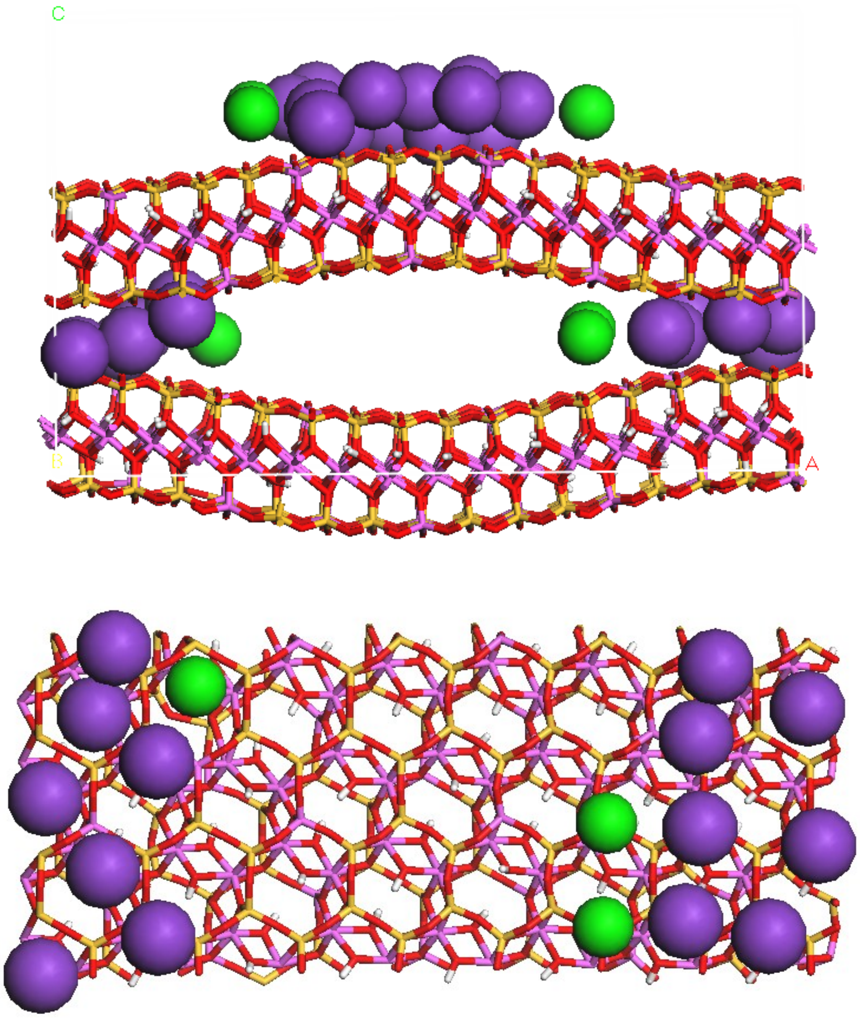

Figure 4-15: Geometry optimized Ba in the interlayer of modified HIV model down a-axis (top) and c-axis (bottom), Ba ions are green, K ions are purple.

4.4.3 Data Analysis

The ion adsorption energy for each of the geometry optimized configurations (minimum energy) is calculated by taking differences of the appropriate models with and without the cation being investigated. The adsorption energy is dominated by van der Waals and electrostatic interactions and the equations are shown in section 4.3.1.

4.4.3.1 Adding hydration energies

For pyrophyllite, mica, and vermiculite models, the Case 2 scenarios involved adding water to the interlayer to hydrate the ion being studied. Hydration energies had to be incorporated to get accurate adsorption energies in these cases. Experimental hydration energies were added from values reported in *Ockwig et al*. (2007).

4.4.4 Molecular Dynamics Simulations of HIV Model

The model structure was designed by Dr. Randall Cygan of Sandia National Laboratories using Materials Studio software, and the molecular dynamics simulation was run using LAMMPS (Large-scale Atomic/Molecular Massively Parallel Simulator (*Plimpton*, 1995; *lammps.sandia.gov*) on a parallel Linux cluster by Dr. Stephanie Teich-McGoldrich also at Sandia National Laboratories. For the dynamics simulation, the layer structure of the HIV model was held rigid ("frozen") and the cations and water molecules allowed to move within the interlayer space.

Figure 4-16 shows a snapshot structure of the 2x2x2 simulation cell of the HIV model obtained from molecular dynamics simulation. Molecular dynamics simulations take atomic movement one step further. Time is explicitly included in the calculation and atoms are allowed to move according to classical mechanics equations based on the potential energy surface (CLAYFF) and the kinetic energy of the atoms for a given temperature. Molecular dynamics is the method of choice for studying dynamical properties of molecular systems, such as diffusion or other time-dependent processes.

The 2x2x2 cell is the aggregate of 16 building-block cells of the vermiculite and mica structures and then modified to create the wedge environment. All the interlayer water and ions are allowed to freely move during the simulation. The initial trajectory velocities are assigned to the molecules from a random generation of velocities according to a Boltzmann distribution. The distribution targets the velocities to ultimately give the optimal temperature of the system at 298K. From the initial configuration of the HIV model, the system will dynamically evolve following the deterministic equations of motion. Forces are resolved and new velocities determined after each times step (1 femtosecond); this process is repeated for a total of 5 million success steps to provide 5.05 nanoseconds of simulation.

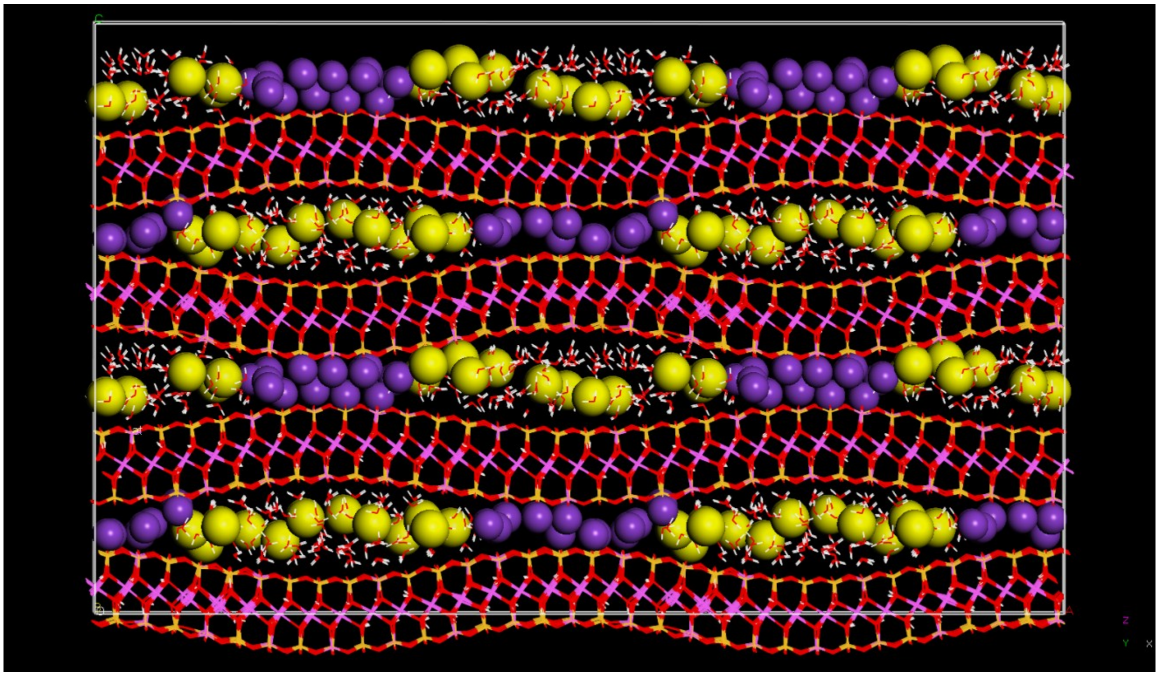

Figure 4-16: 2x2x2 unit cell of the model used for molecular dynamics simulations in the model, Cs is yellow and K is purple.

The HIV model is first run as NVE ensemble (atoms, volume, and energy held constant) for 10-50000 femtoseconds (50000 time steps) until the temperature of the system is equilibrated. Temperature varies only by about ±5K. Then potential energy (PE) starts to stabilize and equilibrium is reached. Once the temperature and PE are equilibrated and the structure behaves properly, the simulation was continued as NVT (atoms, volume, temperature held constant). Diffusion of unconstrained atoms is also occurring in the model. The NVT model is run for 5ns. This is a large amount of computational time and involves 5 million time steps (5 million femtoseconds plus the equilibration NVE time of 50000fs = 5.05ns).

4.4.4.1 Radial Distribution Functions

Radial distribution functions (RDF) were derived from structures saved (trajectory) from the final nanosecond of the simulation. A snapshot of the model was saved every 0.5 picoseconds which amounts to 2000 frames being analyzed to get the RDFs. The radial distribution function, *g(r),* gives the probability that two particles are separated by a distance *r*. The RDF counts the occurrences that the two specific atoms or types of atoms are at separation *r*. This makes the RDF a useful tool to describe the dynamic structure of a system. In a solid, the RDF has an infinite number of sharp peaks whose separations and heights are characteristic of the lattice structure. At short distances (less than atomic diameter) *g(r)* is zero due to the strong repulsive forces. An RDF of 3 at a certain distance separation would mean the two molecules in question are three times more likely be found at this separation than for a random distribution of atoms. At long distances, *g(r)* approaches one which indicates there is no long-range order. To calculate the pair distribution function from a simulation, the neighbors around each atom or molecule are sorted into successive volumes of shells about each atom.

The RDFs reported are for Cs and K interacting with water molecules, the O in the clay, and to each other. A comparison is made for how Cs is coordinating with the water in the interlayer, versus the clay structure itself. RDFs are calculated for the interaction of Cs atoms with the H and O in the water molecule separately, the bridging oxygen (ob) and the tetrahedral O (obts) and to K (Table 4-1). The ob is where Si-O-Si forming the hexagonal ring, whereas obts is the oxygen associated with Al-O-Si when there is a substituted Al in the tetrahedral sheet of the clay. The same RDF calculations are made for K with the same atoms and then for the Cs interacting with K.

4.5 Results

4.5.1 Energy Minimizations

The adsorption energies for each of the interlayer ions in the pyrophyllite, mica, and vermiculite cases are summarized in Tables 4-2, 4-3, and 4-4.

In the pyrophyllite model, in Case 1 (Table 4-2, column 2), there is a noticeable difference in the energies of monovalent cations versus divalent cations. Sr and Ba have the lowest energies. Because they are divalent cations versus monovalent, they have a stronger electrostatic energy component. The preferred order of the ions for adsorption onto pyrophyllite is Sr>Ba>Na>K>Cs>Rb. For pyrophyllite Case 2 (Table 4-2, column 3), the hydration energies were included. In this case, the preference of the ions is now Ba>Rb>Cs>K>Na>Sr.

Table 4-2: Pryophyllite Energy Minimization Values.

Pyrophyllite		
Interlayer Ion	**Energy (kJ/mol)**	
	Case 1 No water	**Case 2 Hydrated**
Na	-117	-25.3
K	-86	-25.8
Rb	-64	-40.4
Cs	-66	-35.3
Sr	-306	-11.9
Ba	-292	-52.7

In the mica model, Case 1 (charges balanced by added appropriate number of cations) has the preference of ions in the order Sr>Ba>Na>K>Cs>Rb (Table 4-3 column 2). In Case 2, where the ions in the interlayer have been hydrated (Table 4-3, column 3), the preference for the ions changes to Na>K>Rb>Cs>Ba>Sr.

Table 4-3: Mica Energy Minimization Values.

Mica		
Interlayer Ion	**Energy (kJ/mol)**	
	Case 1 No water	**Case 2 Hydrated**
Na	-201	-22.8
K	-182	-12.5
Rb	-169	-7.0
Cs	-172	-2.5
Sr	-507	33.9
Ba	-498	9.4

Next, the vermiculite model Case 1 (balanced charge, no water) has the preference Ba>Sr>Na>K>Cs>Rb, and in Case 2 (hydrated ion), Rb>K>Na>Cs>Sr=Ba (Table 4-4).

Table 4-4: Vermiculite Energy Minimization Values.

Vermiculite		
Interlayer Ion	**Energy (kJ/mol)**	
	Case 1 No water	**Case 2 Hydrated**
Na	-127	-18.9
K	-111	-19.5
Rb	-98	-47.1
Cs	-102	-18.8
Sr	-329	37.2
Ba	-331	37.2

Lastly, the HIV model was considered (Table 4-5). As in the previous cases, the divalent cations have much lower energies as the extra charge increases the attraction of the clay layers to the ions. The order of preference here is Sr>Ba>Rb>Na>Cs>K. This model was different from the other three in that the clay structure was held rigid and not allowed flexibility and all the water was removed from the interlayer. If the hydration energy of each ion is subtracted, then the order changes to Rb>Cs>K>Na>Sr>Ba.

Table 4-5: HIV Energy Minimization Values.

HIV		
Interlayer Ion	**Energy (kJ/mol)**	
	Case 1 No water	**Hydration E Subtracted**
Na	-125	-28
K	-119	-42
Rb	-130	-59
Cs	-124	-58
Sr	-358	-13
Ba	-323	-11

4.5.2 Molecular Dynamics Simulations

Molecular dynamics evaluates the forces on individual atoms using an energy force field (CLAYFF), then uses Newton's classical equations of motion to compute new atomic positions after each time step (femtoseconds). Successive evaluation for a large number of time steps provides a time-dependent trajectory of all atomic motions. Figure 4-17 shows the equilibrated structure of the 2x2x2 simulation cell of HIV after 5.05 ns.

.

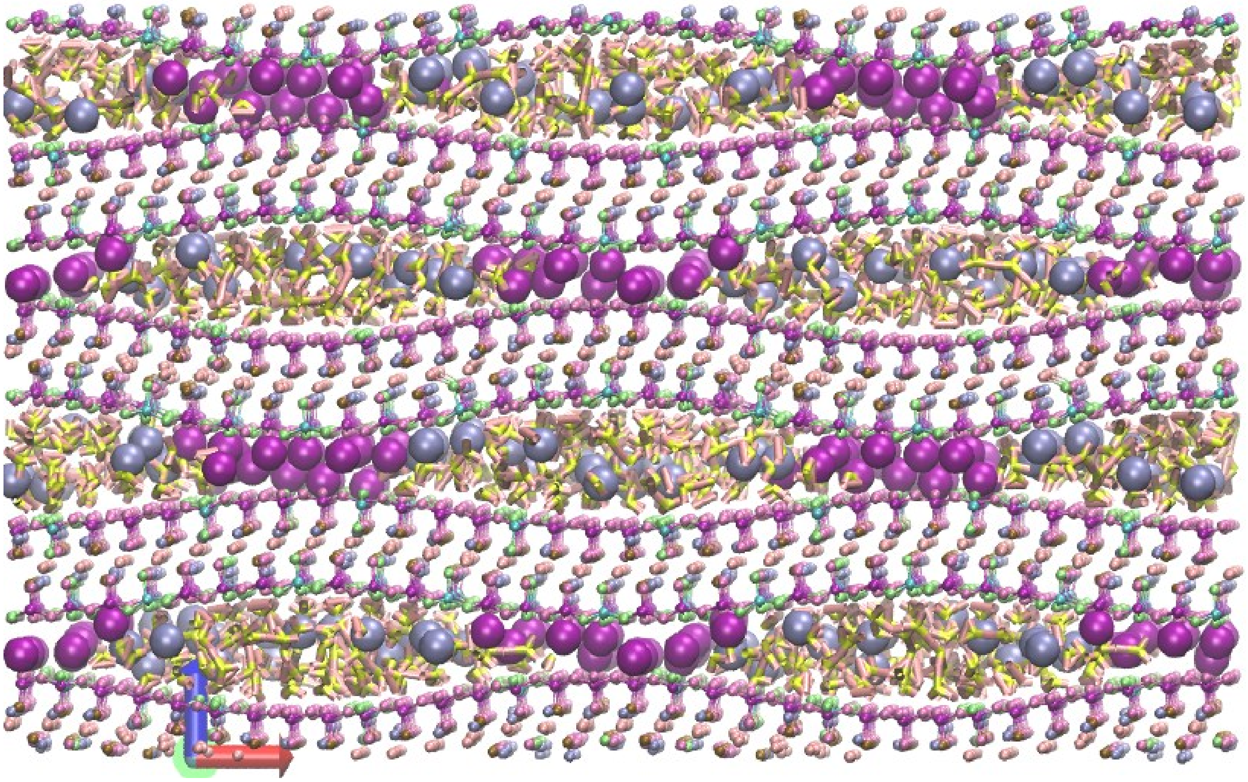

Figure 4-17: Output of the molecular model simulation.
Cs is blue, K is purple. On the figure we look down b-axis so don't see the vacancies. The charge is in the tetrahedral layer. Note that the model is orthogonal where more realistic would need to be monoclinic. Also, not all the waters are graphically clean; some look bonded together but this is not truly represented and is a result of the visualization software. All the interactions in the model are based on CLAYFF.

4.5.2.1 Cesium RDF's for water and clay

Figure 4-18 shows the RDF of Cs with the hydrogen atoms of water. The radial distribution function, *g(r),* gives the probability that two particles are separated by a distance *r*. Here, the first peak in the RDF is at 3.1 Å with an intensity of 4.75. This is representative of the first shell of water molecules coordinating around Cs, with a second peak at 5.5 Å (second sphere of coordination) and a very broad peak at 7.3 Å with 1.75 and 1.2 as the intensity for the second and third shells respectively. Beyond 8 Å the RDF approaches 1 as there is no long range order (the length of the lens shaped interlayer region is only about 10 Å long). The increment between the peaks is approximately the size of a water molecule. As we move away from the first shell of water molecules, there is decreasing intensity and increasing disorder. The electrostatic control of Cs on the H atoms of water is lost as *r* increases.

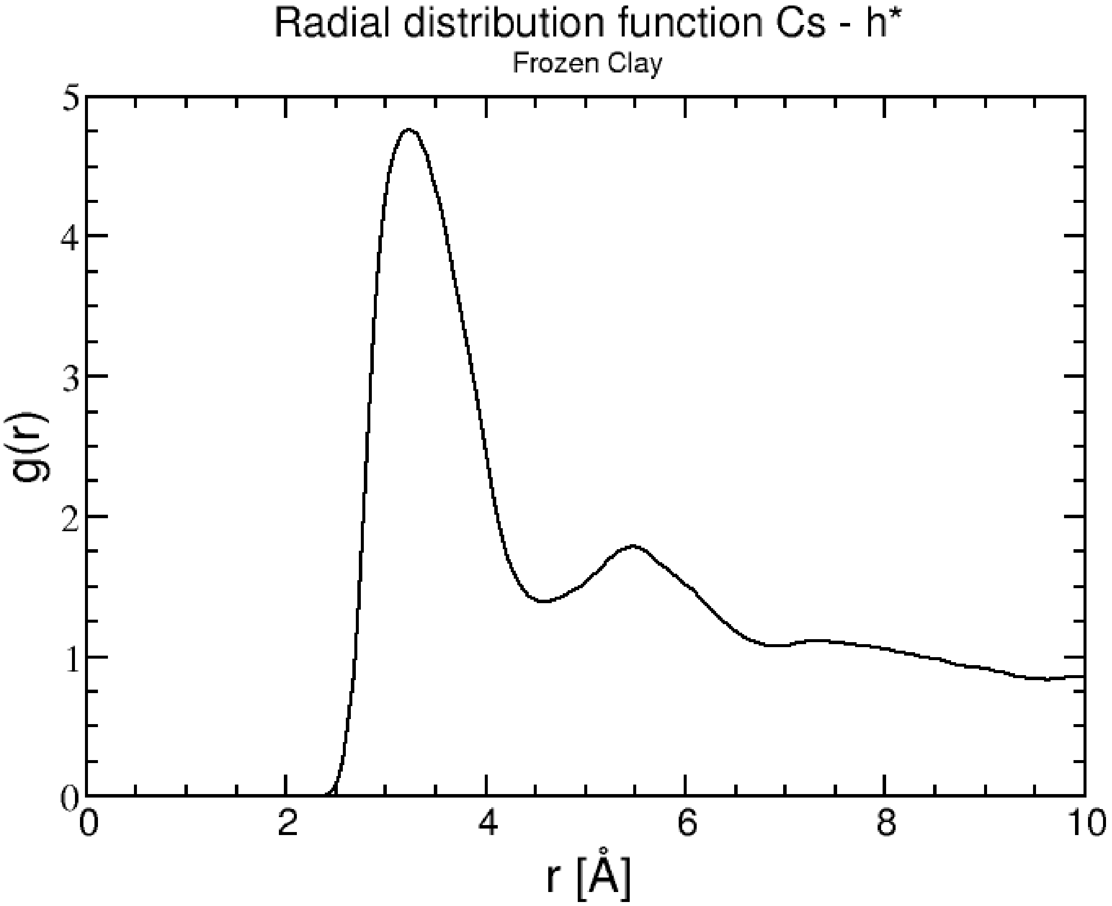

Figure 4-18: Cs RDF with the H in water molecules.

Figure 4-19 shows the RDF of Cs with the O in water molecules. Here the first shell coordination is a much sharper peak with greater intensity. Cs coordination to O in water has a much narrower first peak with a higher intensity at about the same spacing as the H around 3Å at 12.8 intensity value. The second peak is at about 5.2 Å with intensity around 2.4 and lastly a third peak at 7.8 Å with intensity around 1.3. The sharpness of the first peak means there is greater order to this coordination than with H, there are stronger spatial correlations between the Cs and O than the Cs and H. Beyond 8 Å the pattern gets very diffuse, again suggesting there is no long range order.

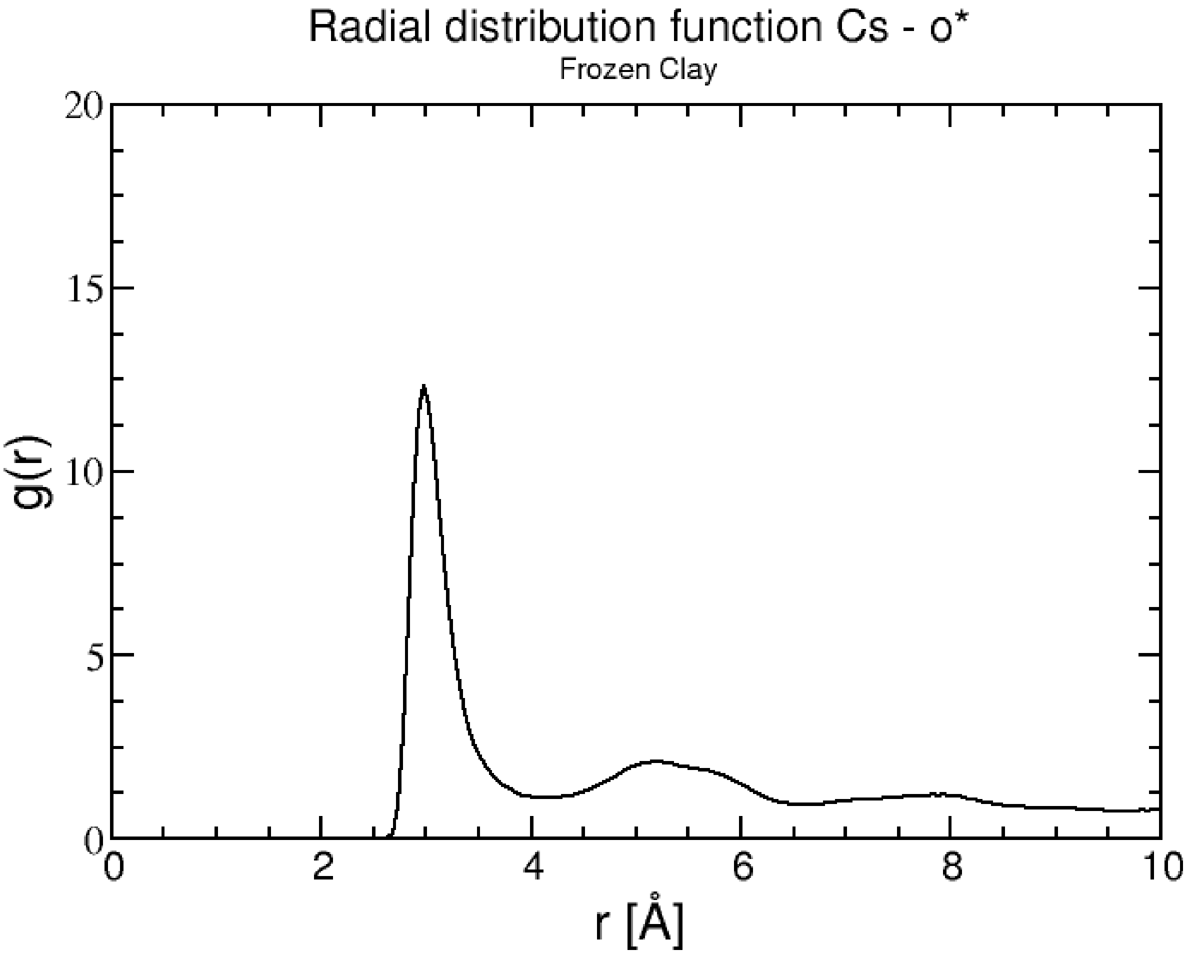

Figure 4-19: RDF of Cs and the O in water molecules.
The radial distribution function, *g(r),* gives the probability that two particles are separated by a distance *r*.

Next, we look at the interaction of Cs with the Os in the clays. Here two the types of Os are the regular bridging O between to Si atoms (ob) and then the bridging O (obts) between a tetrahedrally substituted Al and a Si atom. Figure 4-20 shows the RDF for Cs with obts. The first peak is fairly narrow at 3 Å with an intensity of 2.4. The next peaks are at 4.8, 7.2, and 9.6 Å with decreasing intensities. The Cs is clearly interacting with the clay.

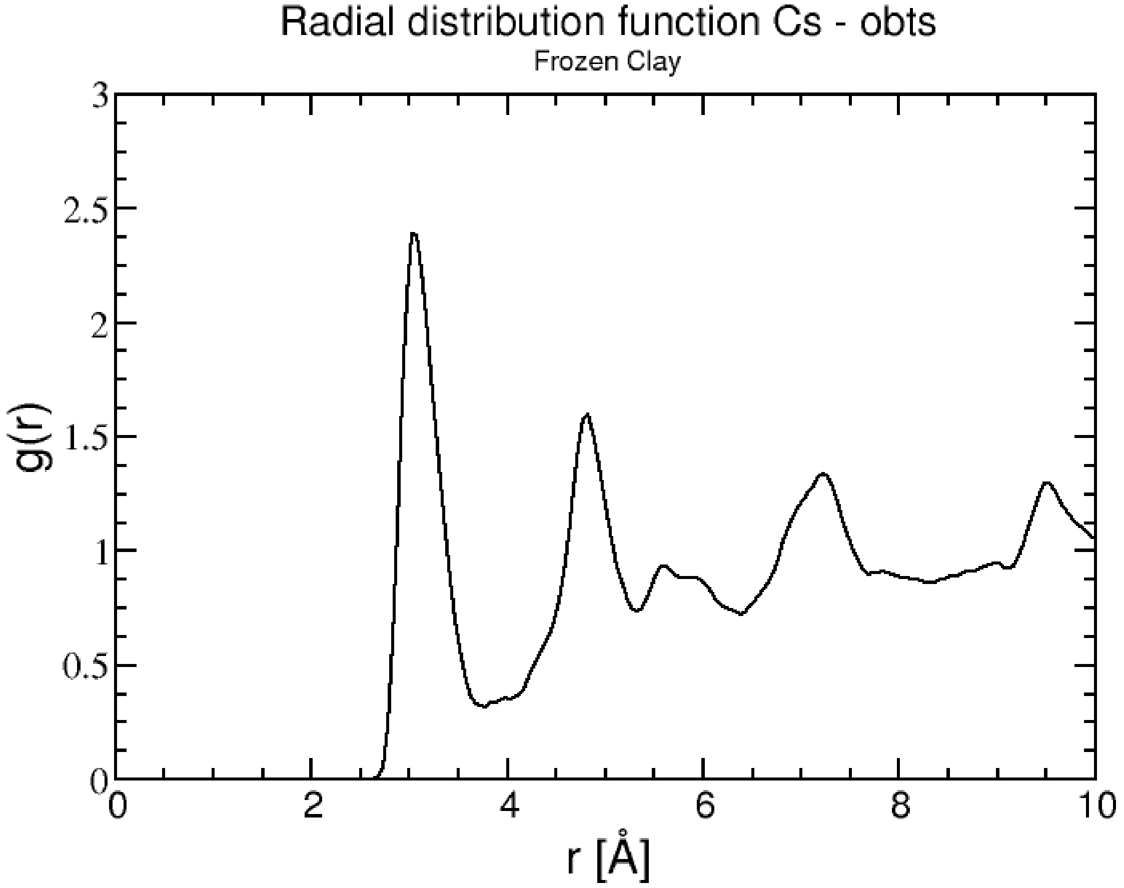

Figure 4-20: RDF of Cs with obst O, Al-O-Si in the clay.

Figure 4-21 is the RDF for Cs with bridging O ob (Si-O-Si). Here is spacing is just slightly larger than for the obts O. The first peak is at 3.1 Å and the following 3 peaks at 4.8, 7.2 and 9.5 Å all have very similar intensities. Comparing the two, Cs prefers to be near Os that are associated with the Al atoms in the structure.

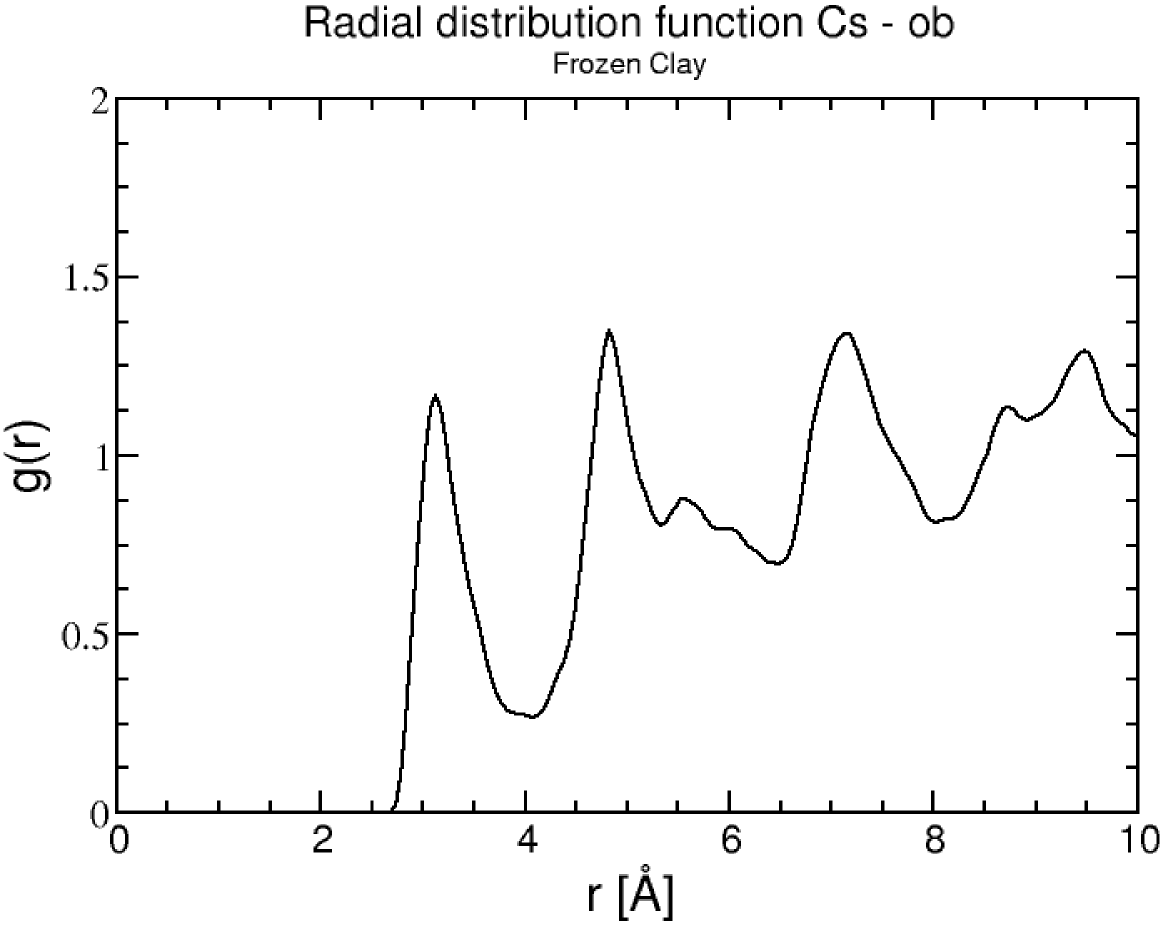

Figure 4-21: RDF of Cs and ob O in the clay structure of the model.

4.5.2.2 K coordination with water and the clay surface

Figure 4-22 shows the RDF of K and the H in water molecules. Here, the *g(r)* is noticeably smaller than for the Cs case. The first peak is at 3.3Å with an intensity of only 1.25. The other peaks are all very small and less than 1, so are not meaningful.

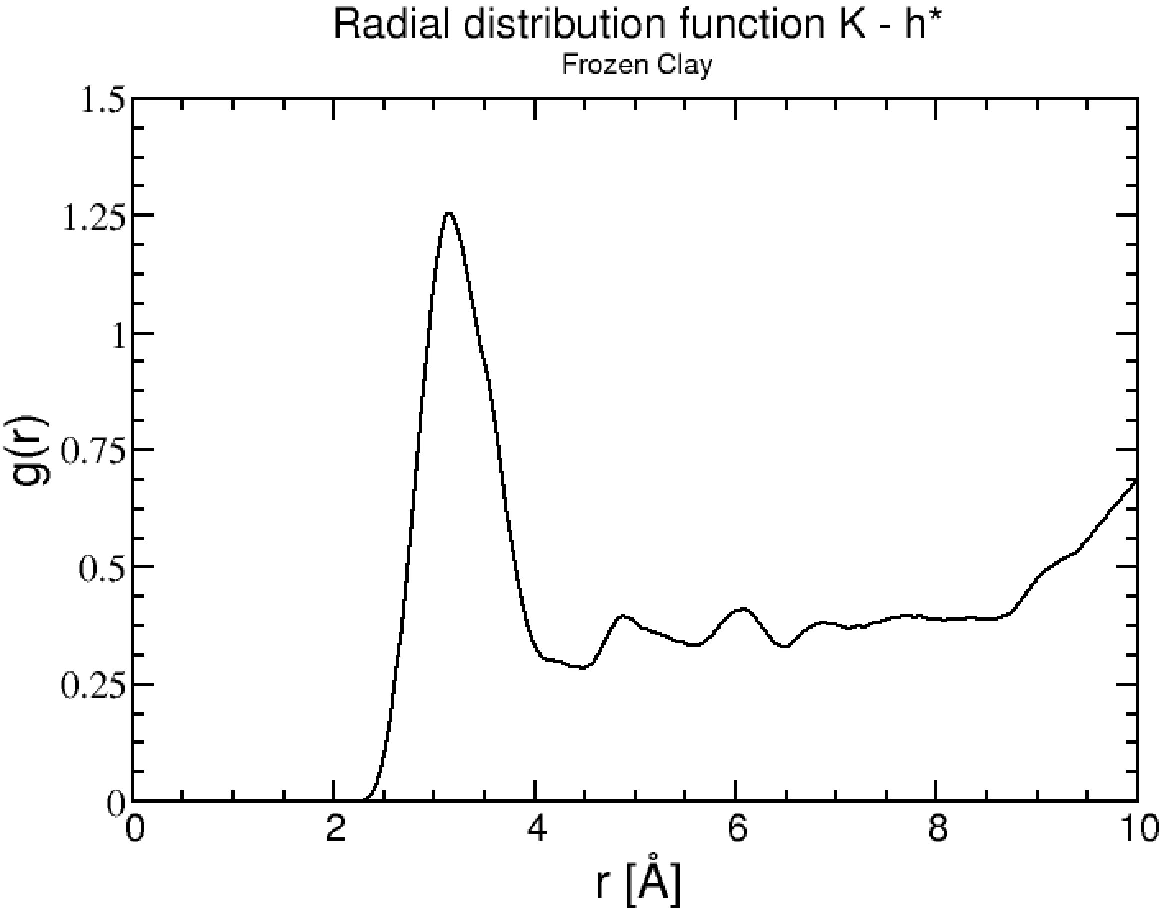

Figure 4-22: RDF of K with H in water.

Figure 4-23 shows the RDF of K with the O of the water molecules in the interlayers. It has narrower peaks and greater intensities suggesting a better coordination with the O than the H. The pattern has several peaks at 2.5, 5.5, 6.5, 7.5 Å, but the main sharp peak has an intensity of 3. K has higher hydration energy than Cs so shows more structure in the RDF than Cs and a narrower peak. The overall intensity is smaller than Cs however because again there are less occurrences of K to contribute to the RDF than Cs and generate the structure. The coordination is strongly driven by the hydration energies of Cs (62.9 kcal/mol) and K (76.7 kcal/mol) (*Ockwig et al.* 2009).

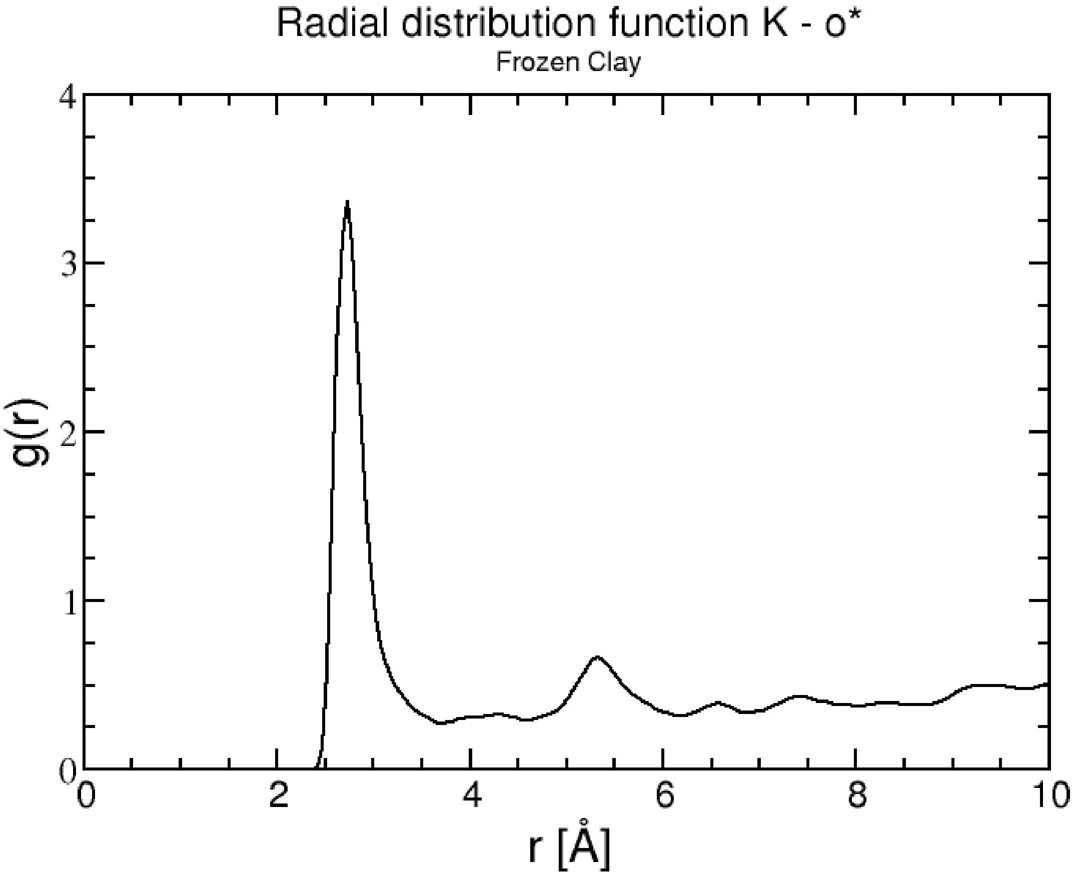

Figure 4-23: RDF of K with O in water.

Figures 4-24 and 4-25 are the RDFs for K with the obts O and the ob O in the clay structure respectively. The first peak for obts is about 2.7 Å and the peak for ob is about 2.9 Å. However the intensity for the obts is about 6.5 whereas for ob it is about 2.9. The higher intensity suggest that K prefers to be associated with the O in the mica section of the clay structure where there are more Al substitutions occurring. For the obts O, the next three shells are at r = 4.6 Å, 7.0 Å, and 9.0 Å with decreasing intensities. Thus, even the second shell of coordination is nearly as intense as the first shell coordination for the bridging oxygen of Si-O-Si. For the ob O the next two peaks are at 4.6 and 7.0 Å with intensities of 2.4 and 1.9. There are also three shoulders beyond these at 7.9, 8.5, and 9.0 Å with intensities between 1.25 and 1.5 that is the K reacting with other Os in the structure.

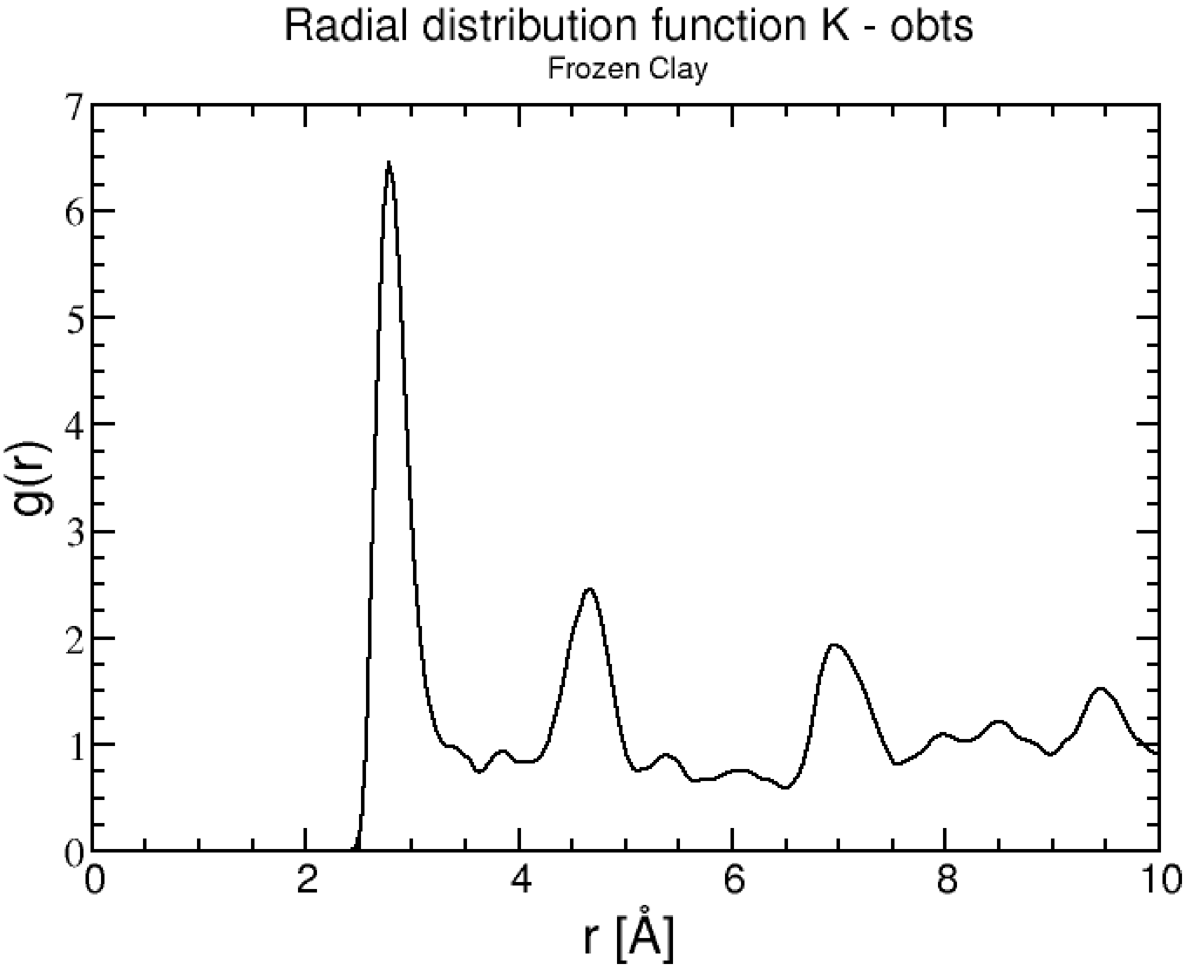

Figure 4-24: RDF of K with obst O in the clay structure.

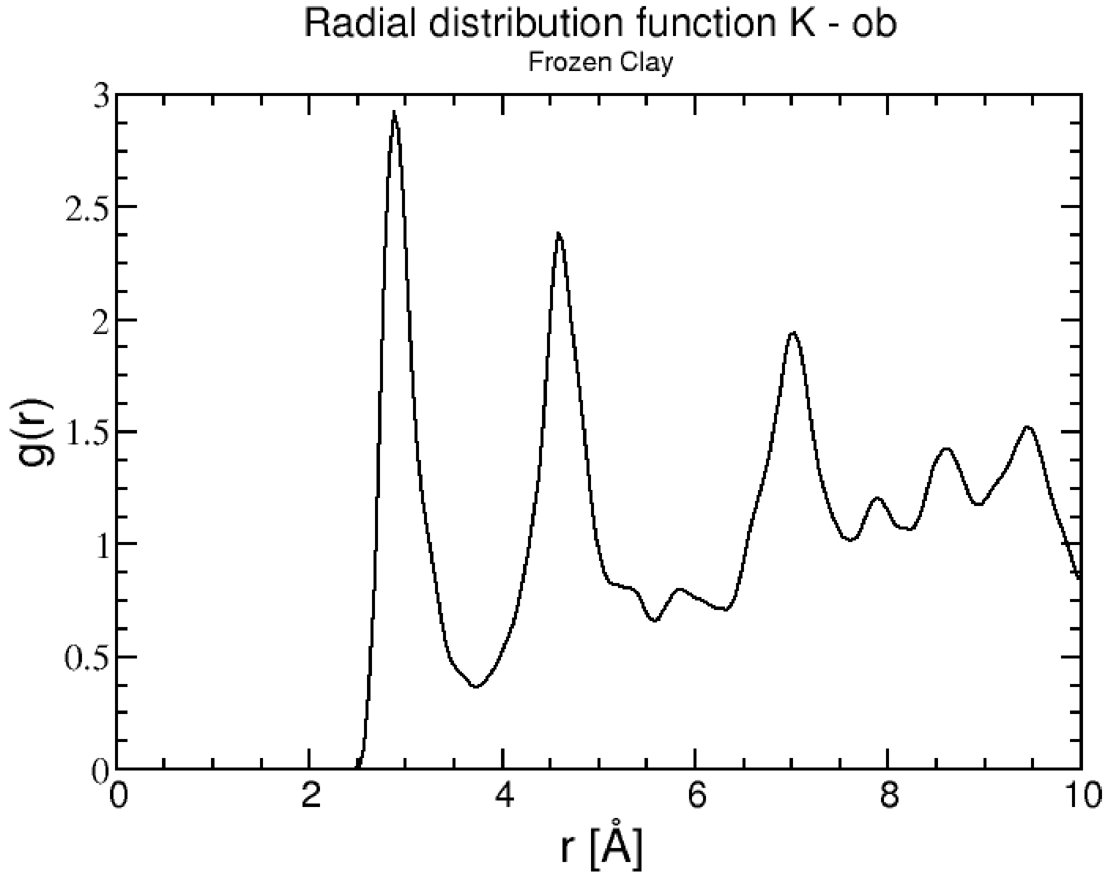

Figure 4-25: RDF of K with ob O.

Lastly, Figure 4-26 is the RDF of Cs to K. This indeed shows Cs interacting with the wedge zone. Cs is close to the K which is effectively contained in the collapsed interlayer at the apex of the wedge. The initial configuration of Cs ions is evenly distributed throughout the widened section of the model. But with time, we see that Cs is migrating towards the wedge. The RDF shows a shoulder around 3.9 Å and a tight peak at 4.5 Å.

For Cs-K, there are 2000 averages of RDFs going into the figure averaging noise and showing where the Cs is located. Cs is diffusing closer to the K than remaining in the center of the wedge where it was originally evenly dispersed.

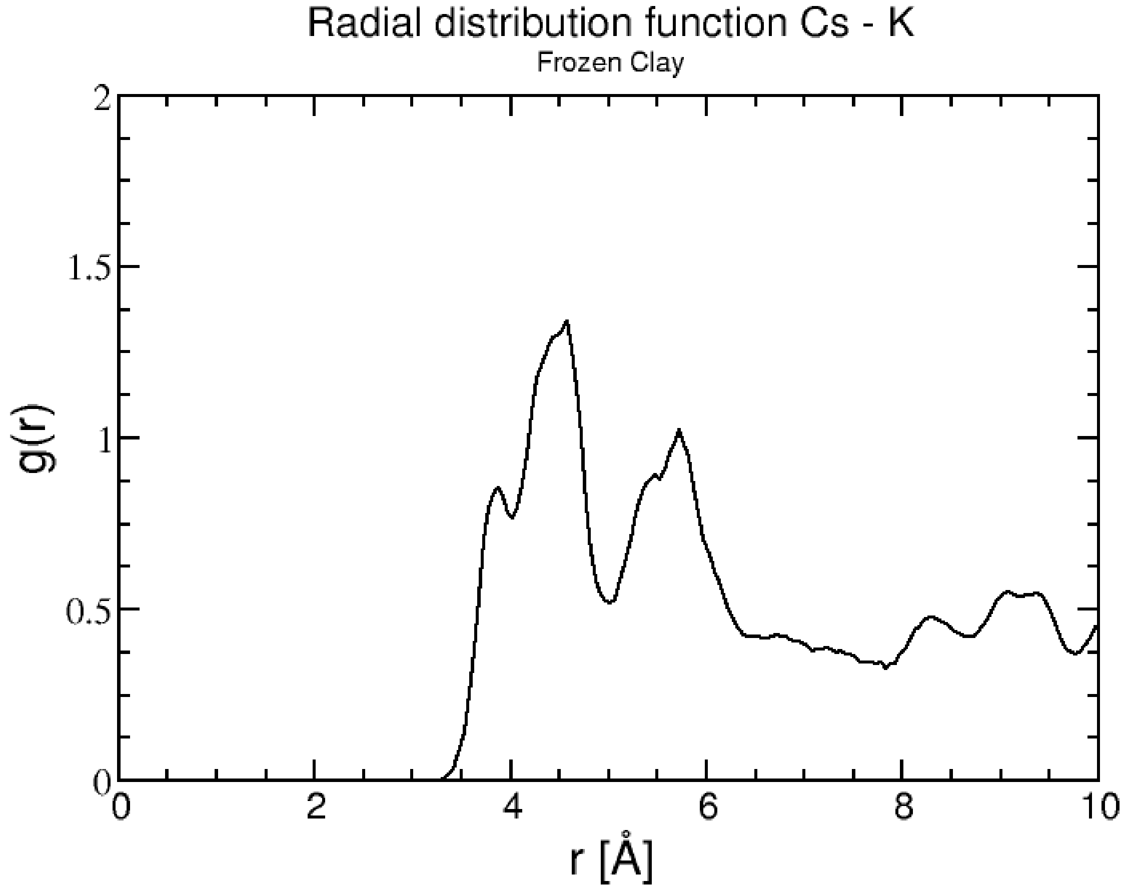

Figure 4-26: Radial Distribution Function of Cs and K ions in the HIV model.

4.6 Discussion

4.6.1 Energy Minimization

Static energy calculations simply take an initial atomic configuration, subject the system to the force field equations, and derive energy for the given state. The models examined an ion or multiple ions in the interlayer region of several clay minerals as either in a collapsed or an aqueous environment. The energy minimization technique (or geometry optimization) lowers the potential energy by modifying atomic positions to achieve a more favorable configuration, and helps identify a favorable binding site. This technique models physical adsorption to the surface, and not chemical reactivity, thus electrostatics and van der Waals forces are considered as the controlling interactions.

With respect to the simulations of mica, mica has a lower CEC relative to smectite and vermiculite because the interlayer region is not exchangeable. Ion exchange is typically limited to external surfaces or edges. Ion adsorption on clays occurs through either inner or outer-sphere complexation on the basal surfaces of clays, within the interlayer region, or at the edge of clay particle on the silicon or aluminum hydroxyls (*Spark et al.* 2005).

For case 1 in mica, the two divalent cations Sr^{+2} and Ba^{+2} have the lowest energy by far. Figure 4-6 shows that the ions are spread out in the interlayer but not binding directly into the ditrigonal holes. It is likely here that the high charge of the ions are strongly attracting the negatively charged clay siloxane surfaces and results in sorption. However, in case 2, when the hydration energies are added, the energy for sorption of the divalent cations is in the positive range (+ ΔG) and the highest values of all the ions. As hydrated ions, Ba and Sr are not energetically favorable in the interlayer of mica. Na and K have the lowest (most stable) energies in the hydrated case. Cs and Rb are intermediate. Both Cs and Rb are weakly hydrating cations so would be more likely to form inner sphere complexes with the clay surfaces and are not likely to become hydrated in the interlayer region.

In the vermiculite model, Case 1 (no water), Sr and Ba are again the most preferable ions in the interlayer region based on negative energies associated with their sorption. As with mica, and the high charge of these ions creates a strong attraction with the negative clay siloxane surfaces and the model shows ions interaction with the clay surface driven by the stronger electrostatic force between divalent cations and the clay surface versus monovalent cations. However, when the ions are hydrated, they again have positive energies and the highest energy values of the ions, so would be less likely to be in the interlayer.

In the pyrophyllite model (Table 4-2), the charge of the structure is neutral, In case 1, (no water) Sr and Ba have the lowest energies by more than 3 times the next most stable interlayer ion, Na. This suggests that this model is strongly driven by the electrostatic component of the interaction and divalent ions interacting more with the clay surface as a result from higher charge. As the clay surface is neutral, these ions are interacting with clay hydroxyls causing the hydroxyls to rearrange and point towards the sorbed cations. Intermediate in this case is the Na and K ions, here the size of the ion allows either Na or K to fit neatly into the ditrigonal holes of the clay structure. These are monovalent cations, so they are not interacting as strong electrostatically with the clay surface as the divalent ions. The large monovalent cations Cs and Rb are the least favorable ions in the interlayer in Case 1.

In the hydrated case for pyrophyllite, Ba, Cs, and Rb are all slightly more stable than K, Na, and Sr, but the energy values are all very close to one another with a variation of only 40 kcal/mol.

4.6.2 Molecular Dynamics Simulation

The models are used to calculate the forces on atoms and the potential energy to find the optimum configuration of a molecule or periodic system. Forces on the atoms are calculated directly from Newtonian physics (F=ma) and predict the evolution of a system with time.

Some caveats to the approach with the molecular dynamics simulation include having to constrain the wedge zone during dynamics simulations. The clay structure had to be held rigid to prevent the collapse of the wedge and the influx of water particles into the interlayer regions of the mica portion of the model. The original model allowed the clay structure to be flexible and it maintained the wedge for approximately 1ns, but when the computation time was increased to a 5 ns simulation, the wedge fully expanded and water penetrated the mica portion of the simulation cell. A fixed clay structure had to be used, thus the "frozen clay" version results are presented and reviewed. Clearly, the model needs adjusting to accurately portray reality but is a good start and is the first model of its kind.

It is realistic to allow for flexibility of the clay layers but this model has such an unusual and unique wedge the rigidity is required to test our hypothesis of the strong sorption of Cs in the wedge zones. Also, there are no hydrated-Al pillars in the structure that would be more realistic to the HIV structure trying to be modeled. However, these simplifications are required at this time as this approach and can be refined in future molecular simulations.

Figure 4-17 shows the final structure of the model after a total of 5.05 ns (50000 fs of initial equilibration time as NVE, then 5ns of NVT). Visual inspection shows clearly that Cs ions have migrated from the evenly distributed arrangement of the initial configuration (Figure 4-16) to be closer to the wedge zones in Figure 4-17. RDFs were calculated and support this interpretation.

The Cs-h* and Cs-o* RDF's (Figures 4-18 and 4-19) show a stronger correlation of water Os to Cs than water Hs. The *g(r)* for water O is nearly three times greater than for water H and the O ions are held closer to the Cs ion than H (3.0Å versus 3.3 Å). Electrostatically dominated forces in the model bring the more favorable negatively charged Os towards the positive Cs ion than the positively charged Hs. The light H atom is twisting and spinning, causing disorder and is very mobile. The preference for the O atom is also demonstrated by the FWHM (full width at half maximum) of the primary peaks in the RDF plots for both ions interacting with Cs. H has a much broader and rounder peak than O. H has a FWHM around 1 Å whereas for O it is about 0.5 Å. Cs is a large ion and its size affects the structure of coordination with water. Essentially, O is the primary control of coordination of Cs with water whereas H is more disordered, so water Os are more correlated to Cs than the Hs. Looking at the following or second and third shells of water molecules, the increment between the peaks is approximately the size of a water molecule. As we move away from the first shell of water molecules, there is decreasing intensity and increasing disorder. The electrostatic control of Cs on the water molecules is lost as the *r* increases.

Next, consider how Cs is coordinated with the O in the clay structure in the two sites: ob and obts. The RDFs of the two Os show a preference for Cs to be closer to Os that are bonded to isomorphically substituted Al sites (obts) versus the Si-O-Si (ob) configuration (Figures 4-20 and 4-21). Due to the control by electrostatics, Al substitution is the preferred site for Cs (so Cs aligns with Al in the tetrahedral sheet). The obts sites are more prevalent in the mica section of the model versus the vermiculite areas of the model to account for the greater charge in this area of the clay structure. The obts sites are in the vermiculite structure as well, but the charge there is only -0.75 versus the -1.0 charge in the mica section. This shows that Cs prefers to be close to the wedge where there are more substituted Al sites. Additionally, due to the low hydration energy of Cs, the Cs would rather be on the clay surface than coordinated to water. So it is more likely to be in an inner-sphere coordination with the clay surface than hydrated by water in the interlayer.

Next, consider the interaction of K with waters in the interlayer. There are a smaller number of K atoms interacting with water molecules than in the case for Cs. A reason for this is that the K is only close enough to interact with water near the edges of the wedge. The majority of the K in the structure is within the mica section and is not coordinated with water at all. The total number of Cs:K in the model is 6:7 but the difference in the coordination potential with water is substantial. The RDF for K and H in water (h*) (Figure 4-22) has a very low *g(r)* for the first peak, only 1.25 and a broad hump. Only edge K can coordinate with water so there are less K atoms contributing to the RDF. Water O (o*) (Figure 4-23) has a higher *g(r)* of about 3.5 with K and a more narrow peak. So O in the water molecules is more likely to be associated with the K at the edge sites than H. As in the case with Cs, this is reasonable as the model is driven largely by electrostatic interaction and the negatively charged O in water molecules will be preferable than the positively charged Hs. The distribution of Os and Hs is also not as uniform as the Cs distribution as there are a lot of peaks; in the RDF patterns that are not significant. There is no consistency in the spacing of these peaks either. For K and H in water there exists a broad tail in the RDF at 10Å that is likely coordinating to Hs across the other side of the Cs-water lens, but the intensity remains below 1. The coordination of the Cs and K to the waters is driven by the hydration energies of Cs is 62.9 kcal/mol and K is 76.7 kcal/mol (*Ockwig et al*, 2007). The overall intensity of K RDFs with water is smaller than Cs only because again there are less occurrences of K to contribute to the RDF than Cs.

The RDFs for K with the Os in clay are similar to those of Cs. The K is strongly bound to the mica and does not migrate towards the vermiculite section of the model. This is in good agreement with K in mica being a good radiometric clock for K-Ar dating, as the K stays strongly within the structure (*Naumann et al*, 2012).

The K prefers the O in the obts site to the ob site by nearly 2:1 in the first shell of coordination. However, there are always ob near the K as there are more available in the structure. The second and third shells (peaks) in both RDFs are nearly the same in intensity, but the first peak is much more prominent and narrow in the obts case. Due to Al-O-Al avoidance principle, the mica model never has Al tetrahedral site next to another Al site as it would be a high energy deficit in the model. NMR data supports the idea that there would not be two Al sites together (*Kim et al.* 1996). So there can always be only 1 or 2 distributed Als in the modeled hexagonal ring.

Lastly, the RDF for Cs to K strongly reinforces the idea that Cs is moving towards the wedge zone in mica-vermiculite structure. There are 2000 structural snapshots contributing to each of the RDFs and showing that the Cs is rearranging to be closer to the K in the wedge zone than the center of the wedge where it was originally evenly dispersed. The peaks at r = 3.9, 4.5 and 5.8 Å demonstrate the migration of Cs towards the wedge (closer to K). Figure 4-27 is the RDF for the first nanosecond of the simulation for Cs and K. Comparing this to Figure 4-26 shows that over the course of the simulation, Cs is moving closer to K, i.e. into the wedge region of the model.

Ultimately, either the energy minimization or molecular dynamics simulations are supportive of the hypothesis that Cs is being sterically preferred in the interlayer wedge region.

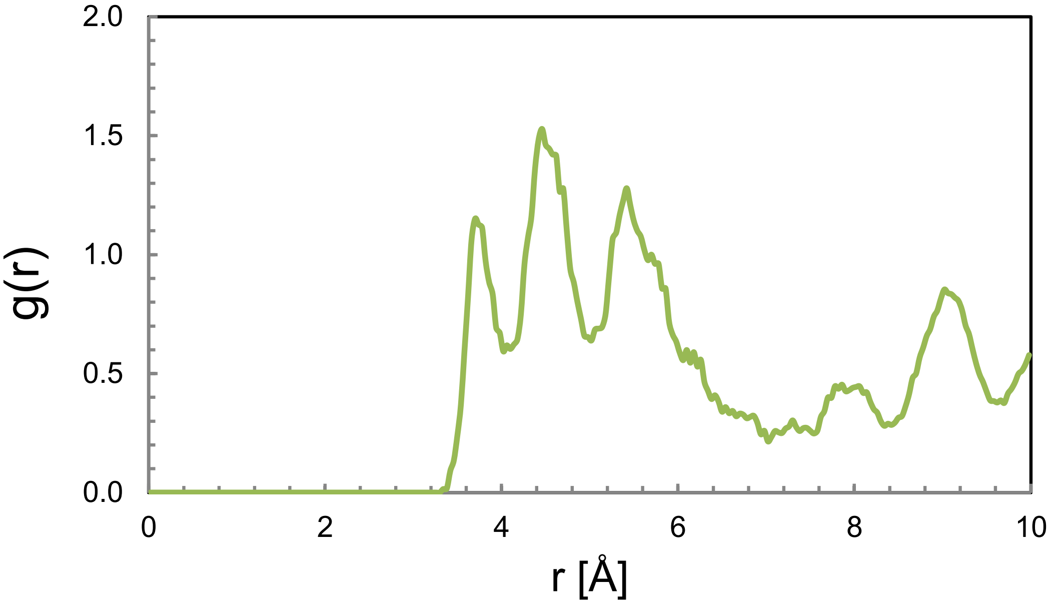

Figure 4-27: RDF for Cs-K of the first nanosecond of the simulation.

5 DISCUSSION

This project combines rigorous mineralogical characterization of soils with a contingent collection of chemical data analyses from these soils and state of the art molecular modeling of clays. Recent previous work by Wampler et al. (2012) shows the enrichment of Cs and Rb relative to K in a select group of SRS soils. The Wampler et al. (2012) argument is encapsulated in Figure 3-14 herein. A similar enrichment is seen from the data gathered in this dissertation where Cs and Rb are enriched relative to K for three soils whose weathering progression differed widely. These data permit a test of our hypotheses that (1) Cs has been favorably enriched with respect to K in the soils at the SRS as a result of long-term weathering processes and (2) that this Cs will negatively affect the ability of soils at the SRS to adsorb ^{137}Cs and (3) the interlayer wedge zones in highly weathered mica particles, now mostly HIV, have been responsible for selective uptake of Cs and Rb from soil solution and for their fixation.

Many studies have focused on frayed edge sites and Cs sorption (*Sawhney*, 1970; *Sawhney*, 1972*; Wauters et al.* 1994, *Brouwer et al.* 1983; *Zachara et al.* 2002) and the results of this study support these views. *Coleman et al*. (1963) found that soils with the greatest affinity for Cs contain HIV. *Rich and Black* (1964) show that deep within particles of HIV, wedge-shaped zones occur where the transition from the 14 Å vermiculite phase to a 10 Å mica phase during weathering narrows the interlayer space between the 2:1 layers. *Rich* (1964) goes on to show that hydrated monovalent cations are preferentially sorbed to these interlayer wedge sites; particularly Cs^+ as it is the most weakly hydrated simple ion. Similar selective behavior of monovalent cations occurs at frayed edge sites (where the structural layers are thought to splay outward from the 10 Å spacing) (*Brouwer et al.* 1983; *Zachara et al.* 2002). Thus, as weathering removes K and Cs from soils, Cs is retained in the interlayer-wedge zones more effectively than

K. In agreement with HIV wedge sites sorption, stable Cs has become significantly enriched (relative to K^+) in subsurface HIV particles as a result of chemical weathering processes in the SRS Fuquay soils.

This study brings a new approach to methods previously applied to SRS soils by looking at ion concentrations and mineral quantities in the depth profiles of soil cores. Other studies only examine soil samples from one depth (e.g. *Goto,* 2001; *Goto et al.* 2008a; *Goto et al.* 2008b; *Wampler et al.* 2012; *Naumann et al.* 2012), whereas my samples span soil horizons from three cores with progressive weathering stages. It should be noted that these studies are limited to the soil zone. HIV was not identified at much greater depths in the drill core SRS BGO 3A, though there is known to be contamination deep under the SRS. The effect of the simple ion exchange with ammonium acetate was minimal in terms of releasing sorbed Cs. However, the effect of 10 % nitric acid and 50% nitric acid extractions showed significant release of Cs and Rb and not K. From these data, weathering occurring in these soils is not thought to release significant amounts of Cs and Rb sorbed in these soils. In more highly weathered soils (FQ and FQTRS), only slightly more Cs, K, and Rb are released compared to FQQAL (Tables 3-5, 3-6).

In terms of pedogenic enrichment of Cs, and Rb relative to soil weathering progression, the total amounts of Cs and Rb relative to K are higher in the FQ, and FQTRS soils. When samples of these soils are leached, the Cs/K and Rb/K vary similarly with respect to type of acid extraction. The greatest enrichment is seen from the moderate 10% nitric acid extraction (Table 3-9) with a Cs/K ratio of 115 and Rb/K ratio of 24 in the FQ core. This large enrichment reflects a lesser release of K into the leach solution. The moderate 10% nitric acid extraction does not dissolve the mica mineral structure as much as the strong 50% nitric acid extraction (Figures 3-1 – 3-6).

The mineral results are consistent with previous work from the SRS (*Harris et al.* 1992; *Goto*, 2001) and are consistent with clay fractions of other highly weathered soils in the southeastern U.S. (*Weed and Nelson*, 1962; *Bryant and Dixon*, 1963; *Rich,* 1968; *Fiskell and Perkins*, 1970; *Barnhisel*, 1978; *Karathanasis et al.* 1983; *Elliott et al.* 1997). Knowing the soil mineralogy is insightful for understanding cation exchange capacity and soil pH, which in turn provide context for understanding sorption and release of anthropogenic metals in these soils. The mineralogy is relatively consistent within each core (intracore) but the mineralogy of each individual core is slightly different (intercore). In FQ, HIV is the likely phase sorbing Cs and Rb because it is the only mineral that has a significant CEC. The other cores FQTRS and FQQAL have HIV and illite, which has already been documented extensity as an effective adsorber of Cs within highly selective sites (i.e. wedge sites) (*Sawhney*, 1972; *Wampler et al.* 2012). The extent of enrichment of alkali metals in these soils appear to correlated with the extent of weathering of the soil rather than mineralogy of each core. The clay content for a given core may explain the sorption of high amounts of alkali metals (Cs, Rb) due to pedogenesis. Ultimately, while HIV was thought to be the most predominant mineral sorbing alkali metals during pedogenesis, the result of this study points to the clay content and soil maturity level as being important to explaining the enrichments of Cs and Rb in these soils. As these minerals weather in time and the ions are released back into soil solution, the Cs and Rb are sorbed by other surrounding mineral particles more selectively than K, resulting in this enrichment of the two ions. The slightly larger size and lower hydration energy of Cs makes it sterically the most favorable ion in the wedge sites of HIV and frayed edge sites of illite, with a slight advantage over Rb as well.

The application of a dynamical molecular model provides the potential to describe the nature of the attraction of Cs (and Rb) in the apex of the wedge site. A wedge site was produced by modeling a 10 Å mica core merging with a 14 Å vermiculite structure and was held as a rigid lattice construct, allowing mobility only to cations in interlayer positions. This forcing was needed otherwise water in the interlayer of the vermiculite portion of the model would proceed further into the mica structure and break apart the two layers, destroying the wedge structure. The nature of the bonding of Cs (and Rb) can be seen as an electrostatic attraction between the layers and these two monovalent cations in this wedge. Molecular modeling study here shows the Cs positioning itself in the apex of the wedge is plausible. The electrostatic configuration of the clay lattice attracts weakly hydrated minerals such as Cs (and Rb). The modeling is limited to the study of the wedge environment. The larger mica-HIV interlayer was not constructed in these preliminary modeling studies.

Cs-137 exchange experiments indicate that for sorption of ions on soils, both clay and silt size fractions should be considered to explain sorption of ^{137}Cs. In these soils, the silt size fraction was a small part of the overall mass, but for soils of different texture (particle size distribution), or a considerable amount of silt, minerals in that silt fraction should also be investigated for exchangeable ions on the surface. The acid extractions in this study were completed on the fine fraction (<62μm) so included metals removed from both silts and clays. To determine definitively how these metals are distributed among the size fractions, will require doing the extraction experiments on the clay size alone. Chemical treatments were conducted on the fine fraction of the soils as we assume the sand portion is not contributing to the sorption of metals. Informal microscope studies of the soil samples sand fraction could only identify quartz grains. These large sized grains have a low surface area to mass and do not provide much area for metals to be sorbed.

This research tests the hypotheses that: (1) Cs has been favorably enriched with respect to K in the soils at the SRS as a result of long-term weathering processes;

Clearly our first hypothesis has been shown to be supported by the data. The longer that a soil has undergone weathering at the SRS, the more enriched it has become in Cs (and Rb) with respect to K. The K is removed as weathering progresses, and Cs and Rb are preferentially retained in the soils (e.g. *Wampler et al.* 2012). As mica weathers, its structure changes with the removal of K, addition of hydrated exchangeable cations, and or oxidation of ferric iron into ferrous iron enabling the change from mica to vermiculite or smectite. Cs is gradually moving into fixed positions in the interlayers of micaceous particle with time (*Lomenick and Tamura*, 1965). Hydrated Al in the interlayer forms HIV (*Barnshisel and Bertsch*, 1989) and can limit the fixation of ^{137}Cs in the interlayer (*Maes et al.* 1999).

(2) That this Cs will negatively affect the ability of soils at the SRS to adsorb ^{137}Cs:

This study is important in that looking at how stable Cs is concentrated in soils allows us to extrapolate what the long term behavior of radiocesium may be in these soils. These soils have been concentrating minerals in a natural weathering environment over the course of thousands of years, and this type of long-term study could never be completed in a laboratory. Being able to predict the rate of movement of cesium (stable or radiocesium) in soil and ground water and how tightly it is bound to particles preventing its dispersion is beneficial for designing environmental remediation actions to control radionuclide contamination at the SRS. These data support the hypothesis that these soils will retain radiocesium for the duration necessary for the nuclide to decay. As the weathering of the soils progresses, the concentration of Cs remains the same (increase with respect to K) and from core to core comparison we see the Cs being retained over time. As these stable ions are concentrated to greater and greater extents, it is possible they may affect the sorption of radiocesium, as the highly selective Cs sites become saturated (*Wampler et al.* 2012).

(3) HIV is the major contributing mineral to the concentrating of alkali metals in the SRS soils at a unique wedge structure provides the appropriate environment for selective sorption of Cs:

Overall, this study does not completely support the work of Wampler et al. (2012). Though HIV is clearly contributing to the sorption of metals in the soils, it seems the progression of weathering of soils is a significant control for sorption of Cs in these soils in this study. The ^{137}Cs experiment gives credence to the theory that, contradictory to Wampler et al. (2012) that the HIV wedge zone is where the majority of amassing of Cs ions occurs, the other exchange sites are important and must be considered, including clay edges and fine silts. Thus, most of the K remaining in the SRS soils is bound in remnants of primary minerals where it has not yet participated in mineral-water reactions, most of the Rb and nearly all of the Cs are located elsewhere and likely have participated in mineral-water reactions within the soil. Acid extraction provides no information to pinpoint the mineral(s), or the microstructures within mineral grains, in which such Cs and Rb are located, but the Cs/K and Rb/K ratios in the extracts show that, somewhere within the soil, Cs and Rb have been retained much more effectively than K.

6 CONCLUSIONS

A vast amount of mineralogical and chemical data has been collected from three soils cores from the Savannah River Site in South Carolina. Stringent testing of these qualities in the soils in combination with a molecular model has allowed us to investigate the location and the steric environment where Cs ions are being concentrated within the clay structure of HIV. Ultimately, soil weathering stage is the major control of ion concentration in the soil cores, with mineralogy playing a secondary role. The following conclusions are derived from this study.

1) During soil formation, exchangeable K is removed as weathering progresses, and Cs and Rb are preferentially retained in the soils. Soil weathering state is a significant factor in explaining the sorption of Cs and Rb in these soils. The longer that a soil has undergone weathering at the SRS, the more enriched it has become in Cs (and Rb).
2) Molecular modeling results show that Cs (and Rb) can be sorbed effectively at the apex sites. The nature of bonding holding Cs (and Rb) in the apex is electrostatic attraction.
3) HIV is thought to be a significant phase in sorbing Cs. The ^{137}Cs experiments show edge and interlayer sites also contribute to sorbing Cs in these soils.

REFERENCES

Aadaland, R. K., Gellici, J. A., and Thayer, P. A. (1995). Hydrogeological framework of west-central South Carolina, *South Carolina Department of Natural Resources*, Water Resources Division Report 5, Columbia, South Carolina.

Anonymous, (2009), Water Report. Chapter 15: Savannah River Site. *Alliance for Nuclear Accountability.* PDF http://www.ananuclear.org/Portals/0/documents/Water%20Report/waterreportsavannahriver.pdf

Barnhisel, R. I., and Bertsch, P. M. (1989). Chlorites and hydroxy-interlayered vermiculite and smectite. *In Minerals in Soil Environments*, 2nd ed.; Dixon, J. B.; Weed, S. B., Eds.; Soil Science Society of America: Madison, WI, 729-788.

Bassett, W. A. (1960). Role of hydroxyl orientation in mica alteration. *Bulletin of the Geological Society of America*, 71, 449-56

Bish, D.L. and Post, J.E. (1993). Quantitative mineralogical analysis using the Rietveld full-pattern fitting method. *American Mineralogist*, 78, 932-940.

Bradbury M. H. and Baeyens B. (2000). A generalized sorption model for the concentration dependent uptake of caesium by argillaceous rocks. *Journal of Contamination Hydrology,* 42, 141-163.

Brouwer, E., Baeyens, B., Maes, A., and Cremers, A. (1983). Cesium and rubidium ion equilibria in illite clay. *Journal of Physical Chemistry*, 87, 1213−1219.

Bryant, J. P., and Dixon, J. B. (1963). Clay Mineralogy and weathering of red-yellow podzolic soil from quartz mica schist in the Alabama Piedmont. *Clays and Clay Mineralogy,* 12, 509-521.

Carlton, W. H., Bauer, L. R., Evans, A. G., Geary, L. A. , Murphy, Jr., C. E., Pinder, J. E., and Storm, R. N. (1996). Cesium in the Savannah River Site Environment, *Westinghouse Savannah River Company*, Savannah River Site, Aiken, S.C, 29808, 96.

Churchman, G.J., Whitton, J.S., Claridge, G.G.C., and Theng, B.K.G. (1984). Intercalation method using formamide for differentiating halloysite from kaolinite. *Clays and Clay Minerals*, 32, 241-249.

Clarke, J.S., and West, C. T. (1997). Ground-water levels, predevelopment ground-water flow, and stream-aquifer relations in the vicinity of the Savannah River Site, Georgia and South Carolina. *U.S. Geological Survey Water-Resources Investigations Report,* 97-4179, 120.

Coleman, N.T., Craig D. and Lewis R.J. (1963) Ion-exchange reactions of cesium. *Soil Science Society of America Proceedings,* 27, 287-289.

Comans, R. N. J., and Hockley, D. E. (1992). Kinetics of cesium sorption on illite. G*eochimica et Cosmochimica Acta*, 57, 1157–1164.

Cremers, A., Elsen, A., De Preter, P., and Maes, A. (1988). Quantitative analysis of radiocaesium retention in soils. *Nature*, 335, 247-249.

Cremers, A., Elsen, A., Valke, E., and Wauters, J. (1990). The sensitivity of upland soils to radiocesium contamination, in Desmet, G. Nassimbeni, P. Belli, M. ed. *Transfer of radionuclides in natural and semi-natural environment*, Elsevier Applied Science, Barking, UK, 238-248.

Cygan, R.T. (2001). Molecular modeling in Mineralogy and Geochemistry, in *Molecular Modeling Theory: Applications in the Geosciences,* Reviews in Mineralogy and Geochemistry, 42, 1-35.

Cygan, R.T., J. Liang, and Kalinichev, A. G. (2004). Molecular Models of Hydroxide, Oxyhydroxide, and Clay Phases and the Developments of a General Force Field, *Journal of Physical Chemistry,* 108, 1255-1266.

Cygan, R. T., Romanov, V. N., and Myshakin, E. M. (2012). Molecular Simulation of Carbon Dioxide Capture by Montmorillonite Using an Accurate and Flexible Force Field, *Journal of Physical Chemistry C*, 116, 13079−13091.

Dennehy, K.F., Prowell, D.C., and McMahon, P.B. (1989) Reconnaissance hydrogeologic investigation of the Defense Waste Processing Facility and vicinity, Savannah River Plant, South Carolina. *U.S. Geological Survey*, Water-Resources Investigations Report 88-4221.

Dolcater D. L., Lotse E. G., Syers J. K., and Jackson M. L. (1968). Cation exchange selectivity of some clay-sized minerals and soil materials. *Soil Science Society of America Proceedings,* 32, 795-798.

Downs, R. T. and Hall-Wallace, M. (2003). The *American Mineralogist* Crystal Structure Database, *American Mineralogist*, 88, 247-250.

Elliott, W. C., Savin, S. M., Dong, H., and Peacor, D. R. (1997). A paleoclimate interpretation derived from pedogenic clay minerals from the Piedmont province, Virginia. *Chemical Geology*, 142, 201-211.

Elprince, A. M., Rich, C. I., and Martens, D. C. (1977). Effect of temperature and hydroxy aluminum interlayers on the adsorption of trace radioactive cesium by sediments near water-cooled nuclear reactors. *Water Resources Research*, 13, 375-380.

Environmental Protection Agency. (1996) Method 3050B, Acid Digestion of sediments, sludges, and soils, *US Environmental Protection Agency*, http://www.epa.gov/wastes/hazard/testmethods/sw846/pdfs/3050b.pdf

Environmental Protection Agency (EPA). (1986). Cation-exchange capacity of soils (sodium acetate), Method 9081, *US Environmental Protection Agency*, wastes- hazardous waste – methods. 9000 series methods, http://www.epa.gov/osw/hazard/testmethods/sw846/online/9_series.htm

Evans, D. W., Alberts, J. J., and Clark, R. A. III (1983). Reversible ion exchange fixation of cesium-137 leading to mobilization from reservoir sediments. *Geochimica et Cosmochimica Acta*, 47, 1041−1049.

Fallaw, W.C., and Price, V. (1995) Stratigraphy of the Savannah River Site and vicinity. *Southeastern Geology*, **35**, 2.1-58.

Findley, M. (1998). Characterizing the environmental availability of trace metals in soils at the Savannah River Site. *M.S. thesis*, Clemson University, Clemson, South Carolina, USA.

Francis, C. W., and Brinkley, F. S. (1976). Preferential adsorption of ^{137}Cs to micaceous minerals in contaminated freshwater sediment. *Nature*, 260, 511-513.

Fiskell, J.G.A., and Perkins, H.F. (1970). Selected Coastal Plain soil properties. *Southern Cooperative Series Bulletins,* 148, University of Florida, Gainesville.

Goto, M. (2001) Development of a quantitative model for binding cesium to SRS soils. M.S. thesis, *Georgia Institute of Technology*, Atlanta, Georgia, USA.

Goto, M., Rosson, R., Wampler, J. M., Elliott, W. C., Serkiz, S., and Kahn, B. (2008a). Freundlich and dual Langmuir isotherm models for predicting ^{137}Cs binding on Savannah River Site soils. *Health Physics*, 94, 18-32.

Goto, M., Rosson, R., Wampler, J. M., Elliott, W. C., Kahn, B., and Serkiz, S. (2008b). A quantitative model for binding Cs-137 on SRS soil, *WSRC-STI-2008-00114*, Westinghouse Savannah River Company: Aiken, SC.

Greathouse, J. A., Cygan, R. T. (2005). Molecular dynamics simulation of uranyl (VI) sorption equilibria onto an external montmorillonite surface. *Physical Chemistry Chemical Physics,* 7, 3580-3586.

Greathouse, J. A. and Cygan, R. T. (2006). Water structure and aqueous uranyl(VI) adsorption equilibria onto external surfaces of Beidellite, Montmorillonite, and Pyrophyllite: Results from Molecular Simulations. *Environmental Science and Technology*, 40, 3865-3871.

Grogan, K. P., Jfeld, R. A., Kaplan, D. I., Shine, G. P., Devol, T. A., and J.C. Seaman, J.C. (2008). "Distribution of Sorption Coefficients (Kd Values) in the SRS Subsurface Environment," *WSRC-STI-00698, Washington Savannah River Company,* Aiken, SC.

Harris, W. G., Morrone, A. A., and Coleman, S. E. (1992). Occluded mica in hydroxy-interlayered vermiculite grains from a highly-weathered soil. *Clays and Clay Minerals*, 40, 32-39.

Harris, M. K., Thayer, P. A., and Amidon, M.B. (1997). Sedimentology and depositional environments of middle Eocene terrigenous-carbonate strata, southeastern Atlantic Coastal Plain, USA. *Sedimentary Geology*, 108, 141-161.

Hinton, T. G., Knox, A., and Kaplan, D. (2002). Field Deployment of Illite Clay as an in situ Method for Remediating *137*Cs Contaminated Wetlands, *Westinghouse Savannah River Company*, Savannah River Site, Aiken, SC 29808.

Jackson, M.L. (1963). Interlayering of expansible layer silicates in soils by chemical weathering. *Clays and Clay Minerals*, 11, 29-46.

Jackson, M.L. (1969) Soil Chemical Analysis Advanced Course (2nd edition). University of Wisconsin, Madison.

Jacobs, D.G. (1960). Sorption of Cesium by Conasauga Shale. *Health Physics*, October 1960, 4 (2), 157-163.

Jacobs, D.G. and Tamura, T. (1961). The mechanism of ion fixation using radio-isotope techniques, *Transactions of the 7th International Congress of Soil Sciences, II*. Madison, Wisconsin, 206-214.

Karathanasis, A.D., Adams, F., and Hajek, B.F. (1983). Stability Relationships in Kaolinite, Gibbsite, and Al-hydroxyinterlayered Vermiculite Soil Systems. *Soil Science Society of America Journal*, 47, 1247-1251.

Kaplan, D.I., Bertsch, P.M., and Adriano, D.C. (1997) Mineralogical and physicochemical differences between mobile and nonmobile colloidal phases in reconstructed pedons. *Soil Science Society of America Journal*, 61, 641–649.

Kim, Y., Cygan, R. T., and Kirkpatrick, J. R. (1996). ^{133}Cs NMR and XPS investigation of cesium adsorbed on clay minerals and related phases. *Geochimica et Cosmochimica Acta,* 60 (6), 1041- 1052.

Lande J, Webb SM, Mehta A. (2007). Area Diffraction Machine 1.0. Software [Available online]. http://groups.google.com.ezproxy2.library.arizona.edu/group/ area-diffraction-machine.

Lanning, A. (2012). "XRD mineralogical analysis of the fine silt fraction of soils from the Savannah River Site, SC." Undergraduate Geosciences thesis, *Georgia State University*, Atlanta, GA.

Leonard, R. A., and Weed, S. B. (1970). Mica weathering rates as related to mica type and composition. *Clays & Clay Minerals*, 18, 187-195.

Lieser, K. H., and Steinkopff, T. (1989). Sorption Equilibria of Radionuclides or Trace Elements in Multicomponent Systems. *Radiochimica Acta*, 47, 55-61.

Lomenick, T. F., and Tamura, T. (1965). Naturally occurring fixation of cesium-137 on sediments of lacustrine origin. *Soil Science Society American Proceedings*, 25, 383-387.

Looney, B.B., Eddy, C.A., Ramdeen, M., Pickett, J., Rogers, V., Scott, M.T., and Shirley, P.A. (1990) Geochemical and physical properties of soils and shallow sediments at the Savannah River Site. WSRC-RP-90-1031, *Westinghouse Savannah River Company*, Aiken, South Carolina, USA.

Maes E., Vielvoye L., Stone W., and Delvaux B. (1999). Fixation of radiocaesium traces in a weathering sequence mica → vermiculite → hydroxy interlayered vermiculite. *European Journal of Soil Science*, 50, 107-115.

McBride, M.B. (1994). Environmental chemistry of soils. *Oxford University Press*, New York.

Moore, D. M., and R. C. Reynolds, Jr. (1997). X-Ray Diffraction and the Identification and Analysis of Clay Minerals (2nd edition). *Oxford University Press*, New York, New York

Mosser-Ruck, R., Devineau, K., Charpentier, D., and Cathelineau, M. (2005). Effects of Ethylene Glycol Saturation Protocols on XRD Patterns: A Critical review and discussion. *Clays and Clay Minerals*, 53 (6), 631-638.

Naumann, Thomas E., (2010). "K-Ar Age Values of Bulk Soil Samples and Clay Fractions: Effects of Acid Extraction and Implications for the Origin of Micaceous Clay in Savannah River Site Soils, South Caroline, USA". Geosciences Theses. Paper 27. http://digitalarchive.gsu.edu/geosciences_theses/27

Naumann, T.E., Elliott, W.C., and Wampler, J.M. (2012). K-Ar age Constraints on the origin of micaeous clays in the Savannah River Site Soils, South Carolina. *Clays and Clay Minerals*. v. 60. 495-505. DOI: 10.1346/CCMN.2012.0600506

Ockwig, N. W., Greathouse, J. A., Durkin, J. S., Cygan, R. T., Daemen, L. L., and Nenoff, T. M. (2009). Nanoconfined water in magnesium-rich 2:1 phyllosilicates. *Journal of the American Chemical Society,* 131, 8155−8162.

Ohtaki, H. and Radnai, T. (1993). Structure and dynamics of hydrated ions. *Chemical Reviews*, 93, 1157-1204.

Pauling, L. (1930). The structure of the micas and related minerals. *Proceedings of the National Academy of Science, USA*, 16, 123-129.

Perdrial, N., Rivera, N., Thompson, A., O'Day, P. A., and Chorover, J. (2011). Trace contaminant concentration affects mineral transformation and pollutant fate in hydroxide-weathered Hanford sediments. *Journal of Hazardous Materials,* 197, 119-127

Plimpton, S. (1995). Fast Parallel Algorithms for Short-Range Molecular Dynamics, *Journal of Computational Physics*, 117, 1-19.

Poinssot, C., Baeyens, B., and Bradbury, M. H. (1999). Experimental and modelling studies of caesium sorption on illite, *Geochimica et Cosmochimica Acta*, 63 (19-20), 3217-3227.

Prowell, D.C. (1996). Geologic map of the Savannah River Site, Aiken, Allendale, and Barnwell Counties, South Carolina: U.S. Geological Survey Miscellaneous Field Studies Map MF-2300, 7 p. pamphlet, 1 sheet, scale 1:48,000.

Rietveld, H.M. (1969). A profile refinement method for nuclear and magneticstructures. *Journal of Applied Crystallography,* 2, 65–71.

Rich, C.I. (1964) Effect of cation size and pH on potassium exchange in Nason soil. *Soil Science,* 98, 100-106.

Rich, C.I. (1968). Hydroxy interlayers in expansible layer silicates. *Clays and Clay Mineralogy,* 16, 15-30.

Rich, C. I., and Black, W. R. (1964). Potassium exchange as affected by cation size, pH, and mineral structure. *Soil Science*, 97, 384-390.

Rogers, V.A. (1990). Soil Survey of Savannah River Plant Area, Parts of Aiken, Barnwell, and Allendale Counties, South Carolina, United States Department of Agriculture, *Soil Conservation Service*, Aiken, South Carolina.

Romanov, V., Ackman, T. E., Soong, Y., and Kleinman, R.L. (2009). CO_2 Storage in Shallow Underground and Surface Coal Mines: Challenges and Opportunities, *Environmental Science & Technology*, 43 (3), 561-564. DOI: 10.1021/es801730v

Rudnick, R.L. and Gao, S., (2004), Composition of the continental crust, pp. 1-64 in The Crust (ed. R.L. Rudnick), Vol. 3, *Treatise on Geochemistry (eds. H.D. Holland and K.K. Turekian)*, Elsevier-Pergamon.

Sawhney B. L. (1964). Sorption and fixation of microquantities of cesium by clay minerals: effect of saturating cations. *Proceedings - Soil Science Society of America,* **28**, 183–186.

Sawhney B. L. (1965). Sorption of cesium from dilute solutions. *Soil Science Society of America Proceedings.* 29, 25–28.

Sawhney B. L. (1966). Kinetics of cesium sorption by clay minerals. *Soil Science Society of America Proceedings,* 30, 565–569.

Sawhney B. L. (1970). Potassium and cesium ion selectivity in relation to clay mineral structure. *Clays and Clay Mineral,* 18, 47–52.

Sawhney, B. L. (1972). Selective sorption and fixation of cations by clay minerals: a review. *Clays and Clay Minerals*, 20, 93–100.

Sawhney, B.L., and Voigt, G.K. (1969). Chemical and biological weathering in vermiculite from Transvaal: *Proceedings - Soil Science Society of America* 33, 625–629.

Schroeder, D. (1974) Relationships between soil potassium and the potassium nutrition of the plant. In: Potassium research and agricultural production: *International Potash Institute, Berne,* 56–63.

Schulz R.K., Overstreet R. and Barshad I. (1960). On the soil chemistry of cesium 137. *Soil Science*, 89, 19-27.

Simpson, A. (2012) Determination of the CEC of SRS soils and the effectiveness of the EPA Model 9081 for CEC of acidic soils." Undergraduate Geosciences thesis, *Georgia State University*, Atlanta, GA.

Spark, K. M., Wells, J. D., and Johnson, B. B. (1995) Characterising trace metal adsorption of kaolinite. *European Journal of Soil Science,* 46, 633.

Stanford Synchrotron Radiation Lightsource (SSRL). (2011). Experimental Station 11-3. January 28, 2011. http://www-ssrl.slac.stanford.edu/beamlines/bl11-3/

Teich-McGoldrick, S, L., Greathouse, J.A., and Cygan, R,T, (2012). Molecular Dynamics Simulations of Structural and Mechanical Properties of Muscovite: Pressure and Temperature Effects. *Journal of Physical Chemistry C*, 116, 15099−15107.

Tamura, T. and Jacobs, D.G. (1960). Structural implications in cesium sorption. *Health Physics*, 2, 391- 398.

Thiry, Y., Gommers, A., Iserentant, A., and Delvaux, B., (2005). Rhizospheric Mobilization and Plant Uptake of Radiocesium from Weathered Micas: II. Influence of Mineral Alterability*, Journal of Environmental Quality* 34, 2174-2180.

Tossell, J. A. (1993). A theoretical study of the molecular basis of the Al avoidance rule and of the spectral characteristics of AI-O-Al linkages. *American Mineralogist*, 78, 911-920.

Vasconcelos, I. F., Bunker, B. A., and Cygan, R. T. (2007). Molecular Dynamics Modeling of Ion Adsorption to the Basal Surfaces of Kaolinite. *Journal of Physical Chemistry C*, 111, 6753-6762.

Wampler, M., Krogstad, E. J., Elliott, W. C., Kahn, B., and Kaplan, D. I. (2012). Long-term Selective Retention of Natural Cs and Rb by Highly Weathered Coastal Plain Soils. *Environmental Science and Technology*, 46, 3837-3843.

Wauters, J., Sweeck, L., Valcke, E., Elsen, A., and Cremers, A. (1994). Availability of Radiocaesium in Soils: A New Methodology. *The Science of the Total Environment*, 157, 239-248.

Weed, S.B., and Nelson, L.A. (1962). Occurence of chlorite like intergrade clay minerals in Coastal Plains, Piedmont, and Mountains soils of North Carolina. *Proceedings - Soil Science Society of America*, 26, 393-398.

Wyatt, D.E., and Harris, M. K. (2004). Overview of the history and geology of the Savannah River Site, *Environmental Geosciences*, 11 (4), 181-190.

Zachara, J. M., Smith, S. C., Liu C., McKinley, J. P., Serne, R. J., and Gassman, P. L. (2002). Sorption of Cs+ to micaceous subsurface sediments from the Hanford site, USA. *Geochimica et Cosmochimica Acta,* 66, 193-211.

Zhao, Q. and Burns, S. E. (2012). Molecular Dynamics Simulation of Secondary Sorption Behavior of Montmorillonite Modified by Single Chain Quaternary Ammonium Cations. *Environmental Science and Technology*, *46* (7), 3999–4007.

APPENDICES

Appendix A: SRS Soil Colors

Table A-1: SRS Soil Color properties from dry samples

Sample	Hue	Chroma	Value	Comments
TRS 0-15	2.5 Y	2	5	Organic material present
TRS 16-31	2.5 Y	3	6	
TRS 32-46	2.5 Y	3	6	
TRS 47-61	2.5 Y	3	6	
TRS 62-76	10 YR	4	5	Color change to more red
TRS 77-89	10 YR	4	5	Color change to more red
QAL 0-15	2.5 YR	2	4	
QAL 16-28	2.5 YR	2	6	Lighter color
QAL 29-38	7.5 YR	4	5	Gray- brown outside with red-orange inside of the aggregates
QAL 39-46	7.5 YR	6	5	
QAL 47-61	5 YR	6	5	
QAL 62-76	5 YR	6	5	Yellow and red lumps
QAL 77-84	7.5 YR	6	5	
QAL 85-91	7.5 YR	6	5	
QAL 92-104	7.5 YR	6	5	Yellow clay lumps

Appendix B: Mineralogy XRD Patterns

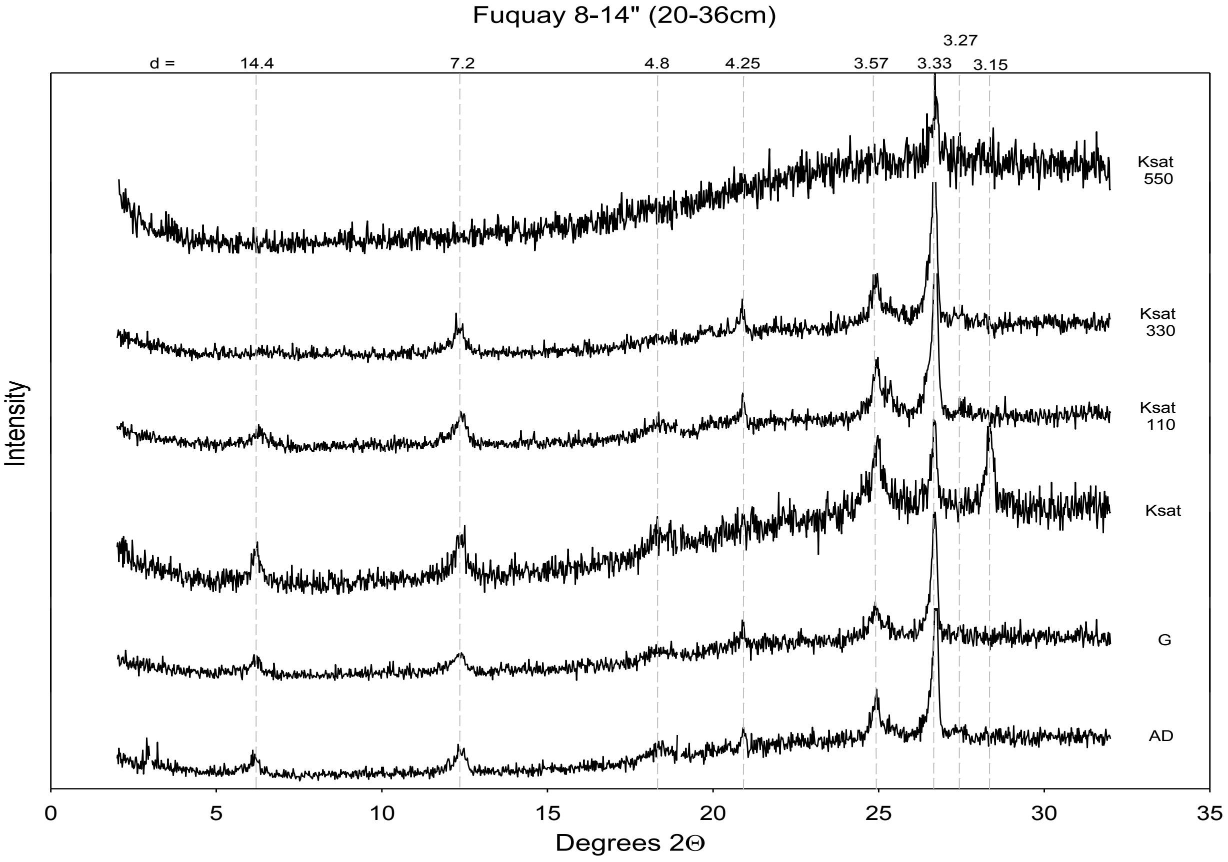

Figure B1: XRD of Fuquay surface soil sample depths 20-36 cm, AD = Air dried, G=Glycol, Ksat = K-saturation, Ksat110= K-saturation and heated to 110°C, Ksat330 = K-saturation at 330°C, and Ksat550 = K-saturation at 550°C. Note the emergence of a KCl peak (3.15Å) after addition of KCl, and the disappearance of the kaolinite peak with heating (7.2Å and 3.57Å). HIV peak (14.4Å) slowly dissipates with heating and a slight collapse to smaller *d* value.

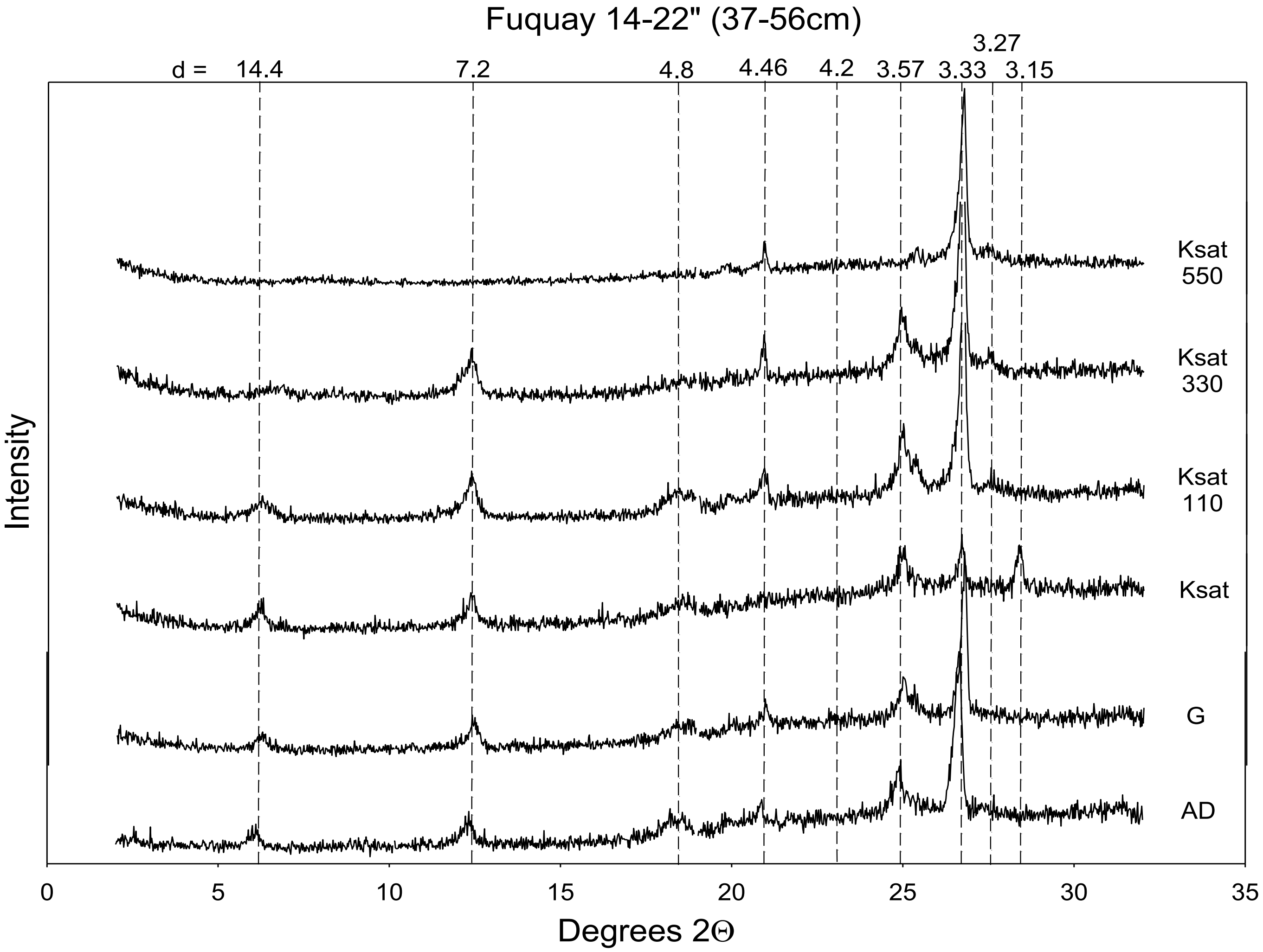

Figure B2: XRD of Fuquay surface soil sample depths 36-56 cm, AD = Air dried, G=Glycol, Ksat = K-saturation, Ksat110= K-saturation and heated to 110°C, Ksat330 = K-saturation at 330°C, and Ksat550 = K-saturation at 550°C. Note the emergence of a KCl peak (3.15Å) after addition of KCl, and the disappearance of the kaolinite peak with heating (7.2Å and 3.57Å). HIV peak (14.4Å) slowly dissipates with heating and a slight collapse to smaller *d* value. Here we also observe an *hkl* peak for phyllosilicates (4.46Å).

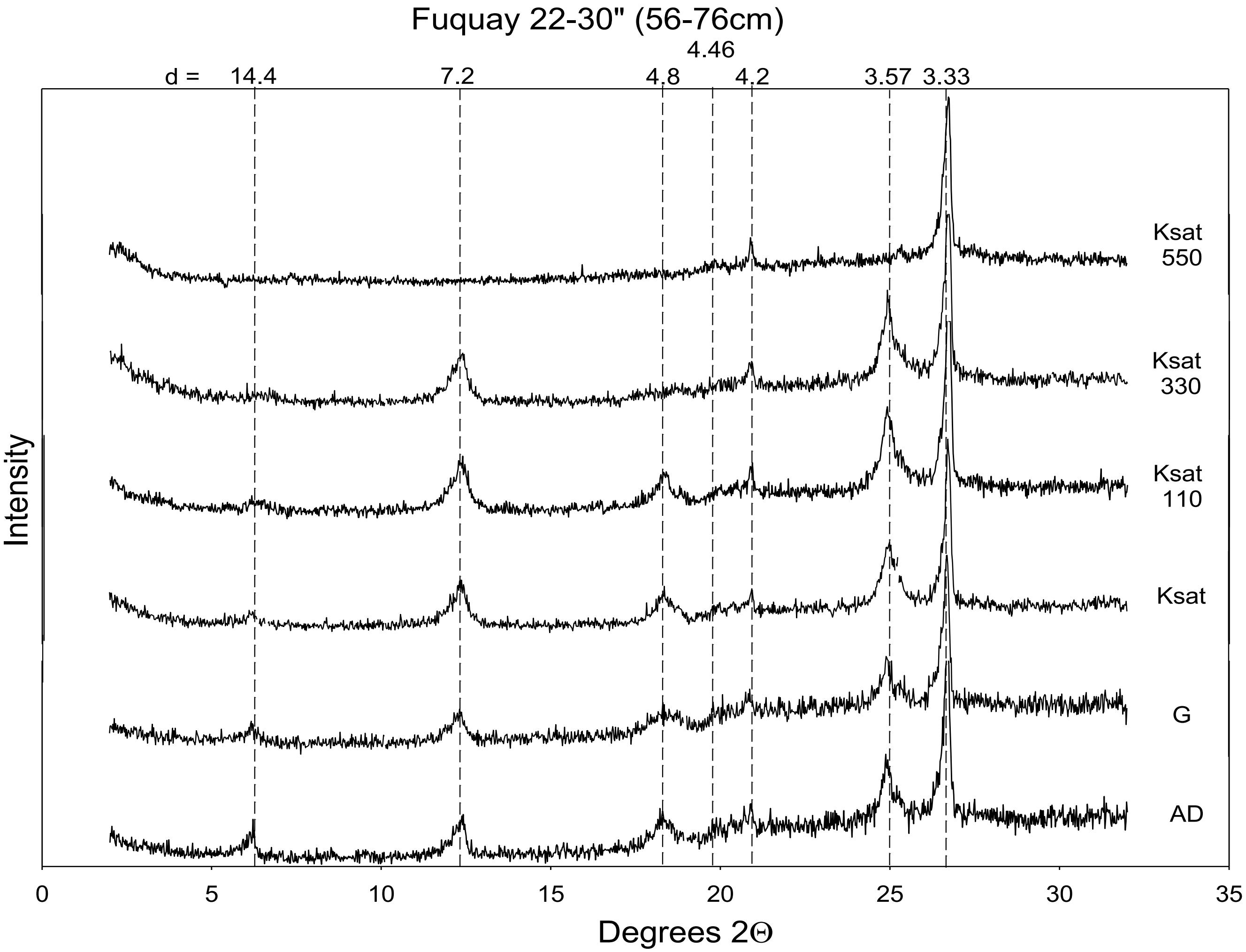

Figure B3: XRD of Fuquay surface soil sample depths 57-76 cm, AD = Air dried, G=Glycol, Ksat = K-saturation, Ksat110= K-saturation and heated to 110°C, Ksat330 = K-saturation at 330°C, and Ksat550 = K-saturation at 550°C. Note the disappearance of the kaolinite peak with heating (7.2Å and 3.57Å). HIV peak (14.4Å) slowly dissipates with heating and a slight collapse to smaller *d* value. Here we also observe an *hkl* peak for phyllosilicates (4.46Å).

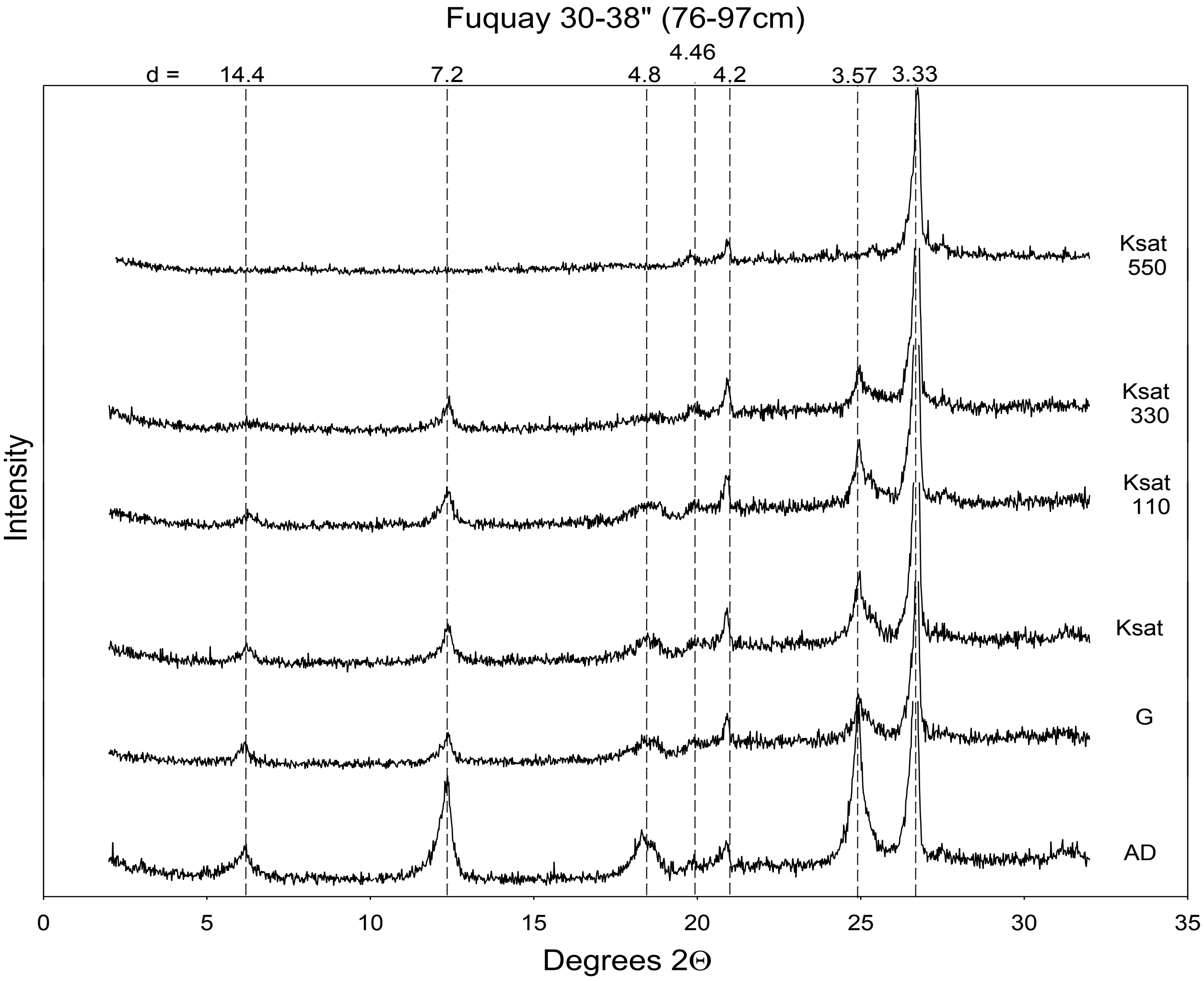

Figure B4: XRD of Fuquay surface soil sample depths 77-97 cm, AD = Air dried, G=Glycol, Ksat = K-saturation, Ksat110= K-saturation and heated to 110°C, Ksat330 = K-saturation at 330°C, and Ksat550 = K-saturation at 550°C. Note the disappearance of the kaolinite peak with heating (7.2Å and 3.57Å). HIV peak (14.4Å) slowly dissipates with heating and a slight collapse to smaller *d* value. Here we also observe an *hkl* peak for phyllosilicates (4.46Å).

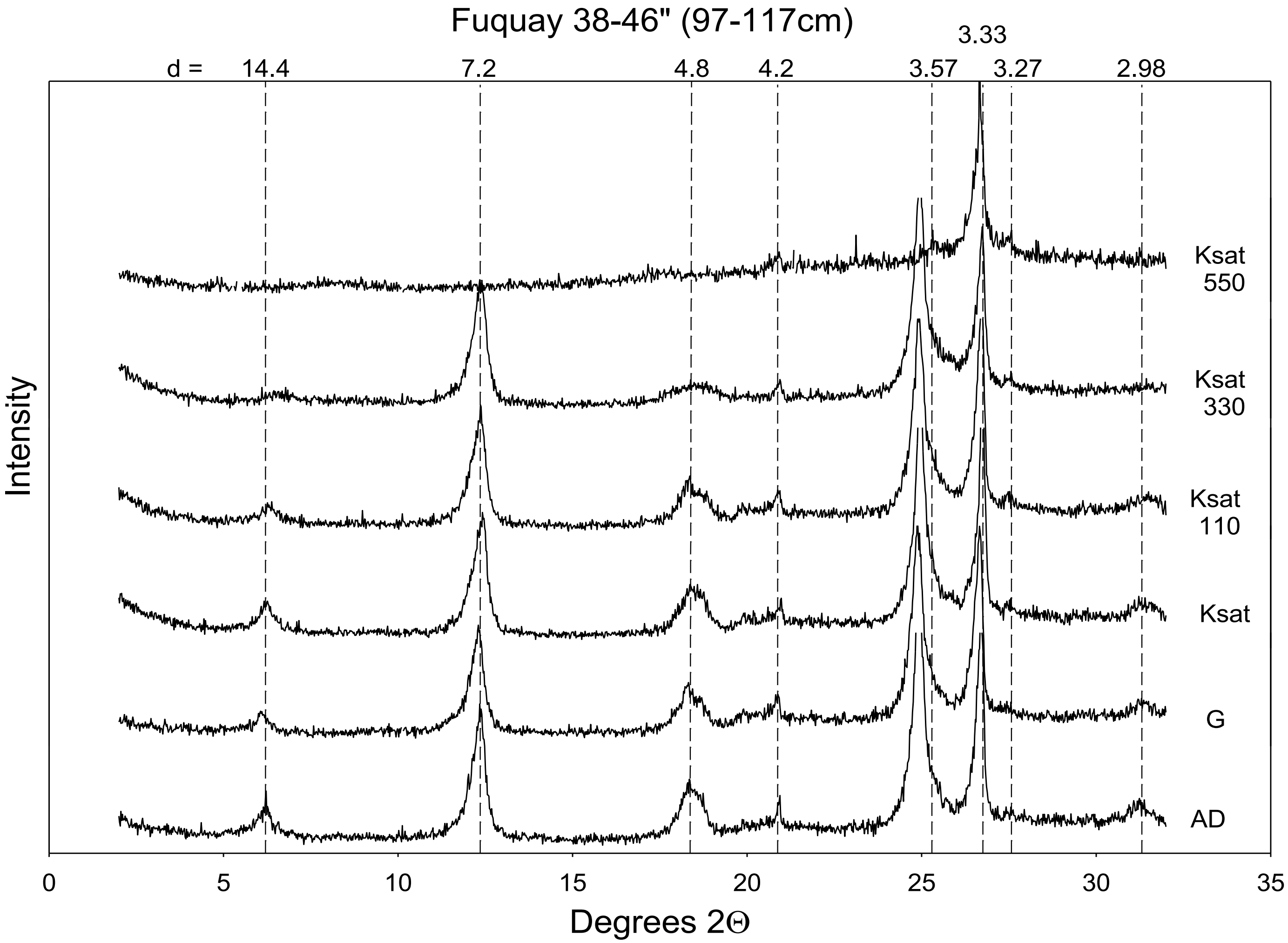

Figure B5: XRD of Fuquay surface soil sample depths 98-117 cm, AD = Air dried, G=Glycol, Ksat = K-saturation, Ksat110= K-saturation and heated to 110°C, Ksat330 = K-saturation at 330°C, and Ksat550 = K-saturation at 550°C. Note the disappearance of the kaolinite peak with heating (7.2Å and 3.57Å). HIV peak (14.4Å) slowly dissipates with heating and a slight collapse to smaller *d* value. Here we also observe an *hkl* peak for phyllosilicates (4.46Å).

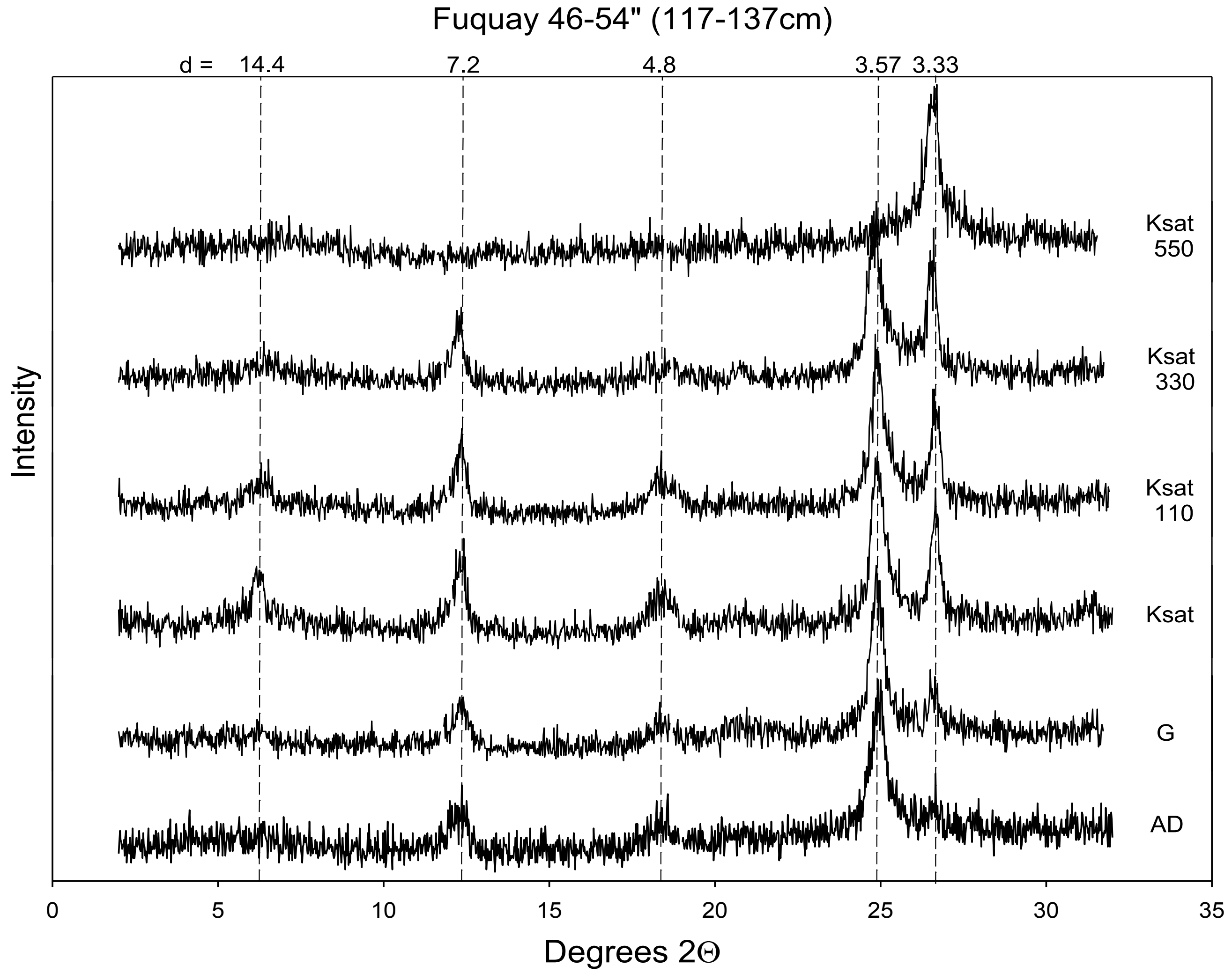

Figure B6: XRD of Fuquay surface soil sample depths 118-137 cm, AD = Air dried, G=Glycol, Ksat = K-saturation, Ksat110= K-saturation and heated to 110°C, Ksat330 = K-saturation at 330°C, and Ksat550 = K-saturation at 550°C. Note the disappearance of the kaolinite peak with heating (7.2Å and 3.57Å). HIV peak (14.4Å) slowly dissipates with heating and a slight collapse to smaller *d* value. Here we also observe an *hkl* peak for phyllosilicates (4.46Å).

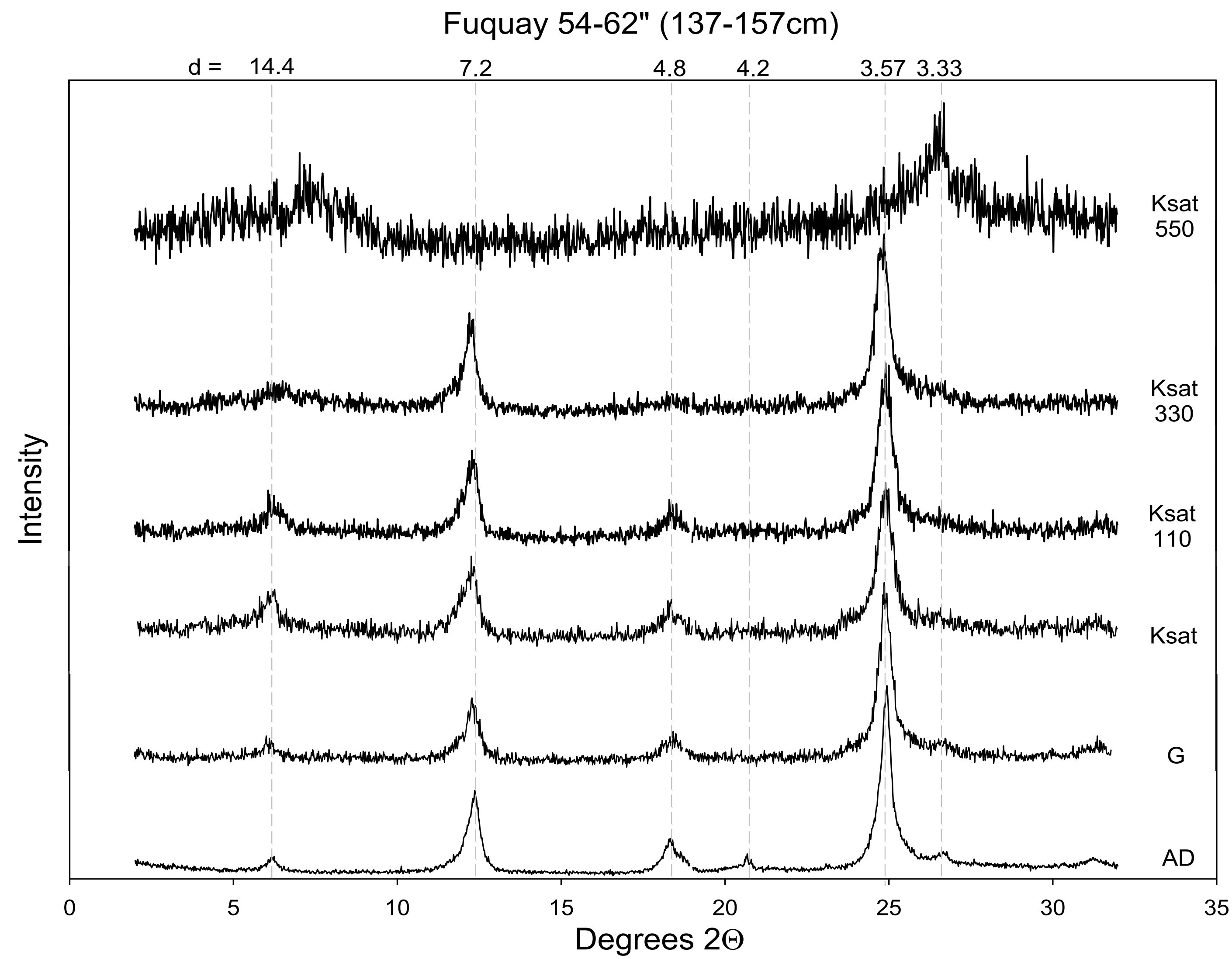

Figure B7: XRD of Fuquay surface soil sample depths 137-157 cm, AD = Air dried, G=Glycol, Ksat = K-saturation, Ksat110= K-saturation and heated to 110°C, Ksat330 = K-saturation at 330°C, and Ksat550 = K-saturation at 550°C Note that there is essentially no quartz peak here.

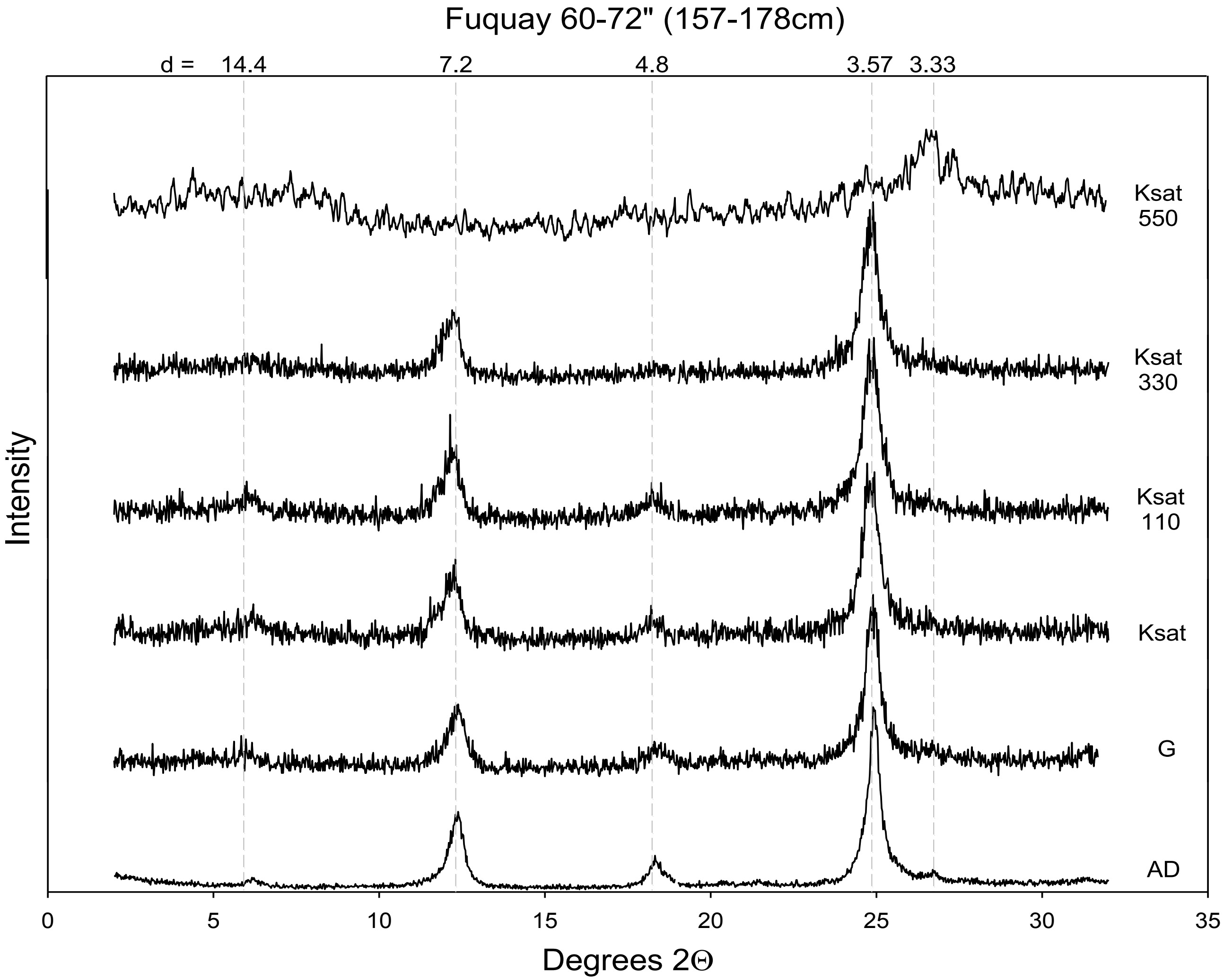

Figure B8: XRD of Fuquay surface soil sample depths 158-178 cm, AD = Air dried, G=Glycol, Ksat = K-saturation, Ksat110= K-saturation and heated to 110°C, Ksat330 = K-saturation at 330°C, and Ksat550 = K-saturation at 550°C. Note that there is essentially no quartz peak here. We see a very small quartz peak for the Ksat550 but intensity is extremely low and exaggerated.

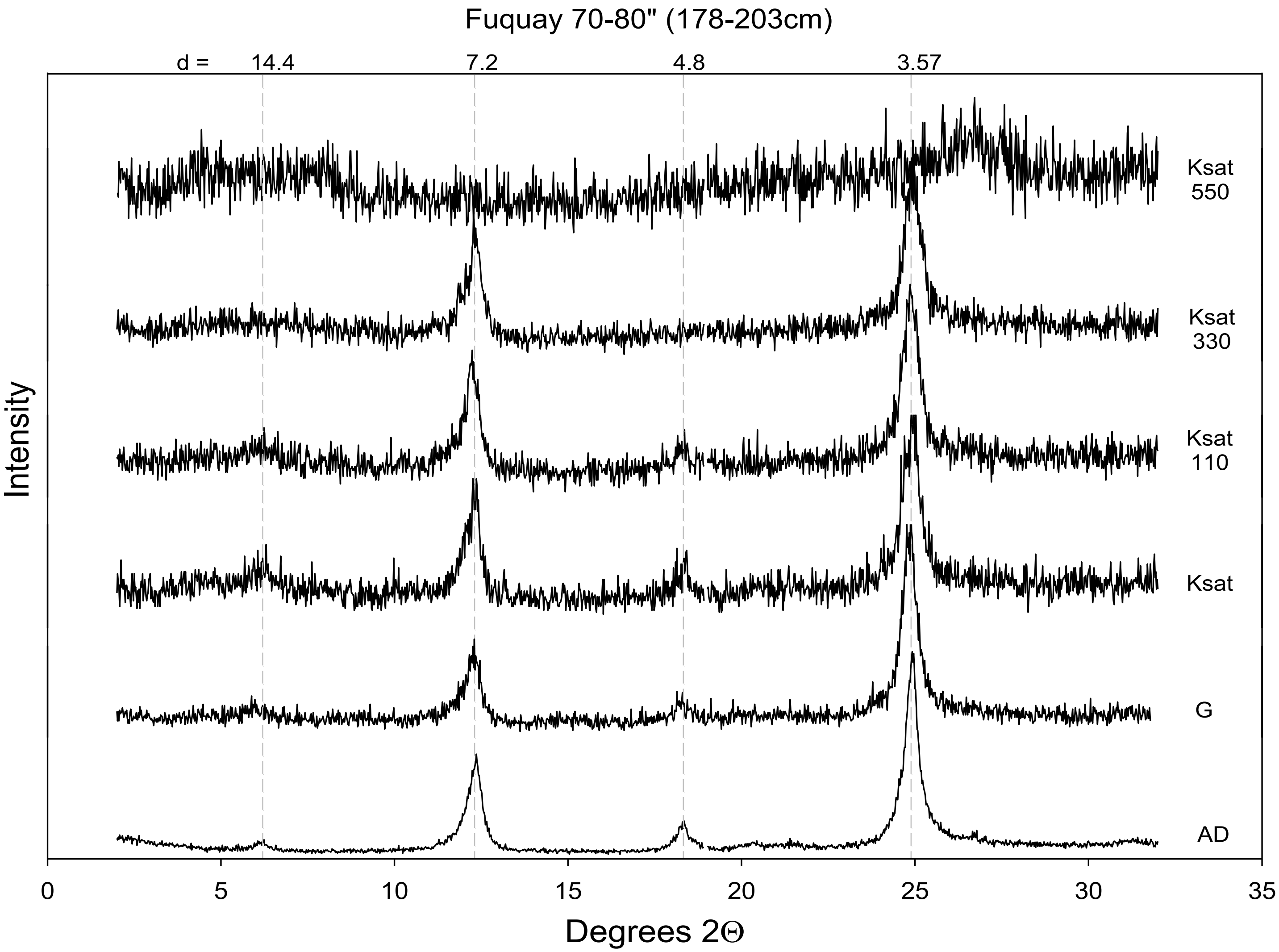

Figure B9: XRD of Fuquay surface soil sample depths 179-203 cm, AD = Air dried, G=Glycol, Ksat = K-saturation, Ksat110= K-saturation and heated to 110°C, Ksat330 = K-saturation at 330°C, and Ksat550 = K-saturation at 550°C. Note that there is essentially no quartz peak here.

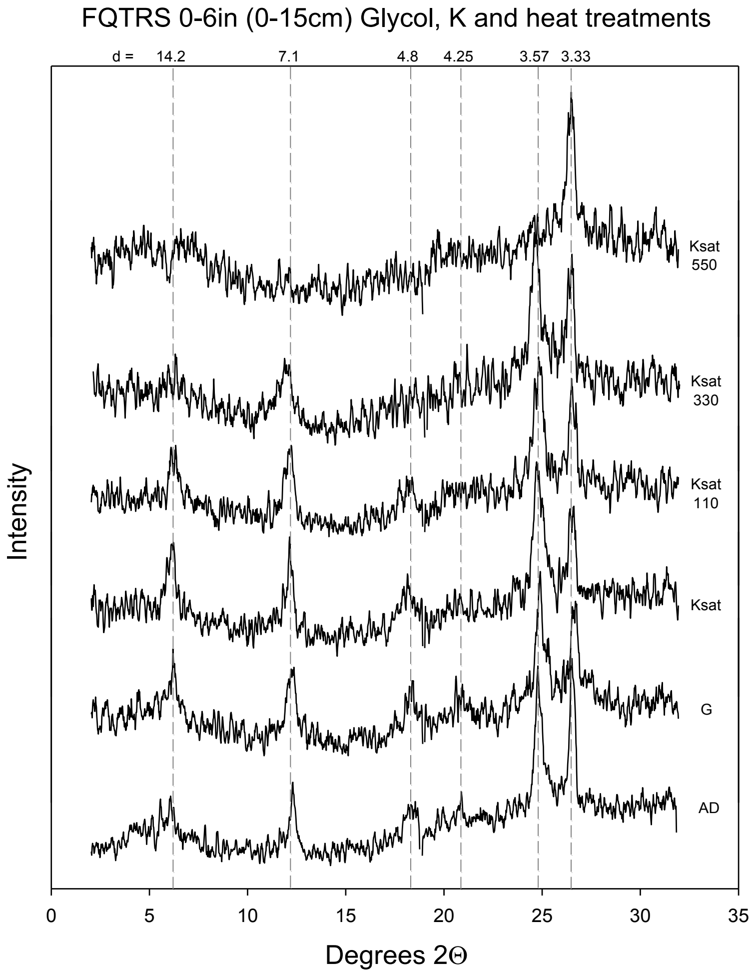

Figure B10: K treatments and glycol saturation of FQTRS 0-15 cm clay (<2µm). This pattern has had a 5 point running mean applied to reduce the noise as these were all low intensity and high noise patterns. The Kaolinite peaks collapse with K saturation and heating to 550C, and there is a slight collapse of the 14.4Å HIV peak.

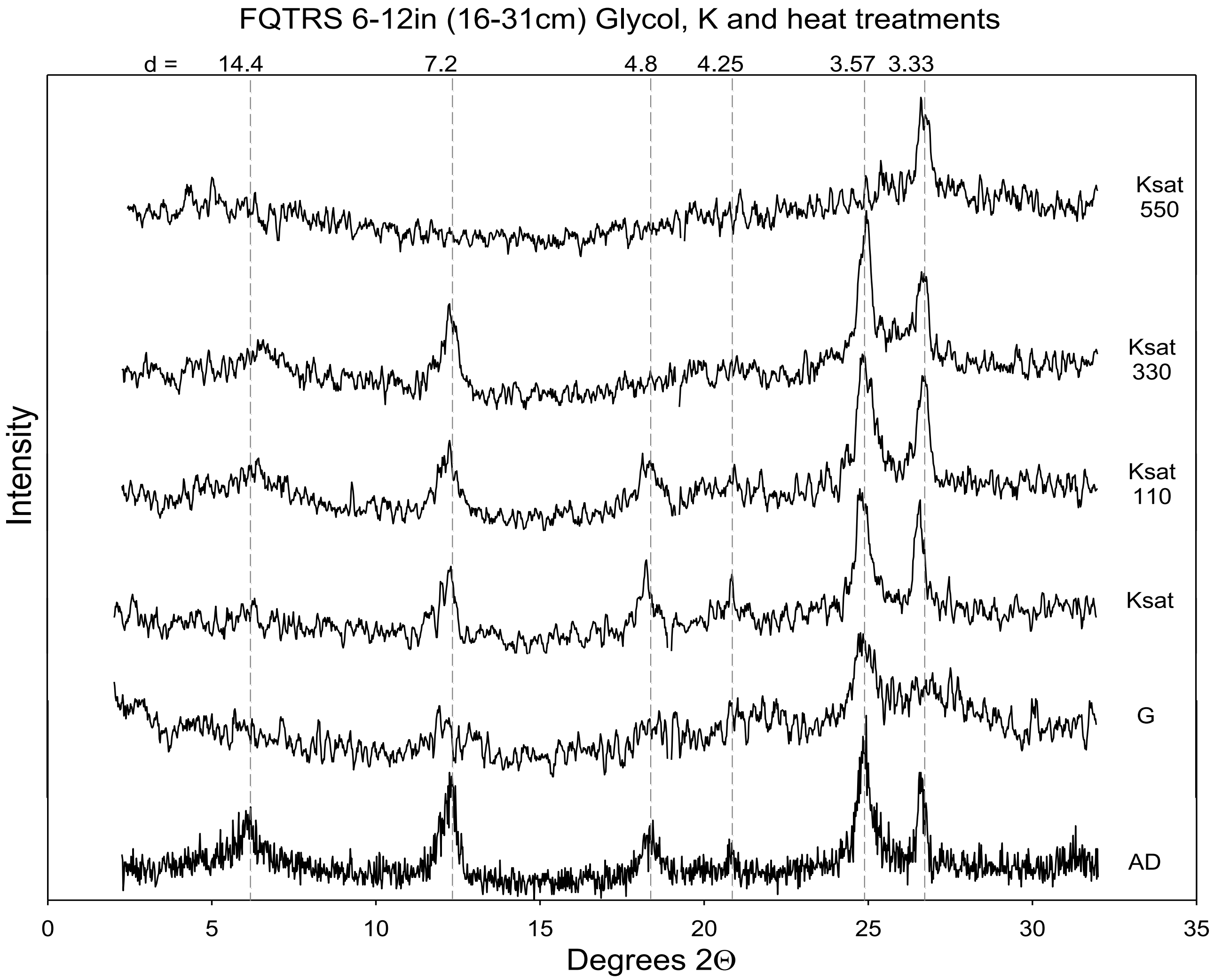

Figure B11: FQTRS 16-31 cm, glycol, K, and heat treatments of clay (<2µm). A 5-point smooth has been applied to this figure to remove noise from very low intensities on the XRD, with the exception of the AD sample.

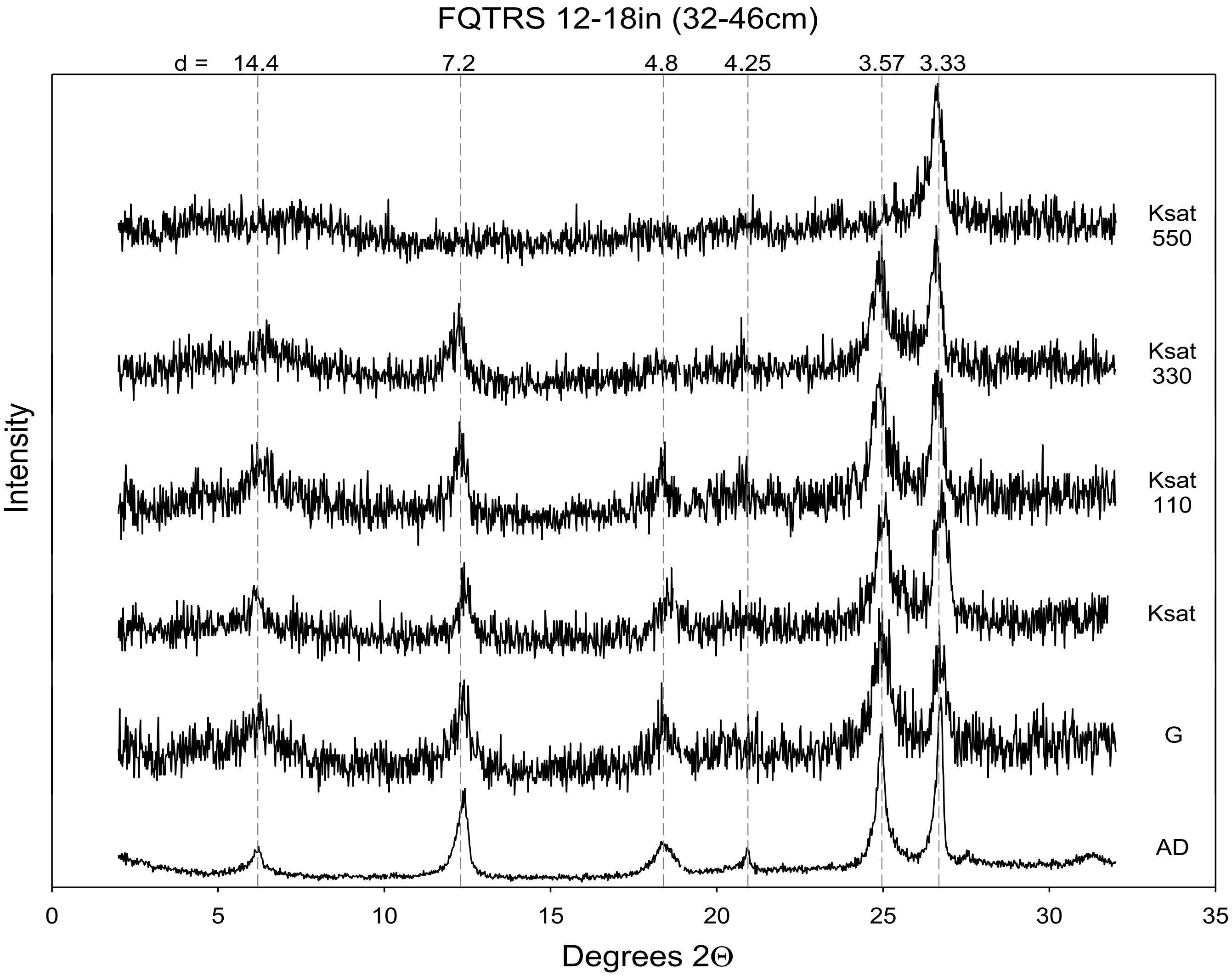

Figure B12: FQTRS 32-46 cm, glycol, K, and heat treatments of clay (<2μm). The Kaolinite peaks collapse with K saturation and heating to 550°C, and there is a collapse of the 14.4Å HIV peak.

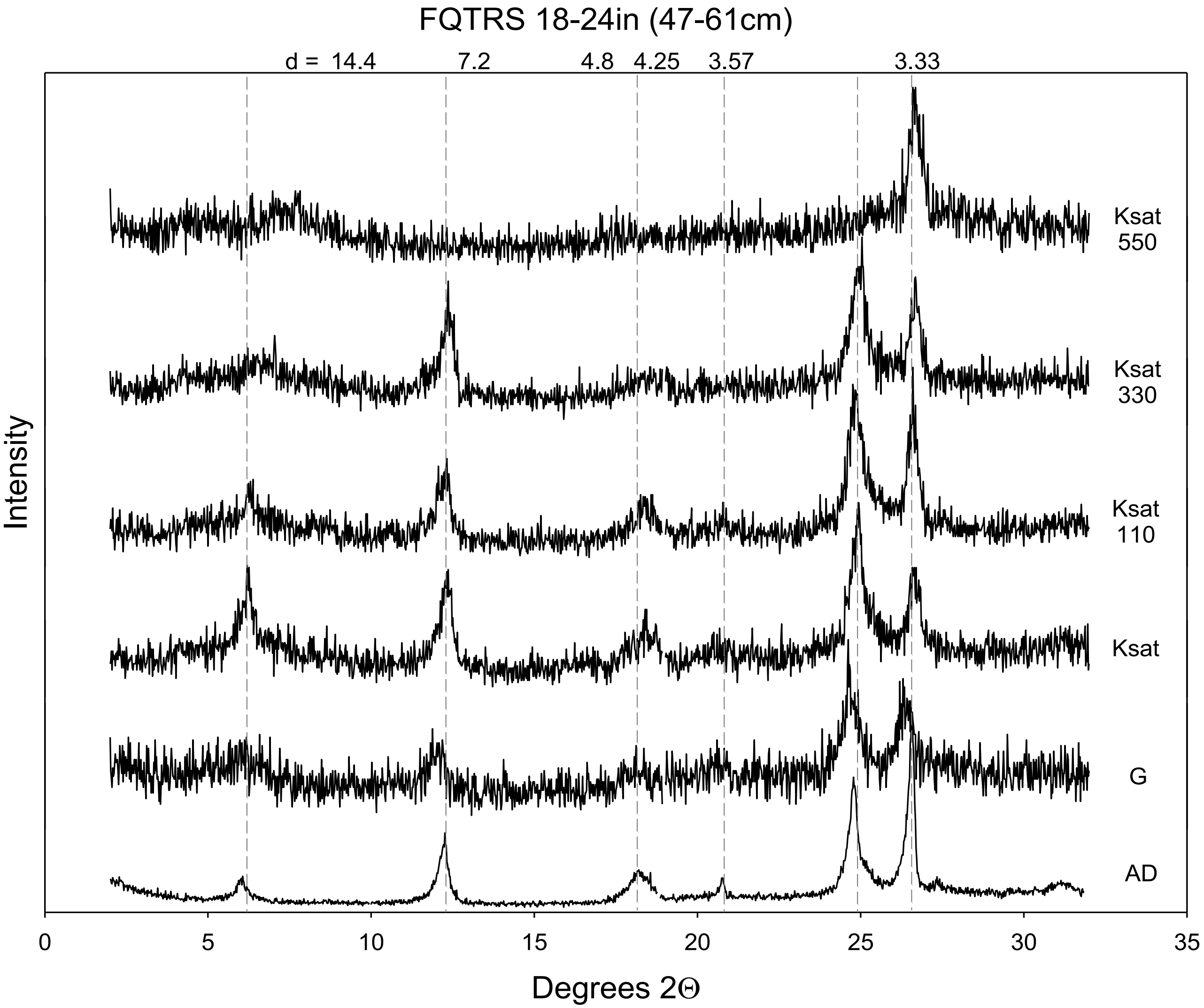

Figure B13 FQTRS 47-61 cm, glycol, K, and heat treatments. Note the collapse of the kaolinite peak with K and heat, and collapse and shift of the HIV peak.

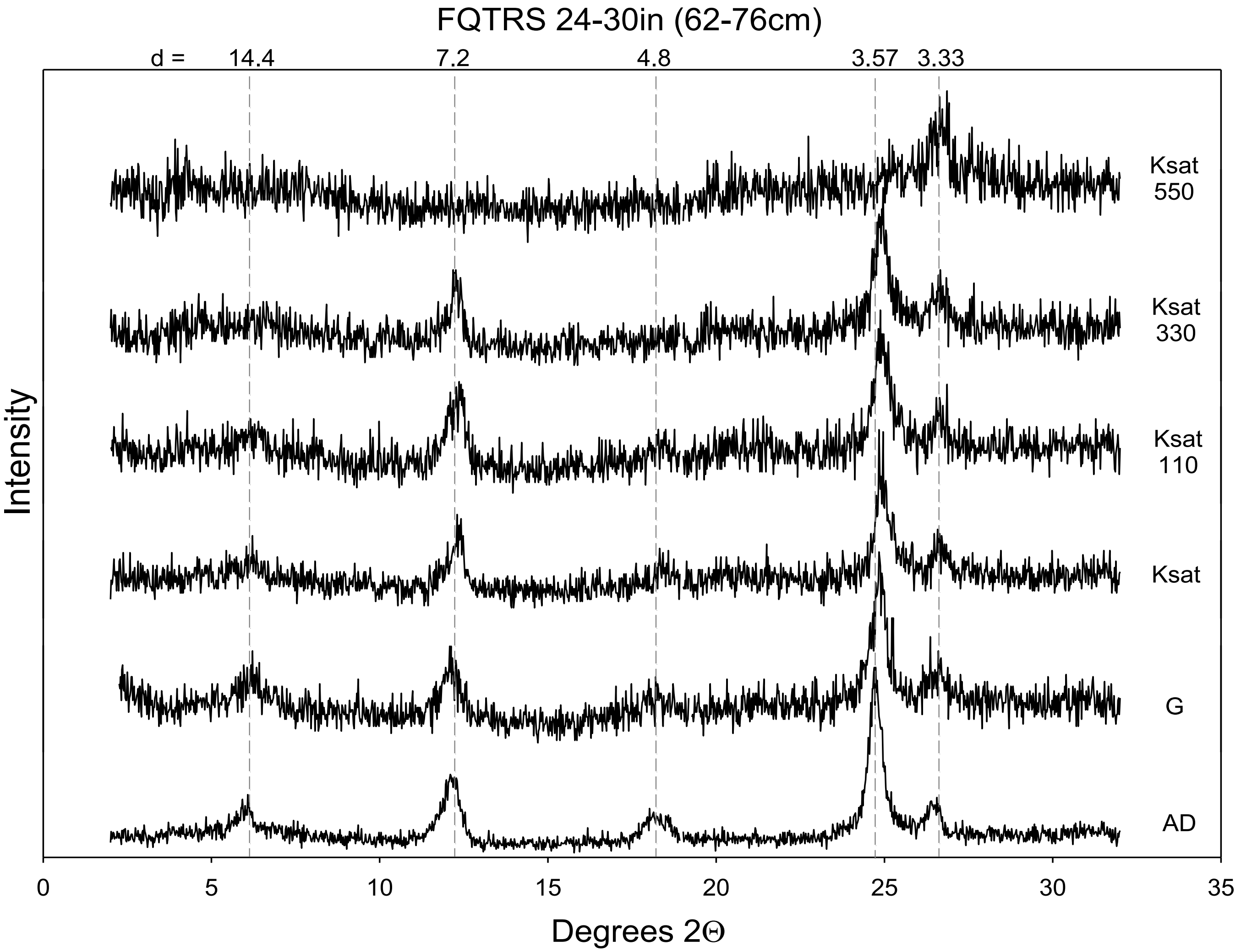

Figure B14: FQTRS 62-76 cm, glycol, K, and heat treatments. Note the collapse of the kaolinite peak with K and heat, and collapse and shift of the HIV peak.

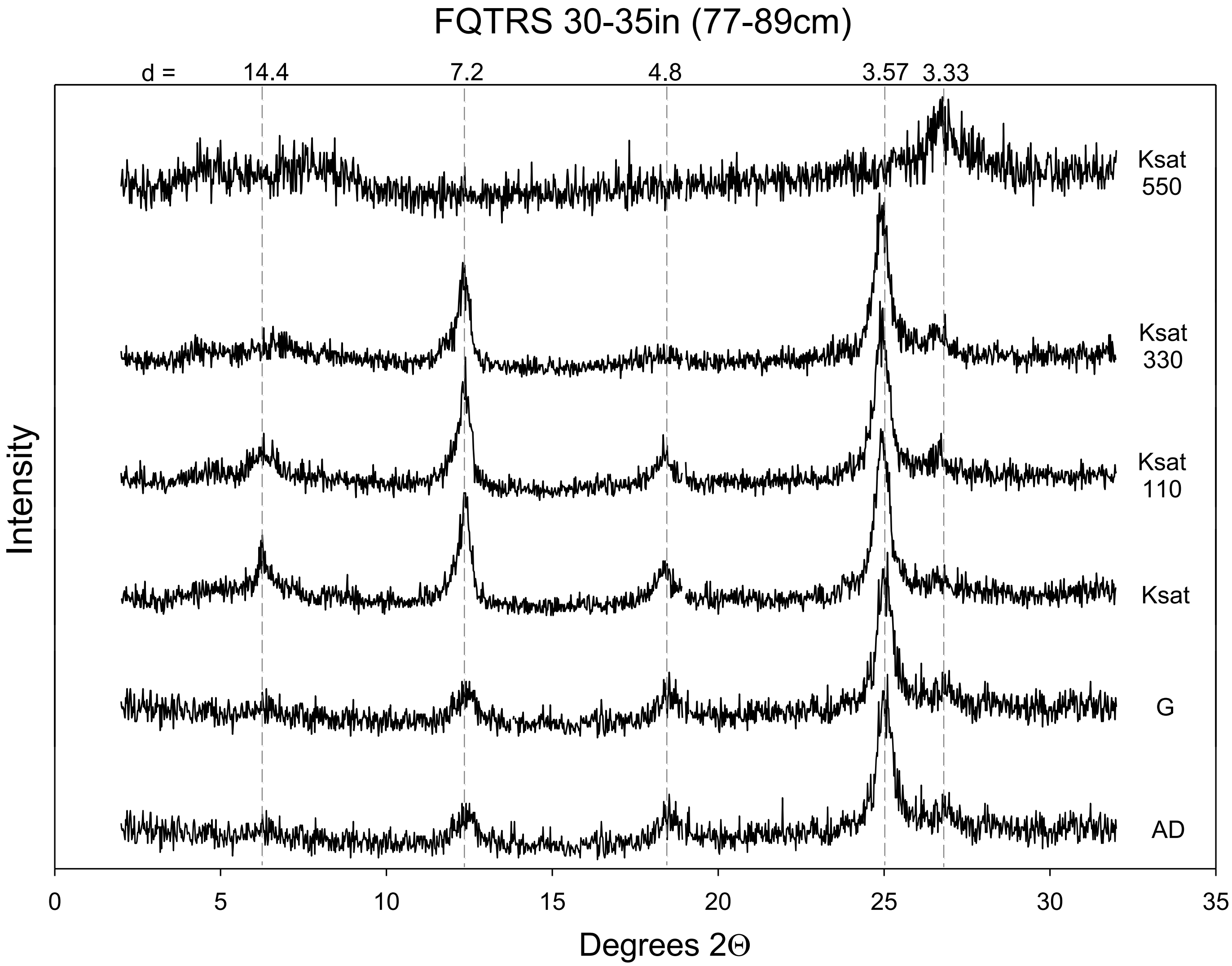

Figure B15: FQTRS 77-89 cm, glycol, K, and heat treatments. Note the collapse of the kaolinite peak with K and heat, and collapse and shift of the HIV peak. There is also very little quartz in the clay size fraction at this depth.

Appendix C: Ion concentration in extraction residues

Table C-1: Concentration of ions in extraction residue.

Sample Name	Cs 50% mg/kg	Cs 10% mg/kg	Rb 50% mg/kg	Rb 10% mg/kg	K 50% g/kg	K 10% g/kg	Ba 50% mg/kg	Ba 10% mg/kg	Sr 50% mg/kg	Sr 10% mg/kg
FQ 0-20	1.3	1.8	15.2	16.0	2.8	3.3	103.2	110.2	17.5	16.5
FQ 21-36	1.3	2.1	20.9	22.0	4.3	4.8	144.9	177.3	22.1	25.4
FQ 37-56	1.0	1.7	22.2	23.7	3.2	4.9	161.9	155.7	23.6	23.4
FQ 57-76	0.9	1.7	21.3	22.4	5.1	4.9	153.8	152.0	22.6	22.3
FQ 77-96	1.8	2.3	27.9	30.3	4.8	5.8	167.4	179.6	24.3	26.4
FQ 97-117	2.7	3.4	28.9	33.5	4.4	5.5	154.9	170.6	24.4	26.3
FQ 118-122	3.2	5.4	35.8	45.6	5.1	5.2	145.3	178.6	27.4	31.3
FQ 123-157	20.	7.7	24.1	37.3	2.6	3.7	81.6	198.5	20.5	42.7
FQ 158-178	2.6	5.3	23.0	28.9	2.2	2.8	63.1	124.6	18.8	31.5
FQ 179-203	2.4	4.3	23.6	25.7	2.3	2.5	63.2	91.0	19.0	24.9
TRS 0-15	1.3	1.8	18.0	9.7	2.9	3.6	99.7	171.5	18.3	18.4
TRS 16-31	0.8	1.4	17.9	21.6	3.8	4.1	110.0	128.5	19.1	21.5
TRS 32-46	0.8	1.2	18.3	22.3	4.6	4.6	126.7	151.3	20.7	24.5
TRS 47-61	1.8	1.6	17.0	24.4	4.0	4.7	133.2	147.1	16.2	24.5
TRS 62-76	2.5	5.6	31.6	45.2	3.9	4.3	104.1	180.3	24.0	33.8
TRS 77-89	2.6	5.1	29.3	45.6	3.3	4.0	91.6	134.6	24.9	30.3
QAL 0-15	0.6	0.8	47.4	50.4	16.1	-	434.3	490.8	39.5	42.2
QAL 16-28	0.9	1.0	61.8	45.3	20.0	18.9	530.5	441.8	49.1	33.8
QAL 29-38	1.7	2.0	61.7	63.1	16.2	17.6	415.6	482.1	36.4	38.7
QAL 39-46	2.1	3.6	54.6	60.6	10.1	10.0	236.0	308.0	20.7	26.9
QAL 47-61	1.6	-	32.6	30.6	7.2	9.4	171.3	-	8.1	10.8
QAL 62-76	2.2	2.4	30.3	44.7	11.5	12.8	245.2	357.6	7.6	27.7
QAL 77-84	1.6	2.5	35.6	53.8	7.0	10.2	210.1	286.3	11.0	23.9
QAL 85-91	1.9	3.4	43.2	47.2	7.7	7.8	170.1	247.1	16.5	25.6
QAL 92-104	1.8	2.7	42.6	44.7	8.1	8.0	180.5	205.3	18.2	20.8